FAST NEUTRON ELASTIC SCATTERING AND POLARIZATION

Thesis

Submitted by

AMENA BEGUM

for the degree of

DOCTOR OF PHILOSOPHY

Department of Physics,

University of Edinburgh,

JUNE 1979.

TO MY PARENTS

ABSTRACT

Fast neutron elastic scattering has been studied for 2.9 MeV, 16.1 MeV and 14.2 MeV energy from medium and heavy nuclei. Angular distributions of polarization and cross-section have been obtained for 2.9 MeV neutrons scattered from Fe,W,Tl, Pb, Bi, and U. Simultaneous measurement of angular dependence of polarization and cross-section has also been done for 16.1 MeV neutrons from Fe, Cu, I, W, Hg, Pb and C by the pulsed beam time of flight technique. The angular ranges covered are from 20° to 160° at intervals of 14°. The experimental distributions have been corrected for the attenuation of the incident neutron flux in the scatterer, neutron mutiple scattering and for the finite source-sample-detector geometry using a Monte-Carlo computer programme. Correction for relevant inelastic scattering has been done wherever possible with available experimental inelastic cross-sections.

The measurements are compared with the optical model calculations based on 'global-fit' parameters as well as parameters reported previously for particular nuclei. These parameters are found not to be very successful in fitting both differential cross-section and polarization for either 2.9 MeV or 16.1 MeV scattering. Much better fits to both cross-section and polarization are obtained by individual analyses for most of the nuclei. The calculations for 2.9 MeV neutrons are combined with Hauser-Feshbach compound elastic calculations done both with and without the Moldauer level width fluctuation correction. It has been observed that while for U both the calculations provide a similar fit to the experimental data, for W, Tl, Pb and Bi calculations including the level width fluctuation correction provide a better fit. For the 16.1 MeV case the fit to the polarization with the optimum parameter set for heavier nuclei are poorer than for the lighter ones, with a marked discrepancy in the magnitude of polarization around 20° for most of the nuclei. The parameter sets which give the best fits to the data at 2.9 MeV and 16.1 MeV are presented. A large spin-orbit potential is observed for the heavier nuclei at 2.9 MeV while for the 16.1 MeV case there is evidence of including a volume imaginary term.

14.2 MeV neutron double scattering measurements on Cu, and Pb for 20° and 34° employing the associated particle time of flight technique resulted in a similarly large magnitude of polarization as observed for the present 16.1 MeV scattering and also reported earlier. Optical model calculated polarization for 14.2 MeV, based on global parameters shows a small magnitude around 20°, as in the case of 16.1 MeV neutrons. Attempts to modify conventional optical model parameters to account for such a discrepancy are made. It is observed that increasing the radius or the diffuseness of the spin-orbit term reproduces the large magnitude of polarization around 20° without affecting the polarization for the rest of the angles or the cross-section.

CONTENTS

C O N T E N T S (Contd.)

C O N T E N T S (Contd.)

CHAPTER 1

INTRODUCTION.

1.1 Neutron Elastic Scattering

Much of the understanding about the microworld up to date has been established by means of collision processes, the most direct form of which is the scattering of an incident particle by a target. A free particle or rather a beam of such particles with known characteristics, e.g. energy and spin impinges upon a target particle, interacts with it and becomes scattered into a modified free state. Observation of the intensity, energy, angular distribution and polarization of the scattered beam enables one to infer the nature and strength of the forces that acted between the projectile and the target during the collision and may even provide some insight to possible structure of the scatterer. Experiments with neutrons as projectile have, ever since its discovery, served as an effective means for investigating the interaction mechanism between nucleons and nuclei. The fact that the neutron is uncharged, makes it a more penetrating probe with which to extract information on typical features of nuclear reactions more clearly.

When a neutron collides with a heavy nucleus, there is considerable probability that it will pass through the nucleus without losing any energy, suffering only a change of direction (There is of course the small transfer of energy to the recoil ing nucleus to conserve momentum). This corresponds to shape elastic scattering. However, a neutron can also be absorbed, thereby producing an intermediate nucleus which can then decay by various modes. In particular, the intermediate nucleus can emit a neutron with smaller energy (inelastic scattering) or with energy equal to that of the initial neutron (compound elastic scattering). The elastic scattering cross-section can therefore be expressed as the sum,

$$\sigma_{el} = \sigma_{SE} + \sigma_{CE} \qquad (1.1)$$

where σ_{SE} is the shape elastic cross-section and σ_{CE} is the compound elastic cross-section. $d\sigma_{el}/d\Omega$ has an angular dependence, and

$$\sigma_{el} = \int \frac{d\sigma_{el}}{d\Omega}(\theta)d\Omega \quad . \qquad (1.2)$$

The formation of the compound nucleus, suggested by Bohr[1], based on the picture of the nucleus as a system of particles with strong interactions and short range forces was found to be a successful model for interpretation of the nuclear reaction mechanism at low energies.

One of the earliest works on fast neutron elastic scattering was the measurement by Amaldi and his collaborators[2], of the angular distribution of 14 MeV neutrons from lead, that demonstrated a diffraction pattern. The first systematic experimental investigation of neutron elastic scattering was performed by Walt and Barschall[3], who measured the differential cross-sections for elastic scattering from a large number of elements at 1 MeV neutron energy. Meanwhile the suggestion that neutrons produced from reactions are, in general, polarized, opened up a straightforward way for investigating spin-orbit forces in nuclear reactions. Since polarization occurs only by interference of different partial waves, it is expected to show a more sensitive dependence on the scattering amplitude than the elastic differential cross-section and reflect the spin-orbit interaction directly. It was first pointed out by Wolfenstein[4] for the specific case of the D-d reaction, that the neutrons produced should be polarized due to spin-orbit coupling, even if both the incident deuteron beam and the deuterium target are unpolarized. This was shown to be true by Huber and Baumgartner[5] and Ricamo [6] who observed polarization of D-d neutrons, using scattering from ^{12}C as polarization analyser.

Since conventional neutron detectors are insensitive to neutron spin direction the detection and measurement of neutron spin is not straightforward. A summary of various approaches is contained in the review article by Haeberli[7]. In the following we outline the principle of the method most commonly employed for fast neutrons, using nuclear elastic scattering as the analyser. In this method use is made of the fact that in the presence of a spin-orbit force, the scattered flux exhibits a right-left asymmetry in the scattering plane. The right-left asymmetry precisely means that the particles with spin up and those with spin down relative to the plane of scattering have different cross-sections for scattering through a given angle if spin-orbit coupling occurs, resulting in a net imbalance. This right-left asymmetry depends on two factors, namely i) the degree of polarization of the incident beam and ii) the extent to which the scattering is sensitive to spin orientation. Thus it is obvious that the measurement of the polarization involves a 'double scattering' process. In a conventional neutron system the first scattering is replaced by the neutron producing reaction (Fig. 1.1). A beam of charged particles with energy E and momentum along the direction $\vec{k}_o$ is intercepted by the target T_1 which acts as the polariser. Neutrons produced at an angle θ_1 from this reaction with energy E_n and polarization P_n proceeding in the direction $\vec{k}_1$ are intercepted by a second target T_2, referred to as the analyzer. The beam of polarized neutrons is thus scattered through an angle θ_2 with final momentum along the direction $\vec{k}_2$ and can be detected at two azimuthal angles $\phi = 0$ and $\phi = \pi$ in the plane of scattering. The number of neutrons moving in the direction $\vec{k}_2$ in a given time is

$$N(\theta_2,\phi) \propto \sigma_u(E_n,\theta_2)[1 + P_n(E,\theta_1)A(E_n,\theta_2)\cos\phi] \qquad (1.3)$$

where $\sigma_u(E_n,\theta_2)$ is the differential cross-section for scattering an unpolarized beam of energy E_n through an angle θ_2 and $A(E_n,\theta_2)$ is

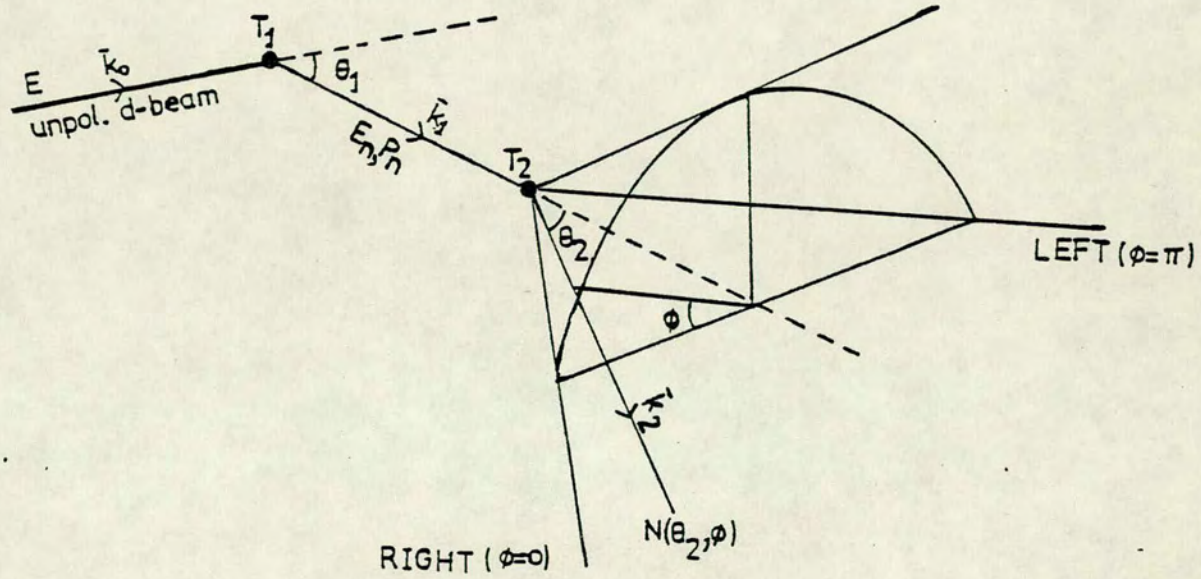

Figure 11 Principle of a typical neutron polarisation experiment

the amplitude of azimuthal variation (the analysing power). It has been shown theoretically and proved experimentally, that for strong interactions, even for targets of non-zero spin, the quantity $A(E_n,\theta_2)$ is equal to the polarization that would result in the elastic scattering of an unpolarised beam of energy E_n through an angle θ_2. We can denote this as $P_S(E_n,\theta_2)$. Thus for a coplanar double scattering process the ratio of the intensities for scattering twice to one side and once to the other side is given by,

$$r = \frac{N_R}{N_L} = \frac{1 + P_n(E,\theta_1)P_s(E_n,\theta_2)}{1 - P_n(E,\theta_1)P_s(E_n,\theta_2)} \qquad (1.4)$$

where N_R and N_L are the scattered intensities to the right ($\phi = 0$) and left ($\phi = \pi$) respectively. From the above expression we get for the product P_nP_s, referred to as the asymmetry,

$$\varepsilon = P_nP_s = \frac{N_R - N_L}{N_R + N_L} = \frac{r - 1}{r + 1} \quad . \qquad (1.5)$$

Thus if the analysing power $P_s(E_n,\theta_2)$ is known for some nucleus then the value of the polarization P_n can be obtained for a number of source reactions. On the other hand if the polarization from a source reaction is known, then the polarization due to scattering from a number of nuclei can be studied. It is worth noting here that according to the sign convention adopted at the Basel symposium[8], particles with spin pointing along the direction $\vec{k}_o \times \vec{k}_1$ are positively polarized.

1.2 Optical Model

Systematization and correlation of experimental data is usually achieved by constructing different theoretical models representing particular features of the system under study and searching for the one that gives the best description of the data. We do not expect any given model

to be completely or uniformly successful, but instead study the situations in which the model succeeds or fails in order to assess its relevance and validity. If the model gives a good fit to the data, then it provides some information about the mechanism of the nuclear reaction process, about the structure of the nuclei and also permits reliable prediction of new information. The compound nucleus model[1)] mentioned in Sec. 1.1, gave a good description of experimentally observed capture cross-sections and closely spaced resonances at low energy and led to a number of qualitative conclusions regarding cross-sections of nuclear reactions[9)]. The shell model structure of the nucleon-nucleus interaction furnished evidence of the free movement of a captured nucleon in the nucleus, differing from the strong interaction model and succeeded in explaining the properties of ground states and low lying excited states. The fluctuations correlated with target mass and incident neutron energy observed in the total neutron cross-section data of Barschall and his collaborators[10)], which were not describable satisfactorily in terms of either of the models mentioned above, led to the introduction of the optical model by Feshbach, Porter and Weisskopf[9)]. This model introduced the important simplification of transforming the many body problem of nucleon-nucleus interaction into a two body problem by replacing the target nucleus by a potential and considering the passage of the nucleon through the nuclear potential in analogy with the passage of light through a material medium which exhibits refraction and absorption. Just as in the case of an optical medium, we can introduce an index of refraction, which is a complex quantity if there is absorption. Thus we require two quantities to characterize the optical properties of nuclear matter. In order to determine these parameters one needs to solve the Schrödinger equation for a neutron (we are concerned with neutrons although the same is true for protons also with addition of the Coulomb interaction) where the motion of the neutron is described by a wavefunction associated with a complex potential

of the form,

$$V(r) = -U(r) - iW(r) \quad , \tag{1.6}$$

where the real part of $U(r)$ describes the average potential energy of the neutron inside the nucleus and may be expected to resemble the shell model potential for bound states and the imaginary part $W(r)$ describes the absorption effect due to compound nucleus formation. This approach to nuclear reaction is called the optical model of the nucleus and the complex potential is called the optical potential. The solution of the Schrödinger equation with such an optical potential yields phase shifts, from which one can calculate the total cross-section, the differential cross-section for shape elastic scattering and also the cross-section for the formation of a compound nucleus. The compound elastic scattering cross-section, which must be added to the shape elastic scattering cross-section, particularly at low energies (< 5 MeV), can be estimated by a method proposed by Hauser and Feshbach[11] utilizing a statistical assumption about the density of levels of the compound nucleus system and an additional assumption that all compound states for which energy, parity and angular momentum are conserved are populated with a probability proportional to the penetrability of the incident neutrons.

The optical model can predict polarization as well, provided that the above form of the potential is modified to include a spin-orbit term as proposed by Bjorklund and Fernbach[12], proportional to $\vec{\ell}\cdot\vec{\sigma}$ where $\vec{\ell}$ and $\vec{\sigma}$ are the angular momentum and Pauli spin operators, respectively. Thus we have for the optical potential describing scattering as well as polarization

$$V = -U(r) - iW(r) - V_{so}(r)\,\vec{\sigma}\cdot\vec{\ell} \quad . \tag{1.7}$$

The explicit expressions and the detailed parametrisation of the various

components of the optical potential will be dealt with later (Chapter 6).

1.3 Review of Past Work and Motivation

A reasonably complete evaluation of an optical model requires that the energy dependence and angular dependence of the differential cross-section and polarization be systematically measured as a function of mass number and compared with the predictions of the model. A great deal of agreement has been achieved between theoretical angular distributions of elastic scattering cross-sections, with due allowance for compound elastic scattering,and experimental results of neutron differential elastic scattering [13,14] cross-sections. However a similar statement about the model regarding the angular distribution of polarization can not be made with confidence because of the lack of systematic and sufficient quantity of experimental data. A brief review of the measurements done so far, presented in Table (1.1), would reveal the state of knowledge of fast neutron polarization in relation to the optical model of elastic scattering. It is clear from the table that, although experiments with scattering of polarized neutrons started more than two decades ago with the work of Adair et al.[15], the amount of experimental material is hardly sufficient with regard to the range of energy, angle or nuclei concerned, to arrive at a general conclusion about the success of the optical model. It has already been pointed out by Galloway[16] from a survey of experiments on the angular dependence of polarization, that there has been a concentration of effort on neutron energies of 4 MeV and below. Around such energies (< 5 MeV) the interpretation of data in terms of the optical model is complicated by competing compound elastic scattering. It has also been shown by Galloway[16] from the survey of the quality of optical model fit to the angular dependence of

polarization, that there is no convincing fit for nuclei lighter than Ti or for neutron energy less than 3 MeV. Around 3 MeV some of the recent measurements[31,34,35] show encouraging results so far as fitting by the optical model is concerned.

Ellgehausen et al.[31], with probably the most accurate measurement, have shown that polarization of 3.25 MeV neutrons elastically scattered by Ti, Cr, Fe, Cu and Zn in the angular range 30° to 138° is well described by the optical model of Rosen[32], with allowance for compound elastic scattering based on Hauser-Feshbach theory[11]. The optical model calculations predicted a positive maximum in the polarization angular distribution at backward angles centred around 160°. Zijip and Jonker[34] have made measurements on angular distribution of polarization of 3.2 MeV neutrons from twenty elements from Ti to Bi. However the angular range they covered was from 30° to 150° for only 9 of the nuclei, including Ba and Bi, with $Z > 50$ and 30° to 75° for the rest of the nuclei. A comparison of their result with those of Ellgehausen[31] for the nuclei in common showed reasonably good agreement except for Zr around 90°. In addition to the calculation, using the known global potentials of Rosen et al.[38] and Becchetti and Greenlees[39], they have attempted individual parametrisation for each element separately. Neither of the global potentials gave a good description for all elements, although the general trends of the polarization pattern was described reasonably. Individual analysis gave much better fits to the data although the parameters showed marked variation from element to element and also unrealistic values in some cases. The model calculations again showed a positive maxima around 160° for all the nuclei in this set. Waheed[35] made measurements on scattering of 2.9 MeV neutrons from Fe, Cu, I, Hg and Pb, covering the angular range of 20° to 160°. While these measurements for Cu and Fe are in good agreement with both those of Ellgehausen[31] and Zijip

Table 1.1

Experimental Data	Neutron Energy (MeV)	Scattering Nuclei	Scattering Angle	Remarks
1. Adair et al.[15] (1954)	0.4	11 nuclei from Cu to Bi	90°	Addition of spin orbit term to the optical potential proposed by Feshbach et al.(9) could describe the variation of polarization with atomic number.
2. Remund[17] (1956)	3.3	Cu,Ta,Pb & Bi	30°-150° at intervals of 15°	The variation of polarization with atomic number appeared similar to calculation done with optical potential, including spin-orbit term.
3. McCormac et al.[18] (1957)	3.1	Be,C,Cu,Zr,Sn & Pb	30°-135°	Poor agreement with available optical model calculations.
4. Clement et al.[19] (1958)	0.38 & 0.98	21 nuclei from V to U.	55°, 90° and 130°	The experimental results could not be reproduced satisfactorily using model calculations.
5. Brown et al.[20] (1961)	0.3 to 1.4 at 50 keV interval	Cu,Zn,Mo & Cd	55° and 90°	Marked departures are found between results obtained and predictions of optical model calculation including spin-orbit potential.
6. Wong et al.[21] (1962)	24.0	C,Al,Fe,Sn,Pb & Bi	20°-80°	Measured polarization showed reasonable agreement with optical model calculations of Bjorklund and Fernbach(12).
7. Durisch et al.[22] (1963)	3.4	Cu, Zr	6 angles from 55° to 120°	Qualitative fit to the optical model calculations obtained for Cu only.
8. Elwyn et al.[23] (1964)	0.275 & 0.85	Zr,Nb,Mo & Cd	5 angles from 24° to 150°	Analysis of the data in terms of an optical model equivalent to the non-local model of Perey & Buck (24) were consistent qualitatively.
9. Bredin[25] (1964)	2.0	Al, Si,Fe & Co	30° to 120°	Reasonable fit for Co and Fe observed with a local optical potential including surface absorption & spin-orbit coupling.
10. Olness et al.[26] (1964)	1.5	18 nuclei from Y to U	51.5°	An additional term proportional to n-excess (N-Z)/A, was required in the optical potential to fit the data.
11. Ferguson et al.[27] (1966)	0.4, 0.7, 1.0	14 nuclei from Ti to Bi	55°	A reasonably good account of the results obtained with optical model calculations using the equivalent local potential of Perey & Buck (24)
12. Mahajan[28] (1967)	4.4, 5.0 & 5.5	20 nuclei from Ti to Bi	40°,60°,90°	Optical model calculation showed reasonable agreement on the average
13. Gorlov et al.[29] (1967)	4.0	11 nuclei from Be to Bi	10° to 170° at intervals of 10°	Only qualitative similarity with optical model calculations for most cases was obtained.
14. Wiedemann et al.[30] (1969)	3.25	Mg, Al, Si, & S	30° to 140°	The results disagree with optical model predictions.
15. Ellgehausen et al.[31] (1969)	3.25	6 nuclei from Ti to Zr	19 angles from 30° to 140°	The overall behaviour for all except Zr could be described by optical model calculations with Rosen (32) parameters.
16. Pasechnik et al.[33] (1970)	1.5, 2.0	Ti and Cr	10 angles from 20° to 145°	Poor agreement between experimental results and calculation with optical potential.
17. Zijip & Jonker[34] (1973)	3.2	20 nuclei from Ti to Bi	30°-75° and 30°-150°	A reasonably good agreement for nearly all the elements except W was obtained.
18. Waheed[35] (1975)	2.9	Fe,Cu,I,Hg,Pb	20°-160° at intervals of 14°	Rosen optical potentials described the polarization data of Cu & Fe whereas very little success was achieved in fitting data for the heavier nuclei (40).
19. Hussein et al.[36] (1977)	10.4	Bi and Pb	2° to 65°	The data over the complete range was reproduced using a standard optical potential with addition of long range interaction between the neutron magnetic moment and the nuclear Coulomb field.
20. Galloway & Waheed[37], (1979)	16.1	Cu and Pb	20° - 90°	The polarization values for scattering angles around 20° markedly different from the optical model fit using global potentials.

and Jonker[34], the polarization for Pb at 34° differs markedly from Zijip and Jonker's value at 30°. Galloway and Waheed[40] have recently shown that optical model calculations combined with Hauser-Feshbach formalism, using global potentials as well as parameters suggested by previous experimenters for particular nuclei were not very successful in fitting both the differential cross-section and the polarization data of Waheed[35].

The present measurements are intended mainly to add more data in the region of the heavier nuclei. They include one set of measurement on the angular distribution of polarization of 2.9 MeV neutrons for Fe, W, Tl, Bi, Pb and U. The measurements for Fe, the polarization values for which are quite well established at about this energy, are included primarily to serve as a test of the reliable performance of the apparatus.

Despite the need for polarization data for energies above 5 MeV where the absence of complication from compound elastic scattering is expected to provide a better test of the optical model, there are only three experiments reported as can be seen from Table 1.1. Measurement by Wong et al.[21] at 24 MeV are well fitted by the Becchetti and Greenlees[39] potential, although the measurements were only for the angular range of 20° - 80°. The 10.4 MeV data of Hussein et al.[36] are also well fitted by the optical model, using the parameters of Becchetti and Greenlees[39]. However Galloway and Waheed[37] have shown recently that the large magnitude of polarization they observed for scattering angles around 20° for 16.1 MeV neutrons scattered from Cu and Pb could not be fitted, using the global potentials of either Rosen or Becchetti and Greenlees. Another set of optical model parameters for Pb, proposed by Fu and Perey[41] from a satisfactory fit of differential elastic scattering cross-section data of about 14 MeV neutrons, also failed to reproduce the 20° value of polarization,although the fit for the rest of the angles is reasonably

good. Thus a repetition of the 16.1 MeV measurement for Cu and Pb was felt necessary in addition to the measurements for C, Fe, I and Hg done in the present work for the same angular range.

Repetition of the 16.1 MeV measurement, discussed in Chapter 4, still showed a large magnitude of polarization around 20^{o} for Cu and Pb. This encouraged the attempt to set up a double scattering experiment with 14.2 MeV neutrons, the nearest achievable energy to provide a value of asymmetry by a quite different experimental technique. The measurement was done for Cu and Pb for angles of 20^{o} and 34^{o}.

Since the complete evaluation of the optical model requires differential cross-section as well as polarization measurements, the present work includes also the determination of the differential elastic scattering cross-section for scattering of 2.9 MeV and 16.1 MeV neutrons for the set of nuclei and the same angular range as for the polarization measurements. From the differential cross-sections for "left" and "right" scattering of the beam of neutrons, the differential cross-section for the elastic scattering of unpolarized neutrons was evaluated by,

$$\frac{d\sigma_{el}}{d\Omega}(\theta) = \tfrac{1}{2}\left[\frac{d\sigma_{el}}{d\Omega}(\theta,0) + \frac{d\sigma_{el}}{d\Omega}(\theta,\pi)\right] \qquad (1.8)$$

In the chapter to follow, we present a description of the detector and polarimeter assembly and the CAMAC system employed in the present work for collection of data. Chapter 3 and Chapter 4 include the experimental technique used, along with experimental results and comparison with available results in nearby energy and angular ranges for the 2.9 MeV and 16.1 MeV data, respectively. The double scattering system is dealt with, along with the results, in Chapter 5. Chapter 6 is concerned with the model fitting of the data.

CHAPTER 2

NEUTRON POLARIMETER AND DETECTION SYSTEM

2.1 Introduction

The fast neutron polarimeter used in the present work is capable of polarization and cross-section measurements at twelve different angles. Detectors in pairs at each scattering angle are placed symmetrically at equal distances from the centre of the scattering sample and can be rotated about the neutron beam to interchange their roles in order to cancel any instrumental asymmetry. Measurements can be made at four azimuthal angles from 0° to 360° at intervals of 90°. The present chapter includes a detailed description of the polarimeter, the detectors and the CAMAC system used for automatic data collection.

2.2 The Neutron Polarimeter

Fig. (2.1) shows the schematic drawing of the polarimeter originally designed[35] for holding six neutron detectors and later modified to hold twelve detectors. Two identical wheels of internal and external diameters 62 cm and 86 cm respectively and 2 cm in thickness fixed together by four steel rods of 3 cm diameter and 57.5 cm length constitute the frame for holding two circular tables. Each table has an arrangement for holding six detectors at three different angles at equal distances of 30 cm from the centre, half of them to the right and half to the left. At the centre of each table there is a holder for the scattering sample made from very finely machined steel in the form of a shallow cup of 2.5 cm diameter. On one table the holder is fixed to a threaded base so that the height of the cylindrical scattering sample can be adjusted with its axis normal to the scattering table. The sample holder on the other table is connected to a compressed air cylinder. The sample is fixed to this holder and can be driven pneumatically either to sit on the sample holder on the other table, to be in the

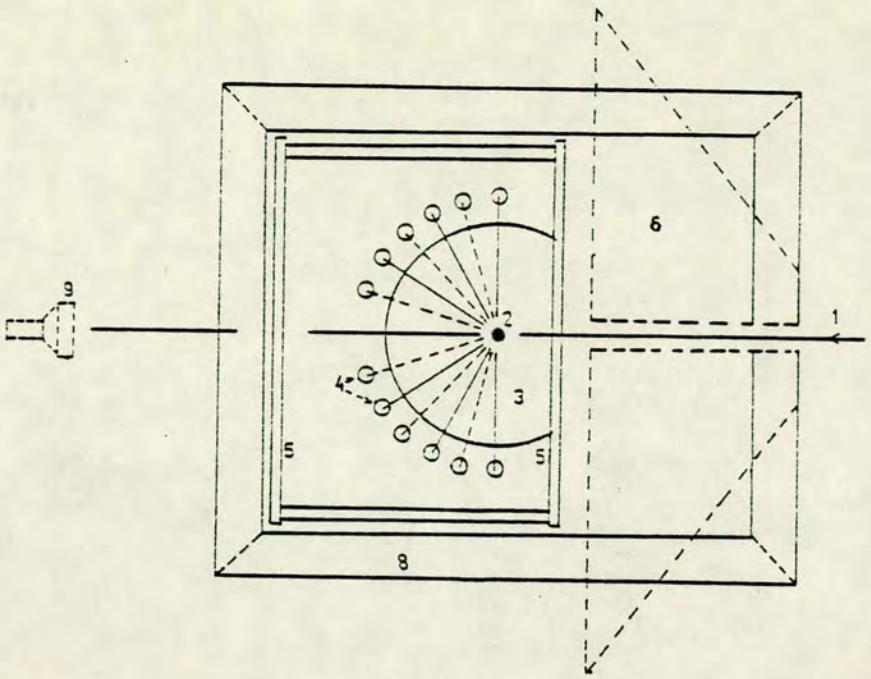

(a)

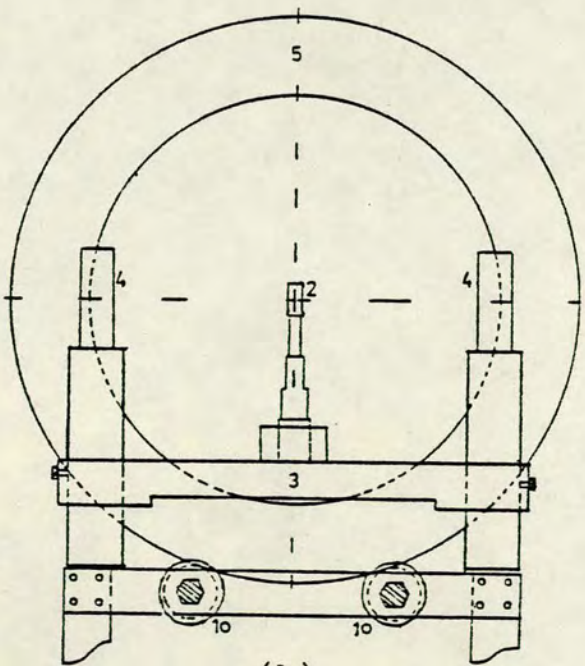

(b)

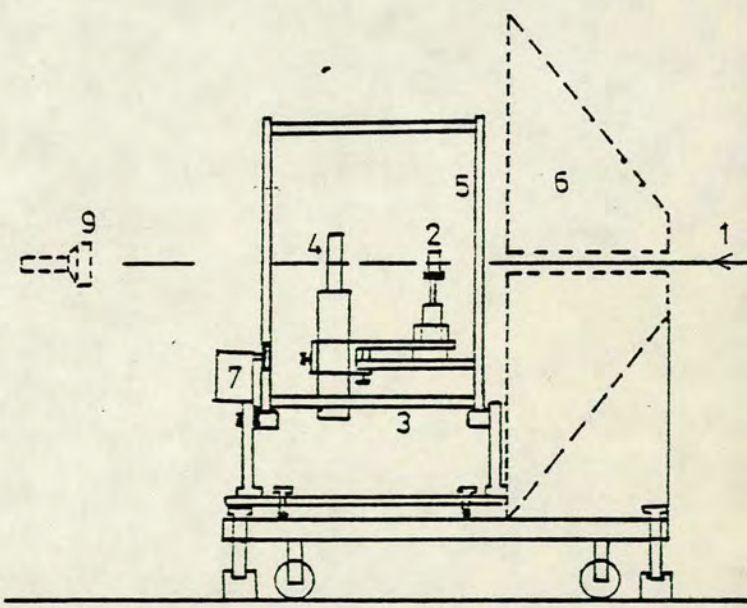

(c)

Fig. 2.1. Fast neutron polarimeter
(a) plan (b) rear view (c) elevation
(1) Incident beam direction. (2) Scattering sample. (3) Scattering table. (4) Scattered neutron detectors. (5) Wheels for rotation of the scattering system about the neutron beam direction as axis. (6) Neutron collimator. (7) Motor for rotating the wheels (5). (8) Main frame (9) Collimated beam monitor. (10) Bearing supporting the rotating wheel.

neutron beam for scattering measurements or can be withdrawn from the beam for background measurements.

The polarimeter in its original design[35] with only one scattering table had six detector holders with arms fixed to two rotatable stainless steel rings at the centre of the table, the other ends being supported on the table by ball bearings. This arrangement enabled measurements to be made at three angles in the range 20° to 90° at a time. In the modified design, the rotating arms on the original table are fixed at the three angles 20°, 48° and 76°. The second table is made with detector holders fixed to the table at 34°, 62° and 90°. Thus the polarimeter in the present form is capable of making measurements at six angles simultaneously. For angles greater than 90°, the polarimeter can be lifted up and rotated through 180° so that the same set of detectors can be used for measurement at six angles from 90° to 160° at intervals of 14°. Repetition of the measurement at 90° for the two positions of the polarimeter serves as a test for the reliable performance of the system. The detectors can be moved up and down in the holders with their axes perpendicular to the scattering table and fixed in position at required height by threaded screws.

The two wheels with scattering tables and the detectors rest on four rotating bearings mounted on two stands, so that they are free to rotate about an axis joining their centres. The two stands with the rotating bearings are fixed rigidly to a thick steel plate which can be moved up and down by jacking screws with four ball races under them. The plate can be adjusted sideways as well by another four screwed rods fixed on to a frame structure. Thus with these facilities the accurate alignment of the polarimeter can be easily achieved. Once the alignment is done satisfactorily, the plate can be fixed rigidly in its position by the four screwed rods and two additional

rods fixed to the rear end of the frame structure.

The polarimeter is rotated by means of a motor which drives the rear wheel. Switching the motor on and off is achieved by means of two relays so that the rotation of the polarimeter can be controlled by an automatic arrangement. The cradle can be stopped at any of the four azimuthal angles by having four microswitches arranged in order and operated by four small projecting hexagonal rods fixed to the rear wheel. Measurements made at $\phi = 0$ and $\phi = \pi$ provide the required polarization and cross-section data, while those at $\phi = \pi/2$ and $\phi = 3\pi/2$ provide a test for any instrumental asymmetry. The direction of rotation of the cradle is automatically reversed at $\phi = 0$ and $\phi = 3\pi/2$ to avoid twisting of the cables connected to the detectors. In any of the four positions of the polarimeter, movement of the sample 'in' or 'out' of the neutron beam is achieved by using a third relay which activates a solenoid valve supplying compressed air to the cylinder connected to the sample holder.

The whole of the polarimeter assembly described above was placed in turn, behind a collimator for neutron collimation and shielding appropriate to each particular experiment being carried out. The collimator was placed in front of the neutron producing target at the particular emission angle selected for each particular experiment. The axial alignment of the polarimeter was attained each time by viewing the neutron producing target through a series of cylindrical and disc alignment inserts with 2mm diameter axial holes. The cylindrical inserts were fitted accurately into each end of the collimator tube, while the two disc alignment inserts were fitted accurately into the holes of the two rotating wheels. The polarimeter was moved vertically and sideways till the centre of the target was in line with the axis of the 2mm holes in all the inserts. The height of each scattering sample, moved to the 'in' beam position, was adjusted so that the centre of the sample

was in line with the centre of the target. The neutron detectors were also adjusted so that the centres of the liquid scintillators were at the same height as the centre of the sample. Fig. (2.2) shows the polarimeter with the detectors at angles from 90^{o} - 160^{o} with the sample in the 'out' position.

2.3.1. The Neutron Monitors

As mentioned above, the polarimeter in the present work has been used with twelve neutron detectors (to be referred to as the side detectors hereafter) simultaneously for the polarization and cross-section measurements. Two more neutron detectors were used in addition for monitoring the yield of the neutrons. One of the monitors was placed very close to the neutron producing target and will be referred to as the target yield monitor (TYM). It was used for normalisation. The other monitor, to be referred to as the collimated beam monitor (CBM), was placed with its axis in line with the axis of the polarimeter forming a part of the polarimeter system. This detector was used to monitor the neutron flux in the collimated beam and to measure the transmitted flux when the scattering sample was placed in the beam. The distance of the CBM from the target was chosen so that the collimated neutron cone irradiated the whole area of the scintillator. The construction of the TYM and the CBM used in each experiment will be described with the particular experiment.

2.3.2 The Side Detectors

The side detectors used are bubble free liquid scintillators (type NE213) in cylindrical containers mounted either on a photomultiplier type EMI9814B or 56 AVP. The cylindrical containers, made from aluminium of

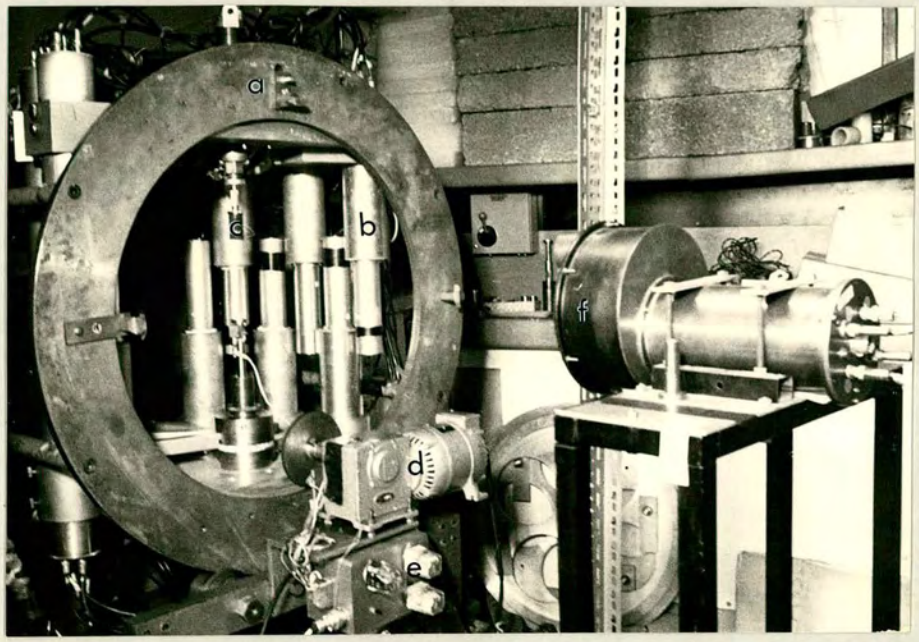

Fig. 2.2. Photograph of the fast neutron polarimeter

(a) rotating wheel

(b) scattered neutron detector

(c) scattering sample (out of beam position)

(d) motor for driving the rotating wheel

(e) relays

(f) collimated beam monitor.

2mm thickness, are 15.24 cm in length and 5.08 cm in diameter. The inner walls of the containers are painted white with light reflector of the type NE526 to improve the light collection efficiency. A small glass chamber with a neck of 2 mm diameter fixed to the top end of the scintillator container keeps the sensitive volume of liquid free from the nitrogen bubble introduced to allow for the expansion of the liquid due to temperature fluctuation. The glass window fitted to the other end of the scintillator container is coupled to the photocathode of the photomultiplier tube, by using optical contact grease. Fig.(2.3) shows a schematic diagram of the bubble free scintillator cell. Each photomultiplier tube is surrounded by a mu-metal shield, to minimise possible gain changes on rotation due to the effect of the earth's magnetic field. The photomultiplier tube with its dynode chain is mounted in a light tight container. The carbon resistor dynode chains used with the two types of tube are shown in Fig.(2.4). Fig.(2.5) shows the different parts of the detector assembly.

2.3.3 The Scintillation Process

The scintillation process is one of the oldest methods of nuclear radiation detection. In the famous Rutherford scattering experiment, Rutherford and his collaborators used this technique for detecting the alpha-particles. The basic principle remains the same, the major difference in the technique is that now photomultiplier tubes are used to register particles instead of individuals looking through microscopes.

A group of transparent dielectric materials, including many of the noble gases, organic and inorganic single crystals, polycrystalline materials and organic liquids, are transparent to some part of the wavelength spectrum of the photons emitted by the excited atoms and ions

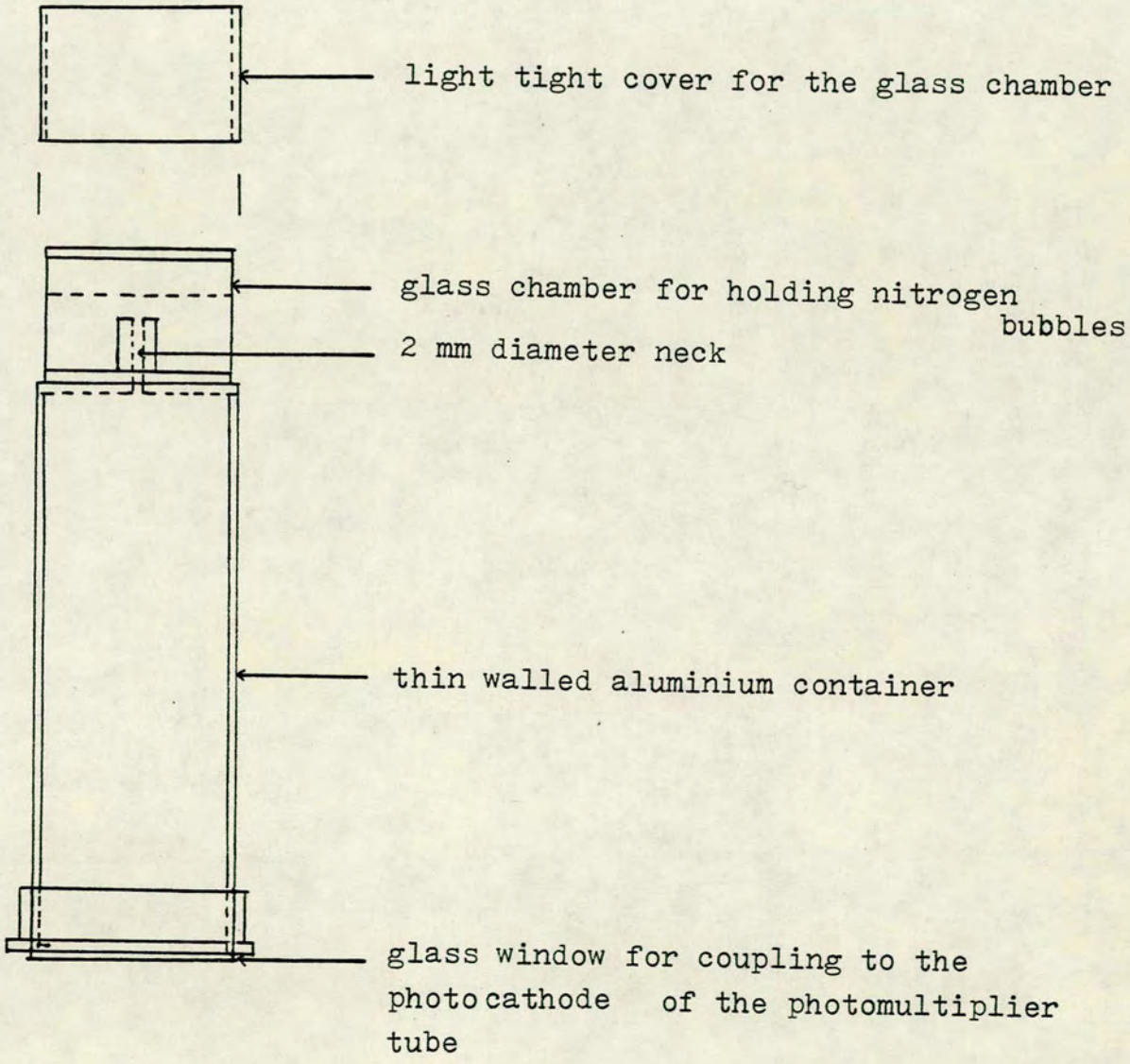

Fig. 2.3. NE213 liquid scintillator container.

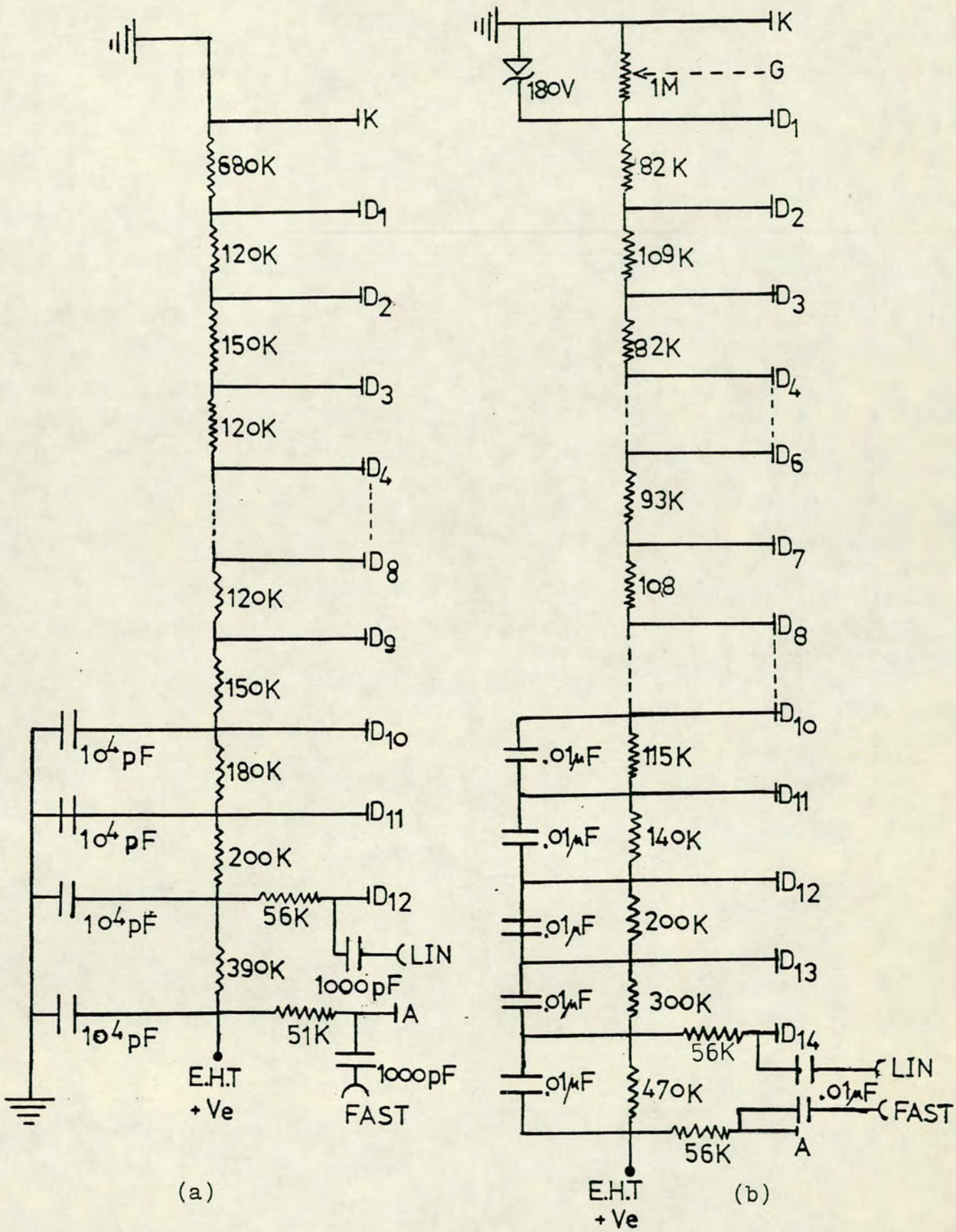

Fig. 2.4. Carbon resistor dynode chain used with

(a) EMI 9814B type photomultiplier tube

(b) 56 AVP type photomultiplier tube.

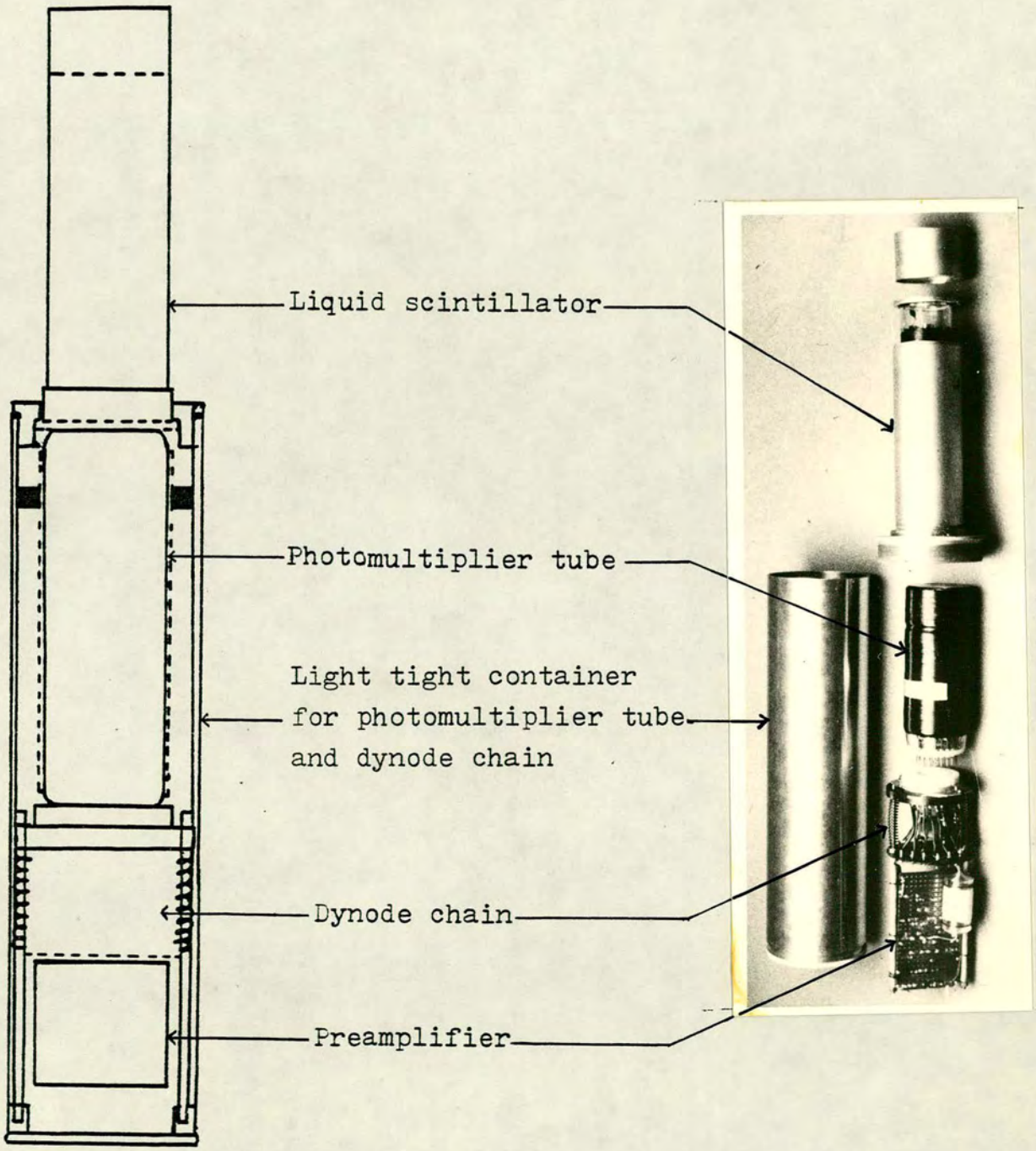

Fig. 2.5. The neutron detector assembly.

along the path of the charged particle. These photons can therefore be detected outside the transparent material and it is found that their number is approximately proportional to the energy lost within the material, in the same way as the number of ions produced within a gas dielectric detector is proportional to the energy lost in that detector. The materials which exhibit this property are known as scintillators and the process as the scintillation process.

Major advances towards the modern scintillation counter came with the development of efficient photomultiplier tubes of high gain, which are sensitive to very small light intensities. The scintillations produced from radiation are converted into amplified electrical pulses at the photomultiplier output. These pulses can be fed to electronic circuits for amplification, selection and counting. Coltman and Marshall[42] first reported the successful detection of α-particles, protons, fast electrons, gamma-rays and neutrons, using a scintillation detector with a well-designed optical system for reflecting the scintillation emission on to the photocathode of the photomultiplier. During the time that has elapsed since 1947, the scintillation detector has become the most versatile type available for nuclear-radiation detection. The development of improved scintillators for higher efficiency, shorter resolving time, and ability to distinguish between types of radiation, has taken place in parallel with major improvements in the design of photomultipliers for better optical coupling, higher photoelectric sensitivity, increased photocathode area, increased gain and improved time resolution.

The theory of the process of scintillation in different classes of scintillators has been studied in detail by several authors[43]. In the present work the organic liquid scintillator type NE213 is used for neutron detection. In organic materials the luminescence arises from the electronic structure of the conjugated and aromatic organic molecules.

The luminescence can occur in all phases, i.e. liquid, solid, plastic, gaseous or vapour state. The scintillation efficiency depends on the ionisation density, i.e. on the mass and charge of the exciting particles. The scintillation emission spectrum of a pure crystal is the same as the fluorescence spectrum apart from any effects due to self-absorption. In a binary system the emission spectrum is mainly characteristic of the solute, the excitation energy obtained by the solvent molecules from the incident radiation being transferred to the solute molecules prior to emission. In a ternary system the emission spectrum is mainly that of the secondary solute, the excitation energy being transferred via the primary solute to the secondary solute. The scintillation emission in these systems has a finite rise time or slightly lengthened time duration due to the finite time of intermolecular energy transfer. The scintillation pulse generally consists of fast and slow components. The fast scintillation decay time is typically of the order of 2-3 ns, while the slow component that is analogous to delayed fluorescence with an emission spectrum similar to the fast component, decays non-exponentially over a period of several microseconds.

When the excitation of molecules is produced by particles that results in high ionization and excitation density in the scintillator, the efficiency of the scintillator, i.e. the number of photons emitted for a given energy deposited, is reduced. This effect is known as ionisation quenching and occurs for all organic scintillators. This effect mainly affects the intensity of the fast component and has little effect on the slow component. However the characteristic decay time of the two components is unaffected by quenching. As a consequence, the shape of the scintillation light pulse is changed and is dependent on the nature of the particle incident on the scintillator. Thus the quenching effect forms the basis for all particle identification

techniques based on the principle of pulse shape discrimination in organic scintillators.

2.3.4 Pulse Shape Discrimination

It is evident from the discussion in the last section that the scintillation pulse from most organic scintillators decays with fast and slow components and the relative intensity of these components is dependent on the nature of the incident radiation. The organic liquid scintillator NE213 used in the present work has the particular feature that the intensity ratio of the fast component to the slow component, due to proton recoils from incident neutrons, is less than that due to electron recoils from incident gamma-rays. Discrimination between these two incident particles is possible by distinguishing the different current pulses resulting at the photomultiplier output from the different intensity ratios. Various techniques have been developed and employed for making such a distinction. The technique used in the present work is the one commonly referred to as the zero cross over timing technique. The technique relies on the fact that the zero cross over instant of an integrated and doubly differentiated pulse from a single dynode carries information about particle identification. The time from the start of such a processed pulse to the zero crossing of the amplitude baseline is longer for neutron associated events than those due to gamme-rays. Thus pulse shape discrimination (PSD) can be obtained by measuring the time intervals between the origins of the pulses and their zero cross over instants, which can subsequently be converted to proportional pulse heights. A time difference of 20-30 nanoseconds can be conveniently obtained between the cross over of pulses produced by recoil electrons and by recoil protons. The different shapes of pulses from one of the lower dynodes of the photomultiplier tube

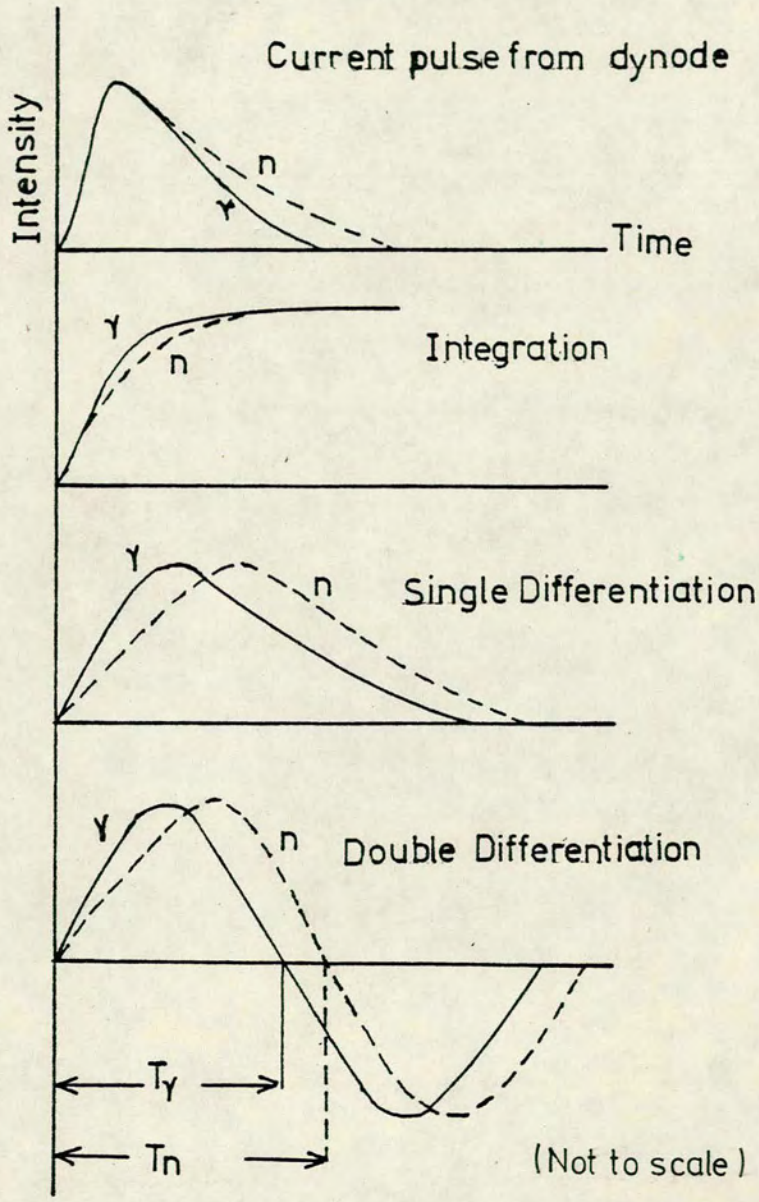

Fig.2.6 PHOTOMULTIPLIER PULSE SHAPES EXPLOITED FOR n-γ PSD

after integration and differentiation are as shown in Fig. (2.6).

The block diagram of the circuit employed for the neutron-gamma pulse shape discrimination is shown in Fig. (2.7(a)). The linear pulse from one of the last few dynodes of the photomultiplier, after passing through a preamplifier, is used as input for both a linear amplifier and a pulse shape discrimination unit. The PSD units use the circuit designed originally by H. Davie[44], with minor modification necessary to use available integrated circuit components. The technique employed is similar to that investigated by Roush et al.[45]. A discriminator is used at the output of the linear amplifier for setting an energy bias and also at the output of the PSD unit for rejection of γ-rays. All the discriminators incorporate a variable delay up to 3 μsec so that the optimum time relationship between the two discriminator output pulses could be obtained for the following ANDgate. Fig. (2.7b) shows a spectrum with separated peaks due to γ-rays and neutrons from one of the twelve detectors, using a PSD unit as described above. The spectrum is obtained by using a ^{252}Cf source and rejecting events with light output less than those produced by 200 keV electron recoils in the scintillator. It is clear that amplitude selection of the output pulses from the PSD unit, using the integral discriminator, will provide the required rejection of γ-ray events.

2.4 The CAMAC System

A CAMAC standard instrumentation interfaced to a PDP 11-05 computer, designed and developed by F.McN. Watson[46], was used for automatic data collection and unattended supervision of the running of the experiment. The system includes a pulse height analysis programme that enables the accumulation of the twelve side detector spectra along with associated

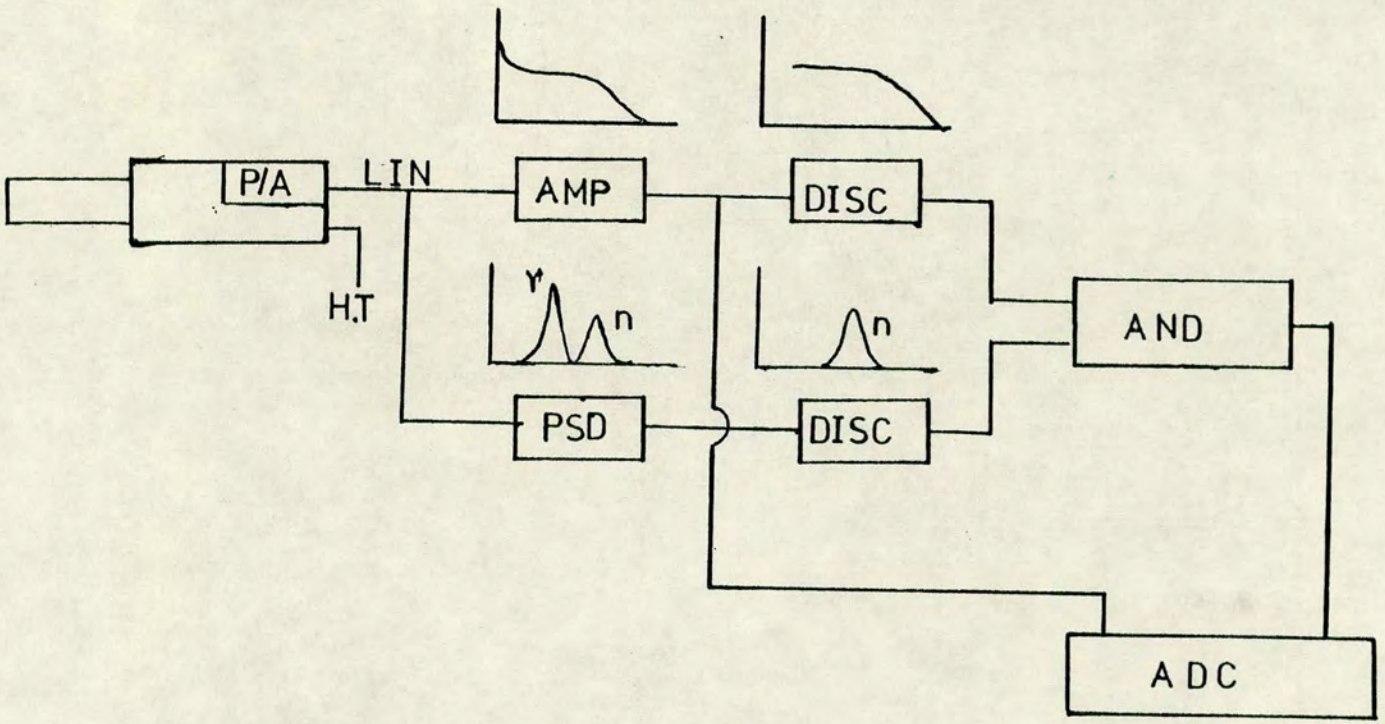

Fig 2.7a BLOCK DIAGRAM OF THE ELECTRONICS USED FOR n-γ PSD

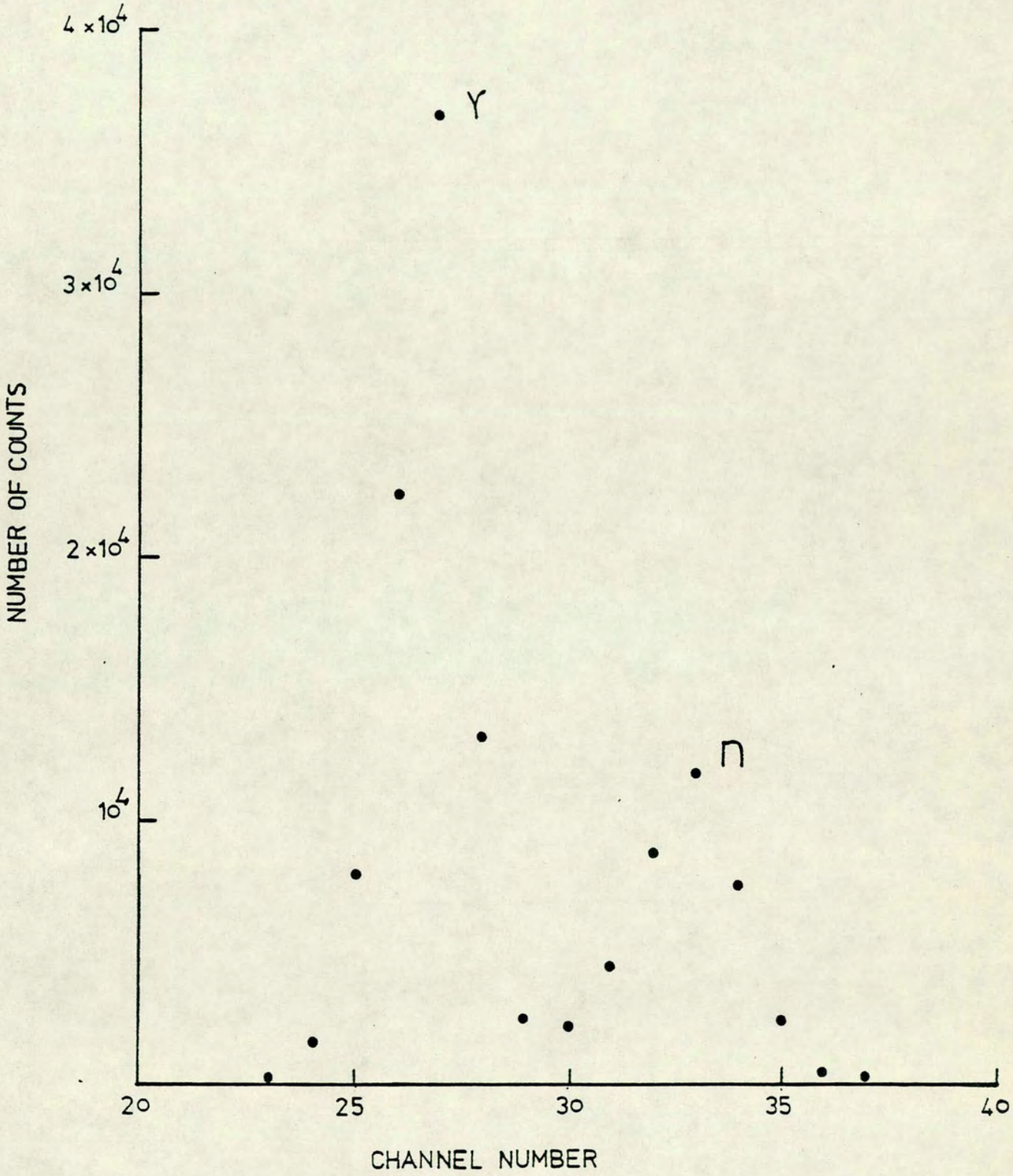

Fig. 2.7.b. Pulse shape discrimination spectrum obtained with a ^{252}Cf source.

monitor counts for each measurement condition of the polarimeter. It also includes provision of driving the polarimeter to any of the four azimuthal positions, as well as sample changing for each position automatically. In addition, facilities for performing routine checks of detector bias settings are included. In order to provide efficient data handling independent of any other computer system, a disk storage system using a flexible disk drive is included. The control programme for the system was written in PAL-11, the PDP-11 family assembly code, using a text editor and assembler programme provided in the Physics Department PDP-11-45 computer and the Edinburgh Regional Computer Centre's multi-access system (EMAS).

2.4.1 Pulse height analysis facilities are provided by two Laben 256 channel ADC's (model 8213). One of these is coupled directly to the CAMAC dataway through a parallel input register. The other ADC is also connected to a similar register through a routing unit, to perform event tagging and pile up detection for the twelve side detectors. The circuit diagram of the routing unit is shown in Fig. (2.8). The routing unit accepts slow coincidence pulses from the twelve 'AND' gate outputs corresponding to the twelve side detectors. These are used to produce a four bit code for each detector to determine the subgroup in which the corresponding event should be registered and a tag bit that is set if a pile up condition is detected. The circuit is constructed from TTL integrated circuits of the Texas 74N range. The binary codes for '1' to '12' for the twelve detector events are produced by using two 7404 hex inverters and four 7430 eight input NAND gates. But activation of two inputs at the same time, produces a code which is the logical 'OR' of the two, resulting in misrouting or pile up. The circuit includes facilities for detecting the misrouted events, by recording the events

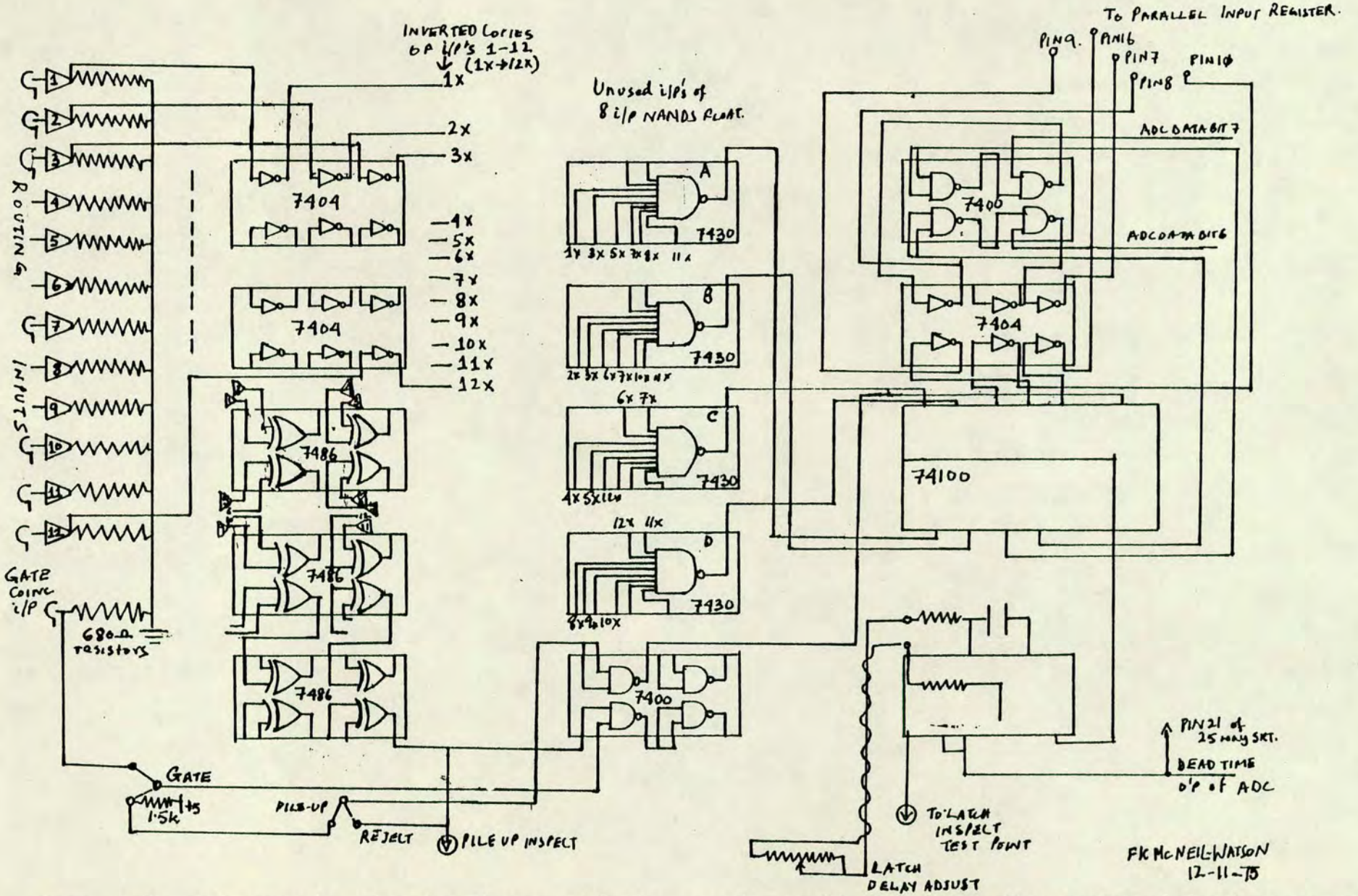

Fig. 2.8. Electronic circuit diagram of the routing unit used with the twelve detector system.

that result in the codes 13, 14, 15. In order to detect such events all the twelve AND gate outputs are fed to a network of exclusive 'OR' gates (7486), which produces a high output when at most one of the inputs is high. This output forms the fifth routing bit. The leading edge of this output is also used to trigger the production of an output pulse, which is fed to the coincidence input gate of the ADC to enable it to accept an event for analysis. This pulse is further gated by an over-riding strobe to the coding unit. This facilitates the provision of a gating pulse to all the neutron detectors from the slow coincidence.

The five routing levels mentioned above form the input of five of the D type flip-flops of an eight bit latch, which is clocked by a strobe pulse of variable duration. This pulse is produced when the dead time output from the ADC switches low, indicating that an input has been detected. The state of the routing information and pile up bit is stored at this instant and does not change until the ADC accepts another input. The 'data-ready' signal causes the ADC's 6 bit of data and the associated five bit code to be transferred to the input register.

In addition to the pulse height analysis facilities described above, the system also provides simple pulse counting by a CAMAC module, containing four independent six decade scaling circuits. The zero scaler is used as the system clock driven by an external 1 MHz oscillator, so that overflows are signalled at the rate of one per second. The scaler counts down from any required counting time to zero, then disables the common control level, stopping the ADC's and scalers simultaneously. The other three scalers are used for general purpose counting like the total monitor counts.

Four data accumulation regions, each of 1024, 16 bit words, are available. In routing mode the first 12 × 64 channels of any area are used for pulse height analysis and the last block is used for the scaler

information. The scaler totals along with the total ADC counts, pile up and misrouting figures are stored in the last block to double precision. For data collection with no associated pulse height information a multi-scaler mode in which the number of events for each detector is recorded to double precision for detector stability or false asymmetry checks with standard sources is also available.

Display facilities for the pulse height analysis are provided by a 19" rack mounted long persistence oscilloscope driven by a CAMAC display driver. Data may be displayed as a complete group of 1024 channels or in groups of 256 or 64 channels. Independent channel limits for each sub-group within an area can be displayed as 'bright up' spots on the oscilloscope. Provision for typing out data, either in complete blocks of 1024 channels or in groups of 256 or 64 channels, are included. Overlapping of spectra of different accumulation region, spectrum subtraction and addition and integration of counts between required channel limits are also available.

Fig. (2.9) shows a photograph of the racks of electronics associated with the neutron detectors and the CAMAC system.

2.4.2 It has been explained in Sec. 2.1 that the polarimeter used in the present experiment can be placed in any of the four azimuthal positions and that the scatterer can be put either 'in' or 'out' of the neutron beam for each polarimeter position. For automatic data collection a system by which the computer programme could drive the polarimeter to a particular condition was devised[46]. A.C. power is supplied to either the 'forward' or 'reverse' coils of the motor via the 'direction' relay. This power is fed from the mains through the 'movement' relay which starts and stops the rotation of the polarimeter. Each of the four positions is entered by a microswitch activated by the hexagonal rods

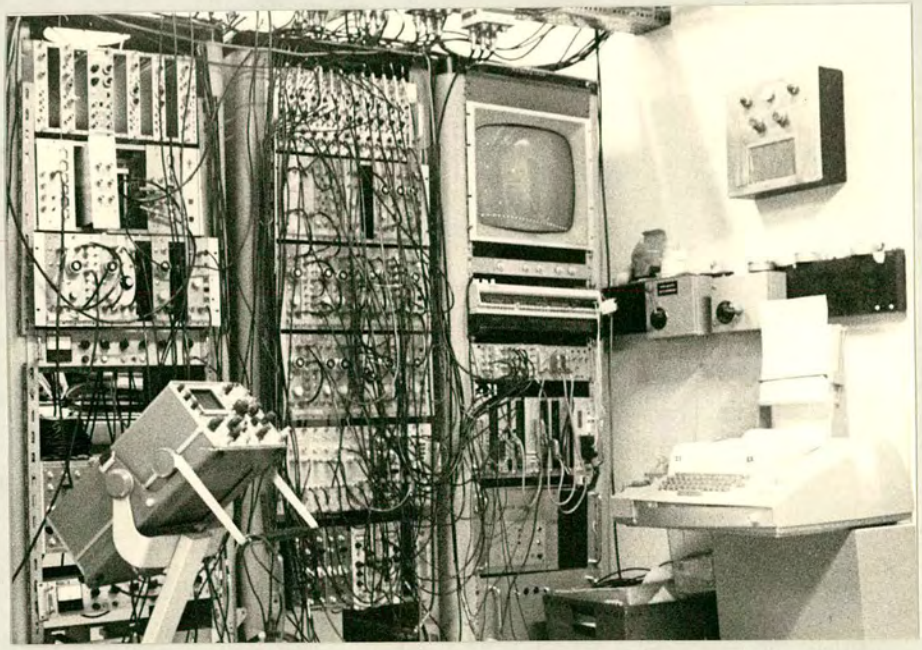

Fig. 2.9. Photograph of the racks of electronics used with the neutron polarimeter system.

fitted to the rear wheel of the polarimeter. For movement to a particular position, the appropriate direction is set, then power is applied to the coil of the 'movement' relay through the microswitch for the particular position. The motor then drives the polarimeter until this microswitch is activated, directing power from the relay coil to a divider network that causes a light emitting diode to indicate that particular position on the control panel. The sample changer relay activates the solenoid valve supplying compressed air to either port of the air cylinder, moving the sample either 'in' or 'out'. Microswitches indicating the sample position illuminate a LED on the control panel. A three position switch on the control panel selects either manual, off or automatic mode of the polarimeter control. For manual control power can be fed to the direction and movement relays by four position selecting switches and a direction switch and to the sample control relay by a changeover switch. Each of these switches has a relay in the CAMAC switch module connected across it, power being routed either through these or through the manual switches. The status indicated on the control panel LED's is monitored by a CAMAC parallel input gate. Automatic control is effected by the computer loading the appropriate relay code into the switch module and then waiting till the code is replicated on the input gate when the requested position is attained.

Automatic data collection is implemented by typing in a sequence of desired measuring positions, each associated with a distinct data accumulation area, with the three way key in the control panel switched to automatic mode. A measuring time to be used for all positions in the sequence and a repetition count for the number of cycles of the selected sequence are entered as well. When a command to begin the sequence is typed in, the computer drives the polarimeter to the first position and then works through the requested sequence. While in automatic mode

the position of the polarimeter is checked on every clock interrupt and an external error input, normally fed from the accelerator control system, is inspected. Whenever a fault in the polarimeter or the accelerator shut down is detected, execution of the sequence is automatically suspended. Execution can be restarted from where it stopped after the fault has been removed manually.

2.4.3 For independent and large scale data storage, a disk unit using a flexible disk drive, developed by F.McN. Watson[46], was used. The circuit of the CAMAC controller for the disk drive is given in Ref. 47. Each disk has a capacity of 153 blocks, each block consisting of a standard 1024 word data area with associated title and error checking code so that data from each accumulation area can be stored in a single block. A file system in which the disk is regarded as an array of sequential blocks, with a pointer to the first available space, was implemented. The current value of the pointer is recorded on a disk cartridge when it is unloaded, the value being read when the disk is loaded again. Any block up to the current pointer value can be read by specifying the disk address. A directory of the disk addresses followed by the title information from the current value of the pointer to the beginning of the disk can be typed out at any time. The programme also signals when no more space is available on a disk.

A data link to the PDP 11-45 computer of the Physics Department is established, using a CAMAC peripheral drive module. This is connected to a simple programme interrupt interface. Using this link, data blocks of 1024 channel can be transferred to the PDP11-45 and thence to the computing network of EMAS for off line analysis.

CHAPTER 3

SCATTERING OF 2.9 MeV NEUTRONS

3.1 Introduction

A deuteron beam accelerated to an average energy of 300 keV using the Van de Graaf accelerator was employed to produce 2.9 MeV neutrons from the $^{2}H(d,n)^{3}He$ reaction. The neutrons emitted at an angle of 49^{o} were collimated and scattered from cylindrical samples for studying the angular distribution of polarization and the differential elastic scattering cross-sections. Measurements were done for Fe, W, Tℓ, Pb, Bi and U for the angular range of 20^{o} to 160^{o} at intervals of 14^{o} using the polarimeter described in Chapter 2.2. Section 3.2 of the present chapter includes a description of the neutron producing target and the collimation and shielding employed for these measurements. The experimental technique and the electronics associated with the neutron detectors and the monitors used for this experiment are described in Section 3.3. Section 3.4 includes a description of the tests performed with standard sources for detector stability and for any instrumental asymmetry. This is followed by the data collection and the method of analysis. Experimental results along with different corrections and comparison with other available experimental results at comparable energy and angle are presented in the last section.

3.2 Neutron Producing Target and the Shielding

The targets used for the production of the 2.9 MeV neutrons were of deuterium absorbed in a thin layer of vacuum evaporated titanium backed by copper. A rectangular piece of such a target about 12 mm long and 3 mm wide was soldered on to the copper base of a stainless steel target holder in the form of a finger, with provision for water cooling. A liquid nitrogen cooled copper tube mounted near the target holder

helped to reduce oil contamination and carbon deposition on the target. An insulated disc of aluminium with an aperture of 6 mm × 2 mm was mounted before the liquid nitrogen cooled copper tube. This helped in obtaining a well focussed spot of the incident d-beam on the target by minimising the current on this disc by adjustment of the deuteron beam focus. The target was mounted, making an angle of 90^{o} to the incident d-beam, thus making the energy loss of the beam in the target material a minimum.

To stop the direct neutrons from the source reaction from being registered by the side detectors, a shielding construction which provided a collimated beam of neutrons, was used. Fig. 3.1 shows a schematic drawing of the target, collimator, polarimeter and the extra shielding described below. The collimator used was of the form of a trapezium, made from 1.27 cm thick steel, 46 cm in length with 30 cm square face nearest to the target end and 150 cm square face at the other end. The collimating tube for the neutron beam consisted of a brass cylinder of 5 cm diameter. A brass insert with tapering ends slid to the end nearest to the target and provided a throat of 1.5 cm diameter. Polythene inserts in the rest of the tube provided a taper from the throat towards the exit end. The position and diameter of the throat was such that the whole of the scattering sample was illuminated by the neutron beam. The tapering angles were chosen such that the cone of the neutrons from the target defined by the throat were not scattered from the surfaces of the tapering inserts. To reduce the energy of the direct neutron flux passing through the shielding by inelastic scattering a cylindrical block of lead, 20.3 cm in diameter and 20.3 cm in length, was introduced round the collimator tube near the target end. The rest of the volume of the collimator was filled with paraffin wax which moderates the neutrons which are subsequently captured and produce gamma-rays. To reduce this gamma-ray flux a

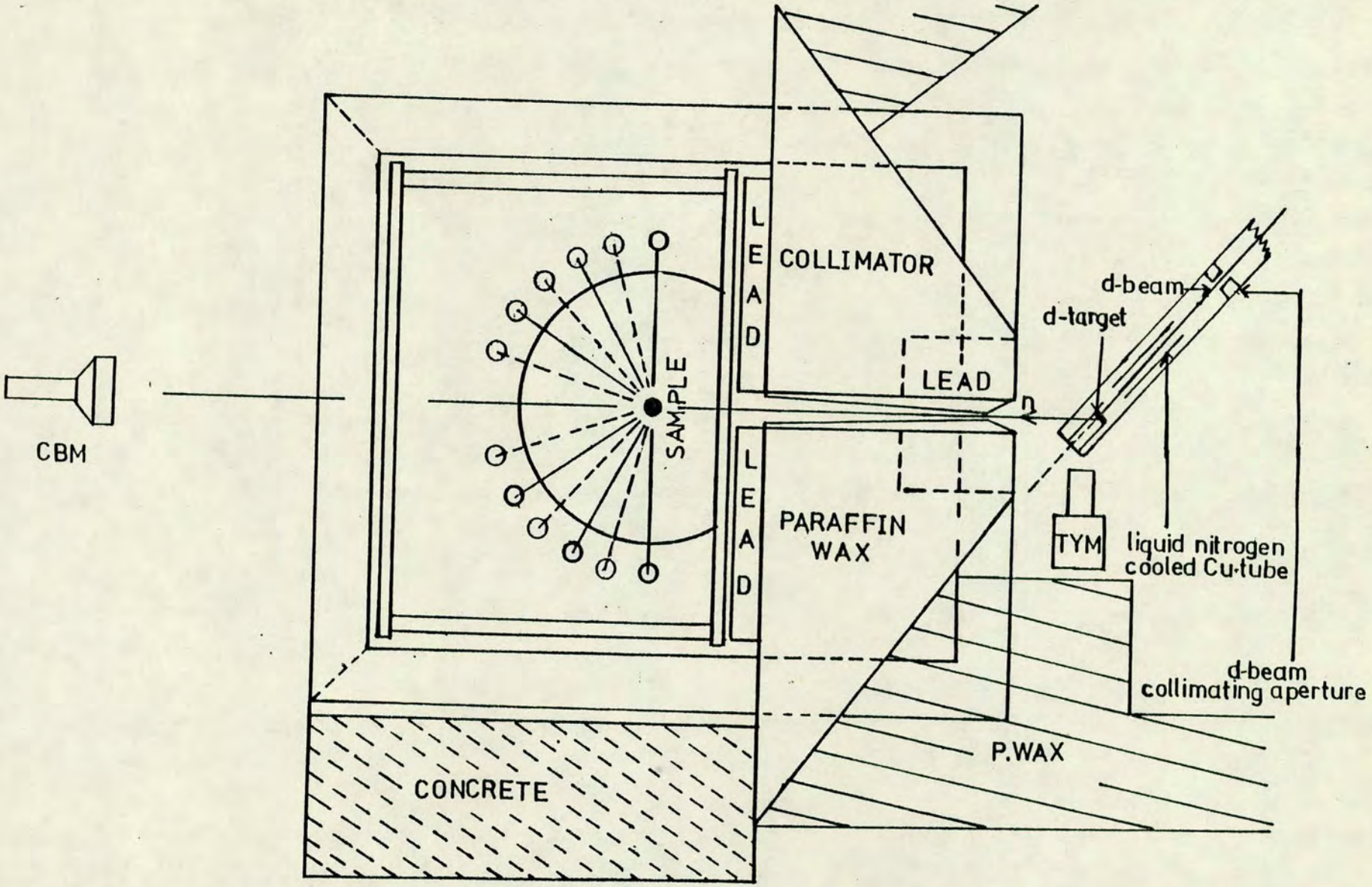

Fig 3.1 EXPERIMENTAL ARRANGEMENT FOR SCATTERING MEASUREMENT ON 2.9 MeV NEUTRONS

7.6 cm thick wall of lead was erected at the back of the collimator. The background due to scattering from the walls, floors and surrounding objects was minimised by shielding the polarimeter with walls of concrete blocks and a roof built from blocks of paraffin wax. The axial alignment of the polarimeter on the deuterium target was done as described in Chapter 2.1 and checked each time the deuterium target was changed.

3.3.1 Electronics of the side detectors

The system of electronics used with the twelve side detectors for the measurements of angular distribution of polarization and elastic scattering cross-section for 2.9 MeV neutrons is shown schematically in Fig. (3.2). As already described in 2.2.4, the linear output from the preamplifier of each detector was used as input for both a linear amplifier and a PSD unit. Two integral discriminators were employed at the output of the amplifier and the PSD unit for setting the energy bias and rejecting gamma-ray events. The linear energy bias was set to reject noise and events below about 150 keV recoil electron energy. The discriminator at the output of the PSD unit was adjusted to reject the gamma-ray events by setting the bias in the valley between the gamma and neutron peaks (Fig. 2.7). The logic outputs from the two discriminators were then fed into a three input AND gate. Thus the linear output from each detector in coincidence with the corresponding AND gate output provides a spectrum of events associated with neutrons of energy above about 0.5 MeV. The amplifier outputs from all the twelve detectors were fed into a linear OR gate while all the AND gate outputs were used with the routing unit. The OR gate output, used as input for the ADC handling routing, in coincidence with the output from the routing unit accumulates pulse height spectra in particular sections of the memory selected by the routing

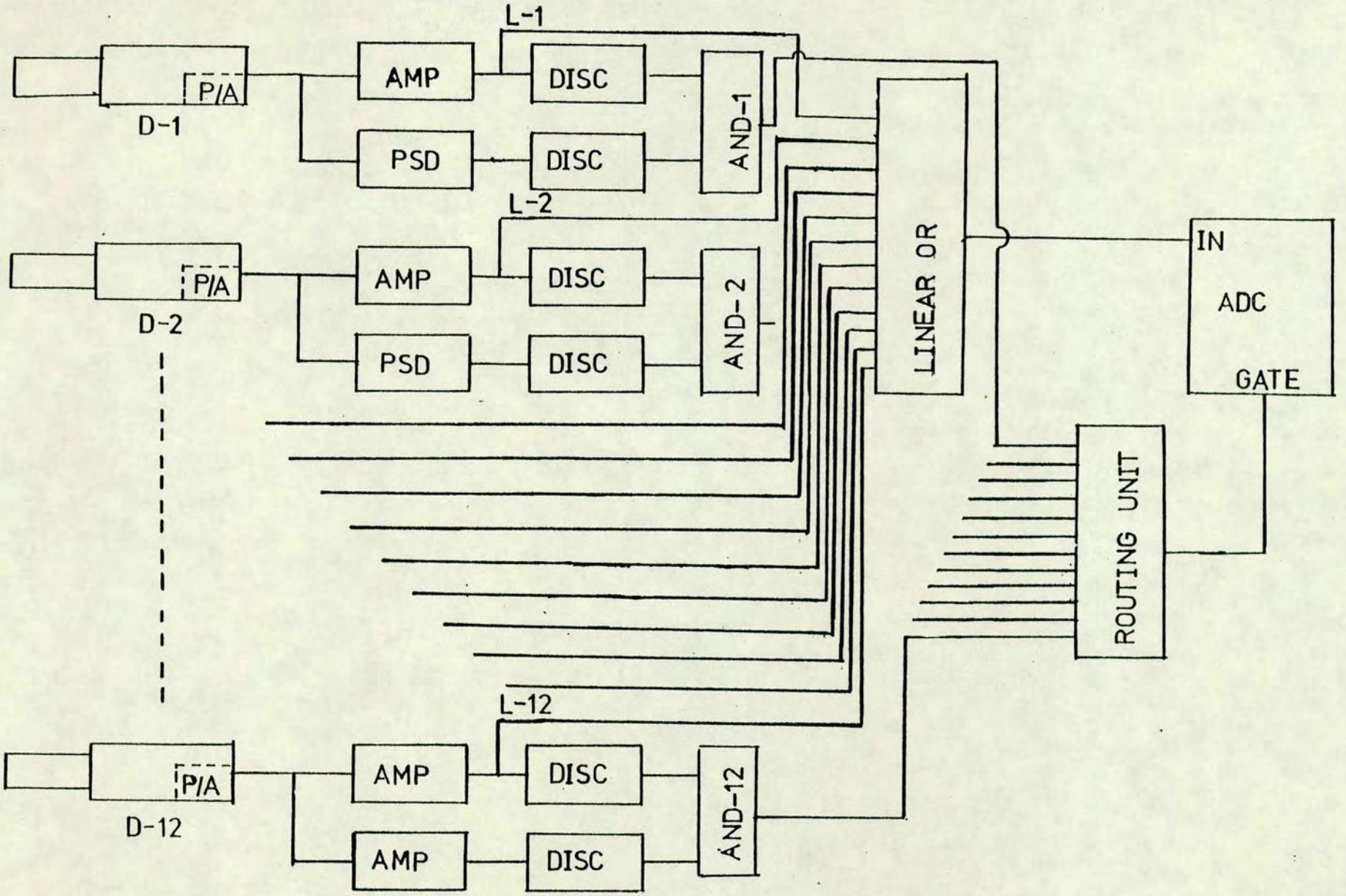

Fig. 3.2. A block diagram of the electronics used with the twelve detector system for scattering measurements on 2.9 Mev neutrons.

pulses as described in Chapter 2.3.1.

3.3.2 Target Yield Monitor

The TYM used to monitor the neutrons from the $D(d,n)^3He$ reaction consists of a LiI scintillator activated with Europium. A 2 mm thick layer of the crystal enriched to about 96% in ^6Li was coupled to a EMI6260 type photomultiplier tube. The scintillator was surrounded by 10.2 cm of paraffin wax to thermalise the fast neutrons. The neutrons were detected by the $^6Li(n,\alpha)^3H$ reaction, which has a very large cross-section for thermal neutrons. Any pulses due to gamma-rays would have a very small amplitude compared to the thermal neutron pulses and were rejected by pulse height discrimination. The detector with its container and the carbon resistor dynode chain used with it are shown in Fig. (3.3). No pulse height spectrum was collected and the number of neutrons detected for any fixed time was recorded in the CAMAC scaler by using the discriminator output.

3.3.3 Collimated beam monitor

The collimated beam monitor used consisted of a bubble free NE213 liquid scintillator of 12.7 cm diameter and 3.8 cm thick, contained in a glass cell. A small glass bulb above the sensitive volume of the liquid contained the nitrogen expansion bubble. A EMI 9814B type photomultiplier tube was coupled to the scintillator through a light guide of perspex in the form of a circular cone of 2.5 cm height and end faces of 10.2 cm and 2.5 cm diameter. The distance of the CBM was chosen (about 2 metres from the target) such that the whole area of the scintillator was illuminated by the collimated beam defined by the throat and, at the same time, distant enough to avoid contribution to

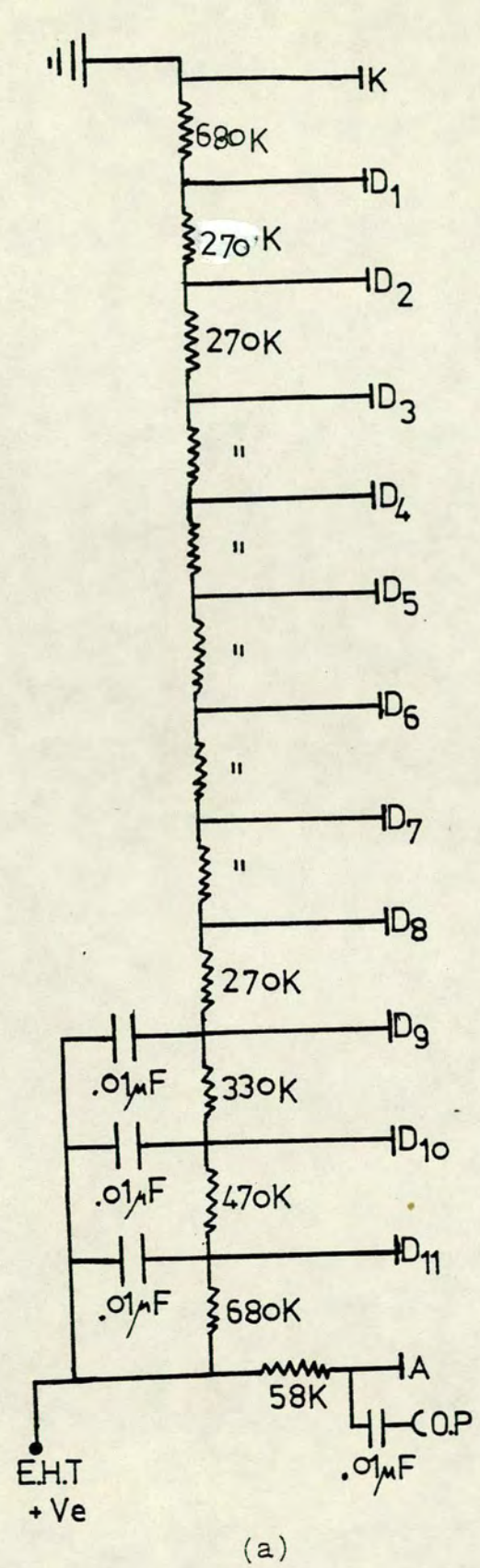

(a)

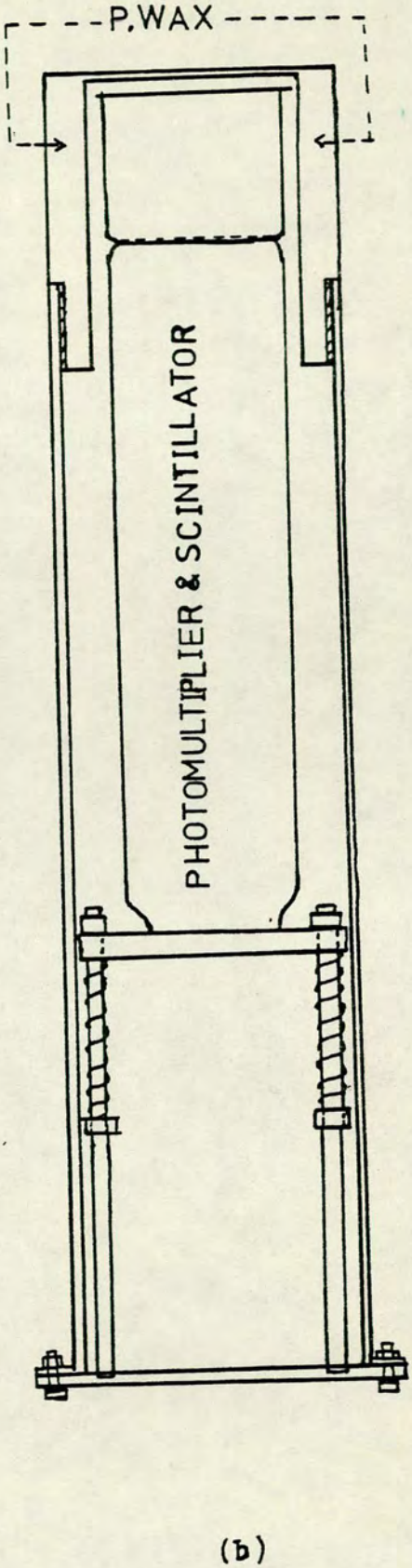

(b)

Fig. 3.3. Details of the TYM

a) Dynode chain used with the EMI 6260 type photomultiplier tube.

b) Detector with light tight container.

the background of the side detectors by neutrons scattered from the monitor. Pulse shape discrimination against gamma-rays was obtained by the zero cross-over technique described in Chapter 2.2.4. The system of electronics used with the CBM is essentially the same as with the side detectors, with the exception that instead of using an ADC for pulse height analysis, the AND gate output, after proper shaping, was used as an input for the CAMAC scaler to count the number of collimated neutrons only.

3.4 Tests for Instrumental Asymmetry

Before starting actual data collection for polarization and cross-section measurements one has to make sure that the detectors are stable and the polarimeter system is free from any false asymmetries. This was done in two phases using standard gamma and neutron sources and the multiscaler mode of the pulse height analysis system described in Chapter 2.3.1.

Initially the pulse shape discrimination circuits were disabled to allow the detection of gamma-rays in the scintillators. A strong ^{60}Co source ($\sim$ 1 mCi) was used for this test. The source was contained at the end of a cylindrical brass rod. A brass disc of 25 mm diameter was fixed to the other end of the rod so that it could be mounted in the sample holder. The height of the sample holder was adjusted accurately so that the source was at the centre of the polarimeter. Having the source fixed, the polarimeter was rotated to the two azimuthal positions for $\phi = 0$ and $\phi = \pi$ and recoil events were collected in all the detectors for the same length of time in the two positions. The rotation was done frequently after every 1000 seconds for better statistical accuracy. The number of recoil events in the two positions were

accumulated for about 30 hours, a length of time comparable to an actual data collection period. Table (3.1) shows the asymmetries resulting from such a test for all the twelve detectors.

The second phase of the test was to check for false asymmetry, using a ^{252}Cf source (0.5 μg, 268 μCi) of neutrons. This source was chosen, since the average energy of the neutrons from the source is about 2.5 MeV and is therefore comparable to the energy of the neutrons used from the reaction. A holder was made for the stainless steel capsule containing the source such that the holder could be fitted to the sample holder of the polarimeter and the height could be adjusted to have the source accurately at the centre. The pulse shape discrimination circuits were incorporated in order to count neutrons only. The polarimeter was rotated to the two positions as before and counts recorded for the same length of time. Table (3.1) includes the asymmetries observed from this test also. It is clear from the table that the contribution of the instrumental asymmetry is not more than 0.6% even for the worst case for tests with both sources. Such a long period test was performed once at the very beginning, before forward angle measurements were made and again after the polarimeter was rotated for backward angle measurements. However tests with both the sources were repeated each time actual data collection was halted, either for changing the deuterium target, the scattering sample or for maintenance work. But in such cases the test was done over a period of 10/12 hours, always checking to keep the gain shift below 0.5% in all the detectors. It was observed that in addition to bubbles appearing within the scintillator, any loose cables, loose capacitors in the photomultiplier dynode chain or a loose mu-metal shield could contribute to a remarkable change in the counting rate on rotation. It was also observed that maintaining a particular orientation of each photomultiplier tube

Detector	Observed Asymmetry with ^{60}Co source	Observed Asymmetry with ^{252}Cf source
1	.0022 ± .0002	.0024 ± .0002
2	.0002 ± .0002	.0011 ± .0003
3	.0019 ± .0002	.0008 ± .0003
4	.0026 ± .0002	.0049 ± .0002
5	.0011 ± .0002	.0005 ± .0002
6	.0010 ± .0002	.0051 ± .0002
7	.0022 ± .0002	.0024 ± .0001
8	.0039 ± .0002	.0003 ± .0002
9	.0017 ± .0002	.0051 ± .0002
10	.0033 ± .0002	.0034 ± .0002
11	.0015 ± .0002	.0018 ± .0002
12	.0004 ± .0002	.0061 ± .0002

TABLE 3.1: False asymmetries of the detectors with standard neutron and gamma sources.

to the scattering plane was important in keeping the false asymmetry to a minimum.

3.5.1 Experimental data collection

After having the system checked satisfactorily for false asymmetries as described in Section 3.4, the 500 keV Van de Graaf accelerator was used to accelerate deuterons up to (300 ± 10) keV. The accelerated beam was then made to strike the deuterium target to produce 2.9 MeV neutrons at an angle of 49°. The focussing of the beam was adjusted for minimum current on the d-beam entrance aperture and the beam was steered to maximise the number of counts in both the TYM and the CBM with the sample removed. Scattering measurements were started after the neutron yield was statistically stable.

Before starting actual polarization and cross-section measurement, another test for any false asymmetry was performed using the 2.9 MeV neutrons from the reaction with the polarimeter in the azimuthal positions $\phi = \pi/2$ and $\phi = 3\pi/2$ i.e. normal to the scattering plane. The neutrons were scattered from the Fe scatterer and the scattered neutrons counted for about 20 hours. The scattering asymmetry in this plane should be zero and the values for 20° and 34° scattering were found to be $.003 \pm .008$ and $.005 \pm .01$ respectively.

Measurements were done in two stages, as already mentioned in Chapter 2. In the first stage data for all the six samples were accumulated for the angular range 20° to 90°. The polarimeter was then rotated through 180° and data accumulated for the range 90° to 160°. The samples used were of natural isotopic abundance and made cylindrical of 5.2 cm length and 2.54 cm diameter on the average, except for tungsten. The measurement time varied from 50-100 hours for the forward angles and 100-150 hours for the backward angles for the different samples

except for tungsten. The tungsten sample used for the forward angle measurement was a hollow cylinder of 5.08 cm length and internal and external diameters 0.4 cm and 1.28 cm respectively, while for backward angles it was a solid cylinder of 5.0 cm length and 2.0 cm diameter. The measurement times for forward and backward angles were 200 hours and 250 hours respectively.

For scattering measurement on each sample, the polarimeter was rotated to the two azimuthal positions $\phi = 0$ and $\phi = \pi$. In each position pulse height spectra for the twelve detectors and the corresponding monitor counts were recorded for both samples in and out of the collimated neutron beam. The data were collected for a short period of 1000 sec. in each condition and the sequence repeated frequently. This ensured minimum effect due to fluctuation of the incident deuteron beam condition. After every 25-30 hours of accumulation the data was stored on the disk, as described in 2.3.3. At the end of the total period for each sample the data was transferred for analysis to the EMAS network using the link interface.

For the determination of the differential elastic scattering cross-section the neutron flux incident on the scattering sample has to be estimated. There is no straightforward method of measuring the direct flux on the sample. However with the CBM in the collimated beam it is possible to determine the effective neutron flux provided the ratio of the detection efficiencies of the CBM and the side detectors are known. For this purpose, each of the side detectors was placed in turn in the direct beam with the scatterer removed and the counts recorded for 100 sec. in each of the azimuthal positions. The number of counts from the CBM when in the direct beam was also recorded for the same length of time and the relative efficiencies determined using a normalisation factor provided by the TYM to account

for any fluctuations in the deuteron beam current. For the measurement on each sample the relative efficiencies were determined both at the beginning and at the end of the measurement and the average was used in the cross-section calculation.

3.5.2 Experimental Data Analysis

Following eqn. (1.5), the polarization $P_s(\theta)$ due to elastic scattering through angle θ, can be determined from the scattering asymmetry by,

$$P_s(\theta) = \frac{1}{P_n} \frac{r-1}{r+1} \tag{3.1}$$

where P_n is the polarization of the incident neutrons and r is the right-left scattering ratio expressed by equation (1.4). However since the role of the detectors were interchanged to compensate for differences in detection efficiencies, r takes the form

$$r = \sqrt{\frac{NR_1}{NL_1} \cdot \frac{NR_2}{NL_2}} \tag{3.2}$$

where NR_1/NL_1 is the right-left ratio for one of the pair of detectors at angle θ and NR_2/NL_2 is that for the other.

The polarization P_n of the neutrons produced in the $^2H(d,n)^3He$ reaction for deuteron energies below 1 MeV has been measured by several experimenters and has been reviewed by Galloway[48] in 1971. In the following years more measurements have been done by Davie and Galloway[49], Sikkema and Steendam[50], Alsoraya et al.[51] and Galloway and Martinez Lugo[52]. From all these measurements the value of the neutron polarization for the 2.9 MeV neutrons at 49^o for incident deuterons of (300 ± 10) keV energy was estimated to be -15% with an uncertainty of ±1%.

3.5.3

If S is the scattered n-flux at the detector at a distance r and at an angle θ to the scattering sample, due to an incident flux I, then the differential cross-section is expressed as

$$\frac{d\sigma}{d\Omega}(\theta) = \frac{Sr^2}{IN} \qquad (3.3)$$

where **N** is the number of nuclei in the scatterer. However for practical evaluation the above expression has to be modified as follows.

If n_d is the counting rate in the side detector of efficiency ε_d, subtending a solid angle Ω_d at the scatterer, due to n_o neutrons incident on the scatterer, then

$$\sigma(\theta) = \frac{n_d}{\varepsilon_d \Omega_d N} \frac{A_s}{n_o} \qquad (3.4)$$

since $I = {}^{n_o}/_{A_s}$, where A_s is the area of the scatterer presented to the incident n-beam. The neutron flux determined by the CBM of efficiency ε_m and surface area A_m is,

$$F = \frac{n_m}{\varepsilon_m A_m} \qquad (3.5)$$

where n_m is the number of neutrons detected/sec by the CBM, with the scatterer moved. If, now, r_s and r_m are the distances respectively of the scatterer and the CBM from the neutron producing target, then.

$$n_o = \frac{F r_m^2 A_s}{r_s^2}$$

$$= \frac{n_m}{\varepsilon_m A_m} \frac{r_m^2}{r_s^2} A_s \qquad (3.6)$$

(replacing F by exp. 3.5).

Substituting this expression for n_o in (3.4), the expression for $\sigma(\theta)$ becomes

$$\sigma(\theta) = \frac{\varepsilon_m}{\varepsilon_d} \frac{r_s^2}{r_m^2} \cdot \frac{A_m}{\Omega_d} \cdot \frac{1}{N} \cdot \frac{n_d}{n_m} \quad . \qquad (3.7)$$

The ratio $\varepsilon_m/\varepsilon_d$ of the detection efficiency for each detector was determined in separate runs, as described in 3.5.1, using the relations,

$$\varepsilon_m/\varepsilon_d = \frac{n_m'}{n_d'} \cdot \frac{M_d}{M_m} \qquad (3.8)$$

where n_m' and n_d' are the count rates in the CBM and a particular side detector in the direct beam and M_m and M_d are the corresponding count rates in the TYM.

3.5.4

A simple computer programme was written for evaluating the polarization and cross-section values for the different angles. The selection of the elastically scattered neutrons was done by setting a threshold in the proton recoil spectra. To set the threshold correctly, the energy scale for each detector was calibrated by using the spectra obtained individually with the direct neutrons. It has been established for long that the recoil protons of a single energy produces a distribution of output pulse height H, about a mean value $\bar{H}$ due to statistical fluctuations in the scintillator and the photomultiplier. It is this mean value which is proportional to the mean light output in the scintillator due to the energy imparted by the protons of a given energy. It has been shown[53] that this distribution is reasonably well represented by a Gaussian function and the observed pulse height spectrum is the result of folding the scintillator output spectrum with the appropriate Gaussian.

Fig. (3.4) shows the pulse height spectrum for one of the side detectors in the direct beam, with the energy bias set to reject proton recoil events below about 0.5 MeV and with the pulse shape discrimination bias set to reject gamma-ray events. The calibration of the spectrum, knowing the neutron energy to be 2.9 MeV, was done by working out the channel number corresponding to the mean of the observed distribution as shown by the solid curve. After calibrating the energy scale of each detector as above, the channel limit for the required energy bias to select only elastically scattered neutrons was determined individually for each of the scattering nuclei, depending on the excited levels of their isotopes. It was not always possible to avoid counting inelastically scattered neutrons completely and at the same time achieve a reasonable statistical accuracy for elastic scattering, as will be seen later. A list of the excitation energies of the levels of the different isotopes of the nuclei employed in the present measurement are presented in Table (3.2) along with the natural abundance[54] of the isotopes (those less than 10% are neglected). For each element the excitation level corresponding to which the energy bias was set is marked with an asterisk. The energy discrimination bias employed for each of the nuclei is also listed.

Using the channel limits determined for accepting elastic events, the computer programme integrates the number of counts above the threshold for the scatterer in and out of the beam for the two azimuthal positions, for each detector. After subtracting the integrated background counts the polarization and cross-section values were evaluated, employing relations (3.1) and (3.7). The cross-sections at each angle were determined for each detector separately and the average taken to be the cross-section for unpolarized neutrons. The uncertainties associated with the measured polarization and cross-section were evaluated as follows.

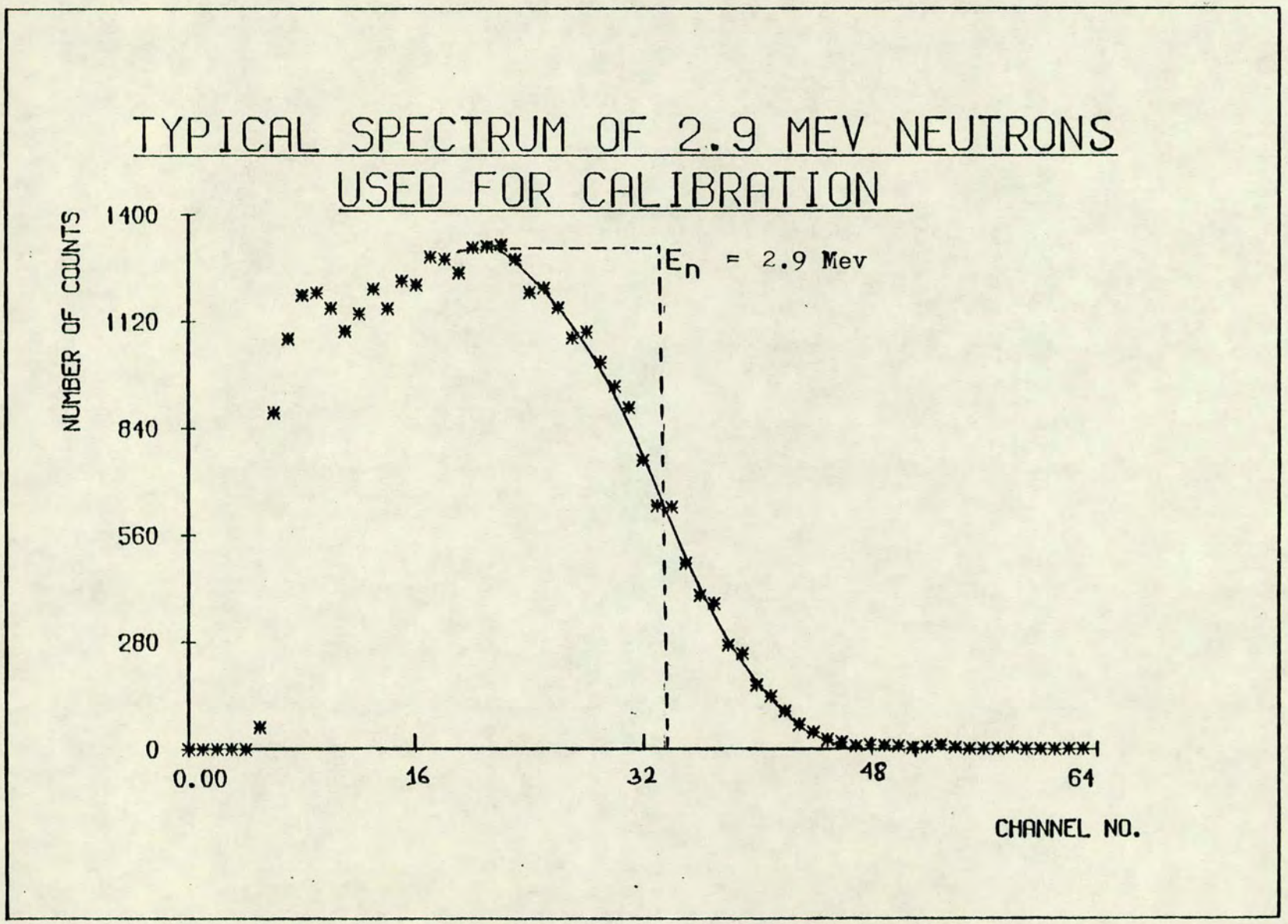

Fig. 3.4. Typical spectrum of 2.9 Mev direct neutrons used for calibration.

	Element	Isotope	Natural Abundance of the Isotope %	Ref.	Excitation Levels (MeV)	Applied Energy Discrimination Bias (MeV)
(1)	$_{26}Fe$	$^{56}_{26}Fe_{30}$	91.66	55	*0.847; 2.09; 2.657	2.05
(2)	$_{74}W$	$^{182}_{74}W_{108}$	26.41	56	0.100; 0.329; 0.681 .... (total of 41 levels up to 2.316 MeV)	2.62
		$^{183}_{74}W_{109}$	14.41	57	0.047; 0.099; 0.20; *0.292 .... (total of 27 levels up to 1.4 MeV)	
		$^{184}_{74}W_{110}$	30.64	58	0.111; 0.364; 0.7488 .... (total of 27 levels up to 2.49 MeV)	
		$^{186}_{74}W_{112}$	28.41	59	0.122; 0.397; 0.738 ; .... (total of 34 levels up to 2.5 MeV)	
(3)	$_{81}Tl$	$^{203}_{81}Tl_{122}$	29.5	60	*0.279; 0.681; 1.045; .... (34 levels up to 2.9 MeV)	2.62
		$^{205}_{81}Tl_{124}$	70.5	61	0.204; 0.620; 0.925; .... (13 levels up to 2.7 MeV)	
(4)	$_{82}Pb$	$^{206}_{82}Pb_{124}$	23.6	62	0.803; 1.165; 1.341; 1.459; 1.689 (20 levels up to 2.9 MeV)	2.31
		$^{207}_{82}Pb_{125}$	22.6	63	*0.589; 0.898; 1.633; 2.397	
		$^{208}_{82}Pb_{126}$	52.3	64	2.615;	
(5)	$_{83}Bi$	$^{209}_{83}Bi_{126}$	100.0	65	*0.897; 1.609; 2.492	2.0
(6)	$_{92}U$	$^{238}_{92}U_{146}$	99.74	66	0.045; 0.148; *0.308; 0.519 .... (total of 58 levels up to 2.308 MeV)	2.59

TABLE 3.2. Table of Isotopes with Excitation Levels.

The uncertainty associated with the polarization of the incident neutrons being very small, the error in the polarization measurement was assumed to be mainly due to the statistical uncertainty of the observed asymmetry. Thus

$$\Delta P_S = \frac{1}{P_n} \Delta\varepsilon \ ,$$

$$\Delta\varepsilon = \frac{r}{(r+1)^2} \sqrt{\left(\frac{\Delta NR1}{NR1}\right)^2 + \left(\frac{\Delta NL1}{NL1}\right)^2 + \left(\frac{\Delta NR2}{NR2}\right)^2 + \left(\frac{\Delta NL2}{NL2}\right)^2}$$

$$\Delta NR = \sqrt{NR_S + NR_B} \ ; \quad \Delta NL = \sqrt{NL_S + NL_B} \qquad (3.9)$$

where the subscripts S and B refers to the counts in the side detectors with the sample in and out of the beam.

The errors associated with the measured differential cross-sections using eqn. (3.7) were

i) Statistical uncertainty in the determination of η_d and η_m which was determined individually for each detector as

$$\Delta(\eta_d/\eta_m) = \left(\frac{NR+NL}{\eta_m}\right) \sqrt{\frac{NR_S+NR_B}{(NR+NL)^2} + \frac{NL_S+NL_B}{(NR+NL)^2} + \left(\frac{\Delta\eta_m}{\eta_m}\right)^2} \qquad (3.10)$$

ii) Statistical error in the determination of $\varepsilon_m/\varepsilon_d$ which was found to be of order of only 0.5% with the high counting rate in the detectors in direct beam.

iii) Error due to the variation in $\varepsilon_m/\varepsilon_d$ during the period of data collection. This was observed to vary from zero to about 5% for the worst case.

iv) Systematic error associated with the measurement of the different geometrical factors involved. This was estimated to be ± 2.5%.

The data collected for the scattering of the 2.9 MeV neutrons from Fe, W, Tℓ, Pb, Bi and U were analysed following the procedure outlined above in Sec. 3.5.2 - Sec. 3.5.4. The numerical results obtained for the distribution of polarizations and cross-sections are quoted in Tables 3.3 - 3.8.

3.6.1 Finite geometry and multiple scattering correction

Angular distribution measurements of elastically scattered fast neutrons have to be done with relatively large scattering samples, because of the small neutron scattering cross-sections and low detection efficiency of the neutron detectors. Such a practice leads to the need for employing corrections to the observed distribution of polarization and cross-section for attenuation of the incident neutron flux in the sample, multiple scattering and the finite angular spread of target-scatterer and scatterer-detector geometry. These effects have been calculated by several authors using either analytical methods[67] or by a Monte Carlo random walk technique[68,69]. Kinney[71] and Cox[70] used a combination of the speed of analytic methods with much freedom from approximation of the Monte Carlo methods. Recently Velkeley et al.[72] investigating the comparison between the two methods in detail for elastic neutron scattering near 9 MeV have quoted agreement within 1% under some experimental conditions.

The differential cross-sections for the different nuclei, deduced from the experimental data in the present work, were corrected for flux attenuation, multiple scattering and finite angular resolution of the target-scatterer and scatterer-detector geometry using the Monte Carlo programme due to Holmqvist et al.[69] and kindly supplied by Drigo[73].

In the programme, the observed cross-section is subjected to a

correction factor of the form

$$\alpha = \frac{\Phi}{\overline{\Phi}} \cdot \frac{F}{\overline{F}} \cdot q \qquad (3.11)$$

where $\Phi/\overline{\Phi}$ is a correction applied for the anisotropic distribution of the source neutrons. The factor $F/\overline{F}$ is for the attenuation of the incoming n-flux in the sample and is given by,

$$\frac{F}{\overline{F}} = \frac{\text{n-flux at the position of the scatter, without the scatterer}}{\text{mean n-flux in the scatterer when in position}}$$

$$= N\sigma_T nV/RA$$

where σ_T is the total scattering cross-section, n is the number of nuclei/volume element of the scatterer of volume V, R is the number of neutrons interacting elastically or non-elastically at least once in the sample and N is the number of neutrons penetrating the area A of the scatterer with no scatterer in position. The factor q accounts for the loss of neutrons in the scatterer by any non-elastic process. The programme transforms the observed distribution to the centre of mass coordinate system and expresses it in the form of a Legendre polynomial expansion. To calculate the probability of elastic scattering to the detectors, the observed distribution is used to calculate differential cross-sections at 41 equally spaced points. In the next step the programme calculates the multiple scattering correction corresponding to elastic and non-elastic multiple interaction in the sample by the Monte Carlo method. The Monte Carlo distribution thus obtained is normalized to give an area equal to that under the observed angular distribution. This normalized distribution is then subjected to an iterative procedure to find the corrected distribution. For each value of $\cos\theta_{cm}$, the quotient of the observed differential cross-section (corrected for α) and the corresponding Monte Carlo distribution is

evaluated. The differential cross-section used as the input of the Monte Carlo calculation at each $\cos \theta_{cm}$ multiplied by the corresponding quotient defines the corrected distribiton. The total, inelastic and capture cross-section values needed as the input for the programme were taken from Howerton[74].

The correction of the polarization data for multiple scattering and finite geometry was also done by using the same programme as follows. From eqn. (1.3) we can write for the differential elastic scattering cross-sections for scattering to the "right' (σ_R) and to the 'left' (σ_L),

$$\begin{aligned} \sigma_R &= \sigma(\theta, 0) = \sigma(1 + P_n P_S) \\ \sigma_L &= \sigma(\theta, \pi) = \sigma(1 - P_n P_S) \end{aligned} \tag{3.12}$$

σ_R and σ_L were calculated from the experimentally determined polarization and cross-section values using the above relations. σ_R and σ_L thus calculated were corrected for finite sample size using the Monte Carlo code. The corrected polarization values were then evaluated as follows,

$$\begin{aligned} P_n P_S &= \frac{\sigma_R - \sigma_L}{\sigma_R + \sigma_L} \\ \therefore \quad P_S &= \frac{1}{P_n} \cdot \frac{\sigma_R - \sigma_L}{\sigma_R + \sigma_L} . \end{aligned} \tag{3.13}$$

3.6.2 Correction for Inelastic Scattering

As already described in 3.5.4, the energy bias for each individual sample was chosen to reject as many of the inelastic levels as possible. The finite energy resolution and the existence of some very low excited states for some of the nuclei are the possible limitations for rejecting

the inelastic contributions absolutely. However the low efficiency with which the inelastically scattered neutrons of lower energy could be detected makes such contributions negligible. The correction to be applied to the observed differential cross-section for inelastic scattering was assumed to be, $\Sigma\varepsilon\sigma_{in}$, where the summation is over relevant excited states. The efficiency factor ε is determined assuming the same intrinsic efficiency for detecting elastic and inelastic scattering and considering the finite energy discrimination bias applied. Assuming the inelastically scattered neutrons to be unpolarized, the observed polarization can be corrected for any inelastic scattering by,

$$P_{el} = P_{obs}\left(1 + \frac{\Sigma\varepsilon\sigma_{in}}{\sigma_{el}}\right) \qquad (3.14)$$

In the case of the scattering of 2.9 MeV neutrons from Fe and Pb, it has already been shown by Galloway and Waheed[40] that the inelastically scattered neutrons make no significant change in the angular distribution of the cross-section or polarization. From published data on the inelastic cross-sections for Fe[75] and for Pb[76] they estimated the contribution to the measured distribution for an energy bias of 1.9 MeV, to be negligibly small. Thus with a bias of 2.05 MeV for Fe and 2.31 MeV for Pb in the present measurement the inelastic contribution can be assumed to be zero even from the lowest excited state.

For Tℓ with the energy bias set at 2.62 MeV, a possible inelastic contribution could be due to the level at 0.204MeV of ^{205}Tℓ. Feicht and Göbel[77] have measured the cross-section for different levels of ^{203}Tℓ and ^{205}Tℓ. Assuming an isotropic distribution the cross-section for the 0.204 MeV level of ^{205}Tℓ, from their measurement is (16 ± 1) mb/sr. With an appropriate efficiency factor the contribution to the elastic scattering cross-section is estimated to be about 5 mb/sr. This can be

considered negligible, being smaller than the error associated with the minima of the measured cross-sections.

For Bi, the energy bias set at 2.0 MeV is high enough to reject any contribution even from the lowest excited state. For W and U no correction to the measured cross-section or polarization could be applied for a possible inelastic contribution, due to the lack of appropriate inelastic cross-section data.

The distributions of polarization and cross-sections corrected for all the effects discussed above are listed in Tables 3.3 - 3.8 for all the nuclei, along with the uncorrected experimental results.

It is clear from the tables that the correction to the polarization values for finite geometry and multiple scattering effects are very small. In the majority of the cases, the correction is within the statistical uncertainty of the experimental values. The experimentally measured values of polarization for Pb and the values corrected for the above-mentioned effects are presented graphically in Fig. 3.5 for comparison. Fig. 3.5 also shows the uncorrected and corrected differential cross-section values for Pb. For the differential cross-section the correction is mostly due to the attenuation of the incident neutron beam in the sample. For the example of Pb, while the flux attenuation correction is about 11% for all the angles, the multiple scattering correction varied from about 8% at 20°, 4% at 90° to 2% at 160°.

TABLES 3.3 - 3.8

Uncorrected and Corrected Distribution of Polarization and Cross-section of 2.9 MeV Neutrons Scattered From Fe, W, Tℓ, Pb, Bi and U.

Lab Angle (Degrees)	Uncorrected		Corrected	
	$\sigma(\theta)$ mb/sr	$P(\theta)$	$\sigma(\theta)$ mb/sr	$P(\theta)$
20	562 ± 20	-0.12 ± 0.01	843 ± 25	-0.12 ± 0.01
34	432 ± 15	-0.13 ± 0.02	636 ± 19	-0.12 ± 0.02
48	211 ± 19	-0.19 ± 0.03	271 ± 24	-0.21 ± 0.03
62	102 ± 12	-0.13 ± 0.05	118 ± 15	-0.13 ± 0.06
76	60 ± 8	+0.16 ± 0.08	58 ± 10	+0.26 ± 0.11
90	55 ± 5	+0.05 ± 0.09	57 ± 7	+0.12 ± 0.12
104	68 ± 3	-0.09 ± 0.07	77 ± 4	-0.11 ± 0.09
118	78 ± 10	-0.10 ± 0.07	96 ± 13	-0.11 ± 0.08
132	66 ± 3	-0.16 ± 0.09	74 ± 3	-0.21 ± 0.11
146	73 ± 7	+0.29 ± 0.11	86 ± 9	+0.42 ± 0.12
160	72 ± 4	-	85 ± 6	-

TABLE 3.3 - IRON

Lab Angle (Degrees)	Uncorrected		Corrected	
	$\sigma(\theta)$ mb/sr	$P(\theta)$	$\sigma(\theta)$ mb/sr	$P(\theta)$
20	3278 ± 110	-0.18 ± 0.02	4391 ± 134	-0.15 ± 0.02
34	1280 ± 99	-0.26 ± 0.04	1583 ± 12	-0.25 ± 0.04
48	348 ± 37	-0.38 ± 0.09	357 ± 45	-0.41 ± 0.11
62	145 ± 24	+0.32 ± 0.18	133 ± 29	+0.53 ± 0.24
76	120 ± 12	+0.05 ± 0.18	114 ± 15	+0.12 ± 0.23
90	147 ± 5	-0.12 ± 0.14	161 ± 11	-0.09 ± 0.12
104	120 ± 5	-0.32 ± 0.17	129 ± 9	-0.47 ± 0.24
118	114 ± 19	-0.04 ± 0.15	134 ± 27	+0.02 ± 0.19
132	64 ± 5	-0.22 ± 0.28	58 ± 8	-0.35 ± 0.47
146	83 ± 8	+0.51 ± 0.41	94 ± 12	+0.76 ± 0.51
160	48 ± 15	+0.60 ± 0.68	47 ± 21	+0.88 ± 1.02

TABLE 3.4 - TUNGSTEN

Lab Angles (Degrees)	Uncorrected		Corrected	
	$\sigma(\theta)$ mb/sr	$P(\theta)$	$\sigma(\theta)$ mb/sr	$P(\theta)$
20	2359 ± 92	−0.13 ± 0.01	3528 ± 119	−0.11 ± 0.01
34	1126 ± 41	−0.12 ± 0.02	1599 ± 54	−0.10 ± 0.02
48	250 ± 15	−0.10 ± 0.05	248 ± 20	−0.09 ± 0.07
62	151 ± 7	+0.03 ± 0.09	151 ± 10	+0.06 ± 0.11
76	142 ± 6	+0.21 ± 0.07	148 ± 9	+0.29 ± 0.10
90	185 ± 24	+0.12 ± 0.08	259 ± 31	+0.16 ± 0.08
104	176 ± 21	−0.18 ± 0.12	185 ± 27	−0.26 ± 0.16
118	158 ± 10	−0.11 ± 0.12	184 ± 13	−0.10 ± 0.13
132	90 ± 5	−0.23 ± 0.13	83 ± 7	−0.34 ± 0.21
146	132 ± 18	−0.11 ± 0.13	145 ± 24	−0.22 ± 0.16
160	201 ± 12	+0.81 ± 0.19	239 ± 16	+0.95 ± 0.22

TABLE 3.5 - THALLIUM

Lab Angle (Degrees)	Uncorrected		Corrected	
	$\sigma(\theta)$ mb/sr	$P(\theta)$	$\sigma(\theta)$ mb/sr	$P(\theta)$
20	2344 ± 85	−0.16 ± 0.01	3383 ± 107	−0.15 ± 0.01
34	1162 ± 42	−0.14 ± 0.03	1588 ± 53	−0.12 ± 0.03
48	321 ± 10	−0.15 ± 0.04	346 ± 14	−0.16 ± 0.05
62	205 ± 24	+0.25 ± 0.07	216 ± 30	+0.38 ± 0.09
76	259 ± 30	+0.17 ± 0.05	283 ± 38	+0.18 ± 0.06
90	254 ± 14	+0.10 ± 0.09	292 ± 18	+0.19 ± 0.09
104	235 ± 8	−0.05 ± 0.10	262 ± 11	−0.13 ± 0.11
118	212 ± 7	+0.12 ± 0.11	232 ± 10	+0.23 ± 0.12
132	165 ± 12	−0.46 ± 0.15	166 ± 15	−0.69 ± 0.20
146	234 ± 12	+0.25 ± 0.15	264 ± 16	+0.37 ± 0.17
160	349 ± 22	+0.24 ± 0.13	429 ± 28	+0.30 ± 0.13

TABLE 3.6 - LEAD

Lab Angle (Degrees)	Uncorrected		Corrected	
	σ(θ) mb/sr	P(θ)	σ(θ) mb/sr	P(θ)
20	2290 ± 194	−0.14 ± 0.01	3182 ± 237	−0.13 ± 0.01
34	1175 ± 78	−0.18 ± 0.02	1588 ± 96	−0.19 ± 0.02
48	374 ± 33	−0.22 ± 0.04	401 ± 41	−0.25 ± 0.05
62	286 ± 34	−0.04 ± 0.05	323 ± 42	−0.03 ± 0.06
76	334 ± 22	+0.15 ± 0.04	377 ± 28	+0.20 ± 0.05
90	322 ± 24	+0.07 ± 0.05	380 ± 30	+0.09 ± 0.05
104	274 ± 23	+0.04 ± 0.11	296 ± 29	+0.11 ± 0.14
118	262 ± 21	−0.14 ± 0.11	299 ± 26	−0.19 ± 0.11
132	199 ± 13	−0.62 ± 0.14	205 ± 17	−0.80 ± 0.20
146	267 ± 18	−0.23 ± 0.16	303 ± 23	−0.27 ± 0.17
160	341 ± 23	+0.26 ± 0.15	406 ± 29	+0.36 ± 0.17

TABLE 3.7 - BISMUTH

Lab Angle (Degrees)	Uncorrected		Corrected	
	σ(θ) mb/sr	P(θ)	σ(θ) mb/sr	P(θ)
20	1926 ± 119	-0.17 ± 0.01	3732 ± 185	-0.17 ± 0.01
34	713 ± 76	-0.23 ± 0.03	1147 ± 118	-0.25 ± 0.03
48	203 ± 39	-0.14 ± 0.05	243 ± 61	-0.12 ± 0.08
62	149 ± 20	+0.07 ± 0.06	170 ± 32	+0.16 ± 0.10
76	194 ± 26	+0.05 ± 0.06	255 ± 41	+0.12 ± 0.06
90	274 ± 42	-0.15 ± 0.06	380 ± 65	-0.17 ± 0.07
104	247 ± 22	-0.13 ± 0.12	362 ± 35	-0.09 ± 0.13
118	122 ± 21	-0.19 ± 0.16	123 ± 33	-0.25 ± 0.27
132	148 ± 32	-0.15 ± 0.17	177 ± 50	-0.18 ± 0.22
146	181 ± 17	+0.05 ± 0.12	229 ± 27	+0.07 ± 0.15
160	169 ± 15	+0.46 ± 0.24	201 ± 25	+0.64 ± 0.31

TABLE 3.8 - URANIUM

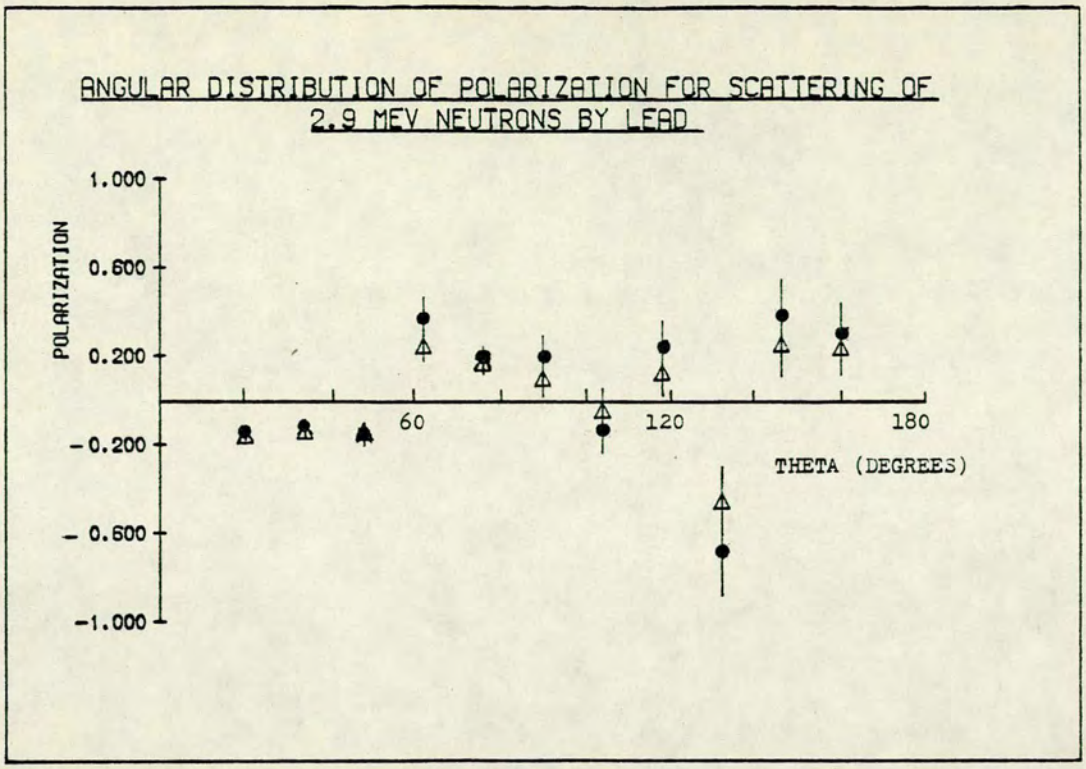

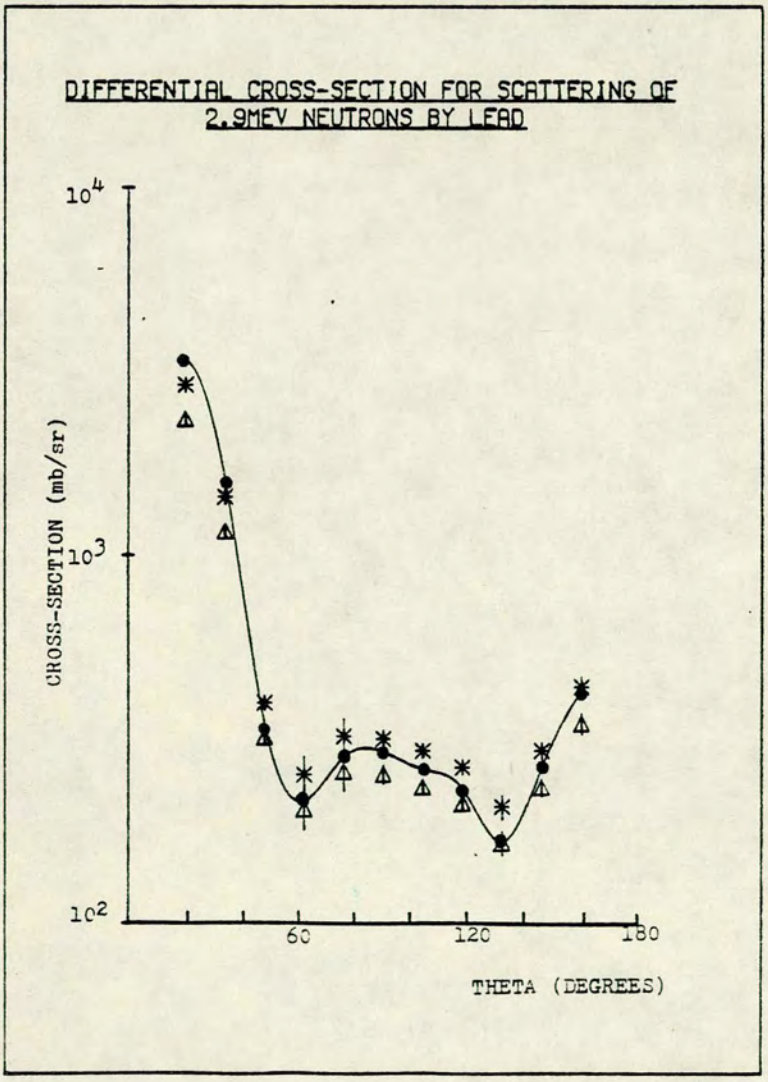

△ — Uncorrected

✱ — Corrected for flux attenuation

●——● -Corrected for flux attenuation and multiple scattering.

Fig. 3.5. Uncorrected and corrected distribution of polarization and cross-section for lead.

3.6.3 Comparison with Other Results for Cross-Section and Polarization

Iron

Fig. 3.6 shows the present polarization values for Fe to be consistent with the measurements of Galloway and Waheed[40] at the same energy, Ellgehausen[31] at 3.25 MeV and the four points of Zijip and Jonker[34] at 3.2 MeV. Thus reliable performance of the system for polarization measurement is established .

The cross-section values are also presented in Fig. 3.6 along with those of Galloway and Waheed[40] and Holmqvist[14]. The present cross-section values for the backward angles are in very good agreement with both the measurements. For most of these angles it is in closer agreement with Holmqvist's[14] values which result from measurement done with a system carefully designed for cross-section measurement, unlike the system used in the present work and that of Galloway and Waheed which is designed with importance to polarization measurement.

The lesser agreement at the forward angles could be due to the fact that the measurement on iron, being the very first done, the calibration for detector efficiency determination could not be done frequently and efficiently. However the discrepancy is not to such extreme as to require discarding of any of the values. The marked difference at 62° and 76° from the values of Galloway and Waheed[40] can not be regarded as too serious, since the Holmqvist points at the nearby angles of 60°, 70° and 80° are intermediate to these measurements.

Tungsten

Comparison of the present polarization values for tungsten at 34°, 48° and 62° with those of Zijip and Jonker[34] at nearby angles in Fig. 3.7, shows fairly good agreement. Although the sign of the polarization at 76° from the present

Key to symbols used in Fig. 3.6 - Fig. 3.11.

⊙ - present experimental values.

Δ - Galloway and Waheed[40].

✳ - Holmqvist[14]

■ - Zijip and Jonker[34]

▲ - Ellgehausen et al.[31]

× - Becker et al.[78]

⊡ - Popov[79]

● - Tanaka et al.[80]

⊗ - Batchelor et al.[81]

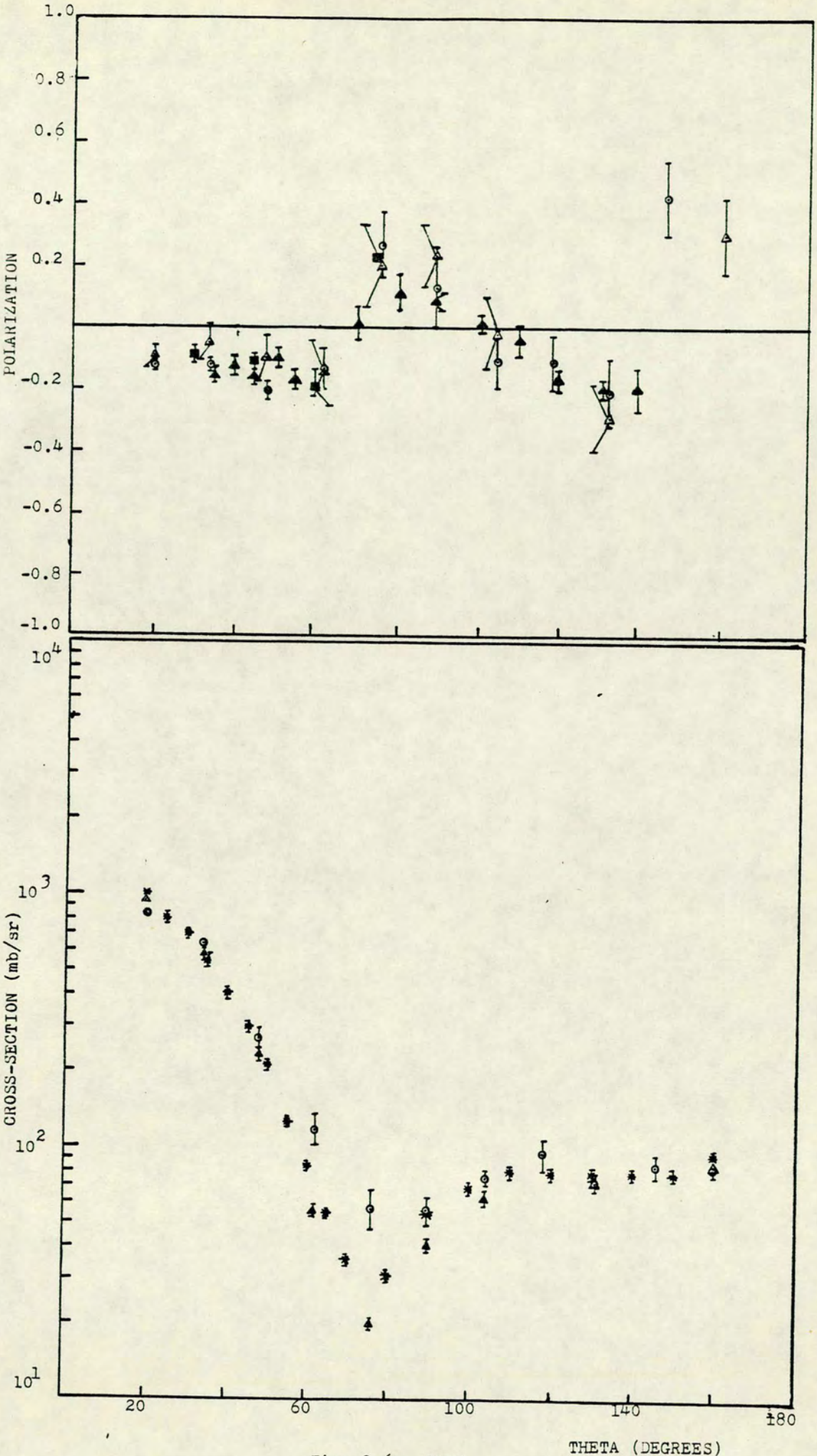
1.0
0.8
0.6
0.4
0.2
-0.2
-0.4
-0.6
-0.8
-1.0
POLARIZATION
10^4
10^3
10^2
10^1
CROSS-SECTION (mb/sr)
20
60
100
140
180
THETA (DEGREES)

Fig. 3.6. IRON

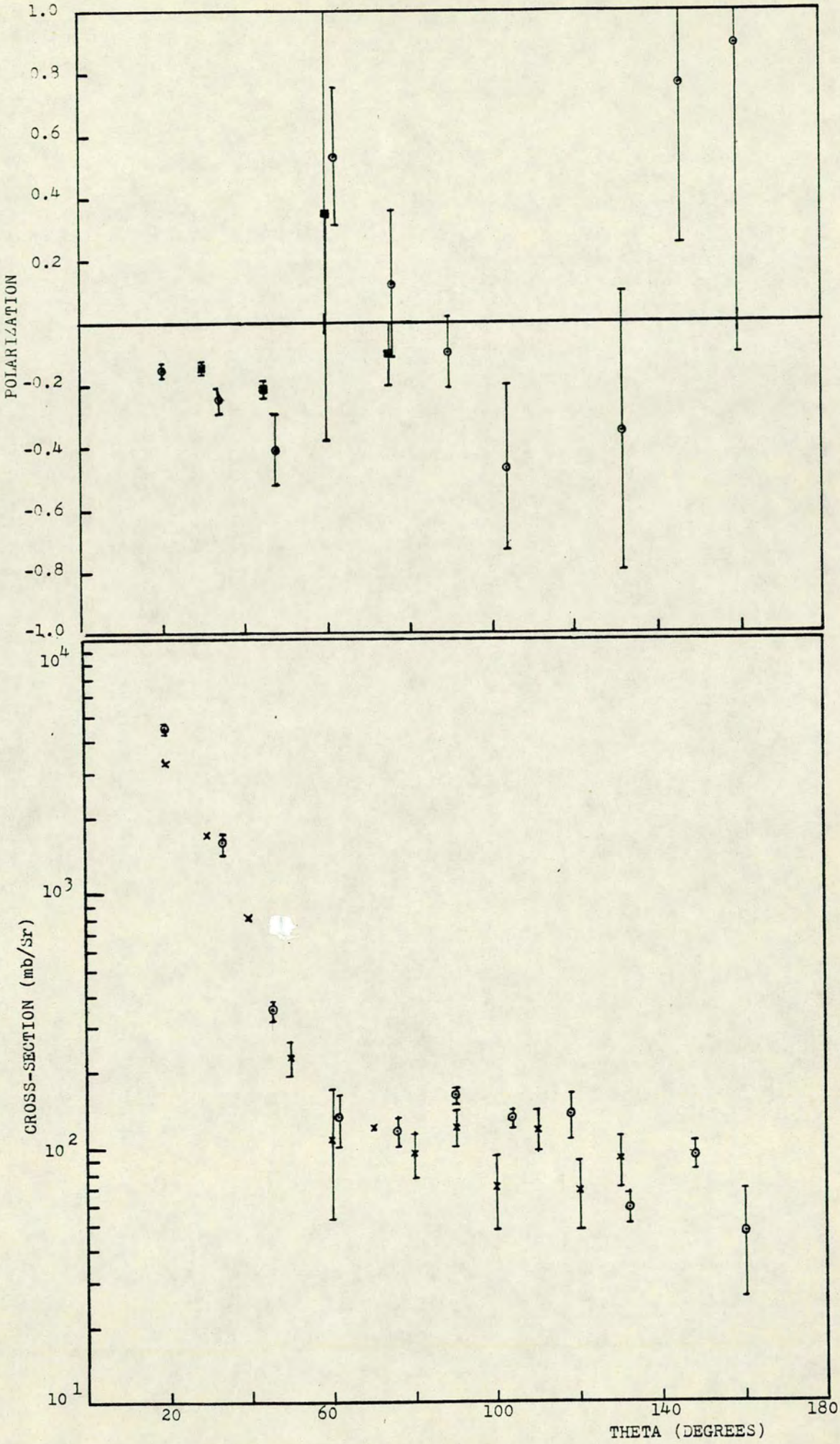

Fig. 3.7. TUNGSTEN

measurement is different from their result at 75°, the two results can be considered to be consistent, taking account of the large error associated with both. No polarization measurements are available for backward angles at comparable energy.

The present cross-section values for tungsten are also consistent with those of Becker et al.[78] at 3.2 MeV as can be seen in Fig. 3.7. However, since the experimental data could not be corrected for possible inelastic contribution, the present cross-section values compared in Fig. 3.7 and quoted in Table 3.4 include contributions from the six inelastic components (Table 3.2), below the one for which the energy discrimination bias was applied.

Thallium

Fig. 3.8 shows the present polarization measurements to be in good agreement with forward angle measurements of Zijip and Jonker[34]. No polarization data for the backward angles at nearby energy are available for comparison.

Fig. 3.8 also includes a comparison of the present cross-section measurement with the measurement of Becker et al.[78] at 3.2 MeV. Although the quantitative agreement is not very close, the present results are consistent with the comparatively less accurate results of Becker et al.[78].

Lead

The results of the present polarization measurement on Pb are compared with the results of Zijip and Jonker[34] and Galloway and Waheed[40] in Fig. 3.9. While the polarization value of Zijip and Jonker at 30° is significantly different from the value of Galloway and Waheed at 34°, it is consistent with the present result at 34°. The other forward angle polarization values of the present measurement (except 20°) are in reasonable agreement with those of Galloway and Waheed[40] at similar angles and Zijip and

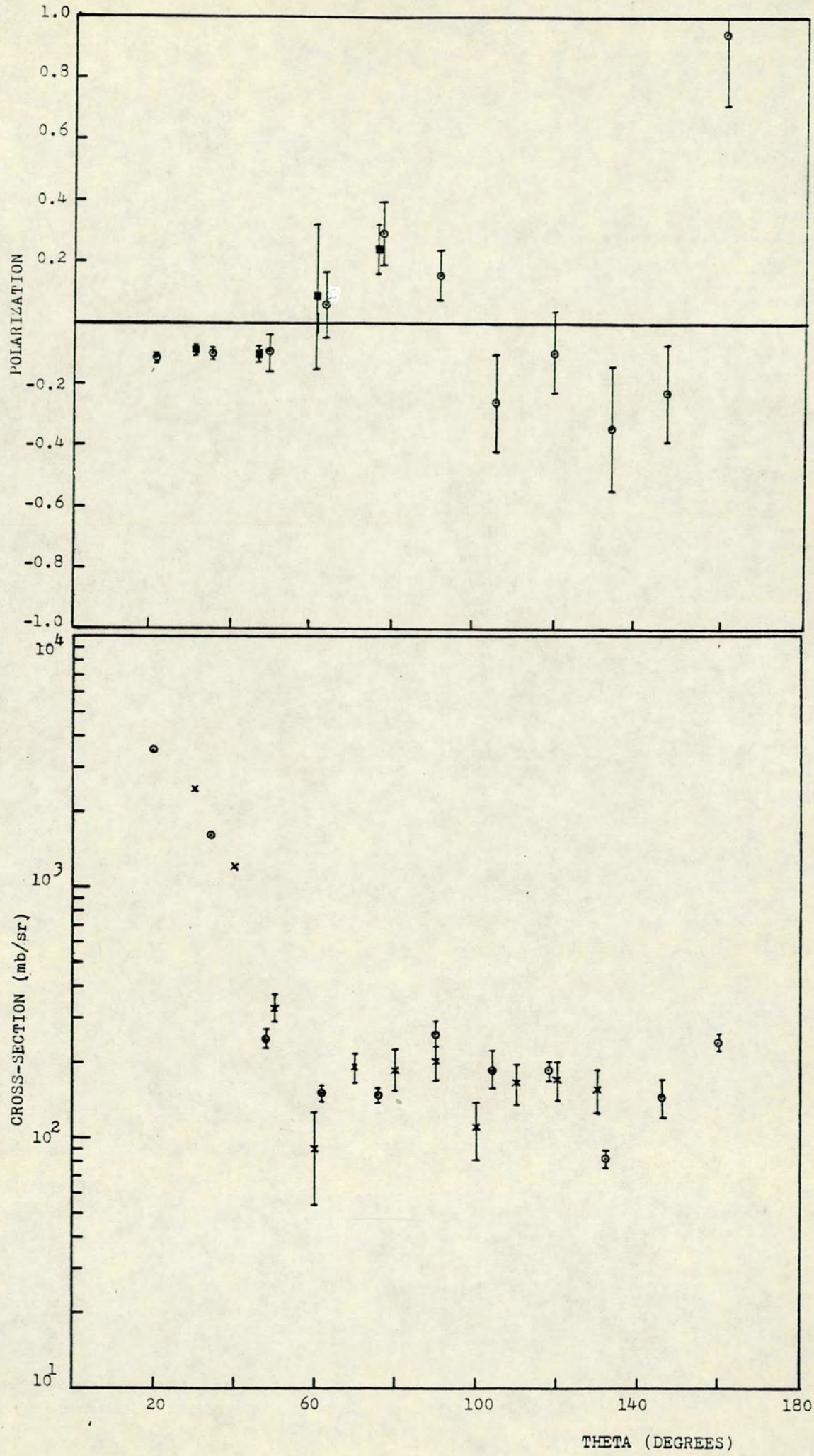

Fig. 3.8. THALLIUM

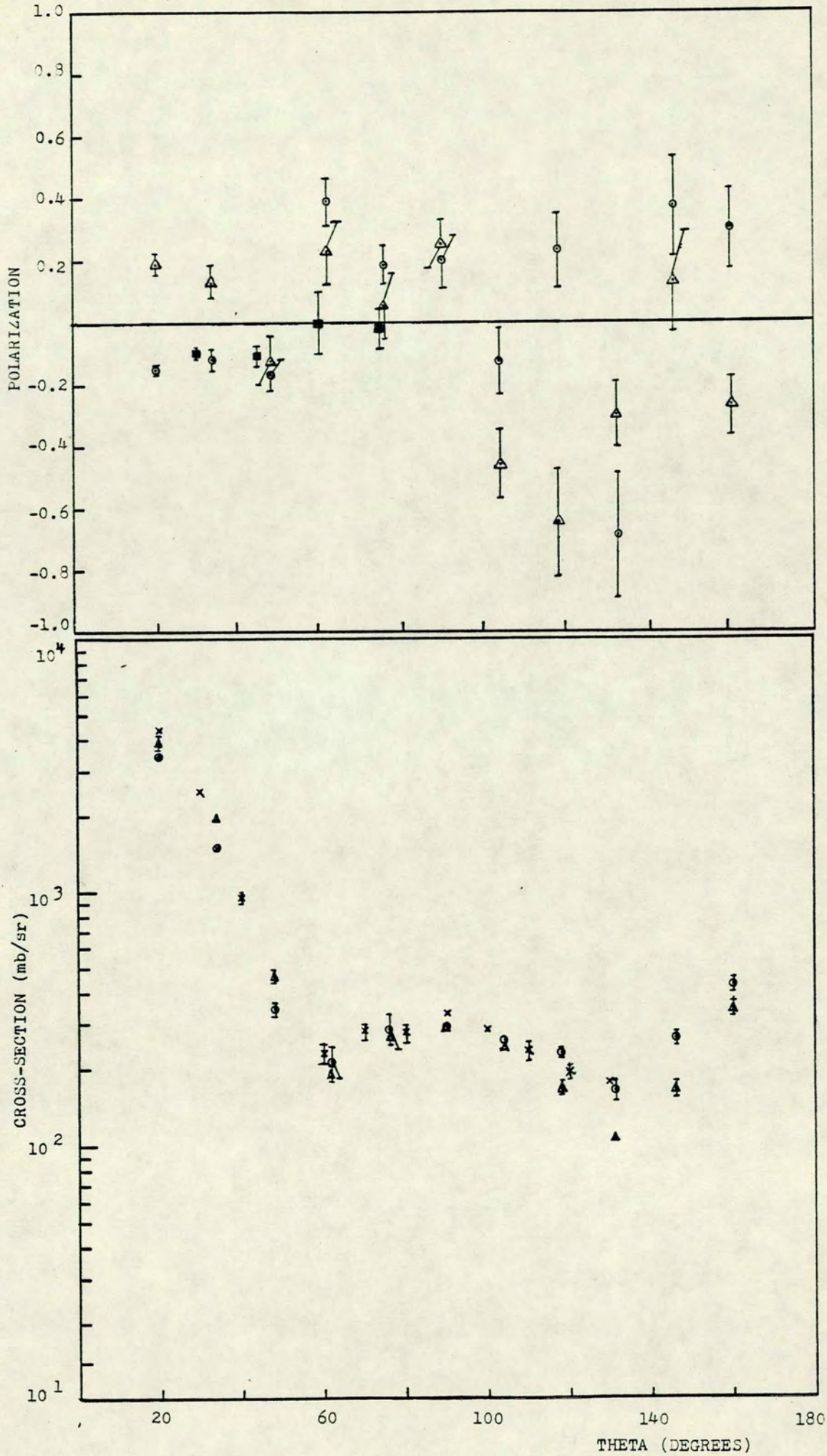
1.0
0.8
0.6
0.4
0.2
POLARIZATION
-0.2
-0.4
-0.6
-0.8
-1.0
10^4
10^3
10^2
10^1
CROSS-SECTION (mb/sr)
20
60
100
140
180
THETA (DEGREES)

Fig. 3.9. LEAD

Jonkers at neighbouring angles. The agreement between the backward angle values of the present measurement and that of Galloway and Waheed[40] is rather poor.

The differential cross-section values of the present measurement are compared with those of Becker et al.[78] and Galloway and Waheed[40] in Fig. 3.9. At the forward angles the present results are consistent with the results of both the measurements. The present values at 104°, 118° and 132° are in closer agreement with the values of Becker et al.[78] at the nearby angles of 100°, 120° and 130°, than those of Galloway and Waheed[40] at similar angles.

Bismuth

The present measurements on the angular distribution of polarization for Bi are compared with those of Zijip and Jonker[34] at nearby angles in Fig. 3.10. At the forward angles the two sets of results agree reasonably although the magnitude of the present measurements are slightly larger for all the angles. At the backward angles the two results are less consistent.

The differential cross-section results for Bi are also presented in Fig. 3.10 with those of Becker et al.[78], Popov[79] and Tanaka et al.[80]. There is significant scatter in the results of the different sets of measurements. While the measurements of Becker et al.[78] and Tanaka et al.[80] are in good agreement in the range 60° - 130°, they differ markedly at the most forward angles. The results of Popov[79] at 30°, 90° and 120° are in close agreement with those of Tanaka et al.[80] but less consistent at the rest of the angles. Although the present measurement falls in the general trend up to 50° and follows the overall pattern of maxima and minima, the values at the rest of the angles are consistently larger in magnitude.

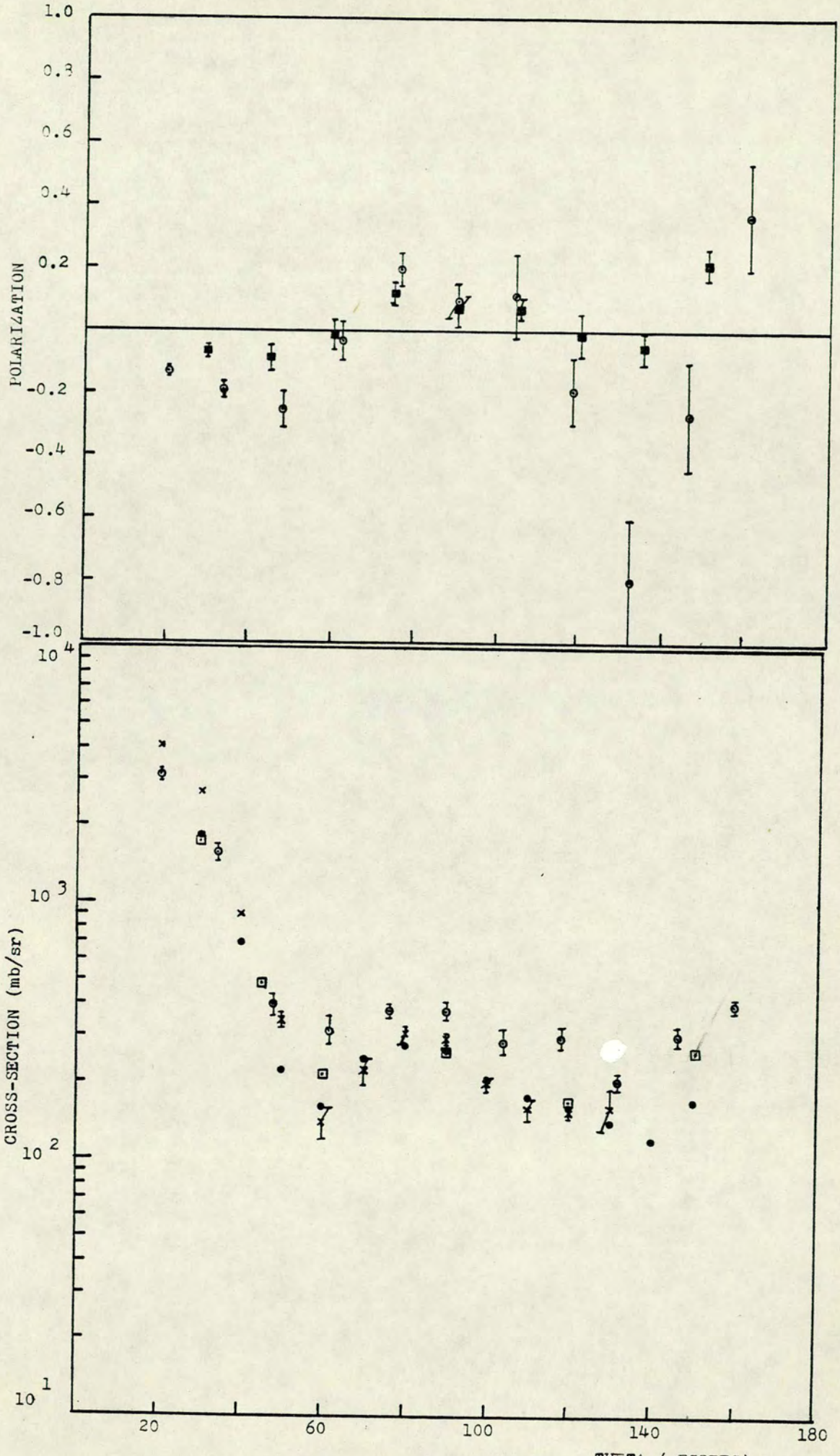

Fig. 3.10. BISMUTH

Uranium

While there is no other polarization measurement available for U at comparable energy, the cross-section values are compared with those of Batchelor et al.[81] in Fig. 3.11. The cross-section values from the present measurements are consistently larger in magnitude than the other measurement. However it is to be noted that the present cross-section values include a contribution from the first two excited states of energy 0.045 and 0.148 MeV, which could not be discriminated by the applied energy bias (Table 3.2) and could not be accounted for in the analysis due to the lack of appropriate inelastic cross-section data.

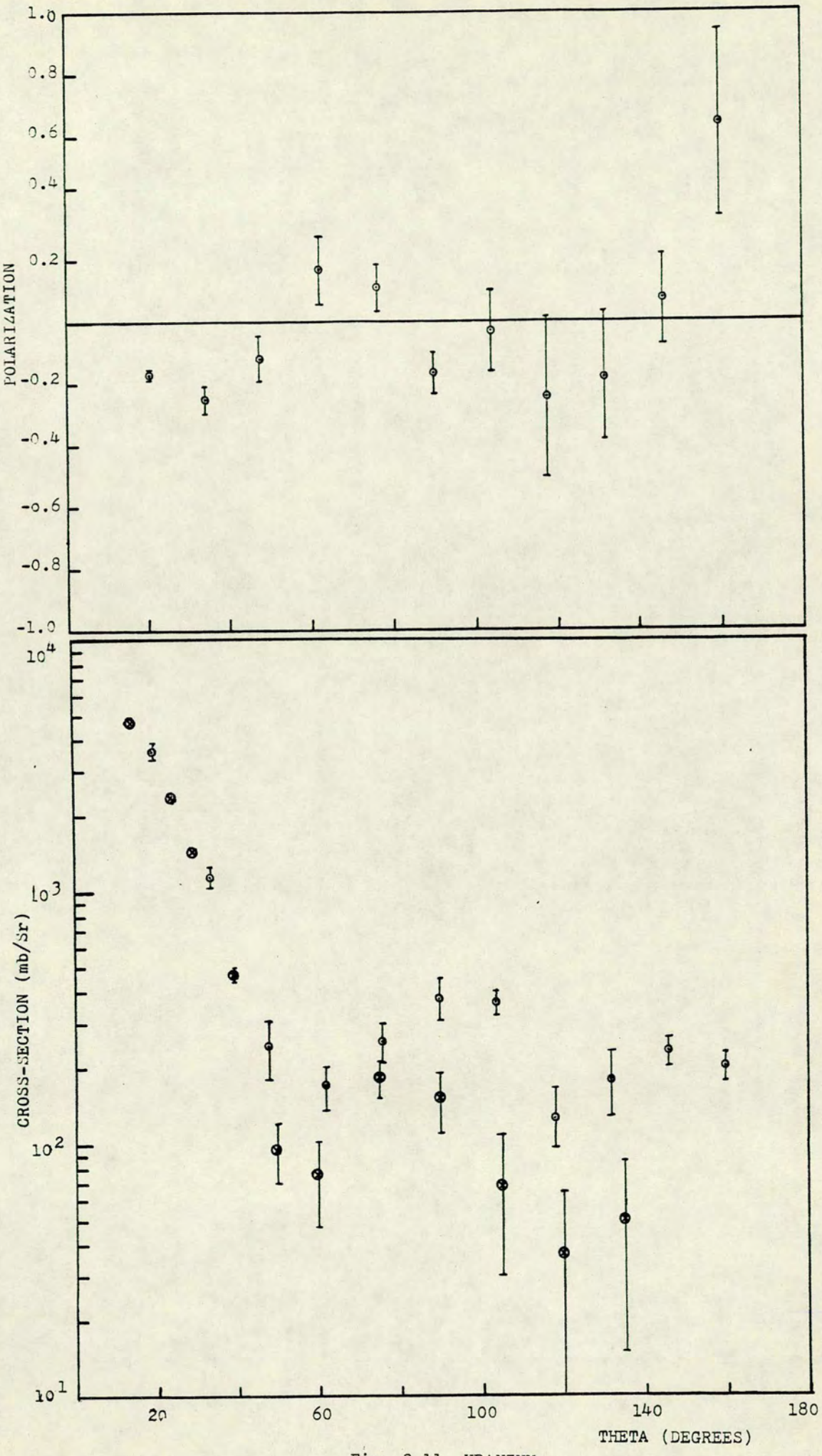

Fig. 3.11. URANIUM

CHAPTER 4

SCATTERING OF 16.1 MeV NEUTRONS

4.1 Introduction

The anomaly in the comparison of the only existing results for 16.1 MeV neutron polarization due to scattering from Cu and Pb, with optical model calculation based on global potentials, leads to the present measurements on neutrons of the same energy and for the same nuclei. The present measurements also included scattering from C, Fe, I and Hg in the angular range of 20° to 90°. The 16.1 MeV neutrons were produced at an angle of 75° to the incident deuteron beam, from the $^{3}H(d,n)^{4}He$ reaction. The incident beam consisted of 1 ns pulses of deuterons provided by the 3 MeV pulsed beam Van de Graaf accelerator IBIS at A.E.R.E., Harwell. The polarimeter, described in Chapter 2 with all the twelve detectors and associated electronics was shifted to Harwell for these measurements. The neutrons were scattered from cylindrical samples and the measurements done by employing the pulsed beam time of flight technique.

In the following section a brief description of the time of flight technique is included. Section 4.3 embodies the experimental arrangement, the electronics involved and the monitors used for the measurement. The results of the angular distribution of polarization and differential elastic scattering cross-section along with different corrections are presented in the last section.

4.2 Pulsed Beam Time of Flight Technique

Time of flight spectrometry in neutron angular distribution measurements has turned out to be profitable in reducing the background from unknown or unavoidable sources. Slow neutron time of flight techniques

have been used for many years. But the extension of this technique to higher energies was delayed by the necessity of improving the versatility of photomultiplier, scintillator and amplifiers to be accessible in the ns range for the fast neutrons. The design of time of flight spectrometers is characterized by the measurement of the time elapsed between the time a neutron is produced and the time at which it is detected. Thus the basic problems involved in the time of flight techniques are

(1) the production of a signal giving the time zero at the start of the flight of the neutrons and

(2) the production of another signal corresponding to the end of its flight.

While the arrival of a neutron in a detector at a definite time after its production from the target marks the end of its flight path, two different methods are adopted for the production of the zero time, i.e. the start signal of the neutrons. On the basis of these methods, neutron time of flight spectrometry bifurcates into two major classes, namely

i) Pulsed beam time of flight technique (P.S.T.) and

ii) Associated particle time of flight technique (A.P.T.).

In the following we discuss the pulsed beam technique, the technique adopted for the 16.1 MeV neutron scattering measurements. The A.P. technique used for the 14 MeV neutron double scattering experiment will be dealt with in Chapter 5 along with the experiment.

The P.S.T., in principle, can be applied to all types of neutron producing reactions and gives a zero time independent of the reaction mechanism. In this method the beam of incident particles which initiate the reaction is pulsed on to the target with the requirements that

(a) the duration of the pulse is short compared to the flight time measured and

(b) the repetition rate is such that the longest flight time of interest can be measured before the arrival of the succeeding beam pulse.

The relationship between the flight time and the energy of a non-relativistic neutron for the flight path d measured in metres is

$$t = 72.3d/E^{\frac{1}{2}}$$

where t is measured in ns and E in MeV. Hence for a flight path of one metre, the interval of time for neutrons of energies in the range 0.5 to 15 MeV is of the order of a few ns to 100 ns. The energy resolution is related to the time resolution by

$$\frac{dE}{E} = \frac{2dt}{t} = \frac{\sqrt{E}dt}{36.2d}$$

It follows from the above that for a given neutron of energy E, the energy resolution can be improved either by increasing d, the flight path or by decreasing dt. Since the counting rate is governed by the inverse square law of flight path, it is advantageous to decrease dt rather than to increase d.

Van de Graaff, Cockroft-Walton and Cyclotron accelerators are commonly used for fast neutron time of flight studies. In the Van de Graaf and Cockroft-Walton machines, which usually accelerate a beam continuously, the beam must be modulated by an external device. Different methods for pulsing the beam are in use. The method adopted for the IBIS accelerator at Harwell, is the Mobley Magnet compression method[82]. In this system the accelerated beam is swept across the double focussing Mobley magnet such that the pulses are compressed to a small width of about 1 ns on to the target. The peak current in such a system can be several milliamperes. The time of emission of the neutrons is indicated by a voltage pulse induced in a pick up tube before the target. The current pulse from the electrode is used to operate a fast sensitive

tunnel diode trigger circuit, whose output is large enough to operate timing equipment.

4.3.1 Experimental Arrangement

The tritium gas target at Harwell being at a height of 32 ft. above the ground, the polarimeter was mounted on a tower in front of the target. The target consisted of a tritium gas cell of 1 cm thickness filled to 1 atmosphere pressure. The main body of the shielding between target and the polarimeter was a water filled tank 120 cm diameter and 120 cm high, fitted with a tapered throated collimating tube. Fig (4.1) shows a schematic diagram of the experimental arrangement. The throat and the tapering for this experiment was designed to have two apertures of different shapes in succession. Near the target end the aperture was made circular, which was then extended to a rectangular aperture, such that the whole of the cylindrical scattering sample could be illuminated by the collimated neutron beam defined by the first aperture. Close to the target end the collimating tube was surrounded by a cylinder of iron of length 15 cm and diameter 20 cm to provide attenuation of the direct neutron flux from the target by inelastic scattering. In the remaining length of the collimator a cylinder of paraffin wax of the same diameter extended as far as the circular aperture, while around the rectangular aperture and throat it was made wider of 37 cm diameter. Tapered polythene inserts were used in the circular aperture while the rectangular throat and the taperings were made of brass. All these arrangements were made to minimize the intensity of the direct neutrons from the target. Along the outer diameter of the water tank, two wedges of the same height as the tank and made of paraffin wax were fixed on either side to provide extra shielding. The collimator and the polarimeter was set at an angle of 75^{o} with respect to the deuteron beam line and the axial alignment of the polarimeter to the target was adjusted as described in Chapter 2.2.

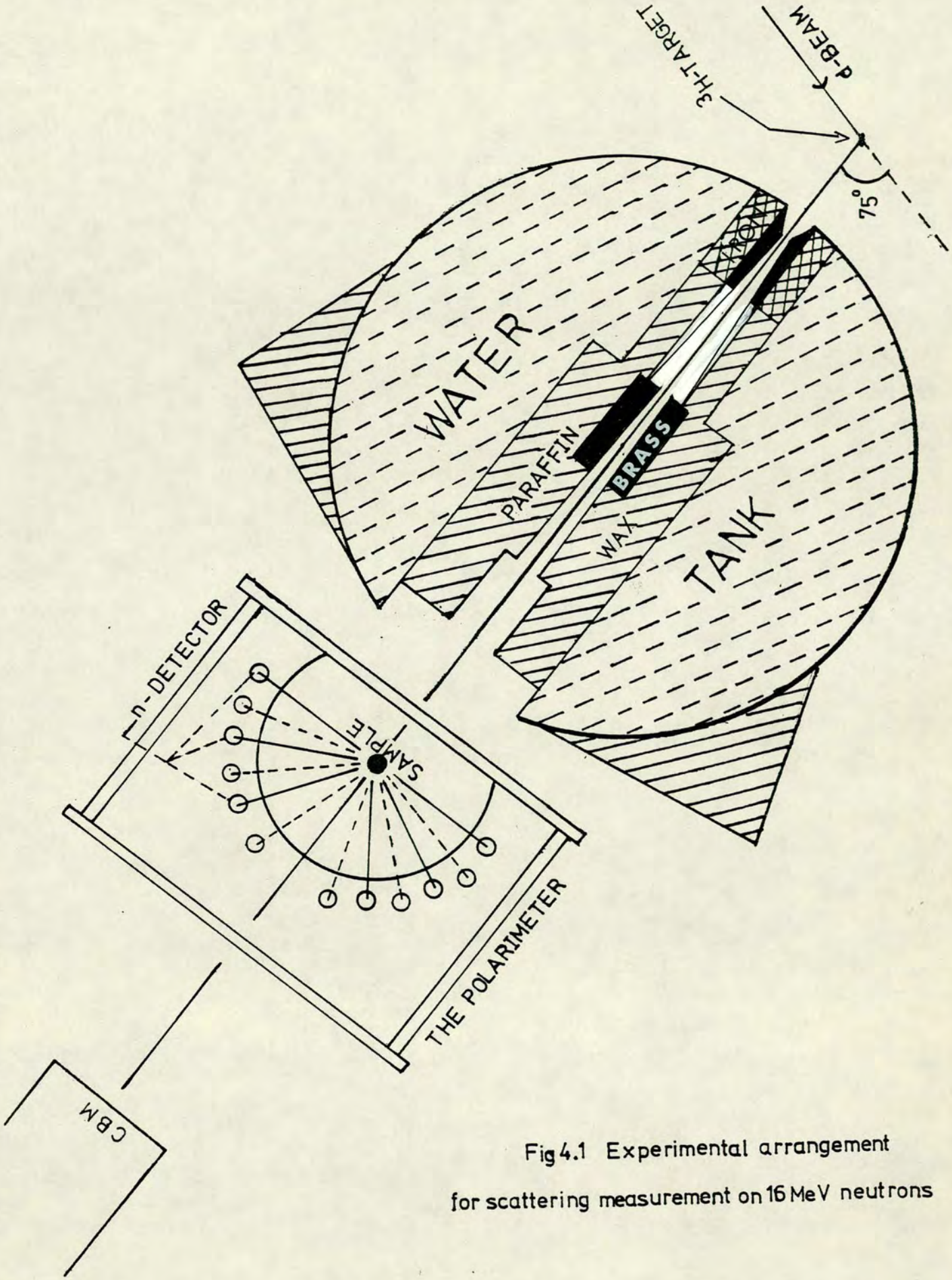

Fig 4.1 Experimental arrangement for scattering measurement on 16 MeV neutrons

The scatterers used were cylindrical, of diameter 5.08 cm and 9.9 cm in height on the average, placed at a distance of 180 cm from the target. Iodine and mercury samples were each contained in a thin walled stainless steel cylinder. The background measurements for these samples were done with an identical empty container in place of the sample.

4.3.2 Electronics of the System

The block diagram of the system of electronics employed with the twelve side detectors for polarization and cross-section measurements is shown in Fig. 4.2. The slow channel of the side detectors was the same as the one used for the 2.9 MeV measurement explained in 3.3.1 except that the linear energy bias in the present case was set to reject proton recoil events below 10 MeV. The fast output from all the twelve detectors were fed to a fast OR unit. The output from the OR unit after amplification through a fast amplifier was used as the start input for a time to amplitude converter (TAC). The stop pulses for the TAC were provided by the pulsed beam pick up unit. The TAC output was used as the linear input for the ADC handling routing. This, in coincidence with the output from the routing unit accepting AND gate signals from the slow coincidences for each detector, stored the neutron time of flight spectra in the appropriate sections of the memory.

The detector used as the collimated beam monitor for the 2.9 MeV scattering measurements and described in Chapter 3.3.3 was used as the target yield monitor for the 16 MeV neutrons, placed on the target side of the water tank. The block diagram of the circuit employed with this detector is shown in Fig. (4.3). The slow coincidence was the same as for the side detectors, selecting only neutrons of energy more than 10 MeV. The timing pulses from the anode of this detector, after amplification by a fast amplifier, were used as the start input

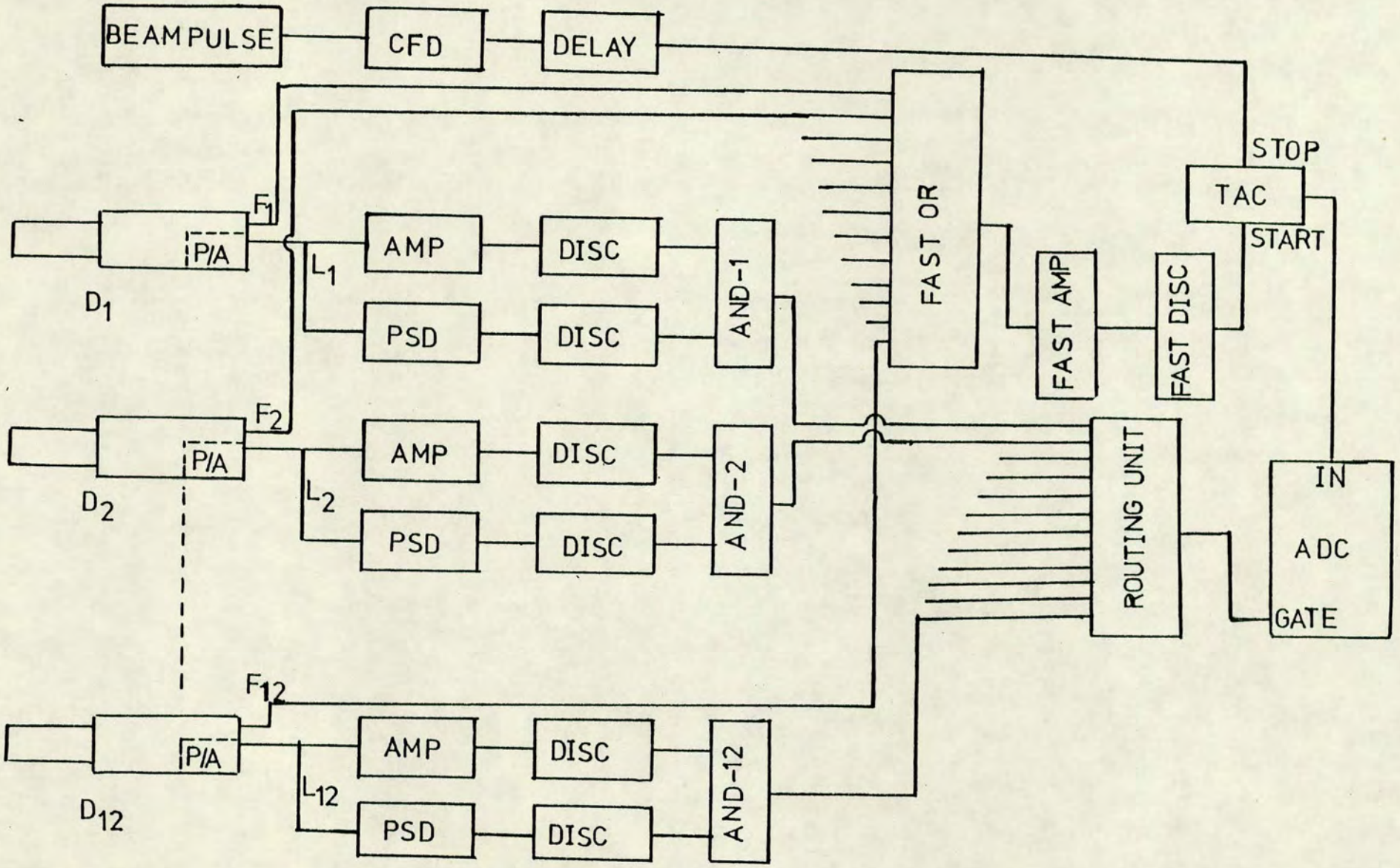

Fig. 4.2. A block diagram of the electronics used for scattering measurements on 16 MeV neutrons using time of flight technique.

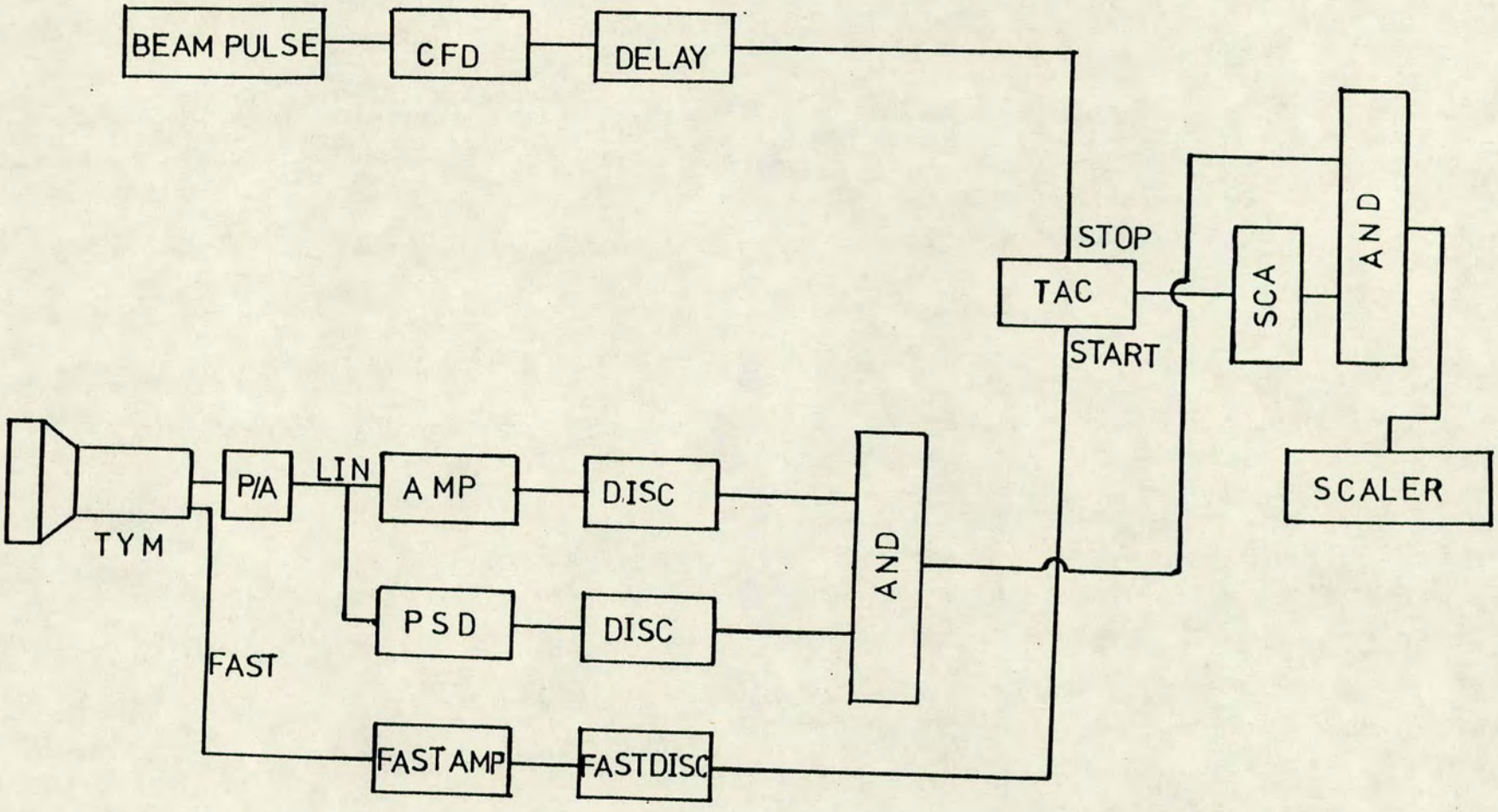

Fig. 4.3. Block diagram of the arrangement of the electronics used with the target yield monitor.

for a TAC, the stop pulses being provided by the pulsed beam pick up unit. The TAC output was used as input for a single channel analyser. The lower and upper limits of the SCA were set to select only the time of flight peak. The SCA output in coincidence with the slow channel coincidence output was used as input for one of the scalers in the CAMAC system to count the number of neutrons produced from the source reaction.

The CBM used for the 16 MeV neutrons consisted of a circular disc of plastic 30 cm in diameter and 5 cm thick, coupled to a XP1040 type of photomultiplier tube[83]. A conical light guide of perspex, 13 cm long with circular end faces of diameters 11 and 30 cm, was used for coupling the scintillator to the photomultiplier tube. The electronics associated with the CBM was the same as the TYM except that no pulse shape discrimination was necessary. The CBM was placed in line with the axis of the collimated neutron beam at a distance of 316 cm from the tritium gas cell such that the whole of the collimated beam was intercepted by the scintillator.

4.4 Experimental Measurement and Analysis

After careful alignment of the polarimeter and the collimator with the tritium target, the detector system was checked for gain change and false asymmetries, using the ^{60}Co source of gamma rays. The test was performed in the same way as described in Chapter 3.4. When the test with the source was satisfactory, the pulsed beam of deuterons from the accelerator was used to strike the tritium gas target and produce neutrons of 16.1 MeV energy at an angle of 75^{o} (lab.). The experimental data were collected with the scatterers in and out of the neutron beam when the polarimeter was rotated to the two azimuthal positions $\phi = 0$ and $\phi = \pi$. As in the case of 2.9 MeV neutrons, the data in each

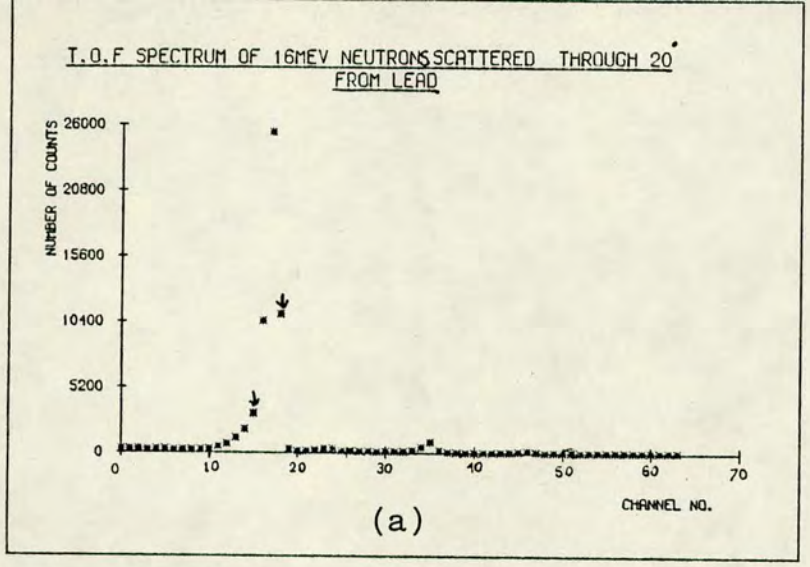

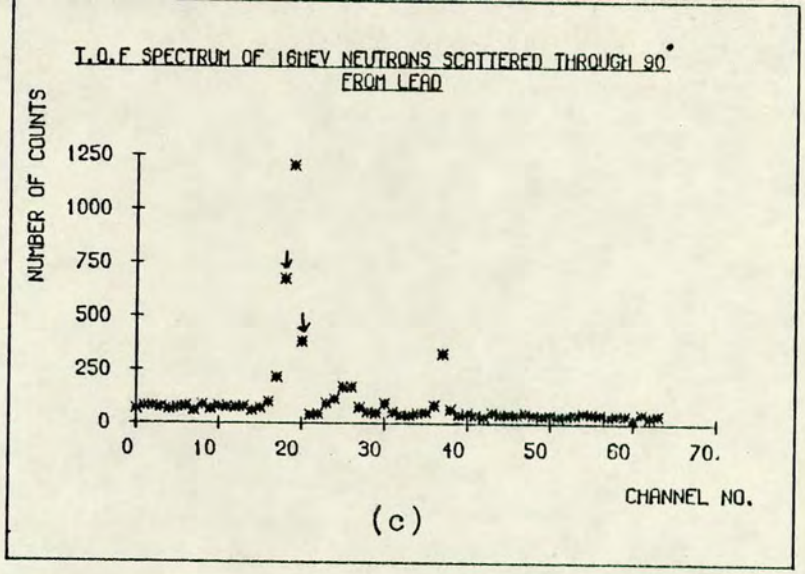

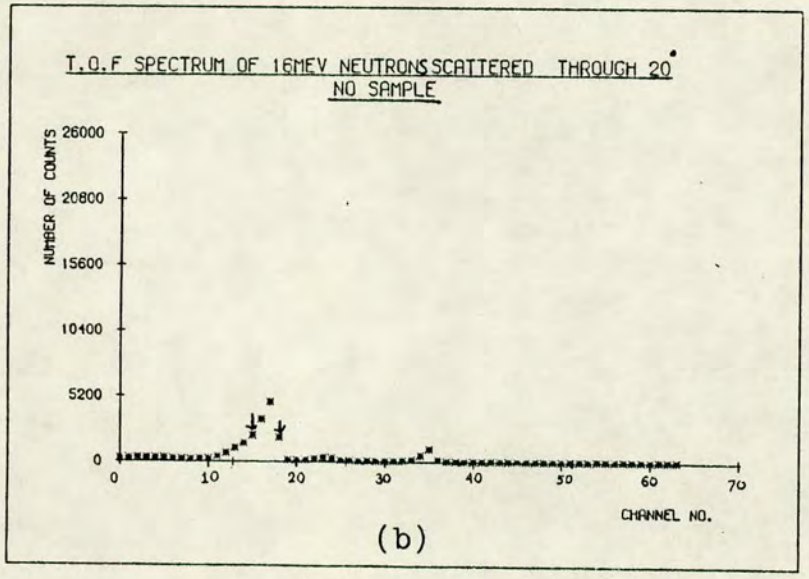

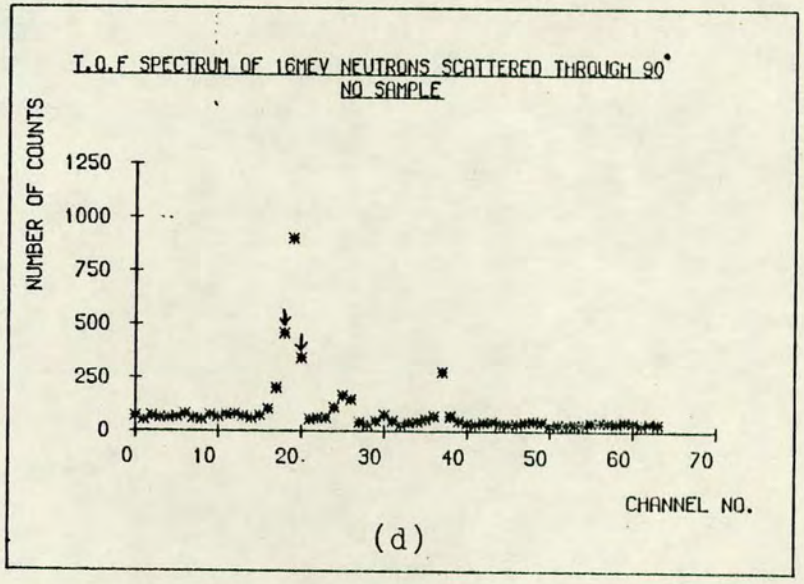

Fig. 4.4. Time of flight spectra.

a) for 20° scattering by lead.
b) background at 20°.
c) for 90° scattering by lead.
d) background at 90°.

position was collected for a short period of 1000 sec. and the sequence repeated frequently. The data for each of the nuclei were accumulated for 12/13 hours, except for C which was done for only four hours. The relative efficiencies of the twelve side detectors were determined at the beginning and at the end of the experiment in the same way as described in Chapter 3.5.1. The relative efficiencies could not be determined separately for the measurement on each scattering sample, as was done for the 2.9 MeV cross-section measurement for two reasons, namely, the limited accelerator running time available and the need for switching the accelerator off each time a detector was to be placed manually in the direct beam. The average of the two measurements was used for the cross-section calculation for all the samples.

The polarization and the cross-section values, from the observed right and left scattered counts were calculated using the formulae 3.1, 3.2 and 3.7 and the same computer programme discussed in 3.5.4. The channel limits in this case were determined to integrate the counts under the time of flight peak only. Fig. 4.4 shows the time of flight spectra for both scattering and background for Pb and for one of the pair of detectors at 20° and 90°. The arrows indicate the channel limits used for integration. The background counts varied from 20% at 20° to about 85% around 90° for the different nuclei.

The polarization of the neutrons from the $^{3}H(d,n)^{4}He$ reaction, required for calculating the polarization analysing power for different nuclei from the measured asymmetries was estimated from established results of different experimenters. Fig. 4.5 shows a plot of the various measurements[84-87] of polarization of neutrons from the above reaction for deuteron energies in the range 1.5 to 4.5 MeV and emission angles from 70° to 80°. From all these measurements a value of $-.24 \pm .03$ was estimated for incident deuterons of 2.8 MeV and a neutron

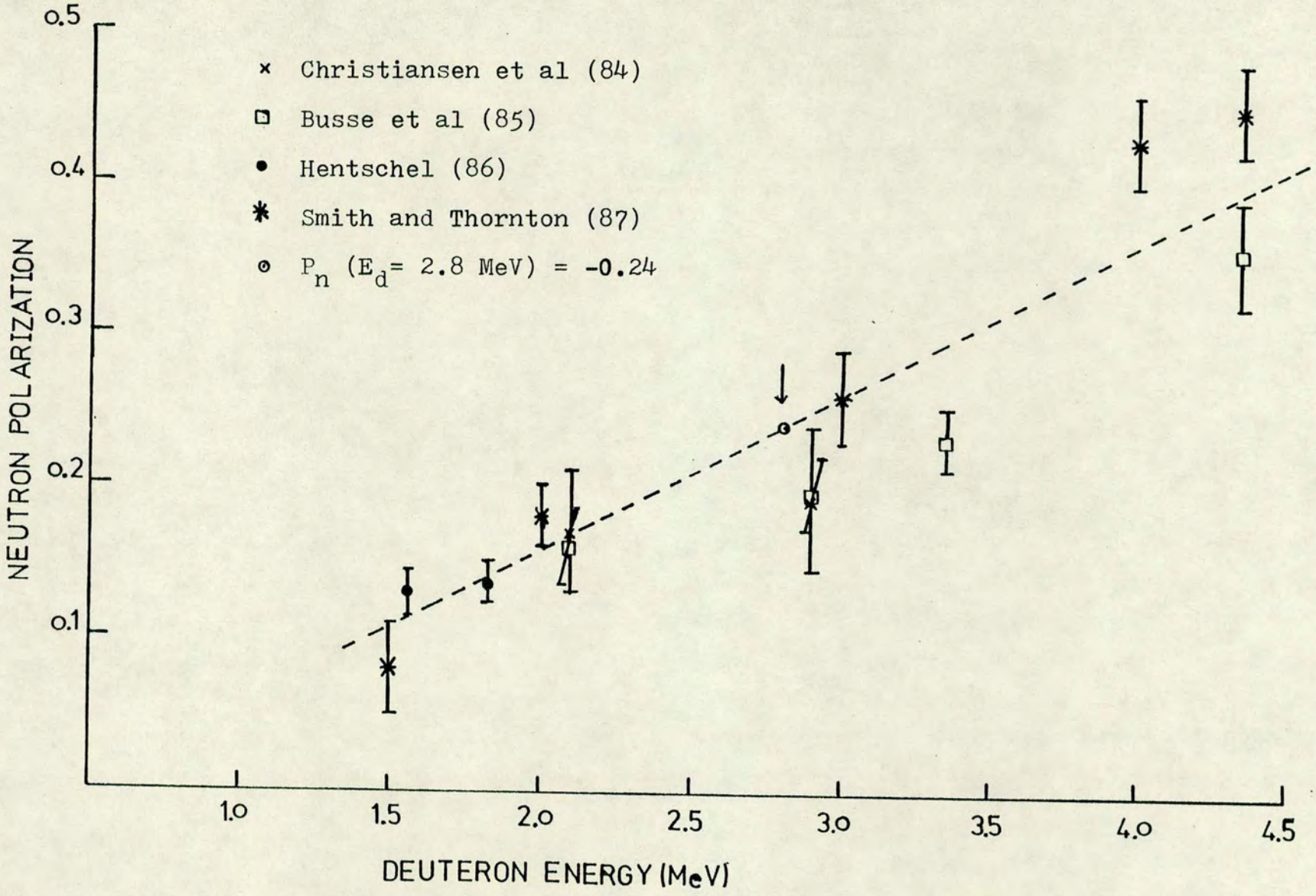

Fig. 4.5. Polarization of the $^{3}H(d,n)^{4}He$ neutrons at $75^{o} \pm 5^{o}$.

emission angle of 75^{o}. This may introduce an uncertainty of ± 12.5% in the values of the polarization analyzing power. However this was found to be less than the statistical uncertainties for all angles except for 20^{o}. The errors associated with the measured polarization and cross-section values were estimated following the same procedure outlined for 2.9MeV scattering in Chapter 3.5.4. However in the present cross-section measurement, the errors due to the variation in the relative efficiency $\varepsilon_m/\varepsilon_d$ was found to be most important and estimated to be about ± 10%. The uncertainty resulted because of the limitation in doing frequent inter-calibration for practical reasons explained in Section 4.4.

4.5.1 Experimental Results

The polarization values for Cu and Pb from the present measurement are presented in the first column of Tables 4.1 and 4.2. In the second column of these tables are listed the values of the previous measurements of Galloway and Waheed[37]. Clearly the large magnitude of polarization at 20^{o} is consistent in both measurements. However, the agreement between the two sets of results for most of the angles are very poor. The error associated with the polarization values from the present measurement, for angles greater than 48^{o} are very large. This was anticipated as the measurement time was chosen in order to achieve reasonable accuracy for 20^{o} and 34^{o} values only. It is therefore difficult to arrive at any conclusive result for all the angles from these sets of measurements. However the existence of data to be analysed, collected for longer periods by F. McN Watson[46], lead to the possibility of conclusive and additional results. These data consist of measurements in the angular range of 20^{o} to 160^{o} for Cu, Pb, Fe, Hg and W, while for C and I in the range 20^{o} to 90^{o}. All

these data were analysed in the same way as described in Section 4.4. The results for Cu and Pb polarization from these measurements are listed in the third column of Tables 4.1 and 4.2, while in the fourth column are the values finally decided from the two recent measurements. The two recent measurements are preferred in determining the final results because of the improvement of the system for background measurement. The polarimeter in its original form, used for the first set of measurements, did not have the pneumatic sample moving system. The 'sample in' measurements were, therefore, done for many hours and then the 'sample out' measurement done for the same time, after removing the sample manually. This involved closing the accelerator off briefly. But with the automatic sample changing system in the two recent measurements, the 'sample in' and 'out' measurement could be done frequently without disruption of the accelerator running and providing improved and statistically accurate background data. Also the improvement in the collimation of the incident neutron beam by incorporating the rectangular aperture described in 4.3.1, and the use of extra shielding, ensured improved scattering data in the recent measurements. In determining the final values, a weighted average of the two measurements is taken for the 20^{o}, 34^{o} and 48^{o} values, while for the rest, the value with the better accuracy is taken to be appropriate. For the backward angles, analysis of the only measurements done by F. McN. Watson are accepted.

The values of differential cross-section for all the nuclei are determined by taking the average of the two recent measurements. The final values of the angular distribution of polarization and cross-section for all nuclei mentioned above are presented in Tables 4.3 to 4.9, along with the values corrected for different effects discussed below.

Angles	Present Measurement	Measurement of Galloway & Waheed[37]	Measurement of F.McN. Watson[46]	Final Values
20°	+0.36 ± 0.02	+0.39 ± 0.03	+0.49 ± 0.01	+0.43 ± 0.06
34°	+0.36 ± 0.09	+0.18 ± 0.08	+0.46 ± 0.04	+0.44 ± 0.04
48°	+0.14 ± 0.15	−0.25 ± 0.06	−0.04 ± 0.06	−0.02 ± 0.05
62°	+0.02 ± 0.39	−0.83 ± 0.15	+0.02 ± 0.10	+0.02 ± 0.10
76°	−0.09 ± 0.28	−0.21 ± 0.09	+0.13 ± 0.10	+0.13 ± 0.10
90°	+0.42 ± 0.29	−0.67 ± 0.19	+0.12 ± 0.10	+0.12 ± 0.10
104°			+0.03 ± 0.07	+0.03 ± 0.07
118°			+0.14 ± 0.08	+0.14 ± 0.08
132°			+0.18 ± 0.18	+0.18 ± 0.18
146°			−0.07 ± 0.09	−0.07 ± 0.09
160°			+0.11 ± 0.07	+0.11 ± 0.07

TABLE 4.1 Uncorrected measured polarization of 16 MeV neutrons elastically scattered by Cu.

Angles	Present Measurement	Measurement of Galloway & Waheed[37]	Measurement of F.McN. Watson[46]	Final Values
20°	+0.44 ± 0.22	+0.71 ± 0.03	+0.66 ± 0.01	+0.55 ± 0.11
34°	+0.03 ± 0.04	+0.13 ± 0.04	+0.14 ± 0.02	+0.12 ± 0.04
48°	+0.21 ± 0.09	+0.04 ± 0.03	+0.40 ± 0.04	+0.37 ± 0.04
62°	+0.24 ± 0.18	+0.41 ± 0.07	+0.27 ± 0.08	+0.27 ± 0.08
76°	+0.06 ± 0.32	-0.24 ± 0.11	+0.13 ± 0.02	+0.13 ± 0.12
90°	-1.29 ± 0.46	-0.14 ± 0.13	+0.09 ± 0.13	+0.09 ± 0.13
104°			+0.13 ± 0.06	+0.13 ± 0.06
118°			+0.02 ± 0.11	+0.02 ± 0.11
132°			+0.63 ± 0.40	+0.63 ± 0.40
146°			-0.11 ± 0.10	-0.11 ± 0.10
160°			+0.03 ± 0.08	+0.03 ± 0.08

TABLE 4.2 Uncorrected measured polarization of 16 MeV neutrons elastically scattered by Pb.

4.5.2 Corrections for Sample Size and Inelastic Scattering

The experimentally measured distributions of cross-section and polarization have been corrected for finite geometry and multiple scattering effects by the Monte Carlo programme, described in 3.6.1. and following the same procedure. The different cross-section values needed as input for the programme were taken from Howerton[74] (Fe, Cu), Fu and Perey[41] (Pb), Haouat et al.[88] (C) and Foster and Glasgow[89] (Hg, W, I).

The limited flight path of 30 cm for the scattered neutrons made it difficult to distinguish any inelastic scattering from elastic scattering by time of flight. At 16 MeV neutron energy a number of levels for most of the nuclei may be excited and therefore may contribute significantly to the supposed elastic scattering distribution, particularly at the minima depending upon the inelastic cross-section. However the linear discrimination bias set at 10 MeV for each detector served to eliminate inelastic events due to states of excitation energy greater than about 5 MeV. Further the high energy bias reduced the detection efficiency for neutrons scattered by lower energy states relative to that for elastically scattered neutrons. Available data on the angular distribution of inelastic scattering modified by appropriate detection efficiency factors and used for correction of the observed scattering distribution for different nuclei are listed as $\Sigma\varepsilon\sigma_{in}$ in Tables 4.3 - 4.9.

For Cu and Pb the factors $\Sigma\,\varepsilon\,\sigma_{in}$ were already calculated by Galloway and Waheed[37] from data of Coon et al.[90] and Fu and Perey[41] respectively for the same energy bias employed in the present measurement. The data of Coon et al.[90] for the differential inelastic cross-sections for scattering of 14.5 MeV neutrons from Fe, measured by detecting neutrons with energy greater than 9 MeV, have been used

for inelastic correction of the present elastic data on Fe.

For Hg, the only available data[91] on neutrons inelastically scattered through 92° with energies 10.76 MeV and 11.9 MeV have been used. For W, the data available[92] on the cross-section of inelastic neutrons with energy in the range 6-14 MeV for scattering through 90° have been used for the correction. The angular distribution measurement on neutrons inelastically scattered from carbon by Haouat et al.[88] have been used for the correction of the present elastic scattering results on carbon. For Iodine, no relevant data on inelastic cross-sections are available and therefore no correction could be applied.

The polarization and cross-section values for all the nuclei corrected for sample size and inelastic contribution, are listed as $P_{Monte}(\theta)$, $\sigma_{Monte}(\theta)$ and $P_{el}(\theta)$ and $\sigma_{el}(\theta)$ in Tables 4.3 - 4.9. It is clear from the tables that for all the nuclei the angular distribution of polarization is not critically dependent on either the sample size or inelastic scattering correction. For the forward angles, particularly 20° and 34°, the correction is negligible and for the rest of the angles the correction is either smaller or, in a few cases, comparable to the statistical error associated with the experimental results. In the case of the differential cross-section results, the major correction arises from the attenuation of the incident flux in the sample. The correction for inelastic scattering for all the nuclei is negligible except at the minima of the elastic scattering distribution. The uncorrected and corrected distribution of polarization and cross-section for Cu are presented in Fig. 4.6 as an example of the above-mentioned corrections.

TABLES 4.3 - 4.9

Uncorrected and corrected distribution of polarization and cross-section of 16 MeV neutrons scattered from Fe, Cu, I, W, Hg, Pb and C.

Angles	$P_{expt}(\theta)$	$\sigma_{expt}(\theta)$	$P_{Monte}(\theta)$	$\sigma_{Monte}(\theta)$ (mb/sr)	$\Sigma\varepsilon\sigma_{in}$ (mb/sr)	$P_{el}(\theta)$	$\sigma_{el}(\theta)$ (mb/sr)
—							
20°	+0.40 ± 0.08	260 ± 60	+0.37 ± 0.08	580 ± 113	-	+0.38 ± 0.09	580 ± 113
34°	+0.43 ± 0.05	77 ± 16	+0.41 ± 0.05	139 ± 29	5.7	+0.43 ± 0.05	134 ± 29
48°	-0.10 ± 0.05	38 ± 4	-0.22 ± 0.06	68 ± 8	5.1	-0.24 ± 0.06	67 ± 8
62°	+0.12 ± 0.10	23 ± 6	+0.16 ± 0.12	36 ± 11	4.6	+0.18 ± 0.14	31 ± 11
76°	+0.04 ± 0.10	18 ± 2	-0.03 ± 0.13	29 ± 4	3.5	-0.03 ± 0.15	25 ± 4
90°	+0.08 ± 0.06	24 ± 7	+0.09 ± 0.07	41 ± 13	2.8	+0.10 ± 0.07	38 ± 13
104°	+0.15 ± 0.09	25 ± 7	+0.02 ± 0.09	45 ± 13	2.3	+0.02 ± 0.09	43 ± 13
118°	-0.01 ± 0.10	15 ± 4	-0.04 ± 0.14	23 ± 8	3.5	-0.05 ± 0.16	20 ± 8
132°	+0.16 ± 0.26	5 ± 2	+0.16 ± 0.45	5 ± 3	3.4	+0.43 ± 1.21	2 ± 2
146°	+0.38 ± 0.12	12 ± 4	+0.37 ± 0.16	18 ± 7	3.6	+0.46 ± 0.20	14 ± 7
160°	+0.19 ± 0.09	37 ± 11	+0.16 ± 0.10	66 ± 22	4.6	+0.17 ± 0.11	61 ± 22

TABLE 4.3 - IRON

Angles	$P_{expt}(\theta)$	$\sigma_{expt}(\theta)$ (mb/sr)	$P_{Monte}(\theta)$	$\sigma_{Monte}(\theta)$	$\Sigma\varepsilon\sigma_{in}$ (mb/sr)	$P_{el}(\theta)$	$\sigma_{el}(\theta)$ (mb/sr)
20^{o}	+0.43 ± 0.06	398 ± 89	+0.40 ± 0.06	945 ± 170	-	+0.40 ± 0.06	945 ± 170
34^{o}	+0.44 ± 0.04	102 ± 31	+0.43 ± 0.05	175 ± 59	4.4	+0.44 ± 0.05	171 ± 59
48^{o}	-0.02 ± 0.05	38 ± 4	-0.11 ± 0.08	60 ± 8	5.6	-0.12 ± 0.09	54 ± 8
62^{o}	+0.02 ± 0.10	26 ± 6	-0.03 ± 0.13	38 ± 11	3.3	-0.03 ± 0.14	35 ± 11
76^{o}	+0.13 ± 0.10	24 ± 3	+0.13 ± 0.11	38 ± 6	3.7	+0.14 ± 0.13	34 ± 6
90^{o}	+0.08 ± 0.05	28 ± 8	+0.02 ± 0.07	44 ± 15	3.0	+0.02 ± 0.07	41 ± 15
104^{o}	+0.03 ± 0.07	39 ± 11	-0.01 ± 0.07	81 ± 21	2.5	-0.01 ± 0.07	78 ± 21
118^{o}	+0.14 ± 0.08	22 ± 6	+0.14 ± 0.12	33 ± 12	2.8	+0.15 ± 0.13	30 ± 12
132^{o}	+0.18 ± 0.18	9 ± 3	+0.19 ± 0.31	10 ± 5	2.6	+0.25 ± 0.42	7 ± 5
146^{o}	-0.07 ± 0.09	20 ± 5	-0.15 ± 0.14	28 ± 10	2.4	-0.17 ± 0.15	25 ± 10
160^{o}	+0.11 ± 0.07	61 ± 18	+0.10 ± 0.08	112 ± 33	-	+0.10 ± 0.08	112 ± 33

TABLE 4.4 - COPPER

Angle	$P_{expt}(\theta)$	$\sigma_{expt}(\theta)$ (mb/sr)	$P_{Monte}(\theta)$	$\sigma_{Monte}(\theta)$ (mb/sr)
20^{o}	+0.41 ± 0.07	1355 ± 160	+0.41 ± 0.07	1775 ± 196
34^{o}	+0.28 ± 0.09	156 ± 45	+0.23 ± 0.13	143 ± 55
48^{o}	+0.32 ± 0.08	89 ± 12	+0.36 ± 0.09	103 ± 15
62^{o}	+0.01 ± 0.16	62 ± 20	-0.05 ± 0.16	67 ± 24
76^{o}	-0.04 ± 0.03	35 ± 15	-0.05 ± 0.35	38 ± 18
90^{o}	+0.06 ± 0.24	52 ± 30	+0.06 ± 0.24	54 ± 37

TABLE 4.5 - IODINE

Angles	P_{expt}	$\sigma_{expt}(\theta)$ (mb/sr)	P_{Monte}	$\sigma_{Monte}(\theta)$ (mb/sr)	$\Sigma\varepsilon\sigma_{in}$ (mb/sr)	$P_{el}(\theta)$	$\sigma_{el}(\theta)$
20^o	+0.52 ± 0.08	687 ± 105	+0.57 ± 0.08	1149 ± 144		+0.57 ± 0.08	1146 ± 144
34^o	+0.05 ± 0.03	193 ± 30	−0.05 ± 0.04	230 ± 41		−0.05 ± 0.04	227 ± 41
48^o	+0.31 ± 0.04	91 ± 14	+0.35 ± 0.05	132 ± 19		+0.36 ± 0.05	129 ± 19
62^o	+0.24 ± 0.09	42 ± 6	+0.15 ± 0.13	48 ± 8		+0.16 ± 0.14	45 ± 8
76^o	+0.08 ± 0.11	36 ± 6	+0.27 ± 0.10	52 ± 8		+0.29 ± 0.11	49 ± 8
90^o	+0.02 ± 0.06	23 ± 3	−0.03 ± 0.08	27 ± 4		−0.03 ± 0.09	24 ± 4
104^o	−0.08 ± 0.10	16 ± 3	−0.04 ± 0.11	20 ± 4	3	−0.05 ± 0.13	17 ± 4
118^o	−0.39 ± 0.12	8 ± 2	−0.50 ± 0.18	8 ± 3		−0.80 ± 0.29	5 ± 3
132^o	+0.31 ± 0.15	8 ± 2	+0.47 ± 0.18	9 ± 3		+0.71 ± 0.27	6 ± 3
146^o	+0.19 ± 0.16	6 ± 2	+0.29 ± 0.18	6 ± 3		+0.58 ± 0.36	3 ± 3
160^o	−0.32 ± 0.14	10 ± 2	−0.33 ± 0.18	12 ± 3		−0.44 ± 0.24	9 ± 3

TABLE 4.6 - TUNGSTEN

Angles	$P_{expt}(\theta)$	$\sigma_{expt}(\theta)$ (mb/sr)	$P_{Monte}(\theta)$	$\sigma_{Monte}(\theta)$ (mb/sr)	$\Sigma\varepsilon\sigma_{in}$ (mb/sr)	$P_{el}(\theta)$	$\sigma_{el}(\theta)$ (mb/sr)
20^{o}	+0.48 ± 0.15	522 ± 125	+0.50 ± 0.15	1087 ± 227		+0.50 ± 0.15	1081 ± 227
34^{o}	+0.12 ± 0.02	235 ± 50	+0.07 ± 0.02	465 ± 91		+0.07 ± 0.02	459 ± 91
48^{o}	+0.40 ± 0.03	85 ± 10	+0.47 ± 0.04	136 ± 18		+0.49 ± 0.04	130 ± 18
62^{o}	+0.40 ± 0.09	48 ± 6	+0.34 ± 0.11	75 ± 11		+0.37 ± 0.12	69 ± 11
76^{o}	+0.10 ± 0.10	32 ± 5	+0.11 ± 0.14	47 ± 9		+0.13 ± 0.16	41 ± 9
90^{o}	+0.04 ± 0.09	32 ± 17	-0.05 ± 0.11	61 ± 31	6	-0.06 ± 0.12	55 ± 31
104^{o}	-0.19 ± 0.15	18 ± 9	-0.22 ± 0.22	23 ± 17		-0.30 ± 0.30	17 ± 17
118^{o}	-0.85 ± 0.20	21 ± 10	-1.17 ± 0.21	34 ± 19		-1.42 ± 0.26	28 ± 19
132^{o}	+0.54 ± 0.29	12 ± 6	+0.96 ± 0.45	15 ± 11		+1.60 ± 0.75	9 ± 11
146^{o}	-0.25 ± 0.23	10 ± 5	-0.44 ± 0.35	13 ± 9		-0.82 ± 0.65	7 ± 9
160^{o}	-0.14 ± 0.18	13 ± 6	-0.27 ± 0.24	19 ± 11		-0.39 ± 0.35	13 ± 11

TABLE 4.7 - MERCURY

Angles	$P_{expt}(\theta)$	$\sigma_{expt}(\theta)$ (mb/sr)	$P_{Monte}(\theta)$	$\sigma_{Monte}(\theta)$ (mb/sr)	$\Sigma\varepsilon\sigma_{in}$ (mb/sr)	$P_{el}(\theta)$	$\sigma_{el}(\theta)$ (mb/sr)
20^o	+0.55 ± 0.11	522 ± 77	+0.55 ± 0.11	1031 ± 127	9	+0.55 ± 0.11	1022 ± 127
34^o	+0.10 ± 0.05	307 ± 51	−0.02 ± 0.05	531 ± 84	7	−0.02 ± 0.05	524 ± 84
48^o	+0.34 ± 0.04	93 ± 9	+0.38 ± 0.05	134 ± 15	6	+0.40 ± 0.05	128 ± 15
62^o	+0.27 ± 0.08	47 ± 8	+0.20 ± 0.10	64 ± 13	5	+0.22 ± 0.11	59 ± 13
76^o	+0.13 ± 0.12	28 ± 3	+0.19 ± 0.15	36 ± 5	4	+0.21 ± 0.17	32 ± 5
90^o	+0.13 ± 0.07	19 ± 2	+0.20 ± 0.23	23 ± 3	3	+0.23 ± 0.26	20 ± 3
104^o	+0.13 ± 0.06	41 ± 4	+0.16 ± 0.06	66 ± 7	2	+0.17 ± 0.06	64 ± 7
118^o	+0.02 ± 0.11	18 ± 2	−0.07 ± 0.17	21 ± 3	2	−0.08 ± 0.19	19 ± 3
132^o	+0.63 ± 0.40	7 ± 1	+1.07 ± 0.83	6 ± 2	2	+1.61 ± 1.25	4 ± 2
146^o	−0.11 ± 0.10	15 ± 2	−0.21 ± 0.16	17 ± 3	2	−0.24 ± 0.18	15 ± 3
160^o	+0.03 ± 0.08	48 ± 5	0.00 ± 0.09	71 ± 8	2	0.00 ± 0.09	69 ± 8

TABLE 4.8 - LEAD

Angles	$P_{expt}(\theta)$	$\sigma_{expt}(\theta)$ (mb/sr)	$P_{Monte}(\theta)$	$\sigma_{Monte}(\theta)$ (mb/sr)	$\Sigma\varepsilon\sigma_{in}$ (mb/sr)	$P_{el}(\theta)$*	$\sigma_{el}(\theta)$ (mb/sr)
20^o	+0.14 ± 0.02	258 ± 60	+0.15 ± 0.02	365 ± 73	8	+0.15 ± 0.02	357 ± 73
34^o	+0.11 ± 0.02	147 ± 25	+0.11 ± 0.02	201 ± 31	8	+0.12 ± 0.02	193 ± 31
48^o	−0.03 ± 0.04	41 ± 4	−0.08 ± 0.06	45 ± 5	7	−0.05 ± 0.07	38 ± 5
62^o	+0.12 ± 0.06	21 ± 2	+0.13 ± 0.07	23 ± 3	5	+0.23 ± 0.09	18 ± 3
76^o	+0.24 ± 0.08	15 ± 4	+0.27 ± 0.10	16 ± 5	2	+0.33 ± 0.12	14 ± 5
90^o	+0.10 ± 0.07	15 ± 3	+0.12 ± 0.10	17 ± 4	2	+0.14 ± 0.12	15 ± 4

TABLE 4.9 - CARBON

* The correction for the contribution of the inelastically scattered neutrons in this case has been done by using,

$$P_{el} = P\left(1 + \frac{\Sigma\varepsilon\sigma_{in}}{\sigma_{el}}\right) - P_{in}\left(\frac{\Sigma\varepsilon\sigma_{in}}{\sigma_{el}}\right) \quad \text{(2nd term added to eqn. 3.14)}$$

where P_{in} is the asymmetry of the inelastically scattered neutrons. The relevant P_{in} for the calculation was taken from ref. 93.

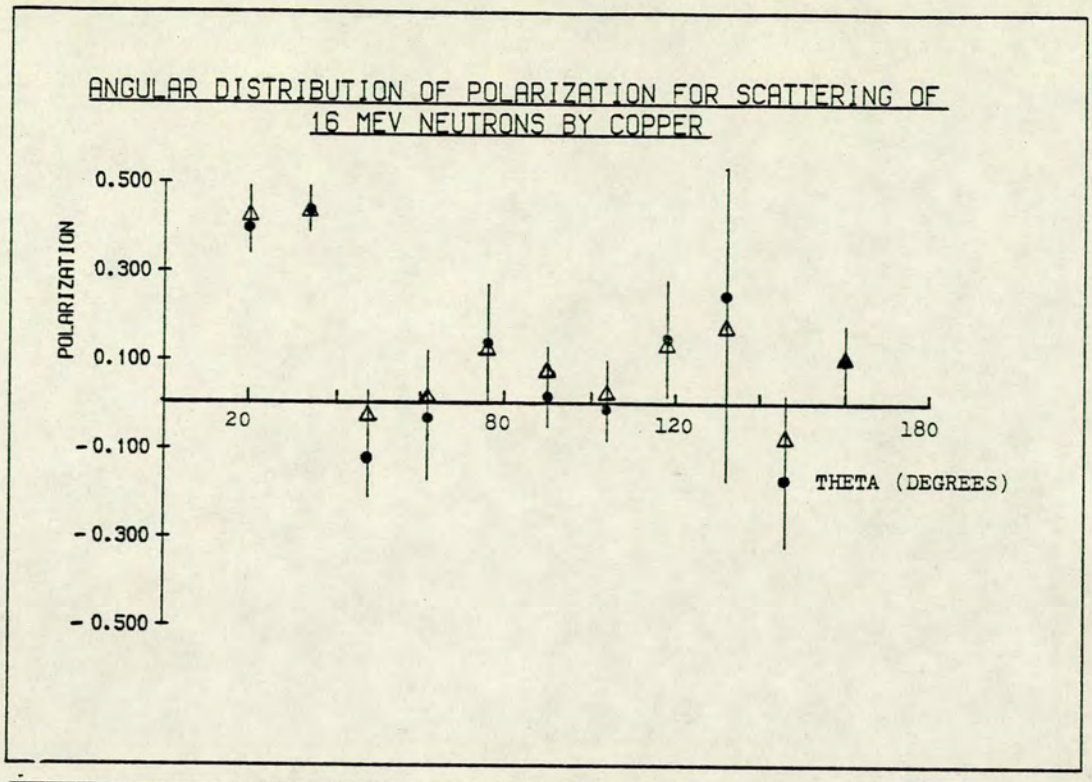

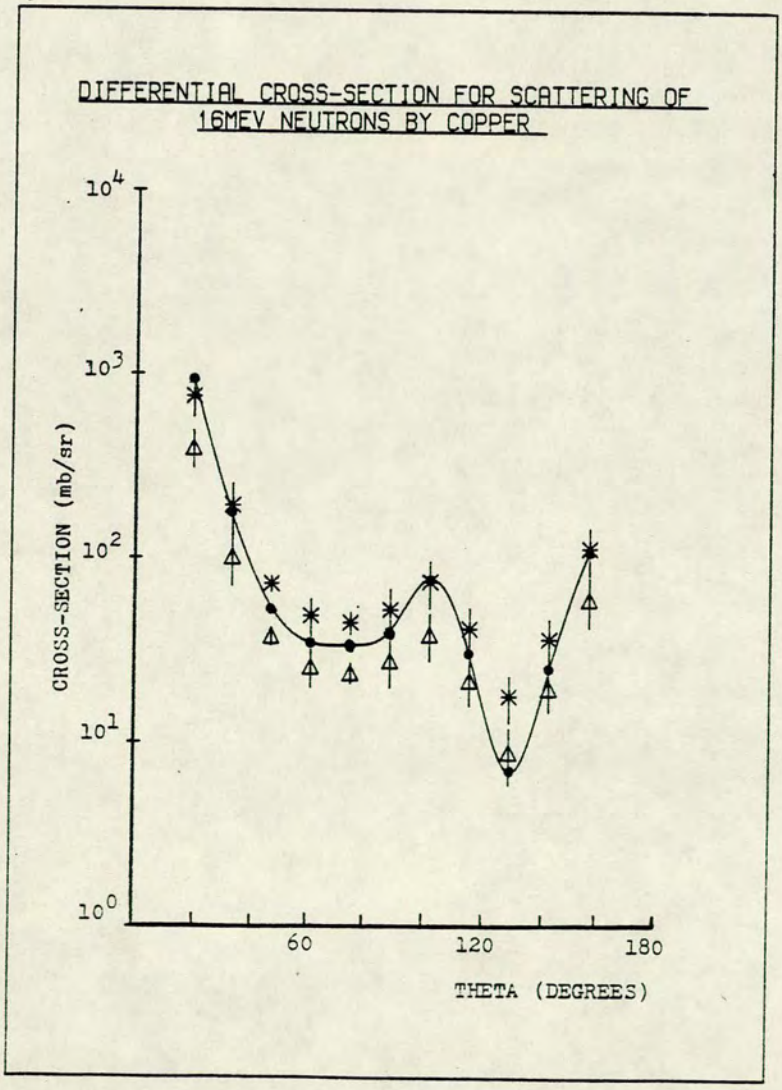

△ Uncorrected.

✱ Corrected for flux attenuation.

●—● Corrected for flux attenuation, multiple scattering and inelastic scattering.

Fig. 4.6. Uncorrected and corrected distribution of polarization and cross-section for copper.

4.5.3 Comparison with Other Results for Cross-Section and Polarization

There are no polarization data available at energies around 16 MeV for any of the heavy nuclei studied in the present work except for the measurements on Cu and Pb by Galloway and Waheed[37] for the same energy and the forward angles. The uncorrected values from their measurement have already been compared with the present values in Tables 4.1 and 4.2 and Section 4.5.1. The present polarization measurement, not only establishes the large magnitude of polarization around 20^{o} for Cu and Pb, found by Galloway and Waheed[37], but also shows a similar behaviour for all the other nuclei studied, except for C. This difference is not surprising, since Carbon is a much lighter nucleus, compared to all the other nuclei considered. For C, polarization measurement for 15.85 MeV neutrons have been reported by Lesiecki et al.[93]. The present polarization measurement compared with their values in Fig. 4.7 shows a significant difference between the two sets. However the presence of a resonance in the n - ^{12}C scattering at 15.8 MeV reported by Boreli et al.[94] may be the source of such a difference.

No cross-section data is available either at 16 MeV. However around 14 MeV differential cross-section data are available for all the nuclei studied in the present work except for tungsten and iodine. The published results available for Fe, Cu, Hg, Pb and carbon for energies between 14 and 15 MeV are presented along with the present measurement in Figs. 4.8 to 4.12 for comparison. Although close agreement can not be expected in view of the difference in the energy of the neutrons, the variation is not so marked and a general similarity of the distribution pattern is observed for most of the cases.

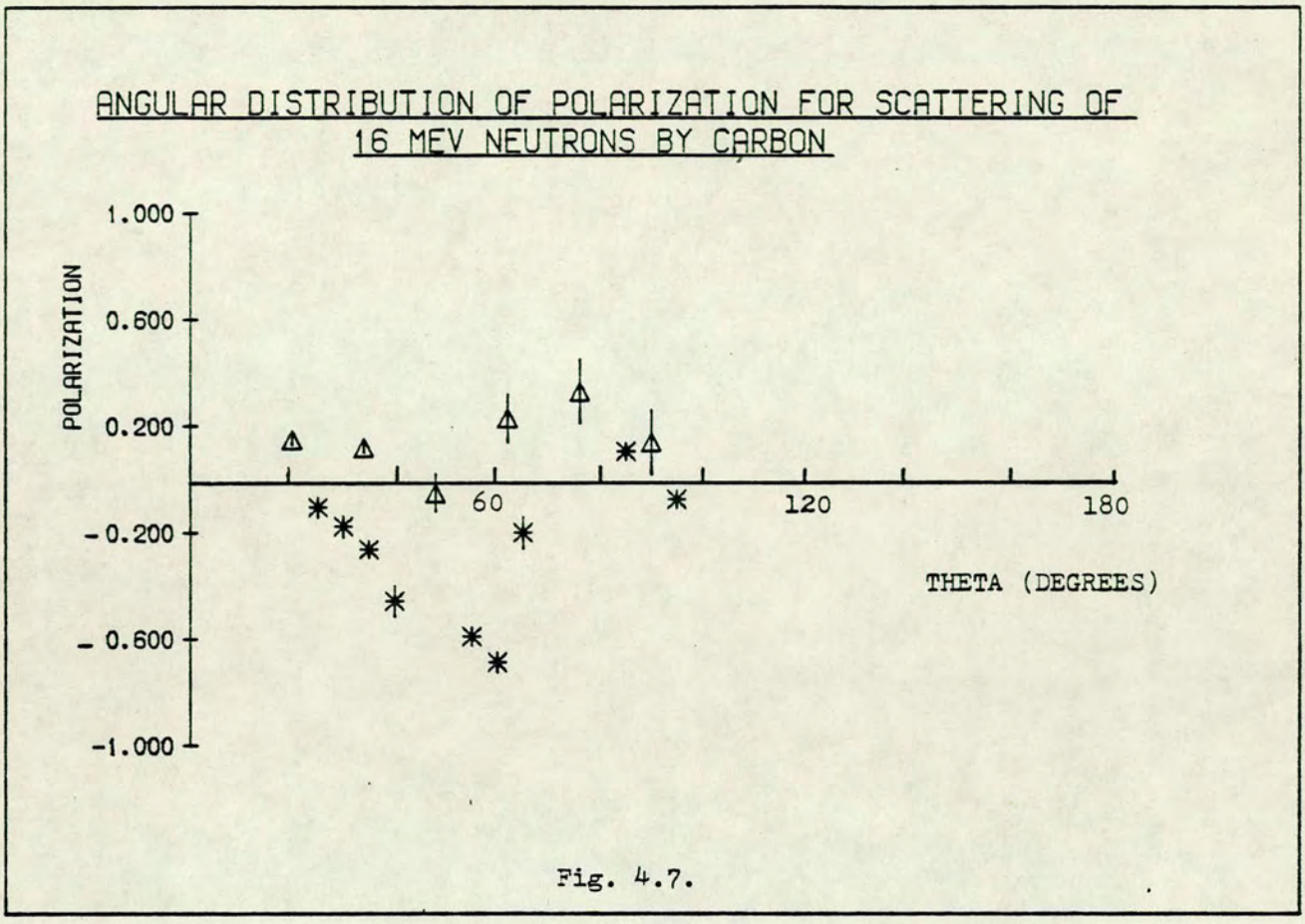

Fig. 4.7.

△ - present measurement

✱ - Lesiecki et al [93] (15.85 MeV)

DIFFERENTIAL CROSS-SECTION FOR SCATTERING OF 16MEV NEUTRONS BY IRON

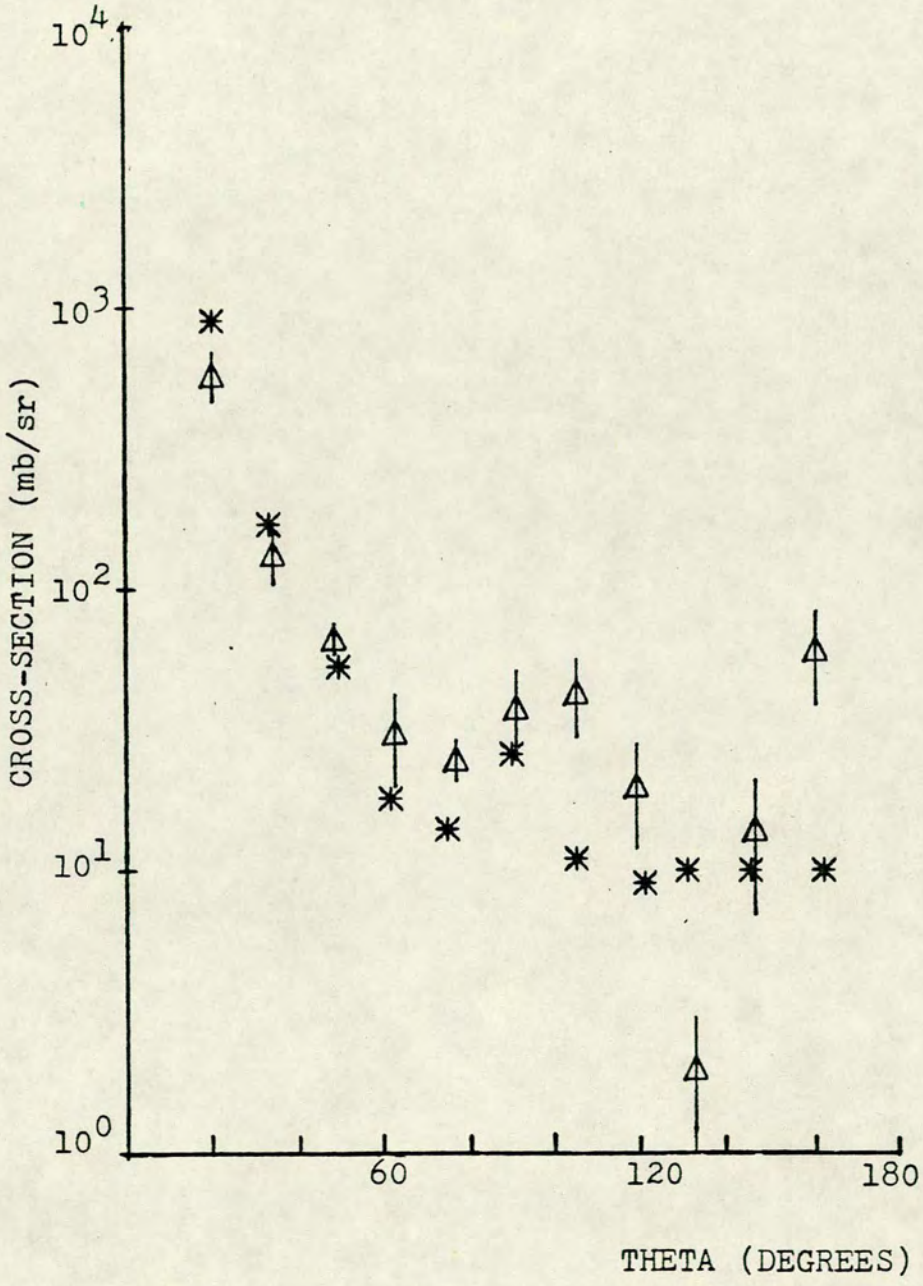

Fig. 4.8.

△ - present measurement.

✱ - Coon et al [90] (14.5 MeV)

DIFFERENTIAL CROSS-SECTION FOR SCATTERING OF 16MEV NEUTRONS BY COPPER

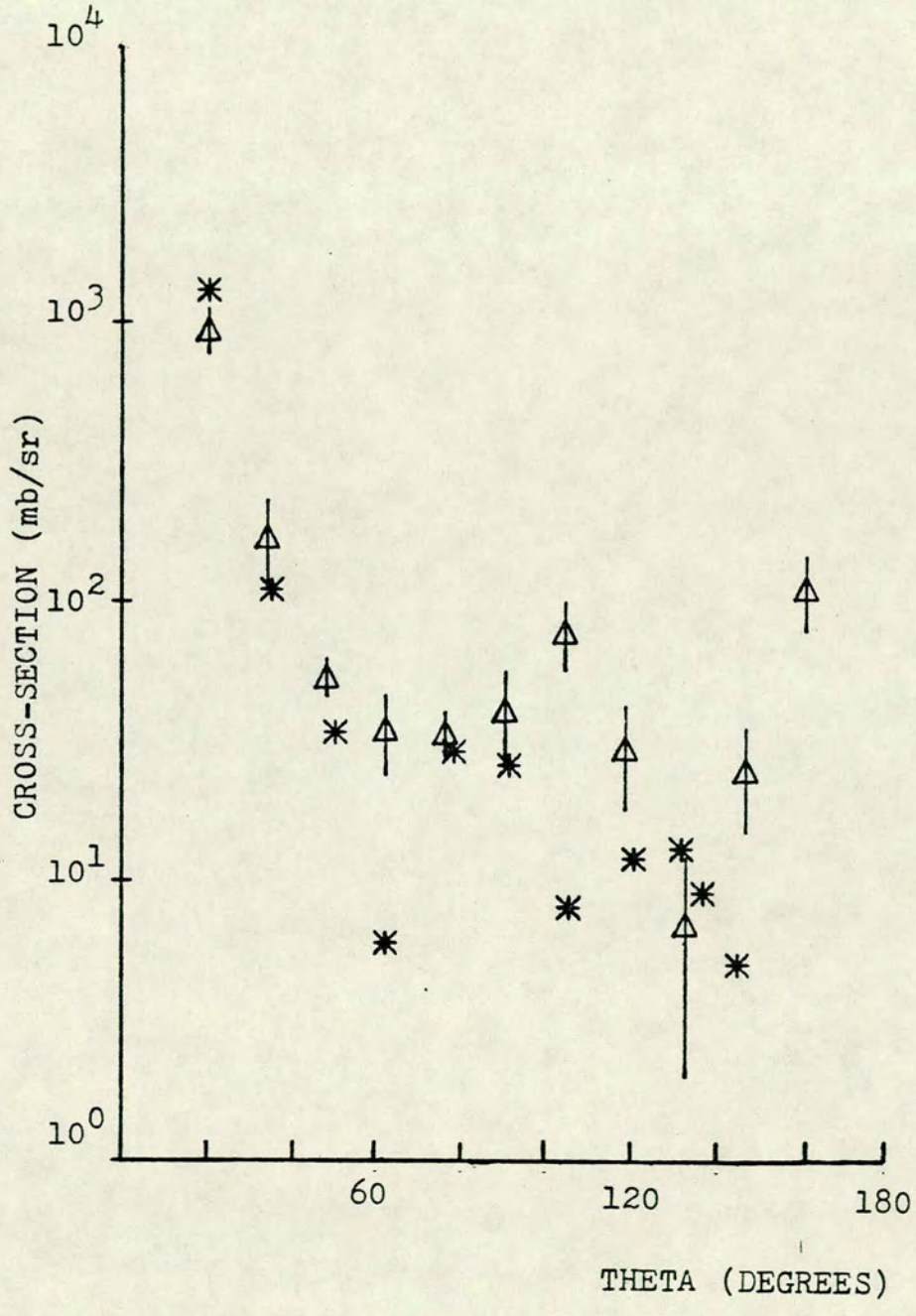

Fig. 4.9.

Δ - present measurement.

✱ - Coon et al [90] (14.5 MeV)

DIFFERENTIAL CROSS-SECTION FOR SCATTERING OF 16MEV NEUTRONS BY MERCURY

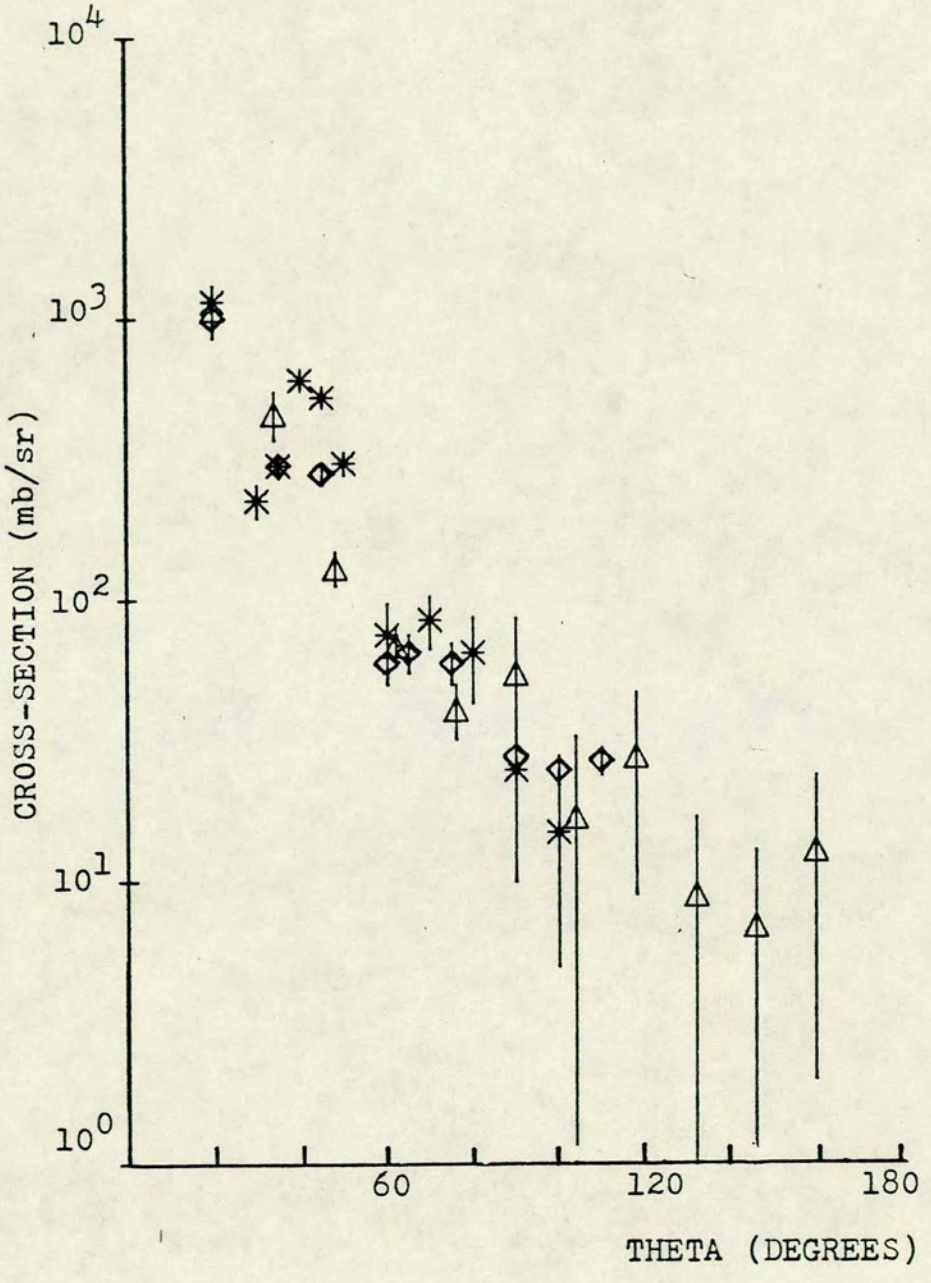

Fig. 4.10.

△- present measurement

✳- Strizhak et al [95] (14.5 MeV)

◇- Nauta [96] (14 MeV)

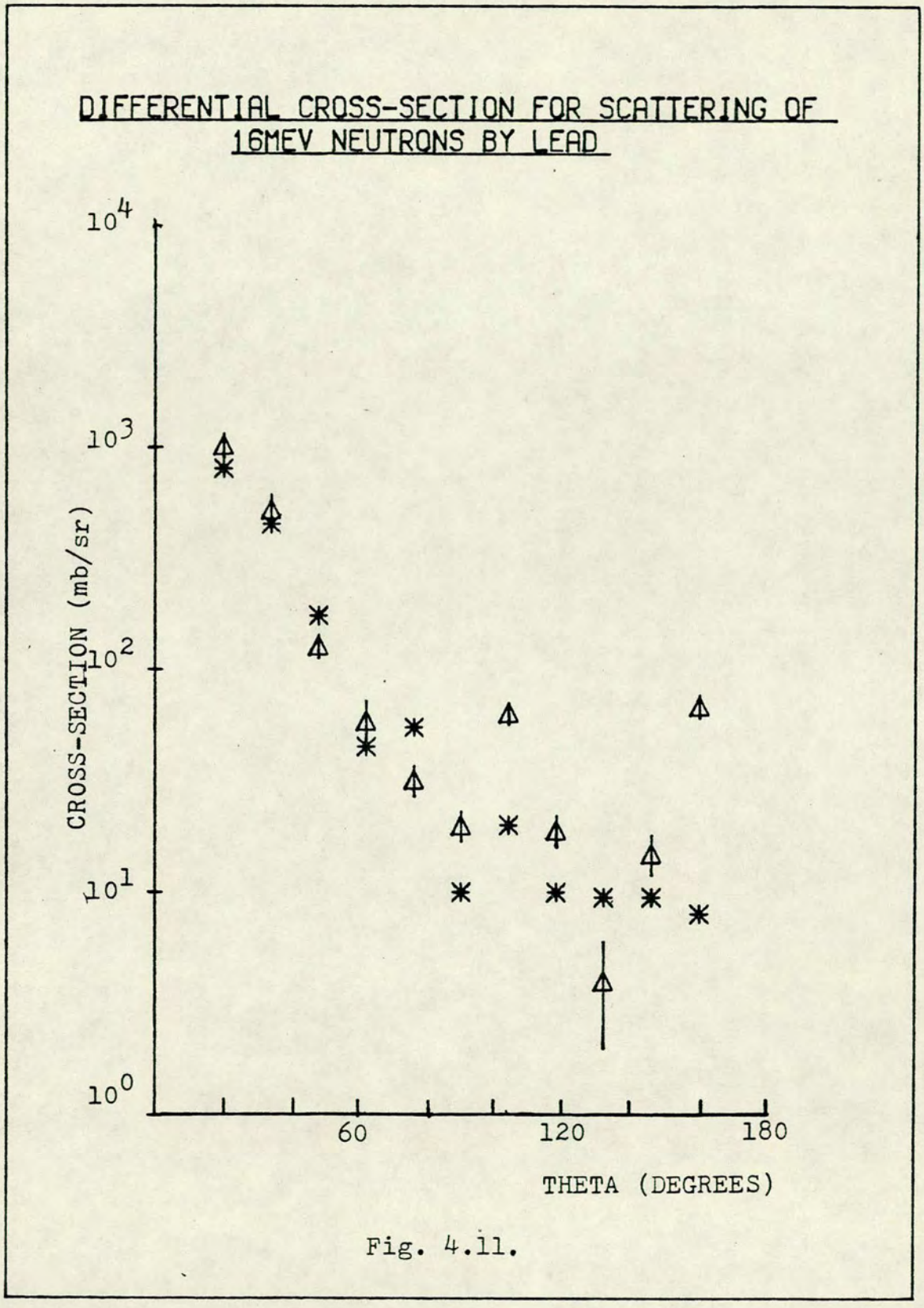

Fig. 4.11.

△ - present measurement

✳ - Fu and Perey [41] (14-15 MeV)

DIFFERENTIAL CROSS-SECTION FOR SCATTERING OF 16MEV NEUTRONS BY CARBON

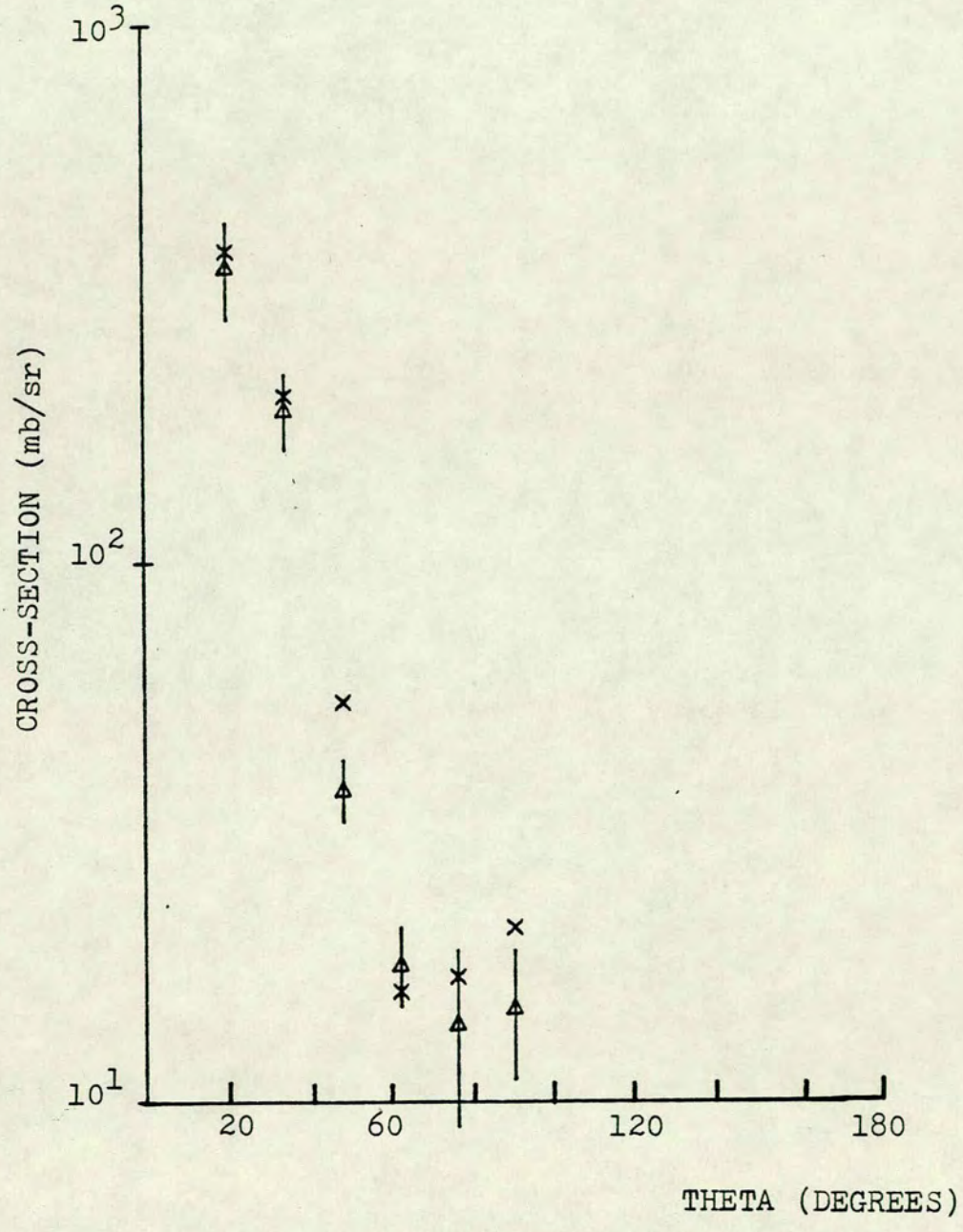

Fig. 4.12.

Δ - present measurement

× - Haouat et al [88] (14.5 MeV).

CHAPTER 5

14.2 MeV NEUTRON DOUBLE SCATTERING

5.1 Introduction

The large magnitude of polarization values measured for 16.1 MeV neutrons around 20° for most of the nuclei presented in Chapter 4 is corroborative of the conclusion reported from earlier measurements[37]. It was observed that the polarization values around 20° due to elastic scattering from Cu and Pb differs significantly from the values calculated with the optical model using global fit parameters. However the success of the model at nearby energies, in contrast, in fitting the elastic differential cross-section at 14 MeV[12] and polarization and cross-section at 10.4 MeV[36] is rather perplexing. As an attempt to remove such confusion a double scattering experiment was set up to provide

1) a direct method of measurement of the absolute polarization resulting from two successive elastic scatterings of initially unpolarized neutrons from the same nucleus and
2) a technique completely different from the one employed for 16.1 MeV scattering to get comparable results at a nearby energy.

The $^{3}H(d,n)^{4}He$ reaction with a Q-value of 17 MeV was chosen as the source of neutrons of about 14 MeV energy. The reason for choosing this particular reaction is manifold.

i) The reaction is fairly easy to realise experimentally.
ii) The neutrons are monoenergetic and accompanied by alpha particles which can be utilised to reduce background problems by employing the associated particle time of flight technique.
iii) Since the reaction produces neutrons with almost zero polarization for incident deuteron energies below 500 keV[97], it is ideal for a double scattering experiment.

Asymmetry measurements were done for Cu and Pb and for scattering angles of 20^{o} and 34^{o}.

5.2 Fast neutron Double Scattering

Fig. (5.1) shows schematically the principle of a double scattering experiment. A beam of unpolarized charged particles incident on an unpolarized target, produces neutrons of zero polarization and of energy E_1 in the direction θ_e. These neutrons, after being scattered elastically by a first sample S_1 through an angle θ_1, are polarized. The polarization of these neutrons of energy E_2 is denoted $P_1(E_1,\theta_1)$. The neutrons are then scattered by a second sample S_2, through an angle θ_2 and azimuthal angle ϕ. The number of doubly scattered neutrons in the direction θ_2, ϕ is,

$$N(\theta_2,\phi) = \sigma_o(E_2,\theta_2)[1 + P_1(E_1,\theta_1)A_2(E_2,\theta_2)\cos\phi] \qquad (5.1)$$

where $\sigma_o(E_2,\theta_2)$ is the differential elastic scattering cross-section for unpolarized neutrons and $A_2(E_2,\theta_2)$ is the analysing power of the second scatterer. In the case of elastic scattering $A(E,\theta) \equiv P(E,\theta)$. Thus the observable of a double scattering experiment, the asymmetry is defined as

$$\Sigma = P_1(E_1,\theta_1)P_2(E_2,\theta_2) = \frac{N_R - N_L}{N_R + N_L} \qquad (5.2)$$

where N_R and N_L are the numbers of doubly scattered neutrons recorded in the side detectors $R(\phi=0)$ and $L(\phi=\pi)$ respectively within the same time interval. When the system includes interchanging of the detectors to compensate for any difference in their efficiencies, the left-right ratio is expressed as,

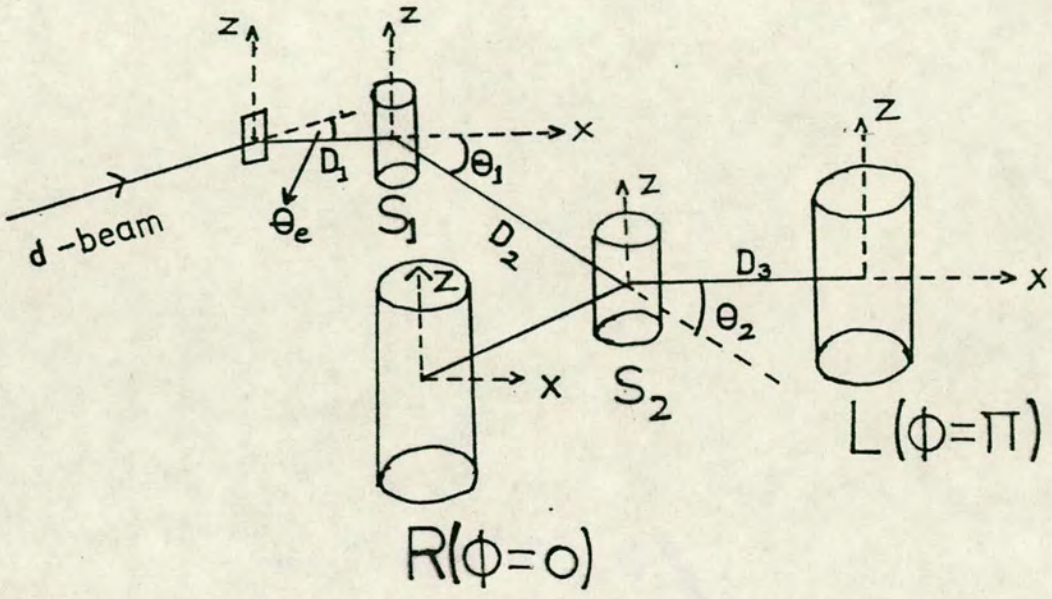

S_1 { Height = 4.6 cm.
Diameter = 2.4 cm.

S_2, R, L { Height = 15.24 cm.
Diameter = 5.08 cm.

D_1= 15.5 cm; D_2= 92 cm

D_3= 30 cm

θ_e= 88 deg.

θ_1= θ_2= 20 deg.

Fig. 5.1. Principle of a double scattering experiment. (The dimensions quoted above refer to those used in the present double scattering measurments(sec.5.4).)

$$r = \sqrt{\frac{N_{R_1}}{N_{L_1}} \cdot \frac{N_{R_2}}{N_{L_2}}} \qquad (5.3)$$

where the subscripts 1 and 2 label the particular detector and L and R refer to the position. The definition of the scattering asymmetry is then,

$$\Sigma = P_1(E_1,\theta_1) \times P_2(E_2,\theta_2) = \frac{r-1}{r+1} \quad . \qquad (5.4)$$

Provided the neutron energy loss from the first scattering is not significantly large so that $E_1 \sim E_2$, then the asymmetry from a true double scattering (two identical targets and the same scattering angle) is equal to the square of the polarization, i.e. $\Sigma = P_n^2$.

Despite the importance of double scattering experiments by providing the most direct method for determination of polarization, such experiments have generally been avoided for reasons of low intensity and high background. All such experiments reported hitherto have been for lighter nuclei like ^{4}He and ^{12}C. Ot-Stavnov et al. [98] was first to measure the right-left asymmetry of doubly scattered, initially unpolarized 4.9 MeV neutrons from ^{4}He at scattering angles $\theta_1 = 90^\circ$ and $\theta_2 = 135^\circ$ (c.m.). The first target S_1 was a gaseous helium scintillator, while the second target S_2 consisted of an arrangement of five proportional counters filled with ^{4}He. Instead of counting the scattered neutrons, they registered the recoil ^{4}He pulses. The pulses from the counters S_1 and S_2 were fed to a coincidence circuit of resolution time 2 μs after pulse height discrimination. About the same time Perkins and Glashauser [99] reported another ^{4}He double scattering experiment with 23.1 MeV neutrons at $\theta_1 = 120^\circ$ and $\theta_2 = 118^\circ$ (lab.) using two liquid helium scintillators as scatterers. Employing only one side detector the asymmetry was measured by using a spin precession solenoid placed between the two scatterers to produce ± 90° precession of the neutron

spin. The double scattering events were detected as triple coincidences between signals from the two helium scintillators and the side detector.

Holt et al.[100] reported measurement of absolute polarization of elastically scattered neutrons in the reaction $^{12}C(n,n)^{12}C$ by true neutron double scattering. The same arrangement has recently been used by Bond and Firk[101] for measuring the n-α analyzing power, employing a neutron beam whose polarization was determined absolutely by true double scattering from ^{12}C beforehand.

Tornow[102] has measured the asymmetry of 15 MeV neutrons after successive scattering from two high pressure helium gas scintillators through $\theta_1 = 75^o$ and $\theta_2 = 76^o$. Measurements were done by recording left and right scattered neutrons with the additional requirement of a fast coincidence between the pulses from the two gas scintillators.

5.3.1 Associated particle time of flight technique

The associated particle time of flight technique employed for the present double scattering experiment is useful, particularly in conjunction with low energy accelerators. The technique provides a potentially higher signal to noise ratio although it is not as versatile as the pulsed beam method, being limited in the neutron energy range attainable from the two reactions $^2H(d,n)^3He$ and $^3H(d,n)^4He$ only. The attraction of this technique is that it provides a means of electronic collimation of the neutron beam by utilising the fact that the energy and angle of emission of the neutrons and the ^3He (or ^4He) resulting from the reaction are not independent of each other. The detection of an alpha or ^3He particle of known energy in a given solid angle uniquely defines the energy and the cone of the outgoing neutrons. While a pulse from the associated particle detector identifies the time of emission of the neutrons, the neutrons scattered from a sample placed in the neutron

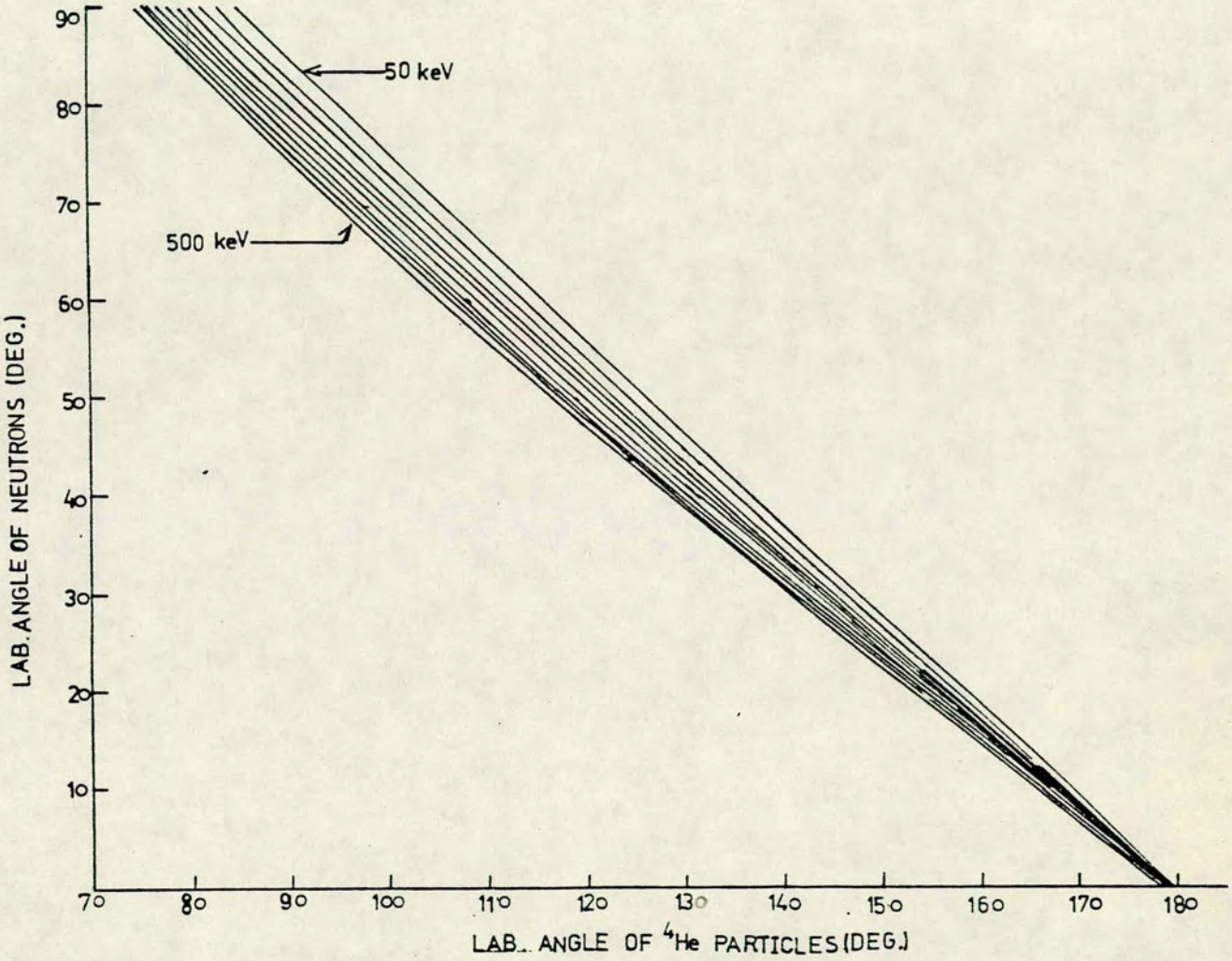

Fig. 5.2. Angular correlation between the neutrons and the ^{4}He particles for incident deuteron energies of 50 KeV to 500 KeV (50 KeV steps) in the $^{3}H(d,n)^{4}He$ reaction.

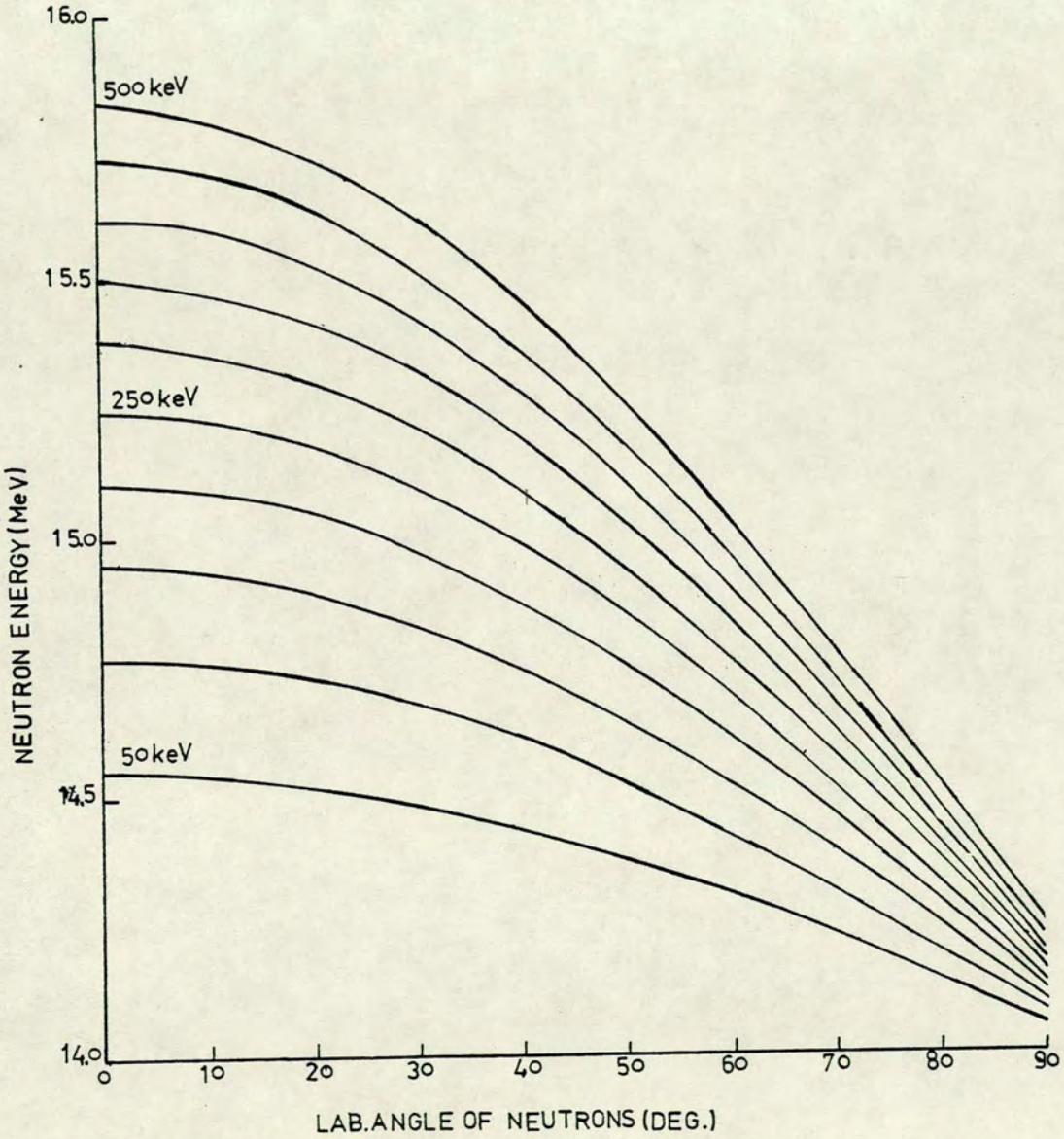

Fig. 5.3. Neutron energies at different emission angles for incident deuteron energy 50 KeV – 500 KeV in 50 KeV steps.

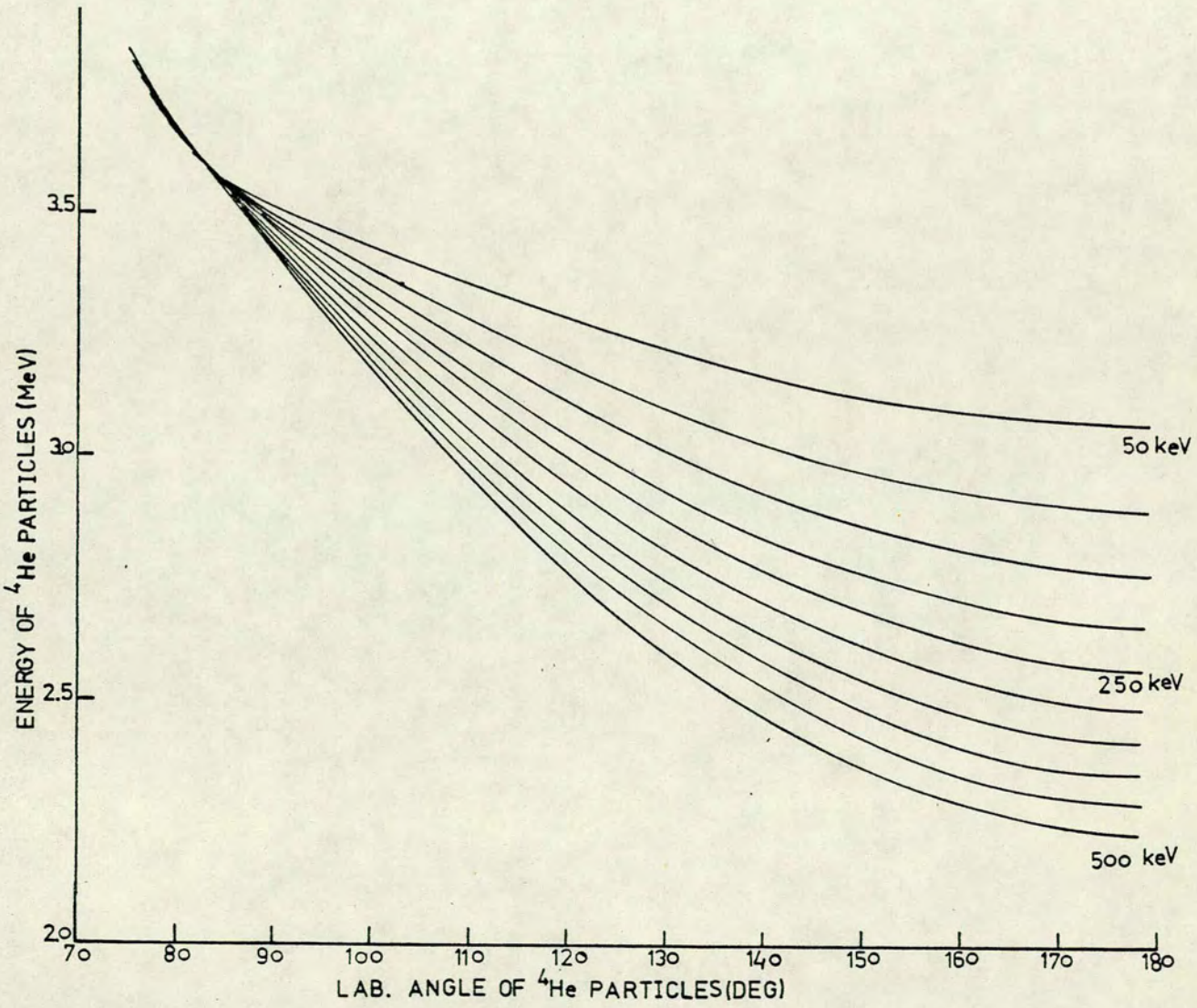

Fig.5.4. ^{4}He particle energy versus angle of emission for deutron energy of 50 KeV – 500 KeV in 50 KeV steps.

cone can be timed over a suitable flight path to a second detector. The time thus measured can be converted to proportional pulse height for analysis using a suitable time to pulse height converter. Efficient background reduction can be achieved from the requirement of a coincidence between the scattered neutrons and the associated particles. To study the relationship between the energy and angle of emission of the neutrons and the alpha particles emitted in the $^{3}H(d,n)^{4}He$ reaction, a simple computer programme using the formulae deduced from reaction kinematics by Marion and Young[103] was used. Figs. (5.2 - 5.4) shows the results calculated for a deuteron bombarding energy from 50 keV to 500 keV in steps of 50 keV and for neutron emission angles from 0^{o} to 90^{o}.

5.3.2 $^{3}H(d,n)^{4}He$ Reaction Chamber

Fig. (5.5) shows the schematic diagram of the reaction chamber in which the neutrons were produced by the $^{3}H(d,n)^{4}He$ reaction. The chamber was rectangular of 193 mm length and 100 mm width made of stainless steel. A cylindrical tube of 60 mm external diameter, fixed to one side of the chamber, coupled it to the deuteron beam line. The tritium target holder, made from thin copper, was 70 mm in diameter and fixed to a circular base of stainless steel, with an arrangement for water cooling. The target holder was fixed to the chamber making an angle of 35^{o} to the incident deuteron beam. The incident deuteron beam can be focussed on to the water cooled target through a 2 mm aperture in a circular disc of aluminium fitted in the beam line. A liquid nitrogen cooled copper tube mounted after the disc and near to the target helped to maintain the useful lifetime of the target by reducing oil contamination and carbon deposition on the target. An aluminium plate with a rectangular aperture of 25 mm height and 12.5 mm width, for the alpha

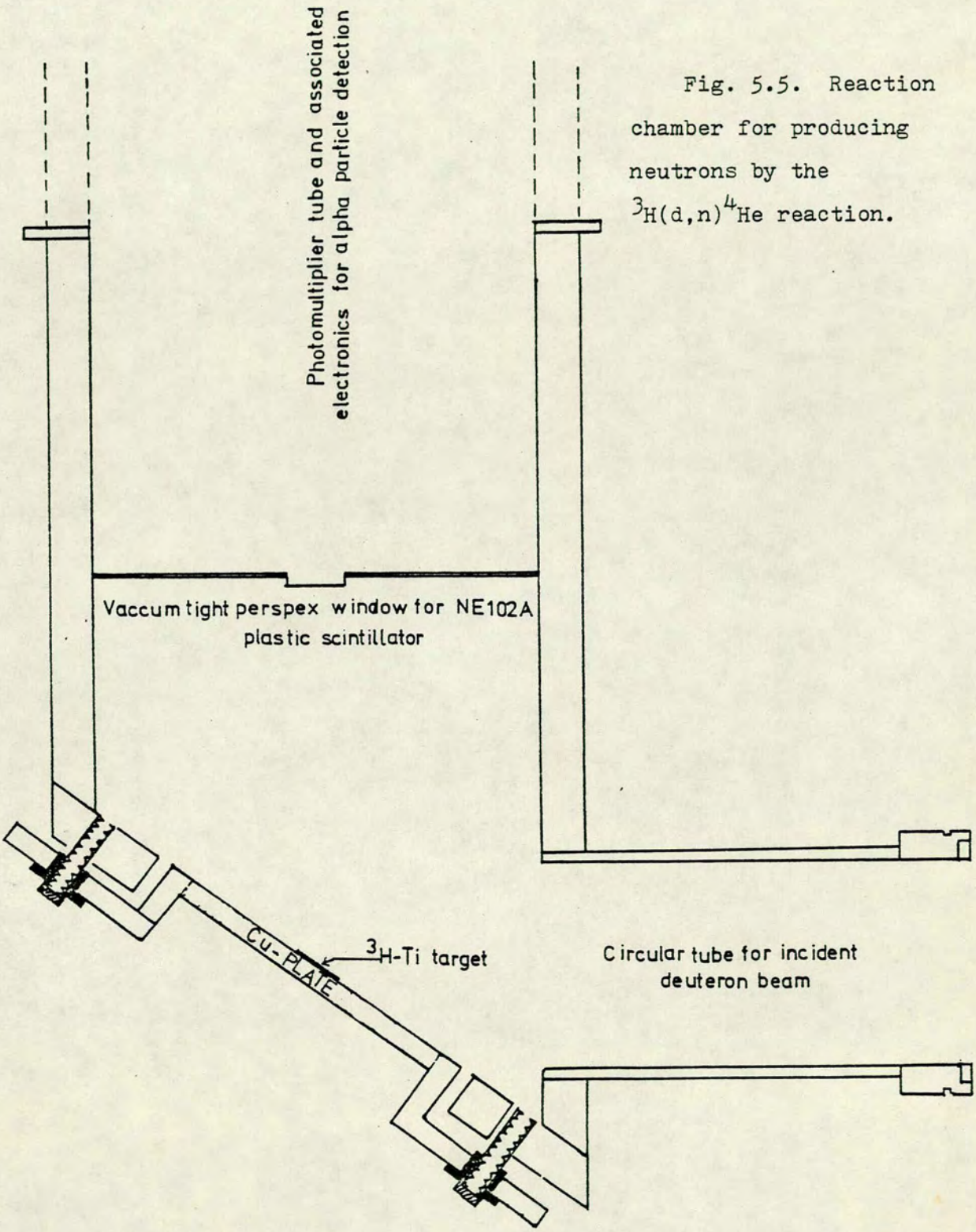

Fig. 5.5. Reaction chamber for producing neutrons by the $^{3}H(d,n)^{4}He$ reaction.

particle detector was fixed to the chamber in front of the target holder at a distance of 84 mm from the centre of the target. The alpha-particle detector was fixed in this aperture, making an angle of $(80 \pm 0.5)^{o}$ to the incident d-beam. The alpha detector used was very thin (0.9 mm) plastic scintillator of the type NE102A coupled to a 56 AVP photomultiplier tube through a vacuum tight perspex window so that the photomultiplier tube and the associated electronics need not be under vacuum. Fig. (5.6) shows the dynode chain used with this photomultiplier. The photomultiplier along with the dynode chain was enclosed in a light tight container and fitted to the target chamber to make the system compact. Fig. (5.7) shows the assembly of the target chamber coupled to the beam line, the liquid nitrogen trap and the alpha particle detector system coupled to the target chamber.

5.3.3 Beam profile measurement

The first step in setting up the double scattering system was to do a beam profile measurement to establish the location of the neutron cone accurately. Deuterons accelerated to a voltage of 360 ± 10 keV were used to bombard a tritium target of $1 Ci/cm^2$ absorbed in a titanium layer of 0.23 mg/cm^2 and backed by a thin copper disc. Taking into account the finite thickness of the target and the inclination of the target to the incident d-beam, the deuteron beam strikes the target with an average energy of 300 ± 10 keV. Throughout the measurement a deuteron beam current of 2μA was used to avoid excessive pile up in the alpha particle detector. A piece of aluminium foil of .002 mm thickness was introduced in front of the alpha detector to exclude light and to stop the elastically scattered deuterons, which have a range of .0014 mm in the foil. The energy lost by the 3.7 MeV alpha particles in the aluminium foil was estimated to be only 0.34 MeV. Reactions other than the $^{3}H(d,n)^{4}He$

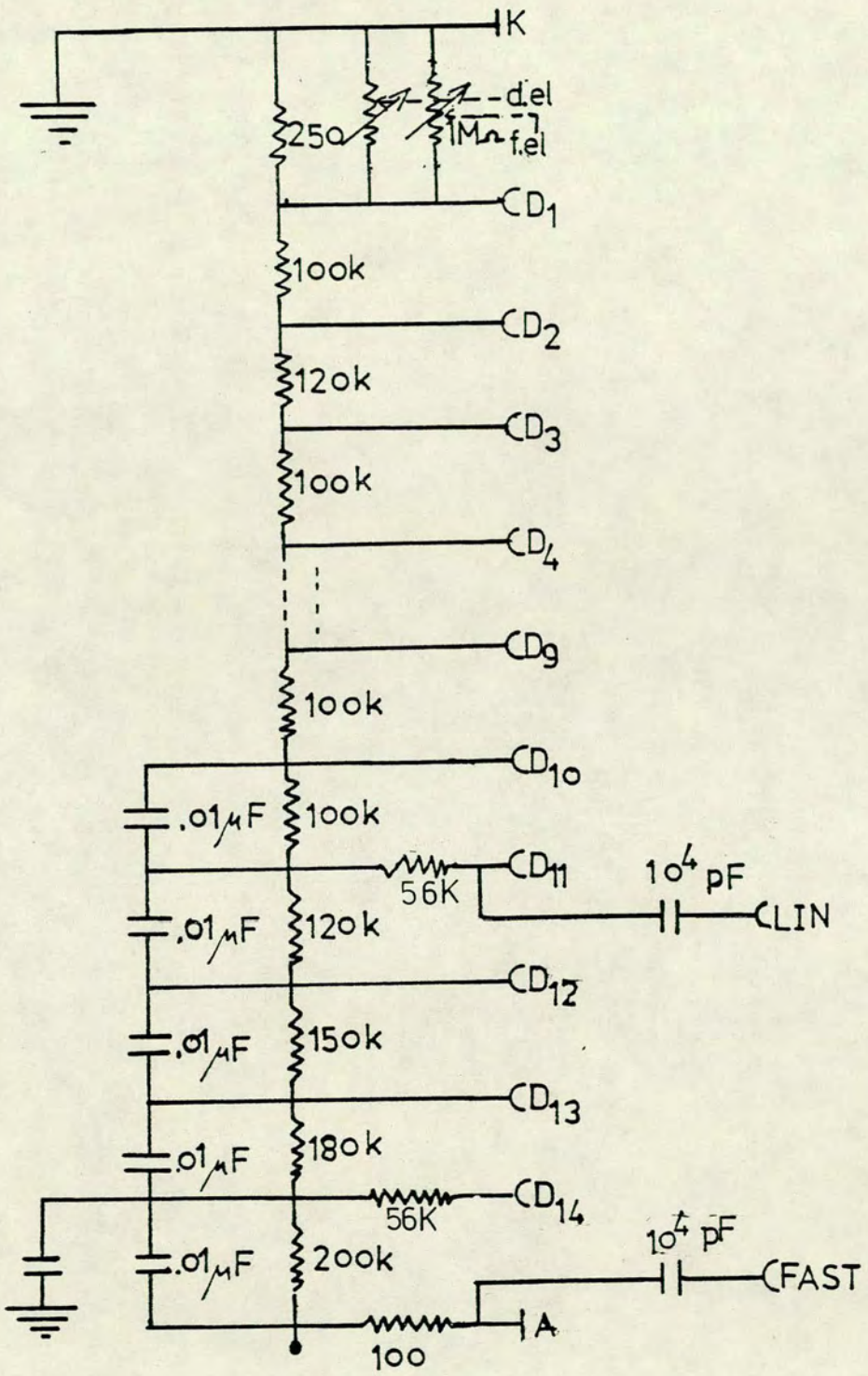

Fig. 5.6. Base circuit for the 56 AVP type photomultiplier used with NE102A plastic scintillator for ^{4}He particle detection.

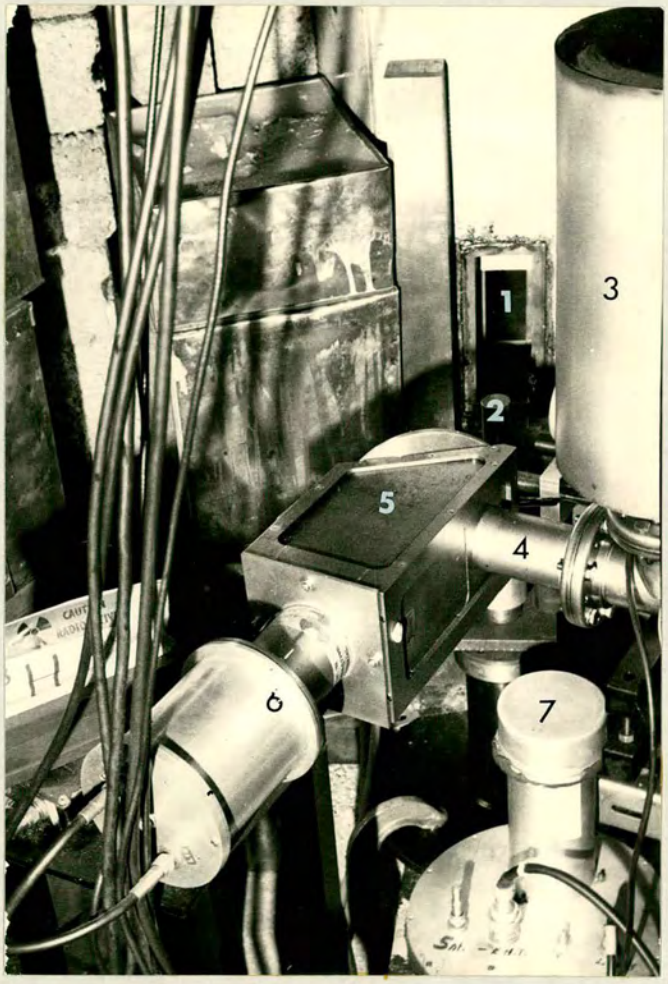

Fig. 5.7. Photograph showing the assembly of the reaction chamber and the ^{4}He particle detection system.

(1) Rectangular collimeter hole.
(2) First scttering sample.
(3) Liquid nitrogen trap.
(4) Deuteron beam line.
(5) Reaction chamber.
(6) Alpha particle detector system.
(7) Target yield monitor.

reaction that might take place in the target are notably[104] $^{2}H(d,n)^{3}He$ $^{2}H(d,p)^{3}H$ and $^{3}He(d,p)^{4}He$. The deuterium and ^{3}He in the target may arise, respectively, from the incident deuteron beam and from the decay of the tritium target. However these secondary reactions have comparatively low cross-sections. Fig. (5.8) shows the linear spectrum of the alpha particles from the reaction. An integral discriminator at the amplifier output was used to set the bias at the valley to reject the low energy tail of the spectrum.

The target yield monitor (TYM) used for normalisation and to monitor the flux of the neutrons from the reaction was placed very close to the target chamber. It consisted of a plastic scintillator of 5.08 cm diameter and 2.54 cm thickness coupled to an EMI9514 type photomultiplier tube. Discrimination against gamma-ray background was obtained by pulse height discrimination rejecting pulses below about 12 MeV recoil proton energy. The neutron detector used for the beam profile measurement was a rectangular stilbene crystal 30 mm wide, 40 mm long and only 3 mm thick coupled to a 56AVP photomultiplier. Fig. (5.9) shows the block diagram of the electronics used for the beam profile measurement. Fast pulses from the anode of the alpha detector with a rise time of 3 ns after a suitable delay were used as the stop pulses for a time to amplitude converter (TAC), while the fast pulses from the stilbene detector with 6 ns rise time provided the start pulses. The time information about the neutrons converted into proportional pulse height by the TAC was fed to the linear input of ADC B for pulse height analysis, using the CAMAC system as described in Chapter 2. To prevent noise and low energy pulses being recorded, a slow coincidence was used. The integral discriminator used for the stilbene detector was set to reject neutron events below 10 MeV. The discriminator outputs from the alpha detector and the stilbene detector were fed into a three input coincidence gate. Using this AND gate output as the gating input for

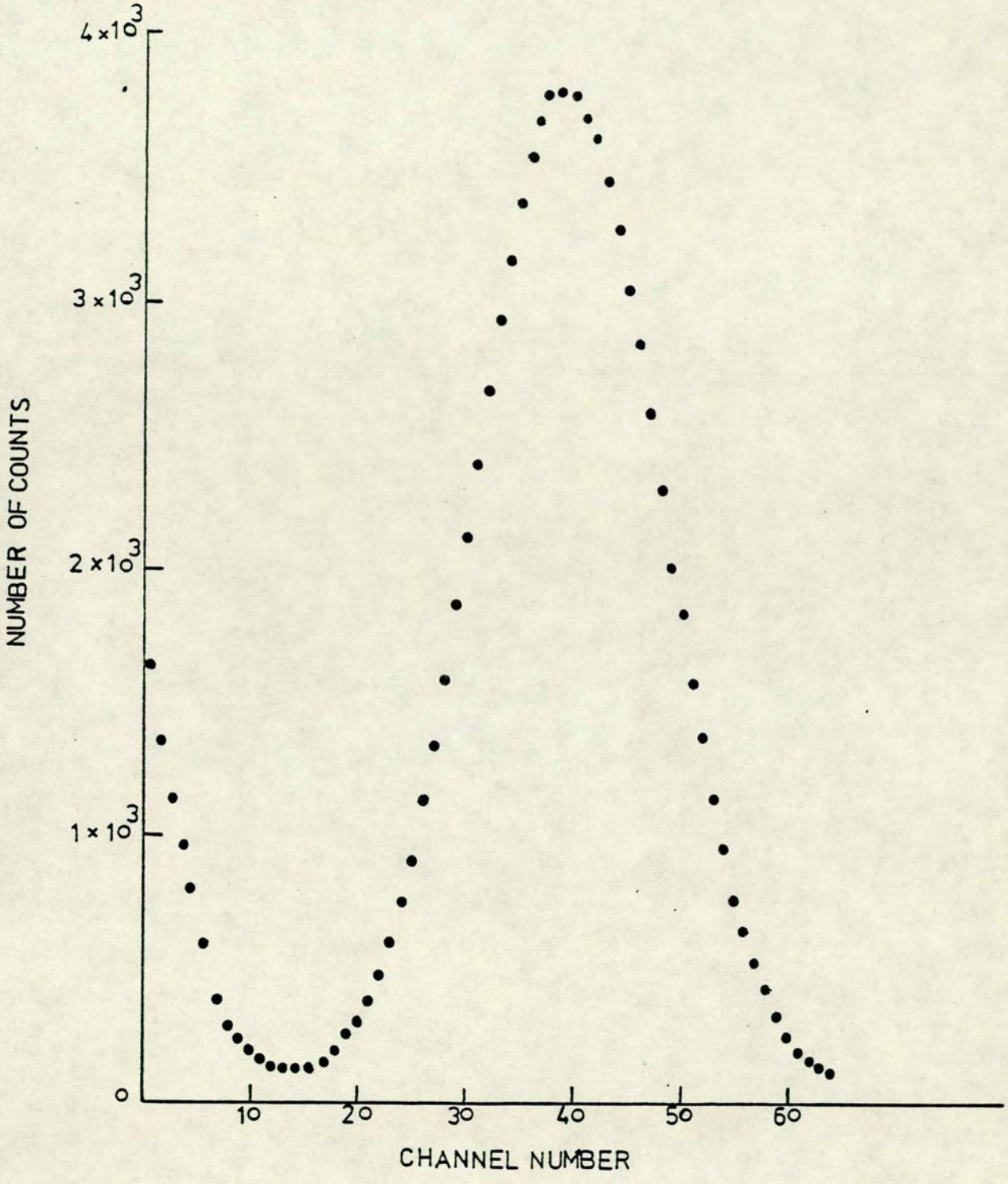

Fig. 5.8. A typical linear energy spectrum of ^{4}He particles from the $^{3}H(d,n)^{4}He$ neutron.

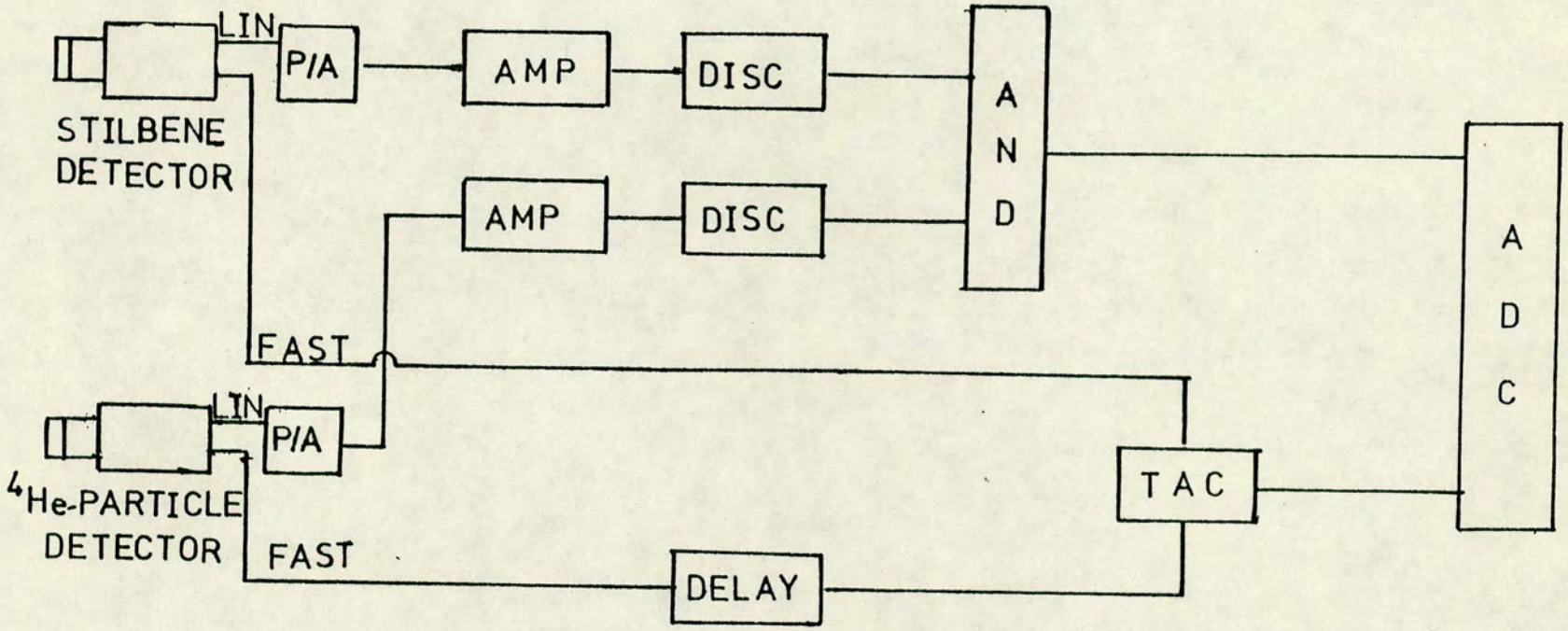

Fig. 5.9. Block diagram of the arrangement of the electronics used for beam profile measurement.

the ADC, neutrons of energy above 10 MeV associated with recoil alpha particles were analyzed. A time resolution of 1.8 ns was achieved for the stilbene detector placed at a distance of 21.8 cm from the target. To measure the beam profile the stilbene detector was mounted on a rail system and made to swing horizontally with the 3mm thick face crossing the neutron beam in steps of 1^{o} until the counts in the detector dropped near to zero. Fig. (5.10) shows the neutron collimation curve obtained by plotting the counts under the time of flight peak, normalised with respect to the TYM counts for the same length of time, against the emission angle of the neutrons. The beam profile shows a collimated beam of neutrons of 8.6^{o} width making an angle of $(88 \pm 0.5)^{o}$ to the incident deuteron beam. This is in close agreement with the estimated value of 8.7^{o} from the geometry of the alpha detector. The energy of the neutrons at this emission angle is 14.2 MeV, while the corresponding angle and energy for the alpha particles are $(80 \pm 0.5)^{o}$ and 3.7 MeV.

After completing the beam profile measurement, the stilbene detector was removed from the vicinity of the first scatterer. However the rail system enabled the stilbene detector to be used from time to time during the measurements to ensure that the first scattering sample was correctly located in the neutron beam.

5.3.4 Preliminary measurement of 14.2 MeV neutron double scattering on Cu

Having established the location of the neutron cone a cylindrical sample of copper of 2.4 cm diameter and 4.6 cm in height was placed in a cup of finely machined aluminium of 2.5 cm diameter fixed to a suitable holder, at a distance of 15.5 cm from the centre of the tritium target. The size and distance of the sample was chosen such that the whole of the neutron cone defined by the alpha detector was intercepted by the sample. To test the feasibility of the double scattering experiment a preliminary

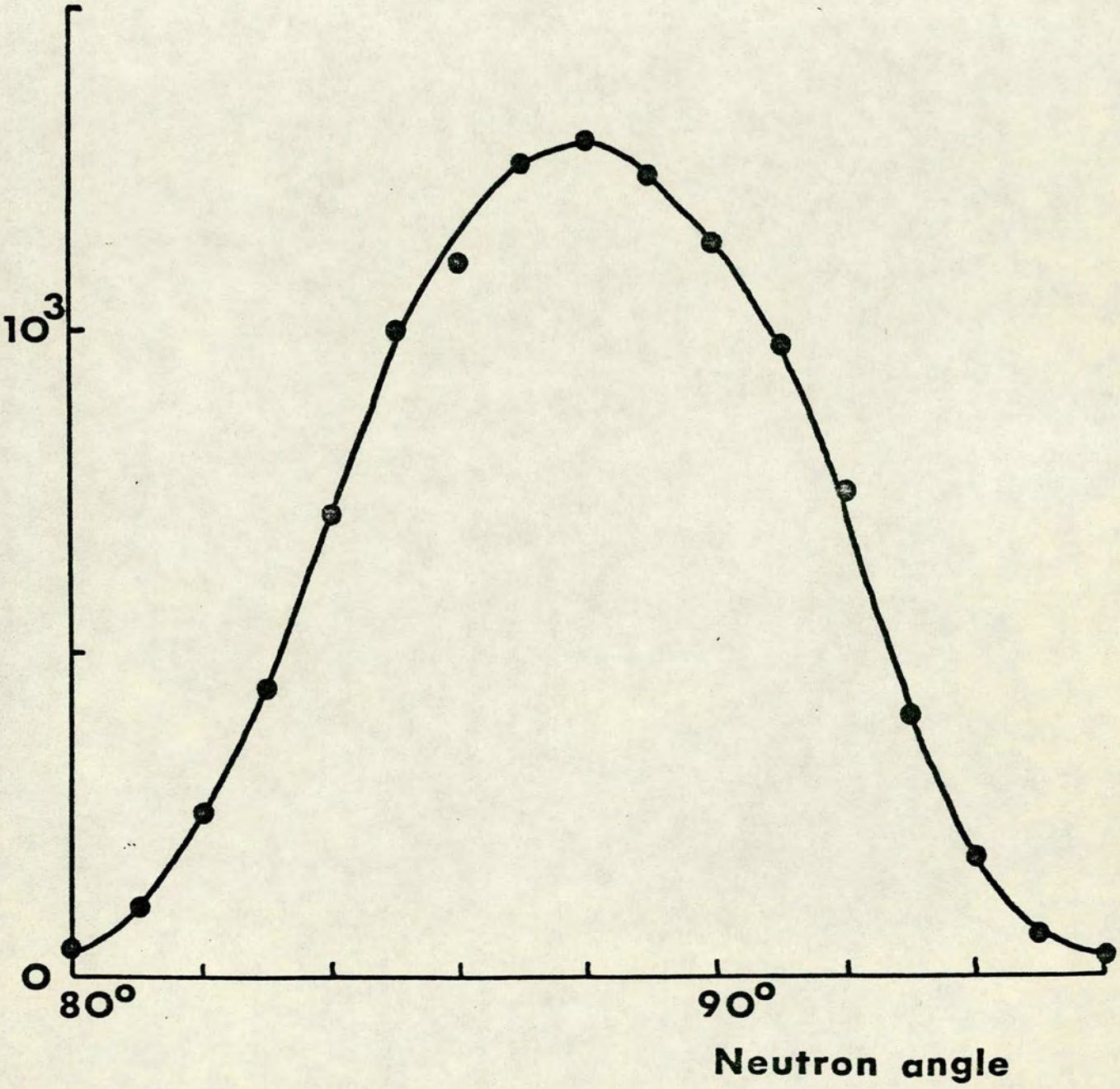

Fig. 5.10. Neutron beam profile determined with the thin stilbene detector.

measurement was done by setting up the system temporarily with spare equipment available. A collimator originally designed and used for scattering experiments with 3 MeV neutrons, with a circular hole of 5 cm diameter was placed at a distance of 18 cm from the first sample at an angle of 20^{o} to the sample. A second cylindrical sample of copper of 5 cm diameter and 5 cm height (limited by the size of the collimator hole) was placed at a distance of 74 cm from the first sample. A throat of 2 cm diameter, at a distance of 21 cm from the first sample, made from tapered polythene inserts, was introduced into the collimator hole such that the whole of the second sample was illuminated by the neutron beam scattered from the first sample. Two liquid scintillation detectors similar to those described in Chapter 2.3.2 were used for measuring the left-right asymmetry at an angle of 20^{o} to the second sample placed at a distance of 30 cm. The moving of the second sample in and out of the neutron beam and the interchanging of the neutron detectors was done manually. Additional iron blocks were required to reduce the intensity of the neutrons scattered by the first sample which penetrated the paraffin wax shielding and entered the detectors.

The system of electronics employed for the side detectors was essentially the same as the one used with the stilbene detector (Fig. 5.9). The fast pulses from the side detectors having a rise time of about 5ns were fed to a fast OR unit. Using an H.T. of 2.1 keV, the detectors provided large enough start pulses to trigger the TAC. The stop pulses were taken from the alpha detector as before, after suitable delay. The output from the fast OR unit was used as input for the TAC unit which was then fed into the ADC handling routing described in Chapter 2.3.1. The slow coincidences were required between discriminator outputs from the alpha channel as described in 5.3.3 and discriminator outputs from the side detectors. The energy bias for the neutron detectors was set to reject proton recoil events below 10 MeV. Calibration of the side detectors was done

by using the response data of NE213 for proton recoil measured by Smith et al.[105]. With such a high energy bias, use of pulse shape discrimination was not important. The routing unit described in Chapter 2.3.1 accepting signals from the AND gate output of the two neutron detectors selects the particular section of the memory to accumulate data for each neutron detector. The time resolution achieved for the side detectors was 5 ns on average.

The collimated beam monitor used in the neutron beam scattered from the first sample was the same as the one used for the 16.1 MeV experiment and described in Chapter 4.3.2. It was placed with its axis in line with the second sample and at a distance of about 1 metre from this sample. The electronic circut associated with it was also the same as before except that, instead of the pulsed beam pick up unit, the stop pulses for the time converter were provided by the associated alpha particle pulses. Accumulation of double scattered events in the two side detectors at the end of 45 hours of running gave a total of 1930 real counts, after background subtraction. The resulting asymmetry for Cu was found to be 0.39 ± 0.13. The background in the two detectors accounted for about 90% of the detected events.

5.4 Modified Double Scattering System and Results

From the results of the preliminary test it was evident that an improvement of the real to background ratio by improving the shielding would give asymmetry results with better accuracy. A collimator was designed and constructed incorporating the following features.

(i) Blocks of iron were used for constructing the major volume of the collimator. Possible gaps between the blocks were filled using iron dust to make the shielding compact.

(ii) To be able to use a large sample for the second scatterer the collimator hole was made rectangular of height 15.24 cm and 5.08 cm width.

(iii) An adjustable rectangular throat with tapering ends was made by using plates of steel such that it can be fixed into the collimator hole at an appropriate position depending on the size of the sample chosen. Use of the throat was to ensure that the second scattering sample was illuminated wholly by the neutron beam scattered from the first sample, while any direct beam from the target failed to strike the second sample.

Fig. (5.11) shows a schematic view of the modified neutron double scattering system. The collimator was placed at an angle of 20° to the first scattering sample and at a distance of 18 cm as before. The polarimeter described in Chapter 2.2 and used for the 2.9 MeV and 16.1 MeV measurements was placed behind the collimator. Two rectangular inserts of the same size as the holes of the collimator, with a circular hole of 5 mm diameter at the centre were made for adjusting the axial alignment of the system. With these inserts fitted accurately to the two ends of the collimator and the disc alignment inserts fitted to the holes of the polarimeter, the adjustment was done following the same procedure as described in Chapter 2.2, by viewing the centre of the first sample in position, instead of the n-producing target as before. With the modified system the asymmetry measurement was done for Cu and Pb and for second scattering angles of 20° and 34°. Thus four neutron detectors similar to the ones described in Chapter 2.3.2 were fixed to the detector holders at the two scattering angles. A sample of 15.24 cm height and 5.08 cm diameter was placed in the sample holder fixed to one of the scattering tables, while the first sample was of the same size as before. The distance between the two samples was 92 cm (18 cm more than in the preliminary measurement for unavoidable practical reasons). The collimated beam monitor was placed at a distance of 97 cm from the second sample such that the whole of the scintillator volume was illuminated by the n-beam from the first sample. This distance was

Fig. 5.11. Experimental arrangement for the 14.2 MeV neutron double scattering measurement.

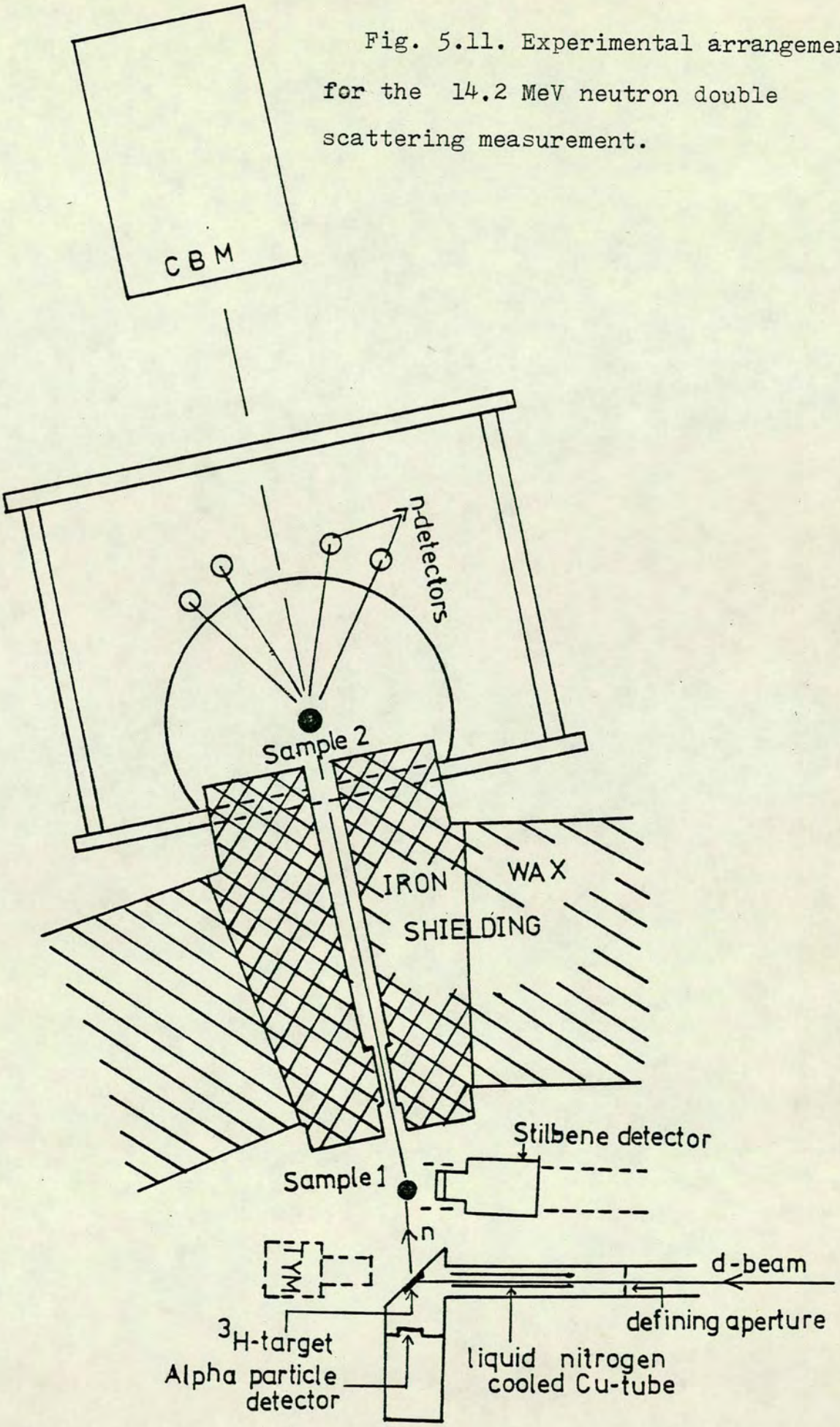

enough to avoid any contribution to the background in the side detectors from scattering by the CBM.

Before starting scattering measurements with neutrons, tests for instrumental asymmetry were done using a ^{60}Co source, mounted in place of the second scattering sample, following the same procedure as outlined in Chapter 3.4. The worst instrumental asymmetry observed in one of the four detectors was 0.0029 ± 0.0002. Scattering measurements were done for periods of 1000 sec. for the second sample in and out of the collimated neutron beam for each azimuthal position. The counts in the CBM and TYM were also recorded in each case. The sequence was repeated for a total period of 96 hours for both the Cu and Pb samples. Fig. (5.12) shows the time of flight spectra for 20° double scattering from Cu samples and for scattering with the second sample removed.

The result of the asymmetry measurement for Cu is presented in Table 5.1. With the modified collimator the background was reduced to 65% for the detectors at 20° and a total of 4414 real events were recorded. The measurement for 34° was done for the same length of time and a total of 921 real events were recorded. At this angle the background accounted for about 84% of the scattered counts. As the aim of the present double scattering measurement was to establish the polarization value around 20°, the length of time for collecting data was determined primarily with regard to the accuracy of the 20° measurement. The measurement at 34° was also done, since this was the nearest angle attainable with the present polarimeter. However an unacceptably long measurement time (∿1000 hours) would be needed to improve the result at 34° significantly. The polarization of the 14.2 MeV neutrons estimated from the measured asymmetry due to double scattering, using the fact that such asymmetry is the product of the polarization for each scattering (eqn. 5.4) is presented in the second column of Table 5.1. These

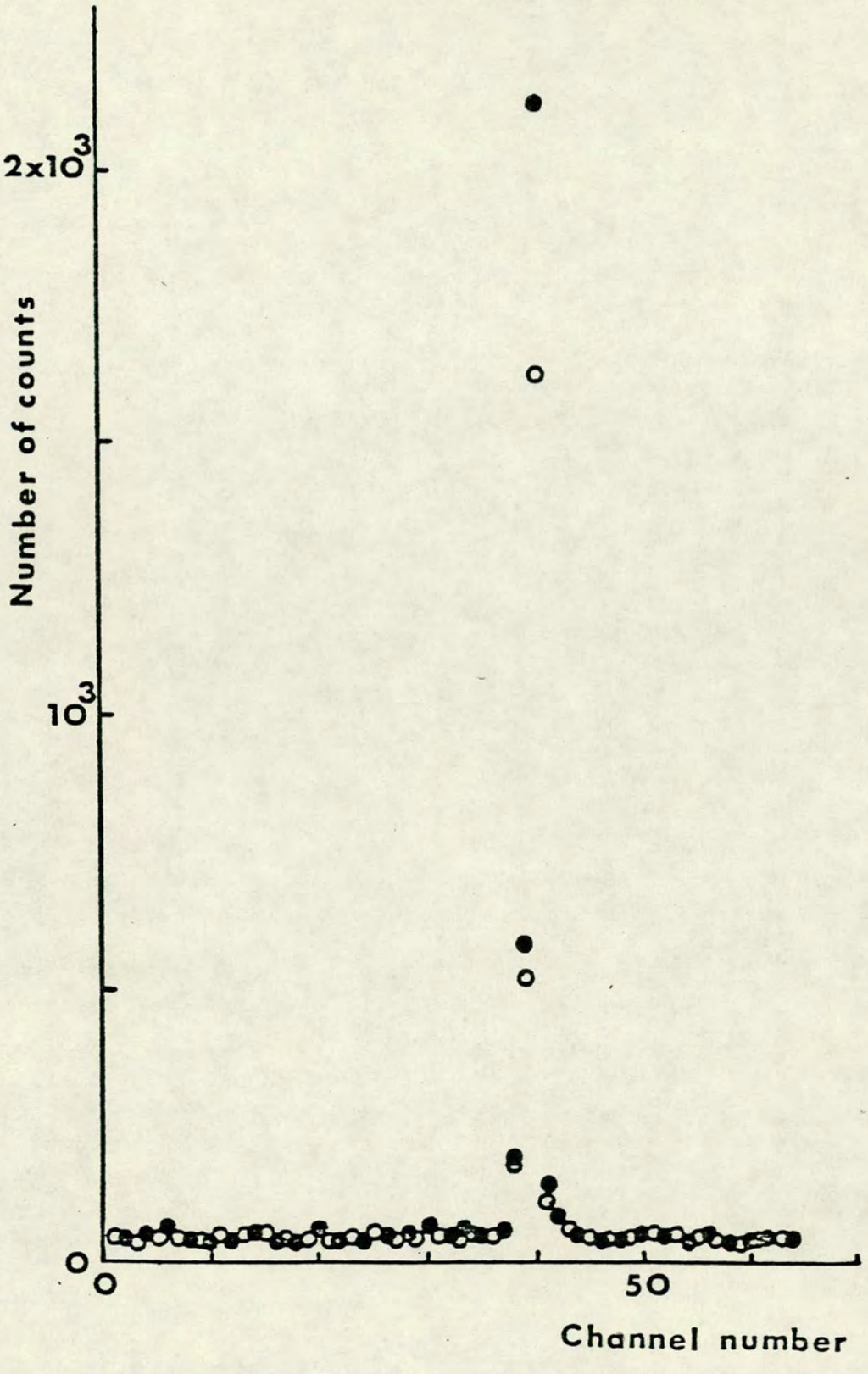

Fig. 5.12. Time of flight spectra

(i) for 20° double scattering by Cu samples, solid circles

(ii) with second sample removed, open circles.

TABLES 5.1 AND 5.2: Measured asymmetry and polarization for 14.2 MeV neutrons scattered by Cu and Pb.

TABLE 5.1 COPPER

Lab Angles (Deg.)	Measured asymmetry for 14.2 MeV neutrons by double scattering	Estimated polarization for 14.2 MeV neutrons	Polarization of 16.1 MeV neutrons
20	0.13 ± 0.04	0.36 ± 0.06	0.43 ± 0.06
34	-0.08 ± 0.11	-0.22 ± 0.30	0.44 ± 0.04

TABLE 5.2 LEAD

Lab Angles (Deg.)	Measured asymmetry for 14.2 MeV neutrons by double scattering	Estimated polarization for 14.2 MeV neutrons	Polarization of 16.1 MeV neutrons
20	0.24 ± 0.09	0.49 ± 0.09	0.55 ± 0.11
34	0.14 ± 0.12	0.29 ± 0.25	0.12 ± 0.04

polarization values were calculated assuming arbitrarily positive sign for 20^{o} polarization. Table 5.2 represents the results for Pb.

It has been observed for the 16.1 MeV measurements for both Cu and Pb (Tables 4.3 and 4.4) that the polarization values at 20^{o} are not critically dependent on either the multiple scattering correction or the correction for inelastic scattering. The effect of both corrections was found to be smaller than the statistical uncertainty at 20^{o} for the 5.08 cm X10.2 cm. sample used. Considering the case of Cu at 20^{o} (showing a larger correction than Pb) the correction for both effects was 7%. An estimate of the correction for the first sample of the double scattering arrangement is 1%, while that for the second sample is about 10%. Thus the overall correction for the 14.2 MeV neutrons for Cu at 20^{o} could be 10%, which is less than the statistical uncertainty associated with the polarization value estimated from measured asymmetry.

Tables 5.1 and 5.2 also include the polarization values for 16.1 MeV neutrons at similar angles for comparison. It is clear from the tables that both for Cu and Pb the values of polarization from double scattering at 20^{o} are in reasonably good agreement with the 16.1 MeV results (within the statistical uncertainty). Because of the large statistical uncertainty attached to the 34^{o} values from double scattering, it is difficult to make any valid comparison with the 16.1 MeV values at this angle. The present values at 34^{o} are, however, not inconsistent with the 16.1 MeV values.

CHAPTER 6

OPTICAL MODEL

6.1 Introduction

The optical model, as already mentioned in Chapter 1, was introduced as an attempt to reconcile the strong interaction model with the weak interaction or the independent particle model by providing for both kinds of processes. A great deal of success has been achieved in correlating large amounts of data through a single optical potential. Feshbach, Porter and Weisskopf[9] demonstrated that even with a simple potential (complex spherical square well), the optical model was capable of reproducing the gross structure of both total cross-sections[10] and the differential elastic scattering cross-section[3] for the neutron-nucleus interaction. Fitting of neutron differential cross-sections between 1 and 25 MeV by Bjorklund and Fernbach[12] provides further example. Recent systematic study by Holmqvist[14] of the optical model in the energy range 1.5 to 8.1 MeV for elastic scattering has also showed good agreement between the experimental results and optical model calculations. However the model has so far been not so successful in fitting experimental data on the angular distribution of polarization as already discussed in Chapter 1.3. It has been shown recently by Galloway and Waheed[40] that global optical model parameters have not been very successful in fitting both differential cross-section and polarization data for 2.9 MeV neutrons. The present experimental results for polarization and cross-section of 2.9 MeV and 16 MeV neutrons elastically scattered from different nuclei from C to U have been used for studying the optical model.

6.2 Properties of the Optical Potential

It is a general feature of theoretical models that they allow the description of certain phenomena in terms of certain model parameters and the purpose of the fundamental nuclear theory is to relate these model parameters to the properties of the many body system. In the majority of optical model analyses, the optical potential is taken as a local potential with a specified functional form and the parameters of this potential are then varied to yield a good fit to the data. The optical potential for a nucleon usually consists of the sum of a spin-independent term, a spin dependent term, a Coulomb term and sometimes a symmetry term. Since we are concerned with neutrons we will neglect the Coulomb term in the parameterisation.

Spin-independent term:- We have already expressed the spin independent term in Chapter 1.2, as the central complex potential of the form,

$$V(r) = - U(r) - iW(r) \quad . \qquad (1.6)$$

The real part of this potential describes the average potential energy inside the nucleus and the imaginary part represents the summed effect of all processes which tend to reduce the flux in the elastic channel. The above form can be written more explicitly as

$$V(r) = -V_o f(r) - iW_o g(r) \quad ,$$

where V_o and W_o are adjustable constants and $f(r)$ and $g(r)$ are form factors characterized by a radius and a diffuseness parameter. The real or the refracting potential that falls to zero outside the nuclear radius is generally chosen to be approximately proportional to the density of nucleons in the nucleus and almost always taken to have a volume form $V_R f_R(r)$, where V_R is the potential depth and $f_R(r)$

is the form factor describing the radial variation of the potential. $f_R(r)$ is chosen to approximate the measured nuclear charge density which is assumed to be proportional to the nucleon density. The most common form used is the Woods-Saxon potential

$$f_R(r) = [1 + \exp(\frac{r - R_R}{a_R})]^{-1} \qquad (6.1)$$

where R_R, the nuclear radius is generally chosen to be, $R_R = R_o A^{1/3}$ and a_R is an adjustable parameter called the diffuseness. The real central term thus involves three parameters, namely V_R, R_R and a_R.

Since the imaginary or the absorptive potential takes account of the reactions which remove particles from the elastically scattered beam, it can not be expected to have the same radial behaviour as the real part. It may be expected to be a combination of volume and surface absorption terms. However the Pauli exclusion principle reduces the absorption of nucleons where the density is high, so that absorption is surface peaked. Thus only a small fraction of the nucleon wave penetrates the interior of the nucleus and because this region is smaller than the surface region, the surface absorption is predominant up to several MeV. One widely used analytical form for the surface absorption potential is the Gaussian,

$$i\, W_o \exp[- \{\frac{(r - R_W)}{a_W}\}^2] \qquad (6.2)$$

where R_W is the nuclear radius $R_o A^{1/3}$ and a_W is the surface diffuseness parameter. Using the derivative of the real potential is another common choice. Thus a Woods-Saxon derivative form is written as,

$$g(r) = 4a_W f'_R(r)$$

$$= 4a_W \frac{d}{dr} [1 + \exp(\frac{r - R_W}{a_W})]^{-1} \qquad (6.3)$$

where the factor $4a_W$ is usually included to make $g(r) = 1$ at the maximum. This form therefore contains three parameters like the real potential. The volume form is correspondingly chosen as $W_v g_v(r)$ with three parameters. If both surface and volume terms are used six parameters are involved in the absorption term.

In addition to the real and imaginary potentials, the spin-independent-term often includes a term called the symmetry term to take account of the isobaric spin dependence of the incident neutron and the target nucleus. The isobaric-spin-dependent term (V_1) is usually assumed real with a radial variation represented by a Woods-Saxon form factor. The depth of the real potential is then expressed as,

$$V_o \sim V_o + \tfrac{1}{4}V_1(N - Z)/A,$$

where $(N - Z)$ is the neutron excess and A is the mass number.

Spin-dependent term: For the optical model to be capable of predicting, as is observed, that scattered neutrons are partially polarized, it is necessary to include a spin dependent term in the potential of the form,

$$V_{SO}(r) = (V_{SO} + iW_{SO}) \frac{b}{r} \frac{d}{dr} h(r) \vec{\ell}\cdot\vec{\sigma} \qquad (6.4)$$

where $\vec{\ell}$ and $\vec{\sigma}$ are dimensionless operators related to the orbital angular momentum and spin angular momentum of the incident neutrons, $\vec{L} \equiv \hbar\vec{\ell}$ and $\vec{S} \equiv \hbar\vec{\sigma}/2$ and the form factor $h(r)$ is usually taken to be of Woods-Saxon form, i.e.

$$h(r) = \left[1 + \exp \frac{r-R_{SO}}{a_{SO}}\right]^{-1} .$$

The constant b is introduced to give the correct dimensions and various choices are adopted. The common choice is the reduced Compton

wavelength $b = (\hbar/m_\pi c)^2$ of the neutrons.

The spin-orbit potential, like the absorptive potential is concentrated on the nuclear surface. Unlike the absorptive potential, it is usually taken as real, because making it complex has not been found to appreciably increase agreement between theory and experiment. Thus the spin-orbit term in (6.4) above is reduced

$$V_{SO}(r) = V_{SO}\left(\frac{\hbar}{m_\pi c}\right)^2 \frac{1}{r}\frac{d}{dr}\left[1 + \exp\frac{r-R_{SO}}{a_{SO}}\right]^{-1} \vec{\ell}\cdot\vec{\sigma} \qquad (6.5)$$

involving three parameters, V_{SO}, R_{SO} and a_{SO}. It is to be pointed out here that the above form of the spin-orbit potential is appropriate for the scattering of spin $^1/2$ particles from the spin zero nuclei. For targets with non-zero spin $\vec{I}$, a large number of interactions involving $\vec{I}\cdot\vec{\sigma}$ is possible. However the usual practice in most of the optical model analyses is to neglect the spin of the target nucleus with the assumption that the spin-spin interaction is negligible compared to the spin-orbit interaction.

6.3 Global Potentials

With the encouraging success of Feshbach, Porter and Weisskopf[9] there have been constant attempts to improve optical model calculations and arrive at a potential that could account for neutron and proton data for a range of energies and mass numbers. A great variety of potentials have been attempted by different authors on this line, and a summary is given by Hodgson.[106] In the following we discuss only the form of the potentials that have been used in the analysis of the present experimental results for comparison and also as starting values for searchs for optimum parameters.

Rosen et al.[38] made an extensive analysis of elastic scattering data at 10.5 and 14.5 MeV. Their analysis was based mainly on polarization data of protons scattered from a wide range of nuclei. From the analysis they derived a potential that predicted reasonably successfully the proton polarization, elastic scattering and reaction cross-section data. Keeping all the geometrical factors as well as the spin orbit strength the same as for protons they determined the values for the real and the imaginary well depths for neutrons by searching for the best fit to 14 MeV neutron elastic scattering data. They found that the same set of parameters shows good agreement for 24 MeV data as well as 6 and 7 MeV data. For data below 6 MeV down to 1 MeV also, they found good agreement after taking account of compound elastic scattering according to the statistical theory of Hauser and Feshbach. The potential they used involved Woods-Saxon and derivative Woods-Saxon form factors for the real and imaginary potentials as in eqns. 6.1 and 6.3 respectively. The spin-orbit potential used was of the Thomas type, while no symmetry term was used. The parameters suggested by them for neutrons are quoted in Table 6.1.

Becchetti and Greenlees[39] made a comprehensive analysis of a wide range of proton and neutron data for energies less than 50 MeV and nuclei with $A > 40$. They arrived at optimum proton parameters, that provided very good fits to differential cross-section, polarization, reaction cross-section and total cross-section data. Using the proton parameters as starting values a search was made for optimum neutron parameters. The central potential chosen consisted of a Woods-Saxon form for the real potential, a combination of Woods-Saxon volume and surface derivative forms for the imaginary potential and a symmetry term, while the spin dependent term was the same as in eqn. 6.5. The optimum neutron

potential that they arrived at is listed in Table 6.1.

Holmqvist[14] fitted the experimental distribution of differential elastic scattering of 1.5 to 8.1 MeV neutrons for 12 elements from Al to Bi. The optical potential used was a local central potential, consisting of Woods-Saxon, derivative Woods-Saxon and Thomas form factors as in eqn. 6.1, 6.2 and 6.5. Optimum parameters calculated independently for each element and energy gave very good agreement between experimental and theoretical angular distributions. The optimum parameter values that they have quoted for the case of Fe and used in the present analysis are listed in Table 6.1.

Zijip and Jonker[34] attempted individual analysis of their 3.2 MeV polarization data for 19 elements, supplemented by the cross-section data of Becker et al.[78] at the same energy. The potential form they used involved Woods-Saxon and derivative Woods-Saxon form factors for the real and imaginary potentials respectively as in 6.1 and 6.3. The spin-orbit term involved both real and imaginary potential terms. For investigation of the symmetry dependence or for comparison of the potentials at various energies they took the real and imaginary potential depths to be,

$$V = V_o - \varepsilon_V E_n - V_1(N - Z)/A$$

$$W = W_o - \varepsilon_W E_n - W_1(N - Z)/A,$$

in which V_1 and W_1 are the real and imaginary symmetry terms and ε_V and ε_W are the coefficients of the energy dependence.

By choosing a fixed geometry and spin-orbit potential they searched for the real and imaginary potential for all the nuclei by fitting the polarization and cross-section data individually and together also. The optimum parameters they quoted for the nuclei studied in the present work are listed in Table 6.1.

Fu and Perey[41] made an extensive survey and subsequently derived cross-section data for lead, covering the energy range from .00001 eV to 20.0 MeV, from experimental results and calculations based on optical model, DWBA and Hauser-Feshbach theories. The set of optical model parameters they arrived at from different cross-section data for Pb covering neutron energies from 1 to 15 MeV are quoted in Table 6.1.

Tanaka et al.[80] determined potential parameters for Bismuth for neutron energies of 1.45 - 3.58 MeV from comparison of their measured cross-sections with calculation. The potential form used in the calculation was of the standard type with a Woods-Saxon derivative imaginary part and with a spin-orbit coupling term.

Compound elastic cross-sections were estimated by the Hauser-Feshbach calculation. The best fit parameter set for Bi which they obtained by searching for the real and imaginary potential depth for 3.06 MeV neutrons is presented in Table 6.1.

Haouat et al.[88] performed optical model analysis of the n - ^{12}C elastic scattering of measurements for neutron energies in the range 11.5 to 14.5 MeV. The parameters they found are listed in Table 6.1.

TABLE 6.1 Summary of global potential parameters and parameters suggested previously for particular nuclei used in the present analysis.

	V(r)	W(r)	$V_{SO}(r)$
(1) Rosen et al.[38] (1-24 MeV)	$V_R = (49.3-0.33E_n)$MeV $r_R = 1.25$fm; $a_R = 0.65$fm	$W_S = 5.75$ MeV $r_W = 1.25$ fm; $a_W = 0.75$fm	$V_S = 5.5$ MeV $r_S = 1.2$fm; $a_S = 0.65$fm
(2) Becchetti & Greenlees[39] (<50 MeV)	$V_R = [56.3-0.32E_n-24\frac{N-Z}{A}$ MeV] $r_R = 1.17$fm; $a_R = 0.75$fm	$W_S = [13-0.25E_n-12\frac{N-Z}{A}$ MeV] or zero whichever is greater $r_W = 1.26$fm; $a_W = 0.58$fm $W_V = (0.22E_n-1.56)$MeV or zero whichever is greater.	$V_S = 6.2$ MeV $r_S = 1.25$fm; $a_S = 0.75$fm
(3) Holmqvist[14] (1.5-8.1 MeV)	$V_R = 51.1$ MeV (Fe, 2.96 MeV) $r_R = 1.21$fm; $a_R = 0.61$fm	$W_S = 10.8$ MeV (Fe, 2.96 MeV) $r_W = 1.15$fm; $a_W = 0.48$fm	$V_S = 8.0$ MeV $r_S = 1.21$fm; $a_S = 0.61$fm
(4) Zijip & Jonker[34] (3.2 MeV)	$V_R = 48.3$ MeV (Fe), 50.4 MeV (W), 45.0 MeV (Tℓ), 46.6 MeV (Pb), 46.2 MeV (Bi) $r_R = 1.25$fm; $a_R = 0.65$fm	$W_S = 9.6$ MeV (Fe), 9.3 MeV (W), 13.0 MeV (Tℓ), 6.9 MeV (Pb), 8.2 MeV (Bi) $r_W = 1.25$fm; $a_W = 0.48$fm.	$V_S = 8.0$ MeV $r_S = 1.12$fm $a_S = 0.65$fm
(5) Fu & Perey[41] (1-15 MeV)	$V_R = (47.0-0.25E_n)$MeV $r_R = 1.25$fm; $a_R = 0.65$fm	$W_S = (3.5+0.43E_n)$MeV $r_W = 1.25$fm; $a_W = 0.47$fm	$V_S = 7.0$ MeV $r_S = 1.25$fm; $a_S = 0.65$fm
(6) Tanaka et al.[80] (3.06 MeV)	$V_R = 46.11$ MeV $R_R = 1.25$fm; $a_R = 0.65$fm	$W_S = 3.59$ MeV $r_W = 1.25$fm; $a_W = 0.48$fm	$V_S = 7.0$ MeV $r_S = 1.25$fm; $a_S = 0.65$fm
(7) Haouat et al.[88] (11.5 - 14.5 MeV)	$V_R = (55.76-0.34E_n)$MeV $R_R = 1.25$fm; $a_R = 0.36$fm	$W_S = 7.86$ MeV $r_W = 1.25$fm; $a_W = 0.27$fm	$V_S = 6.15$ MeV $r_S = 1.25$fm; $a_S = 0.36$fm

6.4.1 Optical model analysis of the experimental data

The first step in fitting the experimental distribution of polarization and cross-section duly corrected for sample size and inelastic components, was to compare with "global fit" parameters and parameters previously quoted for particular nuclei (Table 6.1). The optical model calculations were performed using the programme RAROMP[107]. However the optical model has its limitation in that it predicts only shape elastic scattering, whereas at low energies (< 5 MeV) the compound elastic contribution can be significant. Thus for the analysis of the 2.9 MeV scattering data in the present work, the compound elastic scattering cross-section has to be added to the shape elastic cross-section (eqn. 1.1) in order to be comparable with the measured elastic cross-section. The calculated polarization has also to be corrected for the unpolarized compound elastic neutrons as follows,

$$P_{el} = P_{S.E} \frac{\sigma_{S.E}}{\sigma_{el}}$$

where $\sigma_{el} = \sigma_{S.E} + \sigma_{C.E}$ (1.1)

where $\sigma_{S.E}$ and $P_{S.E}$ are the calculated shape elastic cross-section and polarization respectively and $\sigma_{C.E}$ is the compound elastic cross-section.

The calculations of the compound elastic cross-sections were performed using the programme CINDY[108] based on the Hauser-Feshbach[11] formalism. The programme included the possibility of doing calculations both with and without the Moldauer level width fluctuation (MLF) correction[108]. It has been observed by Galloway and Waheed[40] in the analysis of their data on 2.9 MeV neutrons, that while the C.E calculations made without the MLF correction gave a better fit to their cross-section

data on Fe, Cu and I, the agreement was closer with the calculation including the MLF correction for the case of Pb, whereas it was similar for both with and without the correction for Hg. Thus, in the present analysis it was decided to carry out the calculations both with and without the MLF correction for each nucleus. Some inelastic scattering calculations were also made using the programme CINDY, to account for the contribution due to relevant inelastic components in the case of tungsten and uranium, which could not be discriminated experimentally (Chapter 3.6.2). The properties of the different excited states for the isotopes of each of the nuclei, necessary for the calculation of the compound elastic and inelastic cross-sections were taken from the references listed in Table 3.2.

The next step in the analysis was doing searches for the parameters which give the best fit to the experimental data. The programme RAROMP includes the possibility of automatic searches on all the parameters to minimize the "goodness of fit" criterion,

$$\chi^2(T) = \chi^2(\sigma(\theta)) + \chi^2(P_n(\theta))$$

where $$\chi^2 = \left[\frac{\text{Theory-Experiment}}{\text{error in experiment}}\right]^2 .$$

Each of the parameter sets used for comparison was used as the starting values for a search and the parameters varied in different combinations for each of the nuclei and for each incident neutron energy. In doing the parameter search for the 2.9 MeV case, available cross-section data (Chapter 3.6.3) at comparable energy that are consistent were included with the present cross-section values. All the experimental cross-section and polarization values used as input for the optimum search, for the 2.9 MeV case, were adjusted for the calculated compound elastic scattering and wherever applicable for the inelastic scattering (W and U).

As in the case of calculations with the global parameters and previously suggested parameters, the optimum search was carried out for the compound elastic effect adjusted, both with and without the MLF correction.

6.4.2 Optical model fitting at 2.9 MeV

IRON:- As already discussed in Chapter 1.3 the present measurement on iron was done primarily as a test for the experimental system and as the comparison of the present results on angular distribution of polarization and cross-section, presented in Chapter 3.6.3 is found to show good agreement with the previous results, it is reasonable to expect a similar optical model fit to the data. It was observed by Galloway and Waheed[40] in the comparison of their data with optical model calculation that the compound elastic calculation done without the MLF correction provided better agreement with the experimental data than that including the MLF correction. Thus the present experimental cross-section and polarization values are compared in Fig. 6.1 with calculation done without the MLF correction and with the global potentials of Rosen et al.[38] and Becchetti and Greenlees[39] and those suggested by Zijip and Jonker[34] and by Holmqvist[14]. The parameter set of Holmqvist gives the best overall fit to the present experimental cross-section, while those of Rosen give the closest fit to the polarization data. A similar result was observed by Galloway and Waheed[40]. In the light of the above findings it was felt that there was not much to be gained in repeating a parameter search for the case of Fe. Thus the present experimental results along with other results are compared with the best fit curve obtained by Galloway and Waheed[40] in Fig. 6.2 and the parameter set listed in Table 6.2.

Key to symbols used in Fig. 6.1— Fig. 6.18

✱ - Present experimental measurements.

△ - Galloway & Waheed.[40]

× - Holmqvist.[14]

◇ - Becker et al.[78]

■ - Popov.[79]

● - Tanaka et al.[80]

▲ - Batchelor et al.[81]

The curves used in the figures for comparison of experimental measurements with calculations based on optical model parameterisation of different authors are:

———— Rosen et al.[38]

—·—·—·— Becchetti & Greenlees.[39]

——··——·· Zijip & Jonker.[34]

---------- Holmqvist .[14] in Fig.6.1

Fu & Perey.[41] in Fig.6.9

Tanaka et al.[88] in Fig. 6.12

The solid curve in the BEST-FIT figures represents the calculated distributions obtained with the optimum parameters presented in table 6.2.

Compound elastic scattering cross-section (C.E) calculated using same parameterisation as above are also displayed in all the figures. The key to the C.E curves is the same as that for corresponding differential cross-section fits above.

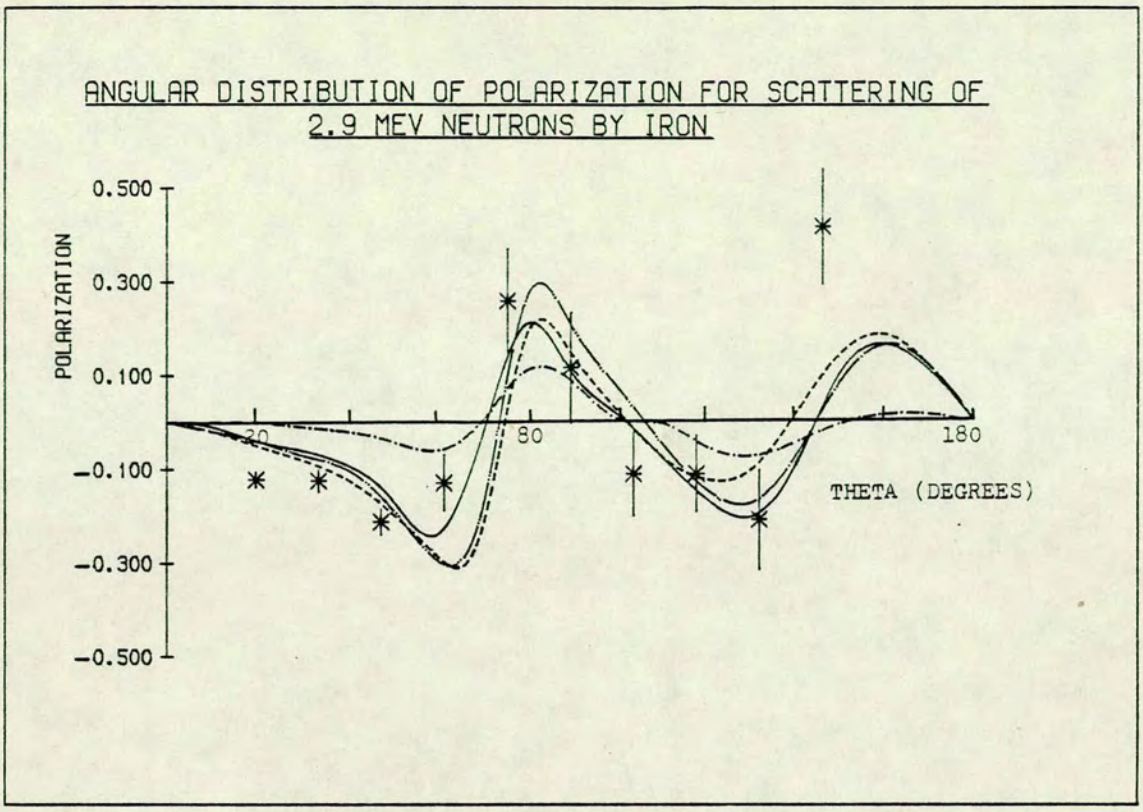
ANGULAR DISTRIBUTION OF POLARIZATION FOR SCATTERING OF 2.9 MEV NEUTRONS BY IRON
POLARIZATION
0.500
0.300
0.100
-0.100
-0.300
-0.500
20
80
180
THETA (DEGREES)

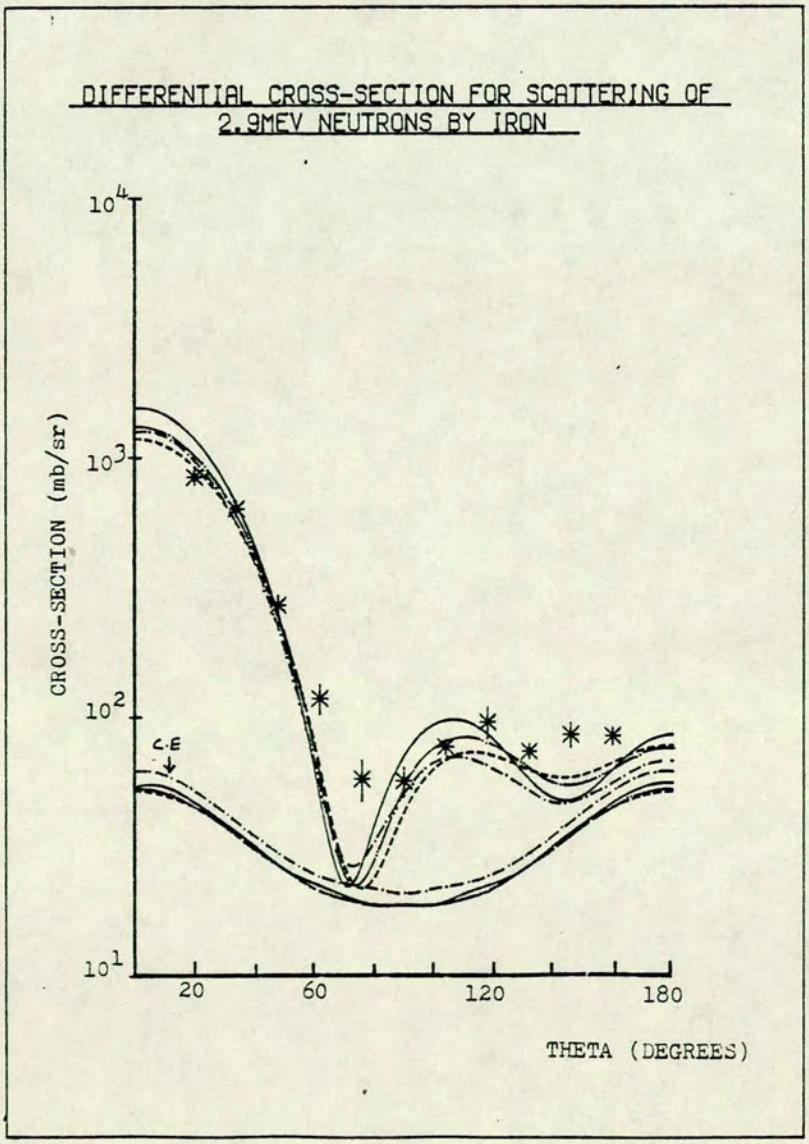
DIFFERENTIAL CROSS-SECTION FOR SCATTERING OF 2.9MEV NEUTRONS BY IRON
CROSS-SECTION (mb/sr)
10^4
10^3
10^2
10^1
C.E
20
60
120
180
THETA (DEGREES)

Fig. 6.1

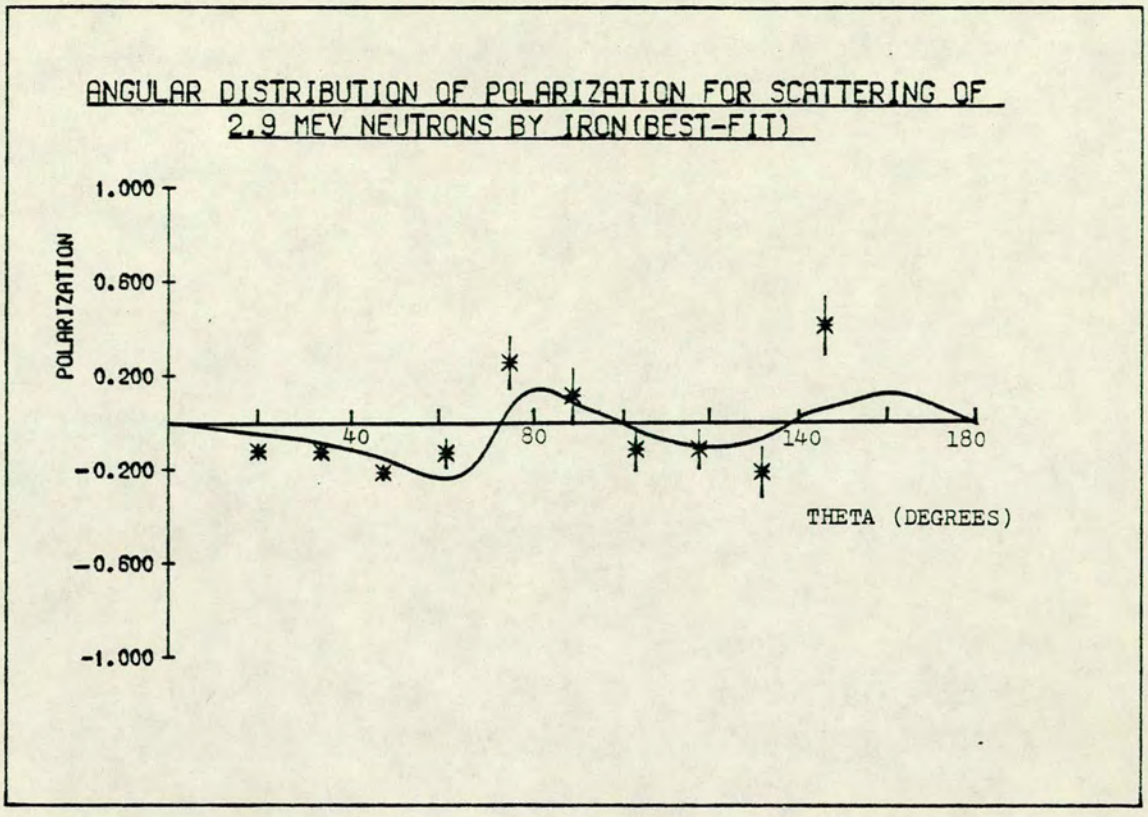
ANGULAR DISTRIBUTION OF POLARIZATION FOR SCATTERING OF 2.9 MEV NEUTRONS BY IRON(BEST-FIT)
POLARIZATION
1.000
0.600
0.200
-0.200
-0.600
-1.000
40
80
140
180
THETA (DEGREES)

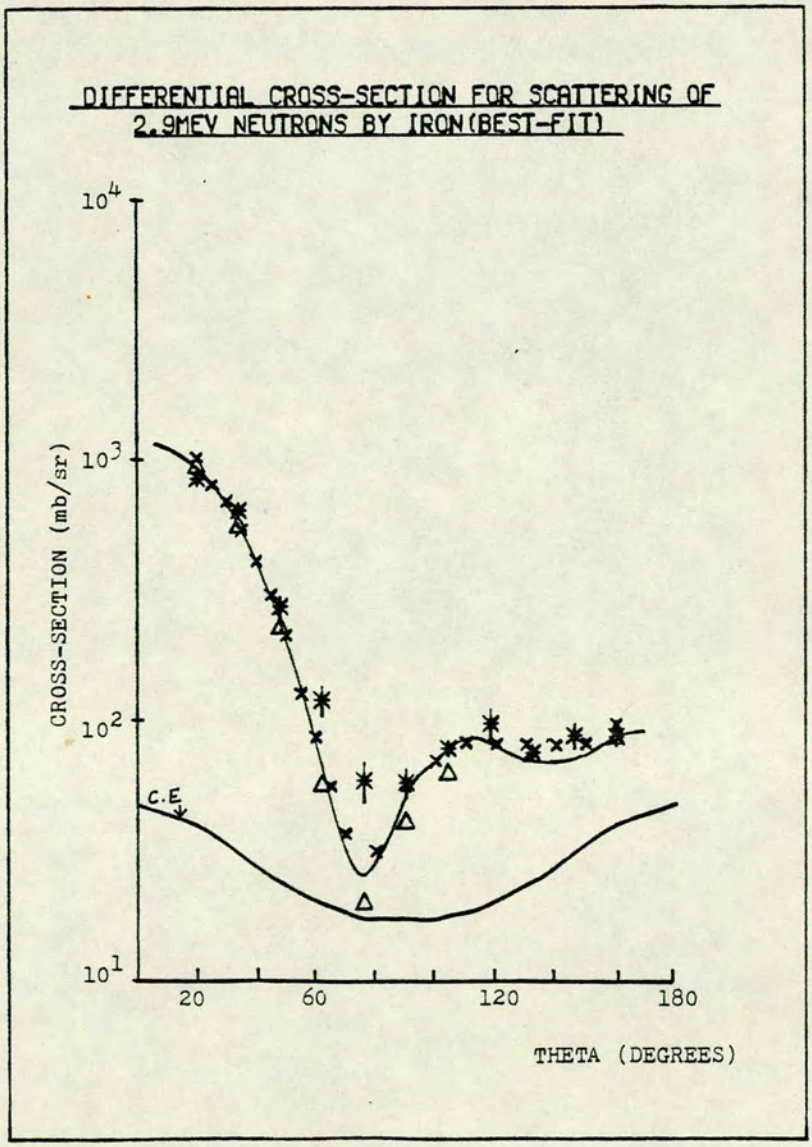
DIFFERENTIAL CROSS-SECTION FOR SCATTERING OF 2.9MEV NEUTRONS BY IRON(BEST-FIT)
CROSS-SECTION (mb/sr)
10^4
10^3
10^2
10^1
C.E
20
60
120
180
THETA (DEGREES)

Fig. 6.2

TUNGSTEN:- For W the optical model calculations were done based on the global parameters of Rosen et al.[38], Becchetti and Greenlees[39] and those proposed by Zijip and Jonker[34] from the optimum fit of their 3.2 MeV polarization data. The calculated cross-sections were adjusted for the compound elastic contribution both with and without the MLF correction. In addition, since the data could not be corrected using experimental inelastic contributions, inelastic differential cross-sections were also calculated for the six states which can contribute neutrons above the discrimination bias applied. These calculated inelastic cross-sections were scaled by appropriate relative detection efficiency factors (Chapter 3.6.2) for the neutron energies concerned and combined with the elastic calculations for comparison with the experimental data. Figs. 6.3 and 6.4 illustrate the comparisons of the measured distributions of polarization and cross-section with the calculations, for the C.E calculations done with and without the MLF correction respectively. Both the calculations show a very similar fit to the differential cross-section data, with the Rosen parameters best. There is very little to choose from the comparison of the experiment with calculation for polarization made with and without the MLF correction or in relation to different parameters. However the gross trend of the distribution seems to be reflected.

The data used in the search for optimum parameters consisted of the present cross-sections, Becker et al.[78] cross-sections and the present polarization values starting from all the three sets of parameters mentioned above based on C.E correction both with and without the MLF correction. The best fit parameter set listed as W(1) in Table 6.2, resulted with a notably large value for the radius R_W. However results from most of the searches showed a similar tendency and the next best fit parameters listed as W(2) give a value of 1.51 fm, while the set that results with $R_W = 1.27$fm has a χ^2 value for polarization

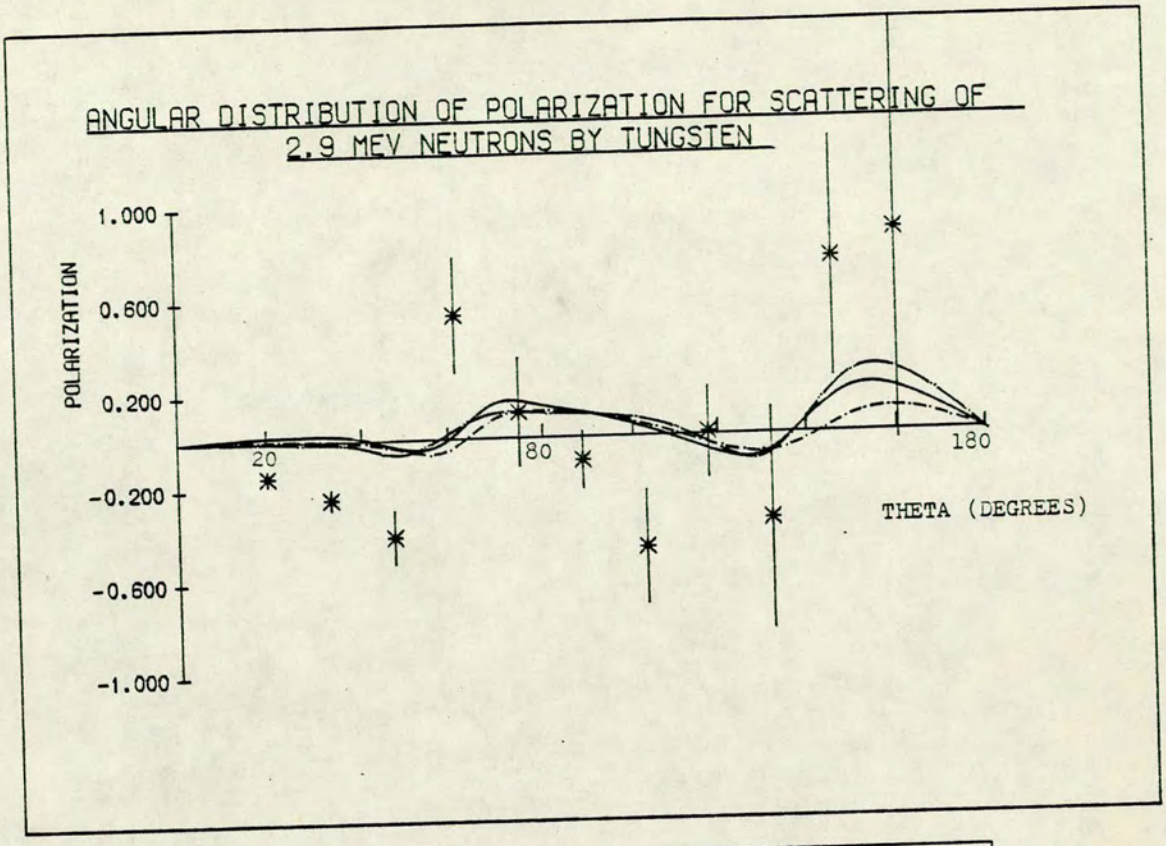
ANGULAR DISTRIBUTION OF POLARIZATION FOR SCATTERING OF 2.9 MEV NEUTRONS BY TUNGSTEN
POLARIZATION
1.000
0.600
0.200
-0.200
-0.600
-1.000
20
80
180
THETA (DEGREES)

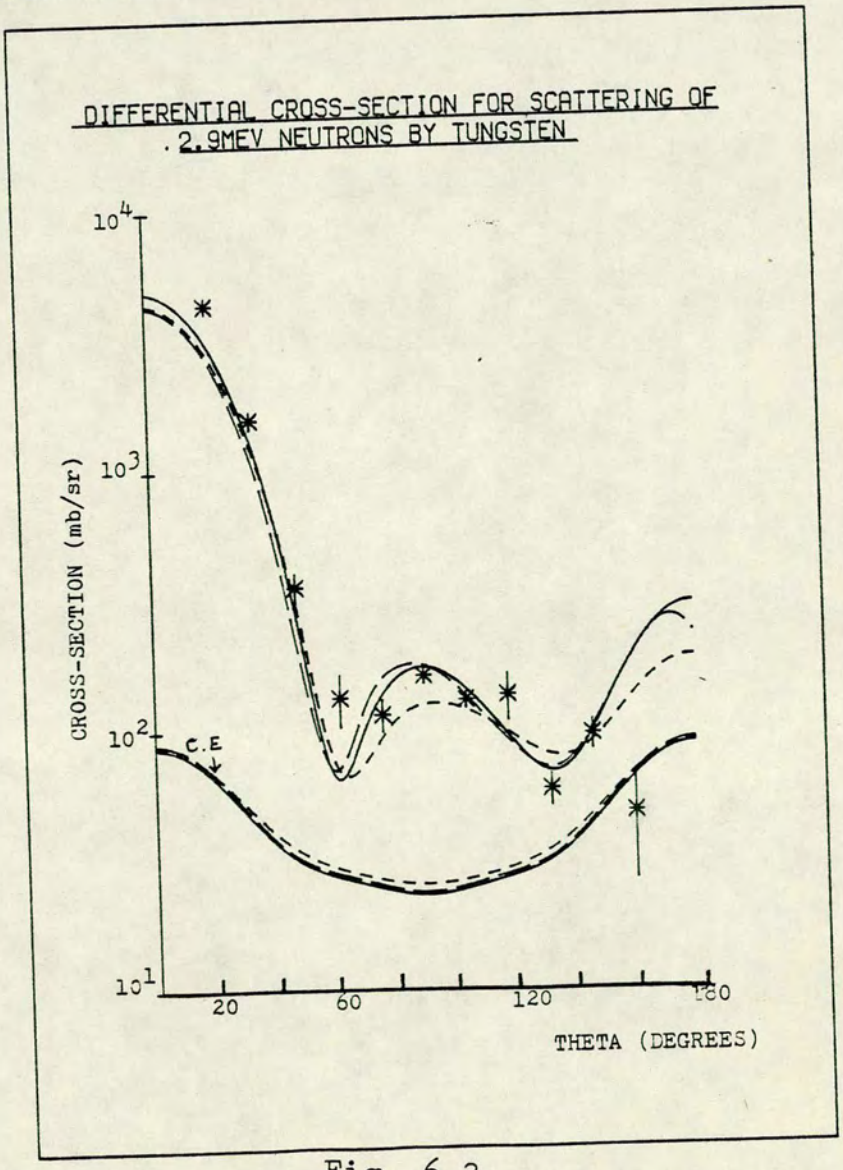
DIFFERENTIAL CROSS-SECTION FOR SCATTERING OF 2.9MEV NEUTRONS BY TUNGSTEN
CROSS-SECTION (mb/sr)
10^4
10^3
10^2
10^1
C.E
20
60
120
180
THETA (DEGREES)

Fig. 6.3

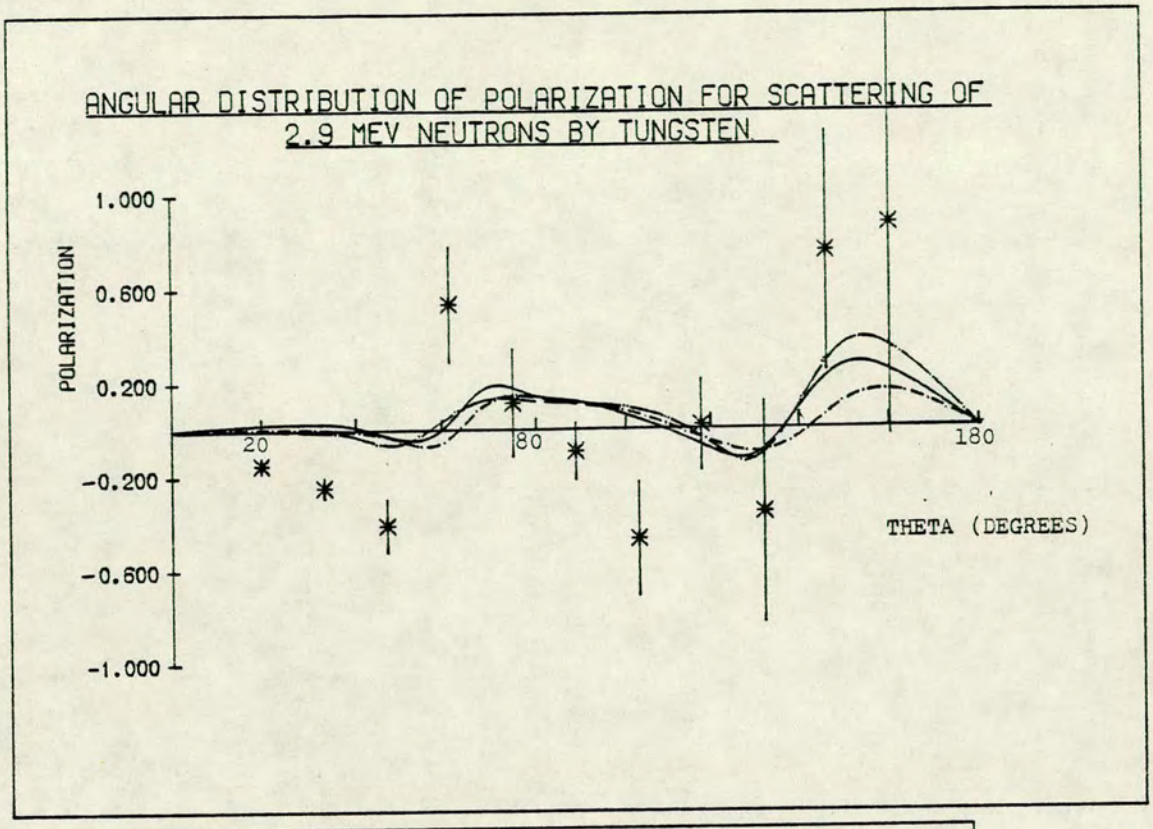
ANGULAR DISTRIBUTION OF POLARIZATION FOR SCATTERING OF 2.9 MEV NEUTRONS BY TUNGSTEN
POLARIZATION
1.000
0.600
0.200
-0.200
-0.600
-1.000
20
80
180
THETA (DEGREES)

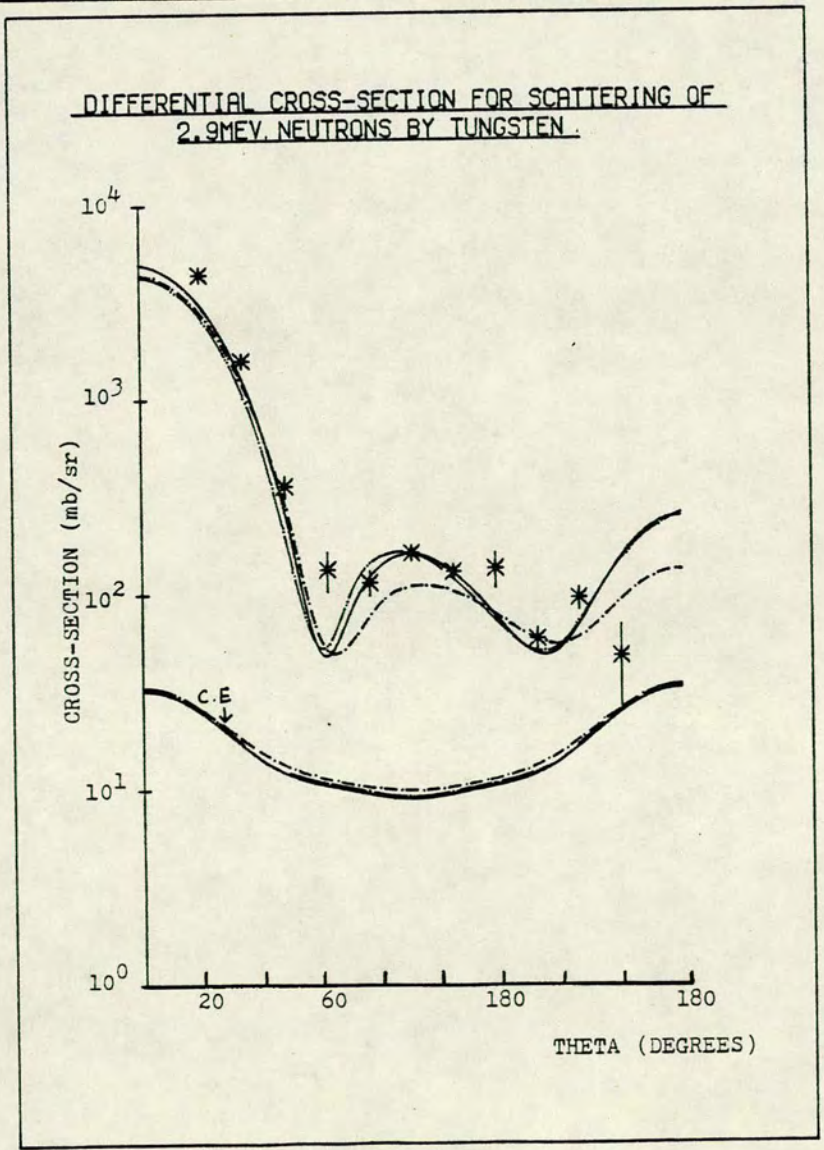
DIFFERENTIAL CROSS-SECTION FOR SCATTERING OF 2.9MEV. NEUTRONS BY TUNGSTEN.
CROSS-SECTION (mb/sr)
10^4
10^3
10^2
10^1
10^0
C.E
20
60
180
180
THETA (DEGREES)

Fig. 6.4

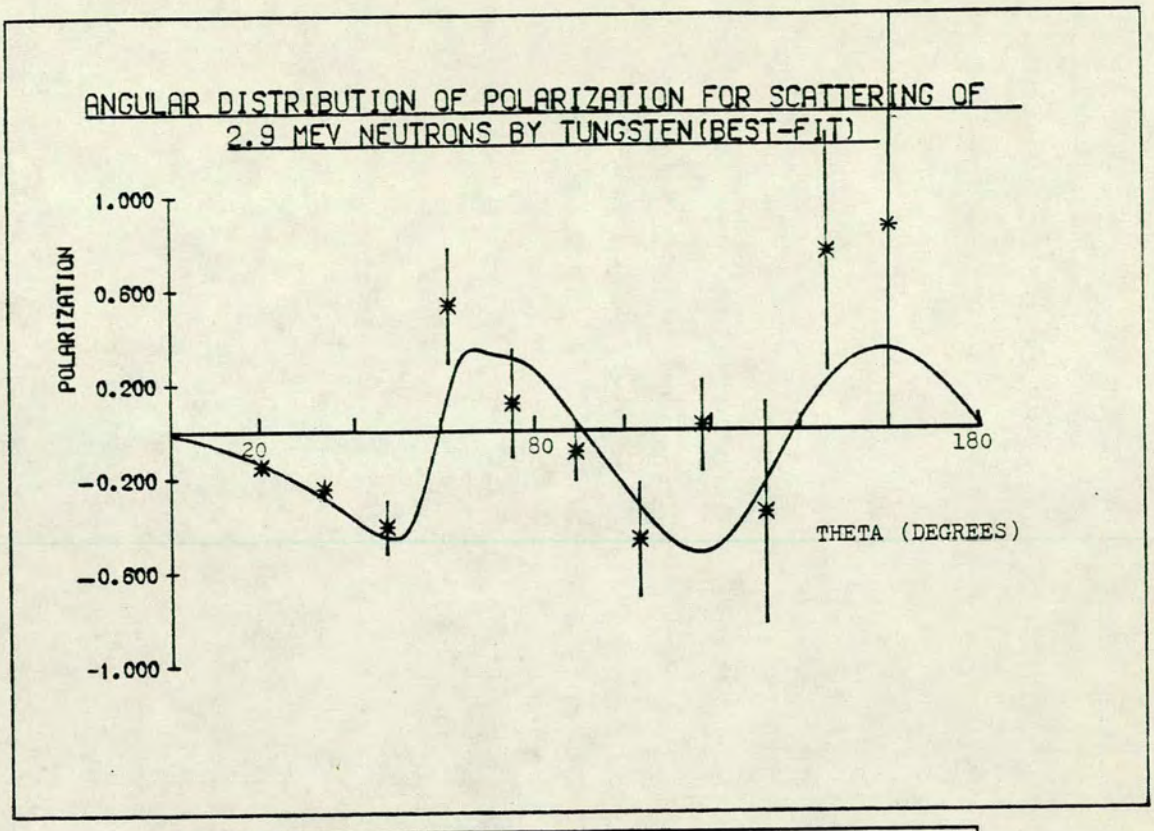
ANGULAR DISTRIBUTION OF POLARIZATION FOR SCATTERING OF 2.9 MEV NEUTRONS BY TUNGSTEN(BEST-FIT)
POLARIZATION
1.000
0.600
0.200
-0.200
-0.600
-1.000
20
80
180
THETA (DEGREES)

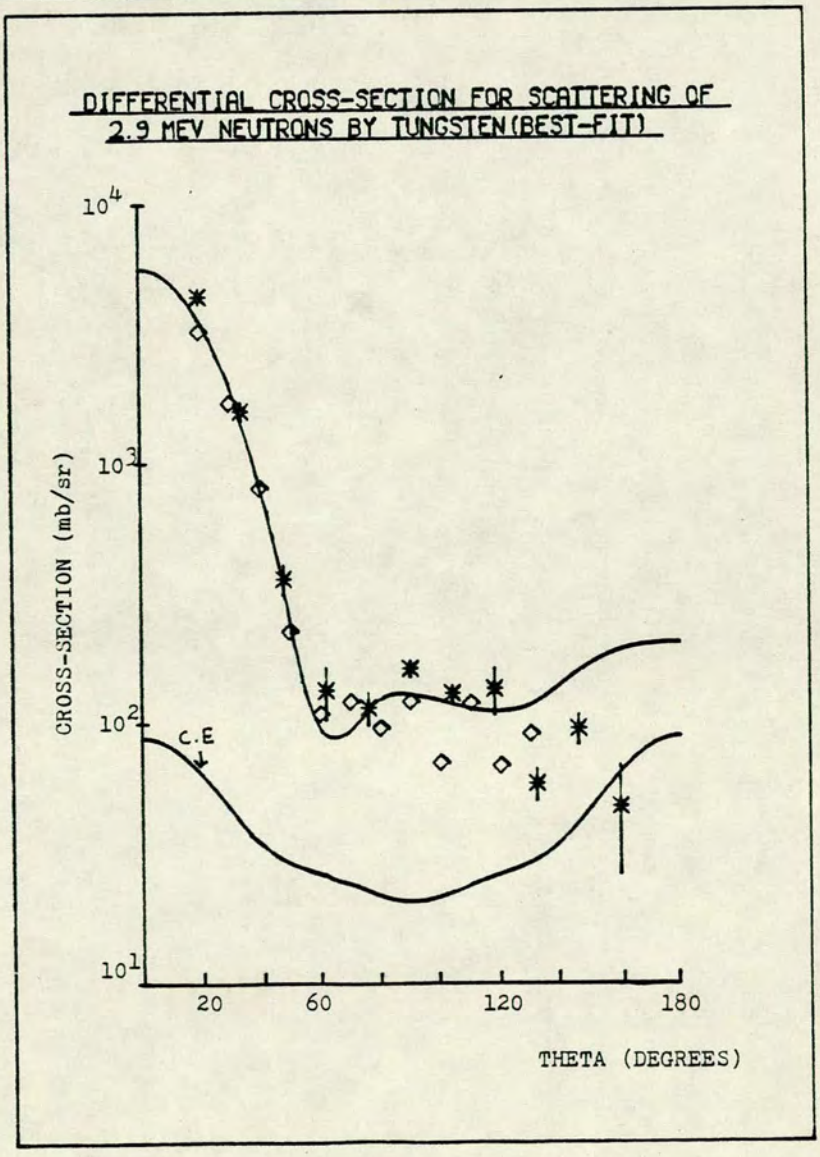
DIFFERENTIAL CROSS-SECTION FOR SCATTERING OF 2.9 MEV NEUTRONS BY TUNGSTEN(BEST-FIT)
CROSS-SECTION (mb/sr)
10^4
10^3
10^2
10^1
C.E
20
60
120
180
THETA (DEGREES)

Fig. 6.5

which is about eight times that of the set W(1). This odd result for W may not be surprising since tungsten has a large deformation. Fig. 6.5 shows the best fit obtained for the parameter set W(1) which was based on the C.E calculation done with the MLF correction, while the set W(2) resulted from C.E calculation done without the MLF correction.

THALLIUM:- The experimental distribution of polarization and cross-section of Tℓ are compared with the optical model calculations combined with the Hauser-Feshbach compound elastic calculations, with and without the MLF corrections, and based on the global parameters of Rosen et al.[38], Becchetti and Greenlees[39] and those proposed by Zijip and Jonker[34] in Figs. 6.6 and 6.7. It is clear from the two figures that as far as the cross-section is concerned, the calculation including the MLF correction, gives a significantly better fit to the data for all the parameters. It is difficult to comment from the graph as to which set of the parameters gives closer agreement although consideration of the χ^2 values suggests Zijip and Jonker's[34] parameters to be best. Coming to the case of polarization, although the quantitative agreement between the calculated and measured values is poor, the general trend appears to be consistent for most of the angles.

The results of the optimum parameter searches, which included the cross-section values of Becker et al.[78] in addition to the present cross-section and polarization data, are summarized in Table 6.2 and the best fit illustrated in Fig. 6.8. It was observed that searches done for similar combinations of parameters, consistently gave better fit for the set of data that included the adjustment for the C.E cross-section with MLF correction. The best fit parameter set for Tℓ has a comparatively large value for the depth of the spin orbit potential.

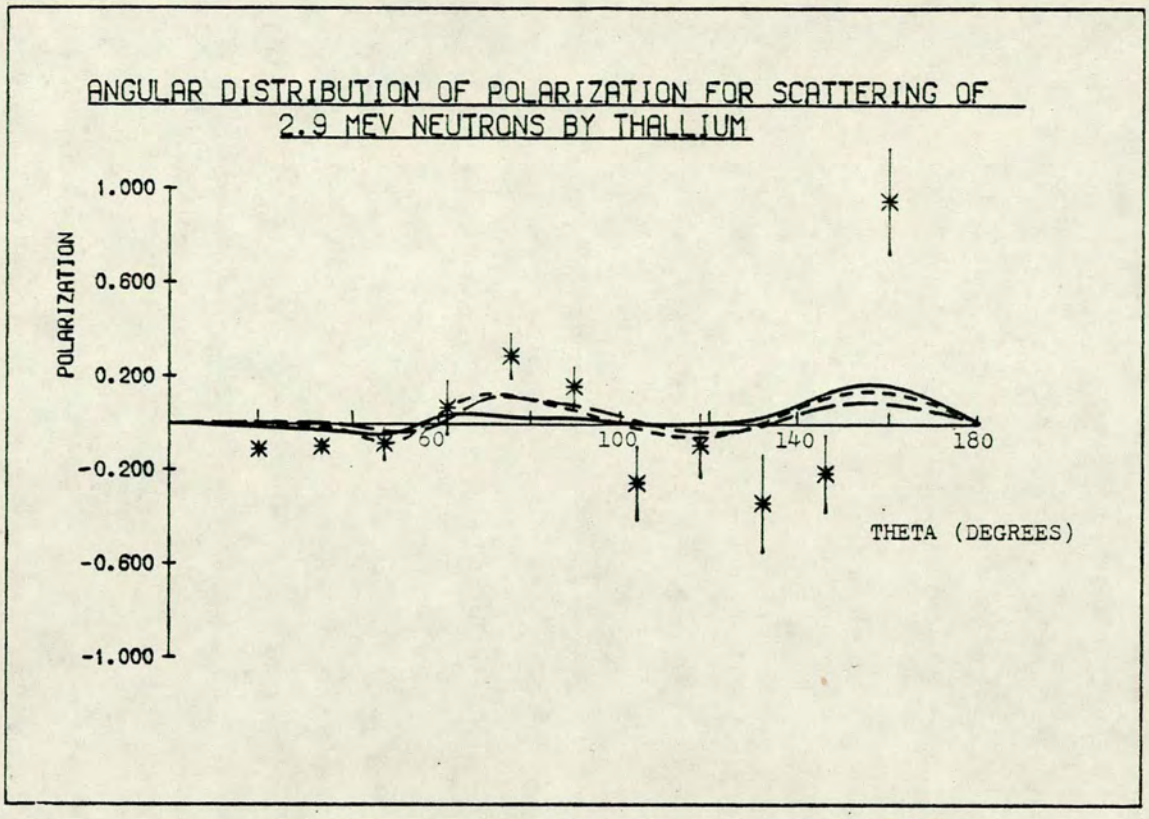
ANGULAR DISTRIBUTION OF POLARIZATION FOR SCATTERING OF 2.9 MEV NEUTRONS BY THALLIUM
POLARIZATION
1.000
0.600
0.200
-0.200
-0.600
-1.000
60
100
140
180
THETA (DEGREES)

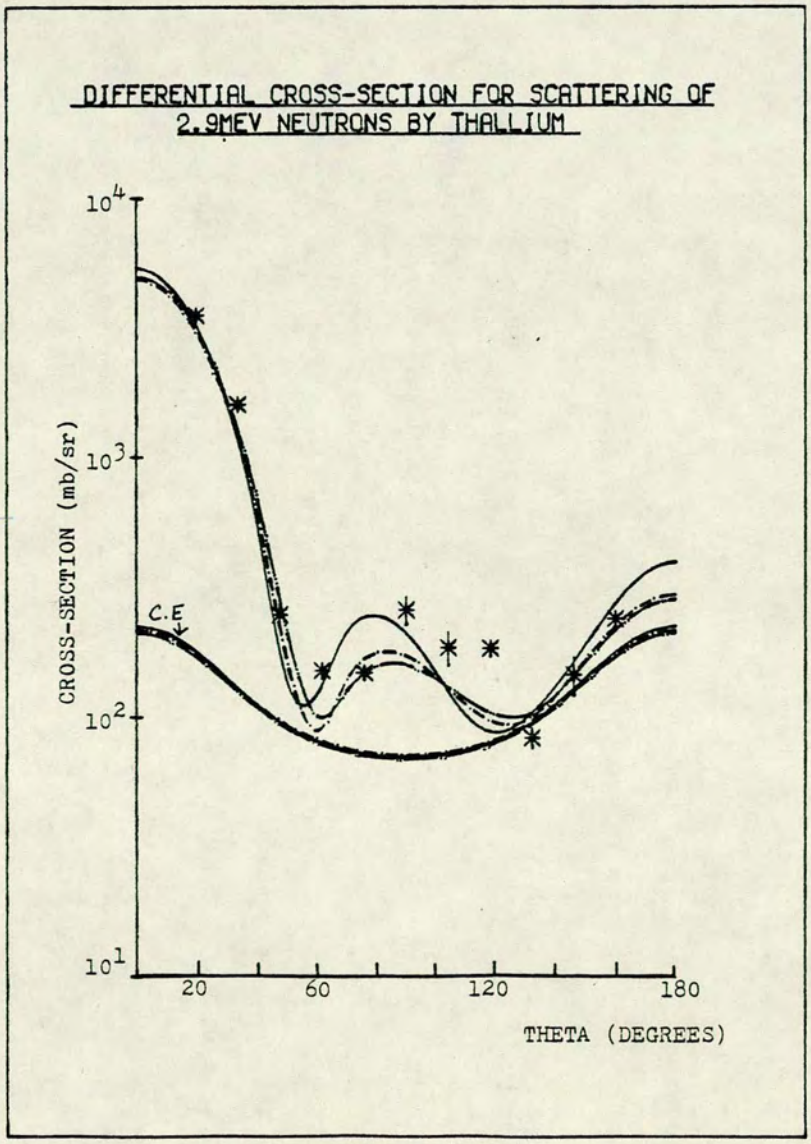
DIFFERENTIAL CROSS-SECTION FOR SCATTERING OF 2.9MEV NEUTRONS BY THALLIUM
CROSS-SECTION (mb/sr)
10^4
10^3
10^2
10^1
C.E
20
60
120
180
THETA (DEGREES)

Fig. 6.6

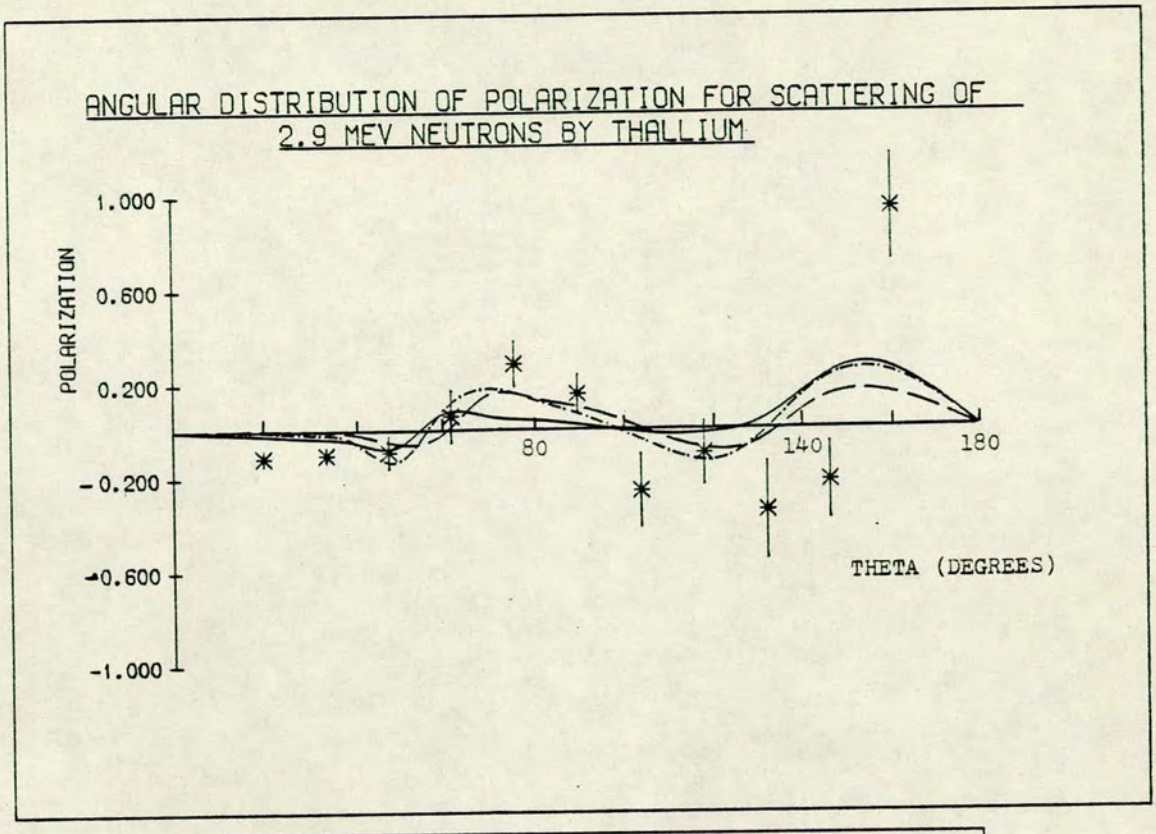
ANGULAR DISTRIBUTION OF POLARIZATION FOR SCATTERING OF 2.9 MEV NEUTRONS BY THALLIUM
POLARIZATION
1.000
0.600
0.200
-0.200
-0.600
-1.000
80
140
180
THETA (DEGREES)

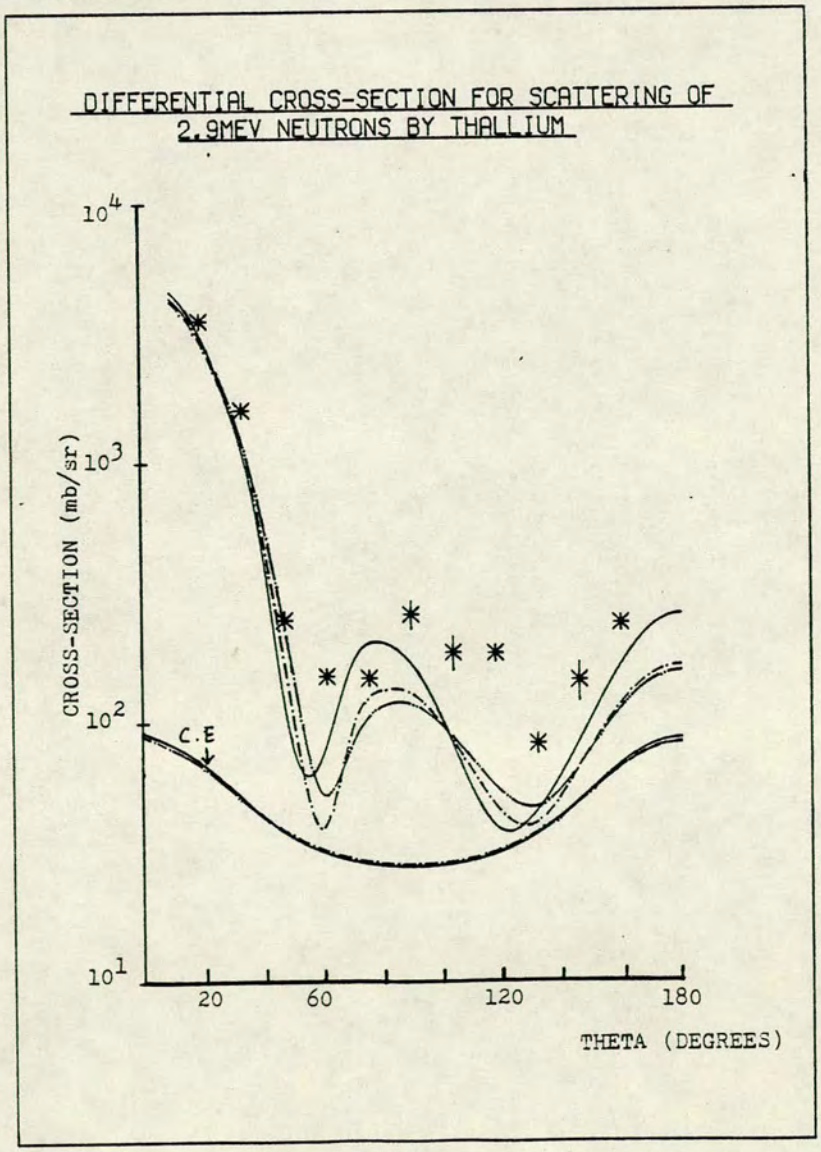
DIFFERENTIAL CROSS-SECTION FOR SCATTERING OF 2.9MEV NEUTRONS BY THALLIUM
CROSS-SECTION (mb/sr)
10^4
10^3
10^2
10^1
C.E
20
60
120
180
THETA (DEGREES)

Fig. 6.7

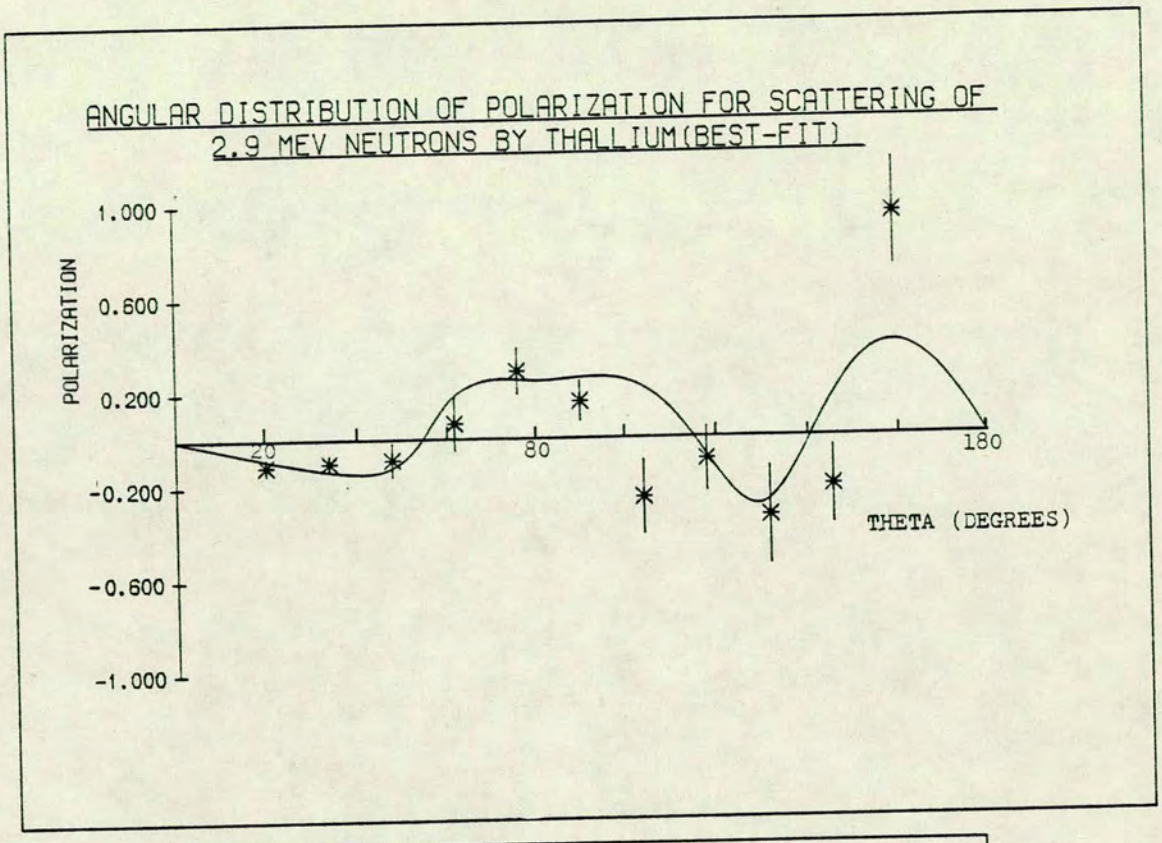
ANGULAR DISTRIBUTION OF POLARIZATION FOR SCATTERING OF
2.9 MEV NEUTRONS BY THALLIUM(BEST-FIT)
POLARIZATION
1.000
0.600
0.200
-0.200
-0.600
-1.000
20
80
180
THETA (DEGREES)

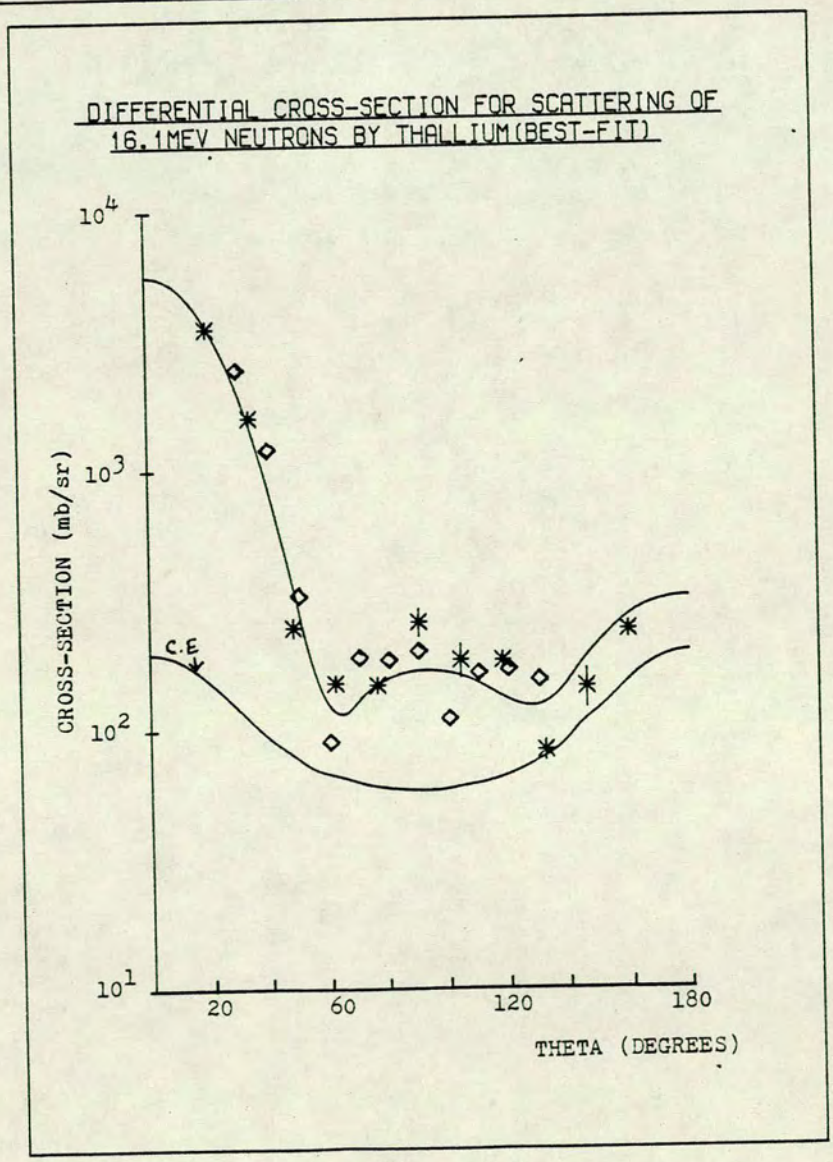
DIFFERENTIAL CROSS-SECTION FOR SCATTERING OF
16.1MEV NEUTRONS BY THALLIUM(BEST-FIT)
CROSS-SECTION (mb/sr)
10^4
10^3
10^2
10^1
C.E
20
60
120
180
THETA (DEGREES)

Fig. 6.8

But it was observed that most of the parameter sets that gave comparable fit to the one listed in Table 6.2 had even larger values for V_S, while the sets with values for V_S between 4 to 7 MeV gave much poorer fits to both the polarization and the cross-section data.

LEAD:- Experimental data of Pb differential cross-section and polarization are presented along with the optical model calculations combined with Hauser-Feshbach calculations, with and without the MLF corrections, in Figs. 6.9 and 6.10 respectively. The calculations were based on the global parameters of Rosen et al.[38], Becchetti and Greenlees[39] and those proposed by Zijip and Jonker[34] and Fu and Perey[41]. A closer fit to the differential cross-section data is provided by the calculations made including the MLF correction and the Fu and Perey parameters give the best overall agreement. So far as the polarization is concerned, there is not much difference in the calculations done with and without the MLF correction and the data is not particularly well fitted by any of the parameter sets.

The search for the optimum optical model parameters, consisted of the present polarization and cross-section data along with the cross-section data of Becker et al.[78] and Galloway and Waheed[40]. As in the case of Tℓ, it was observed for Pb also that the search made on the input data that was adjusted for the C.E effect, including the MLF correction, resulted in better fits for both polarization and cross-section. However the polarization data is less well fitted than the differential cross-section, as illustrated in the best fit curves in Fig. 6.11. The resulting parameters are listed in Table 6.2.

BISMUTH:- Optical model calculated cross-section and polarization for Bi using the 'global' parameter sets of Rosen et al.[38] and Becchetti and Greenlees[39] and those proposed by Zijip and Jonker[34] and Tanaka et al.[80], combined with the compound elastic calculations with and without the MLF

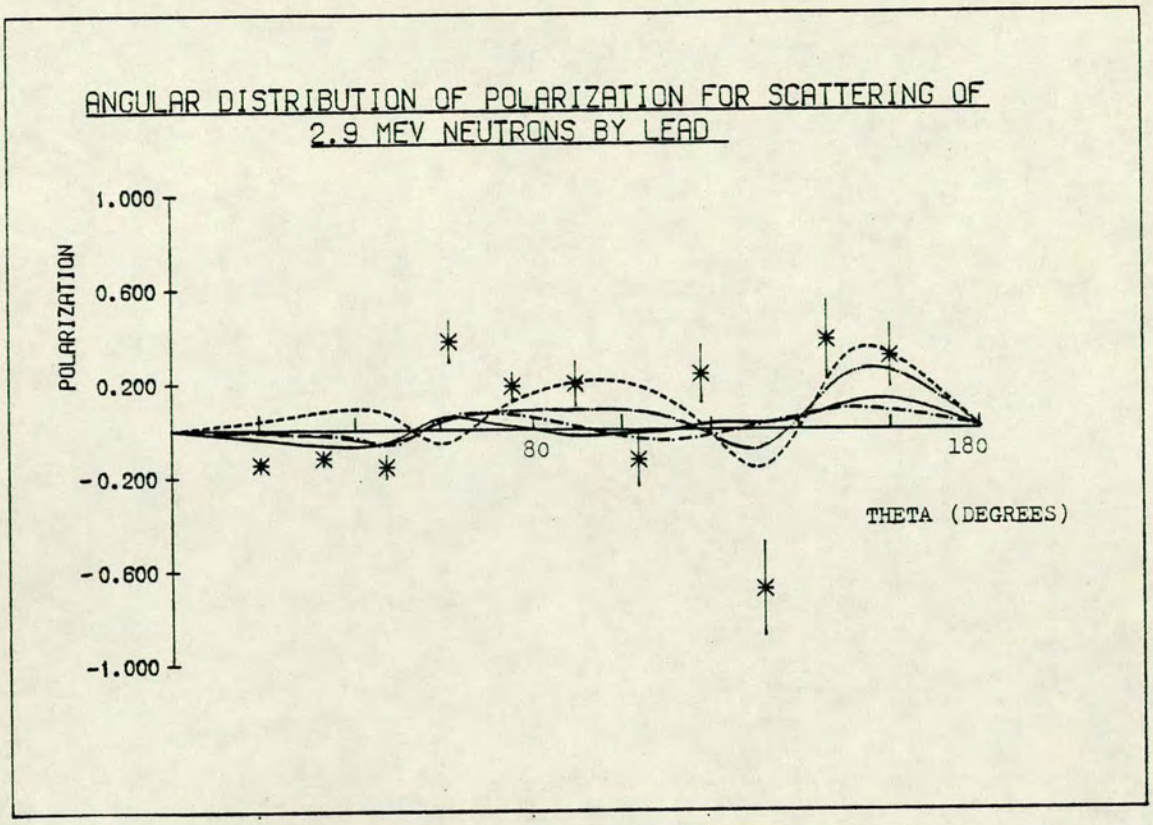
ANGULAR DISTRIBUTION OF POLARIZATION FOR SCATTERING OF 2.9 MEV NEUTRONS BY LEAD
POLARIZATION
1.000
0.600
0.200
-0.200
-0.600
-1.000
80
180
THETA (DEGREES)

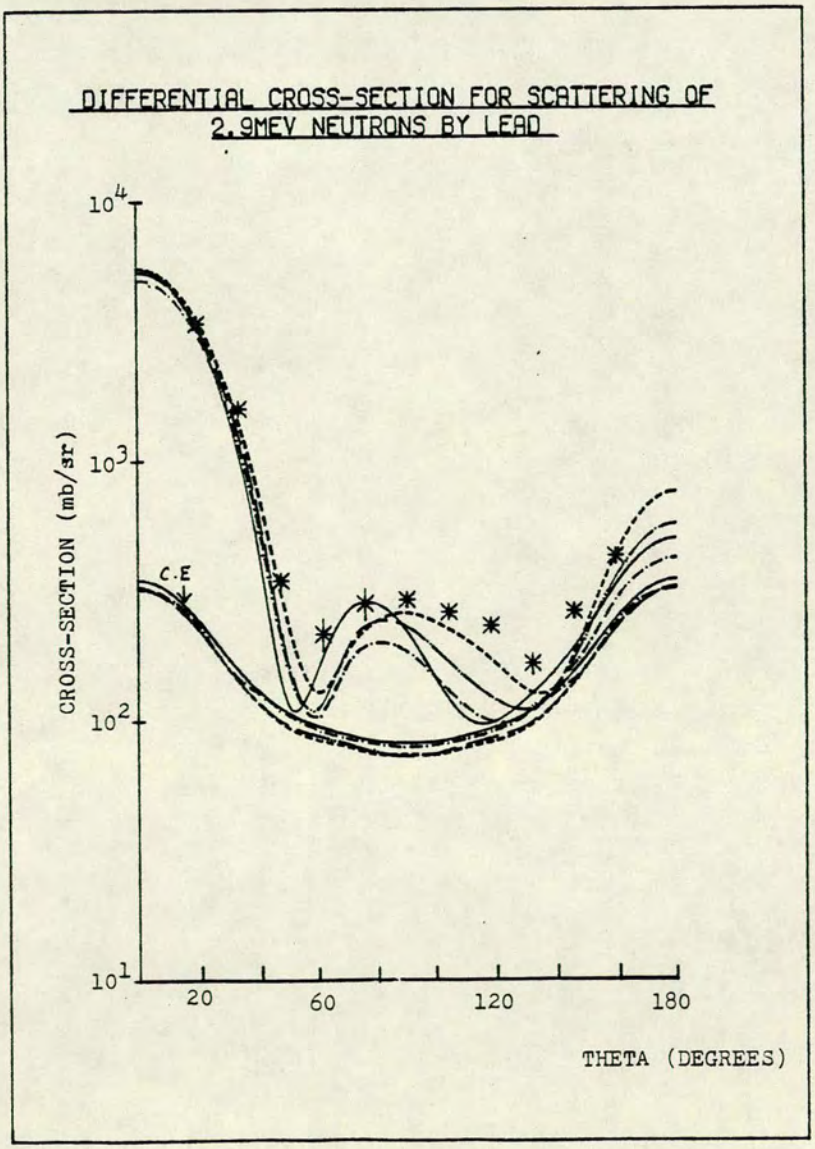
DIFFERENTIAL CROSS-SECTION FOR SCATTERING OF 2.9MEV NEUTRONS BY LEAD
CROSS-SECTION (mb/sr)
10^4
10^3
10^2
10^1
C.E
20
60
120
180
THETA (DEGREES)

Fig.6.9

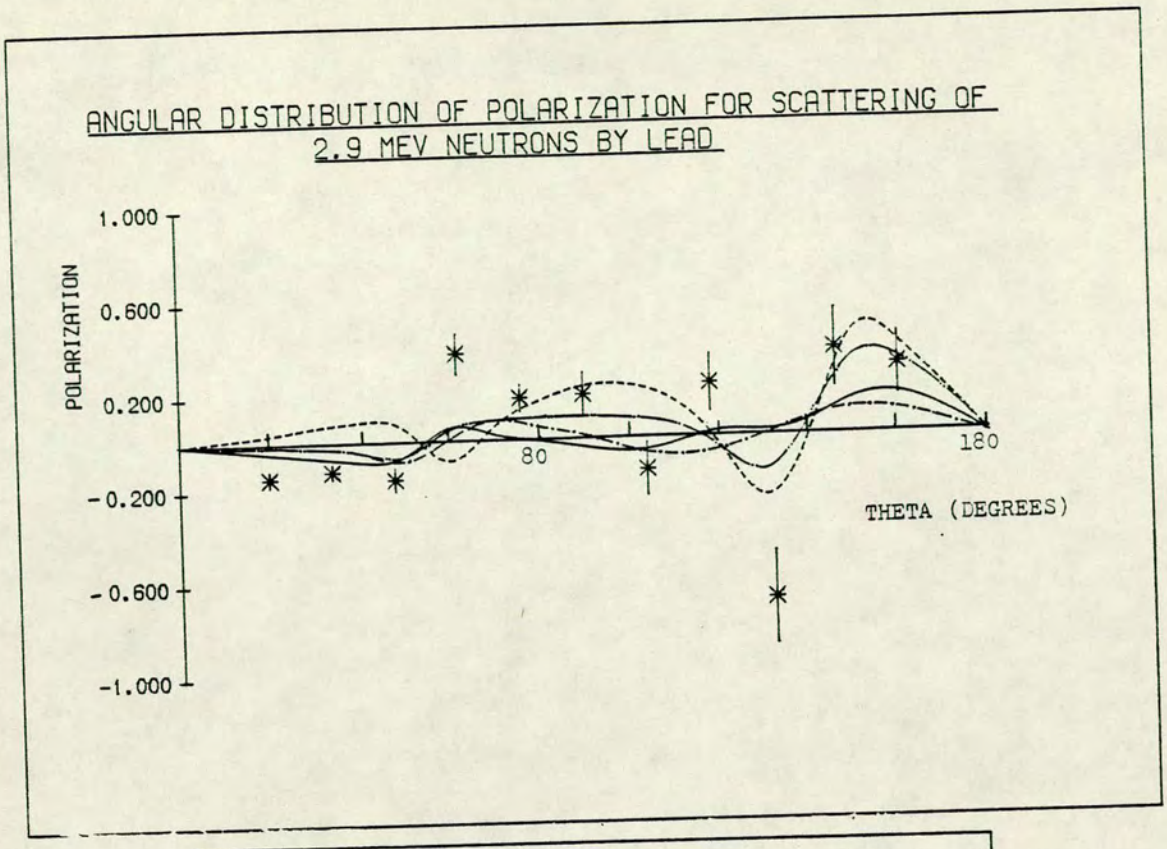
ANGULAR DISTRIBUTION OF POLARIZATION FOR SCATTERING OF 2.9 MEV NEUTRONS BY LEAD
POLARIZATION
1.000
0.600
0.200
-0.200
-0.600
-1.000
80
180
THETA (DEGREES)

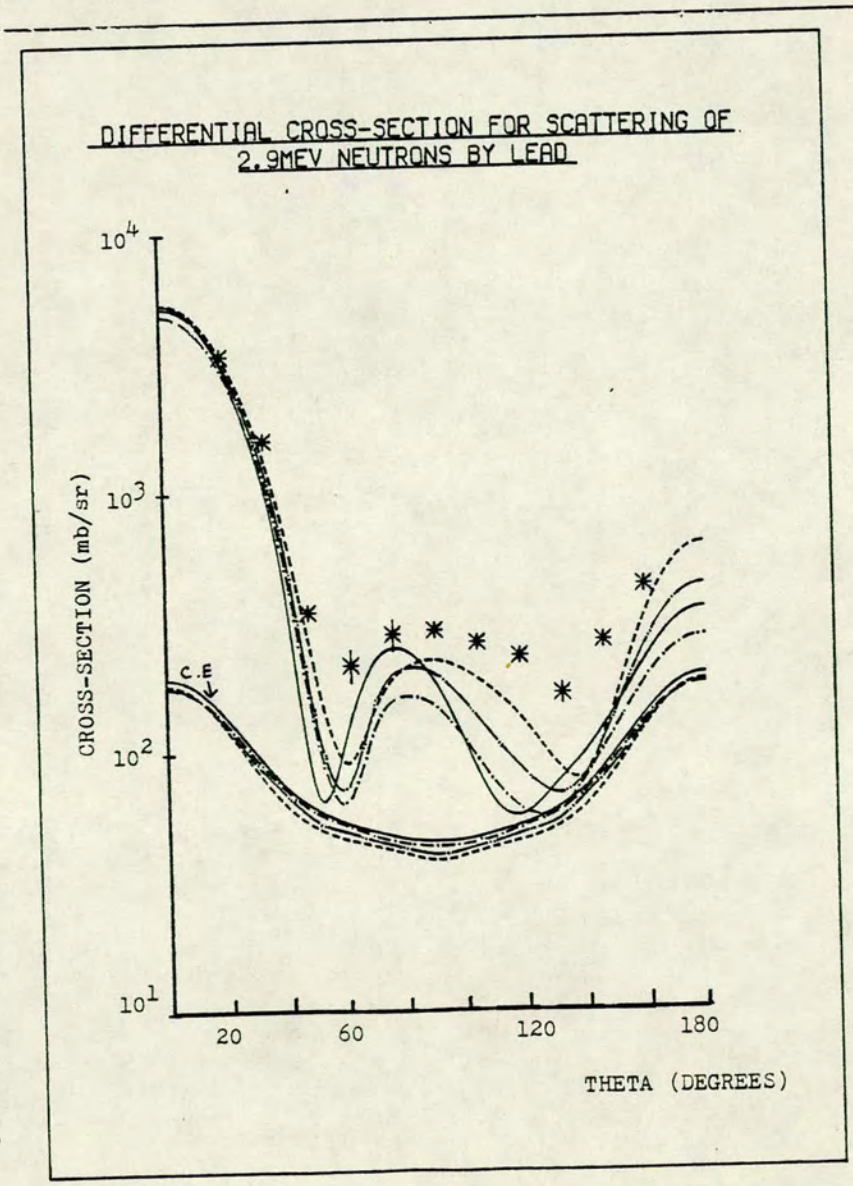
DIFFERENTIAL CROSS-SECTION FOR SCATTERING OF 2.9MEV NEUTRONS BY LEAD
CROSS-SECTION (mb/sr)
10^4
10^3
10^2
10^1
C.E
20
60
120
180
THETA (DEGREES)

Fig. 6.10

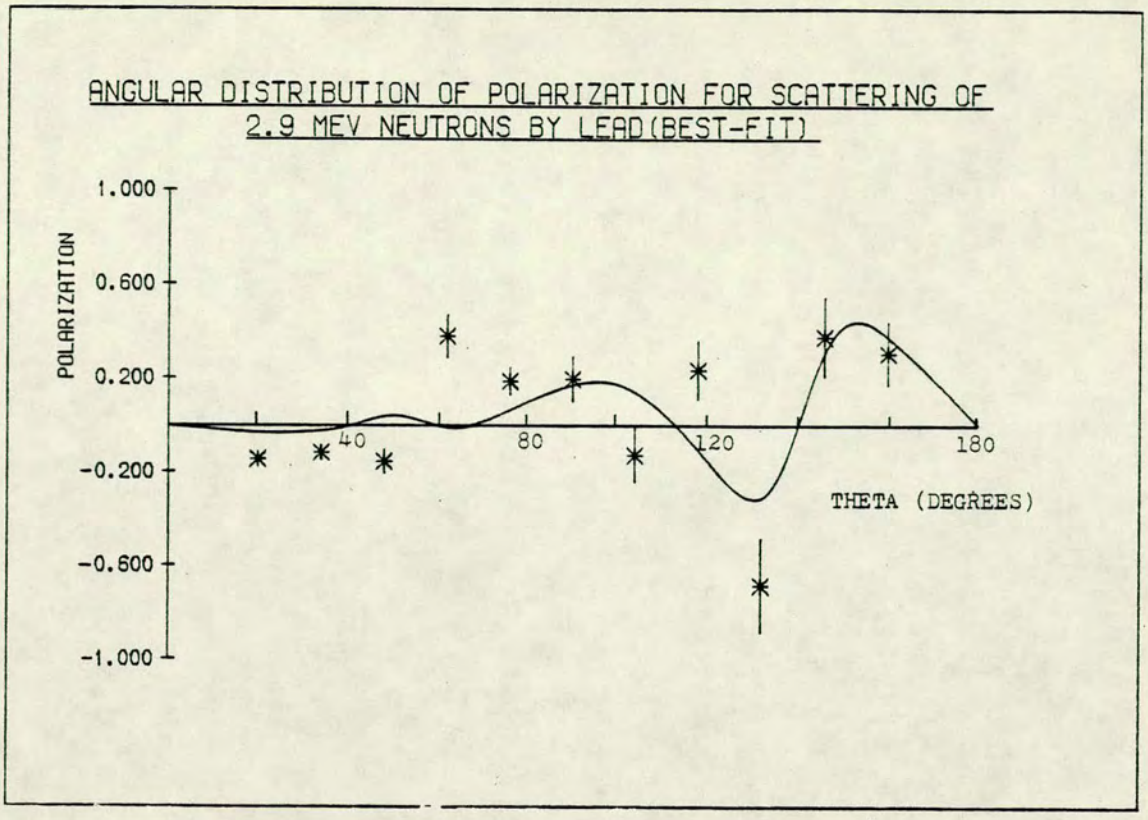
ANGULAR DISTRIBUTION OF POLARIZATION FOR SCATTERING OF 2.9 MEV NEUTRONS BY LEAD(BEST-FIT)
POLARIZATION
1.000
0.600
0.200
-0.200
-0.600
-1.000
40
80
120
180
THETA (DEGREES)

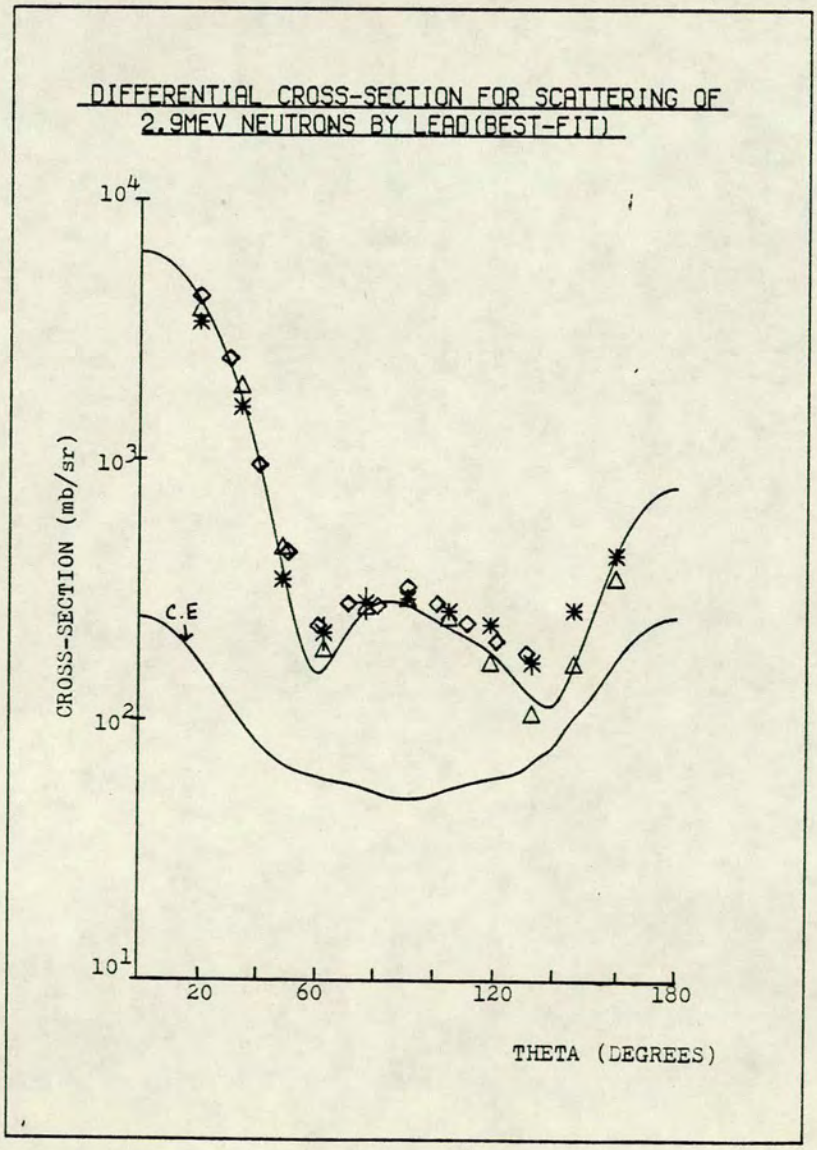
DIFFERENTIAL CROSS-SECTION FOR SCATTERING OF 2.9MEV NEUTRONS BY LEAD(BEST-FIT)
CROSS-SECTION (mb/sr)
10^4
10^3
10^2
10^1
C.E
20
60
120
180
THETA (DEGREES)

Fig. 6.11

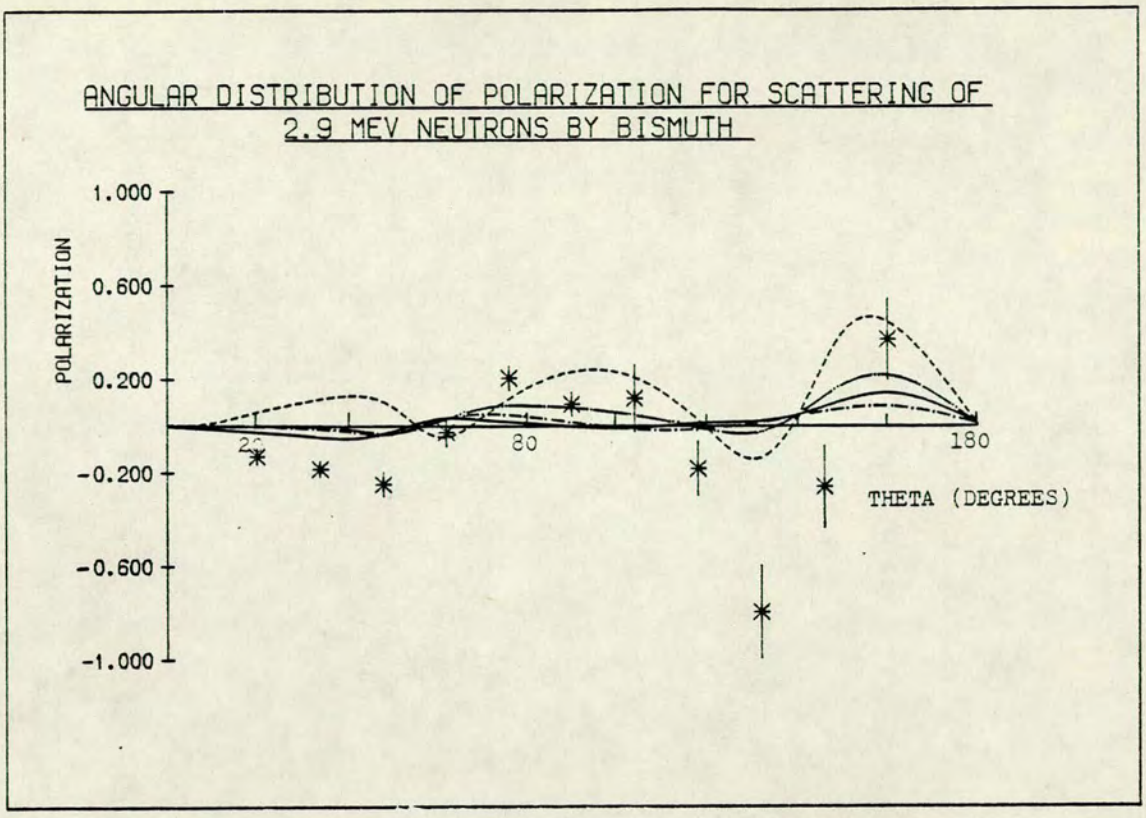
ANGULAR DISTRIBUTION OF POLARIZATION FOR SCATTERING OF 2.9 MEV NEUTRONS BY BISMUTH
POLARIZATION
1.000
0.600
0.200
-0.200
-0.600
-1.000
80
180
THETA (DEGREES)

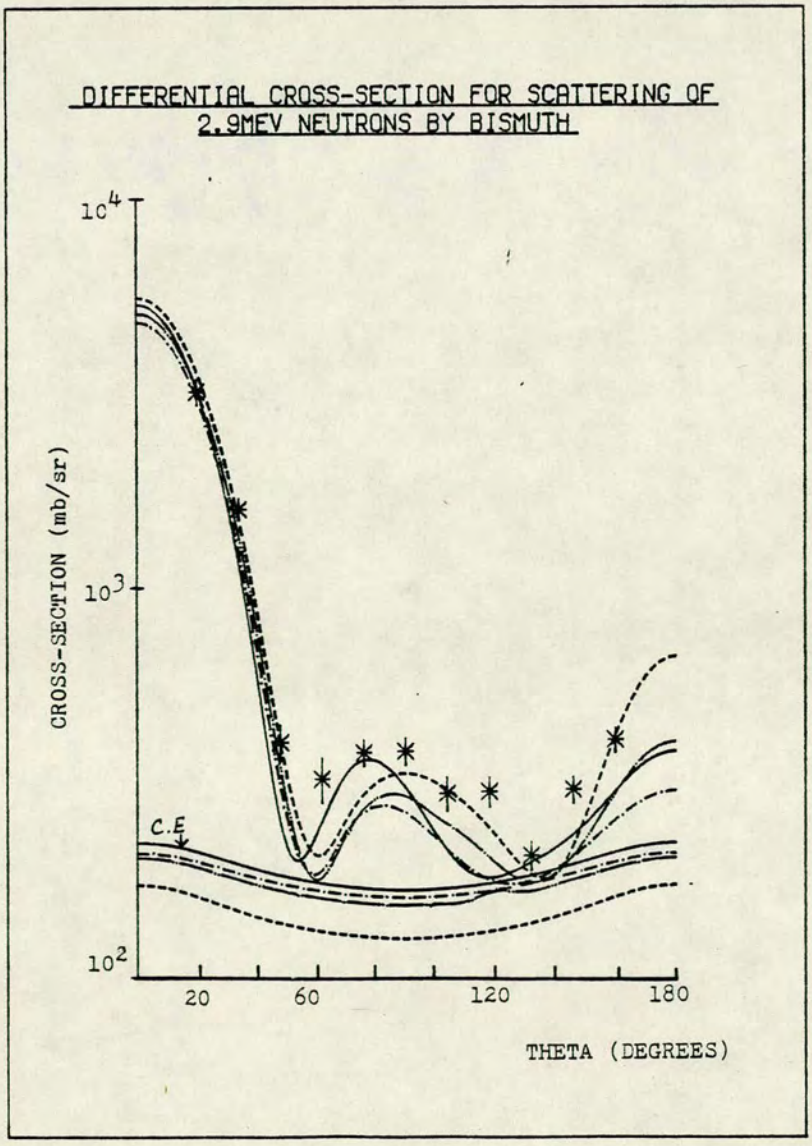
DIFFERENTIAL CROSS-SECTION FOR SCATTERING OF 2.9MEV NEUTRONS BY BISMUTH
CROSS-SECTION (mb/sr)
10^4
10^3
10^2
C.E
20
60
120
180
THETA (DEGREES)

Fig 6.12

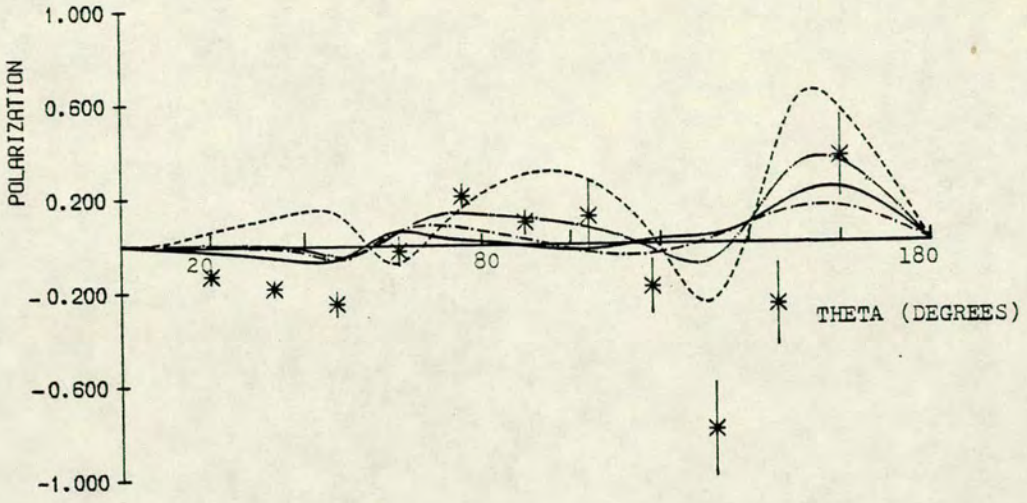

Figure 6.

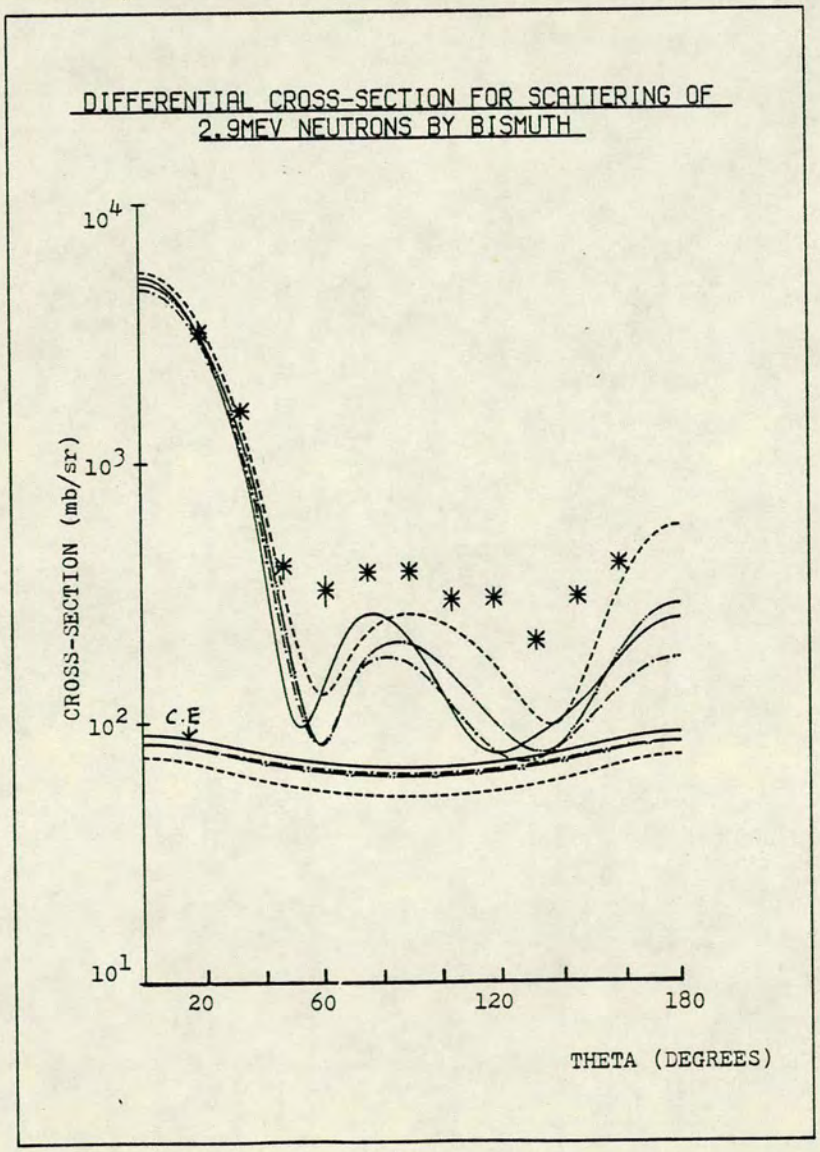

Fig. 6.13

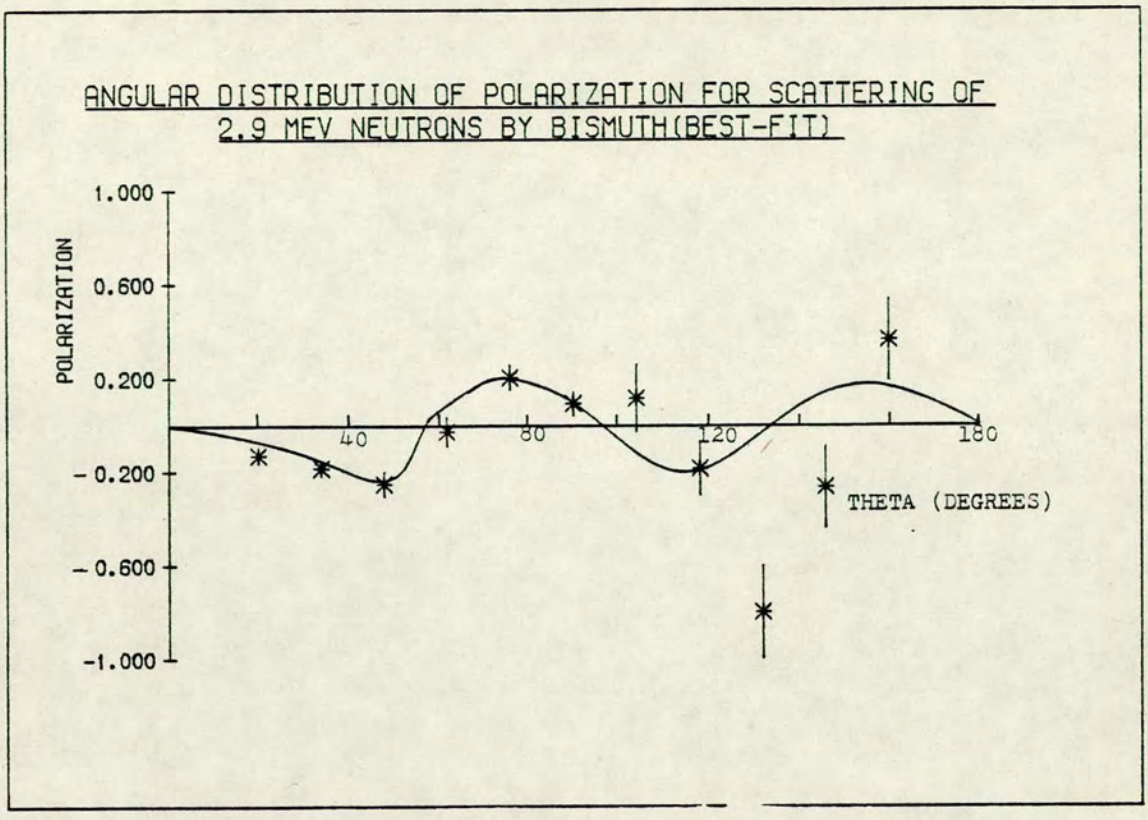
ANGULAR DISTRIBUTION OF POLARIZATION FOR SCATTERING OF
2.9 MEV NEUTRONS BY BISMUTH(BEST-FIT)
POLARIZATION
1.000
0.600
0.200
- 0.200
- 0.600
-1.000
40
80
120
180
THETA (DEGREES)

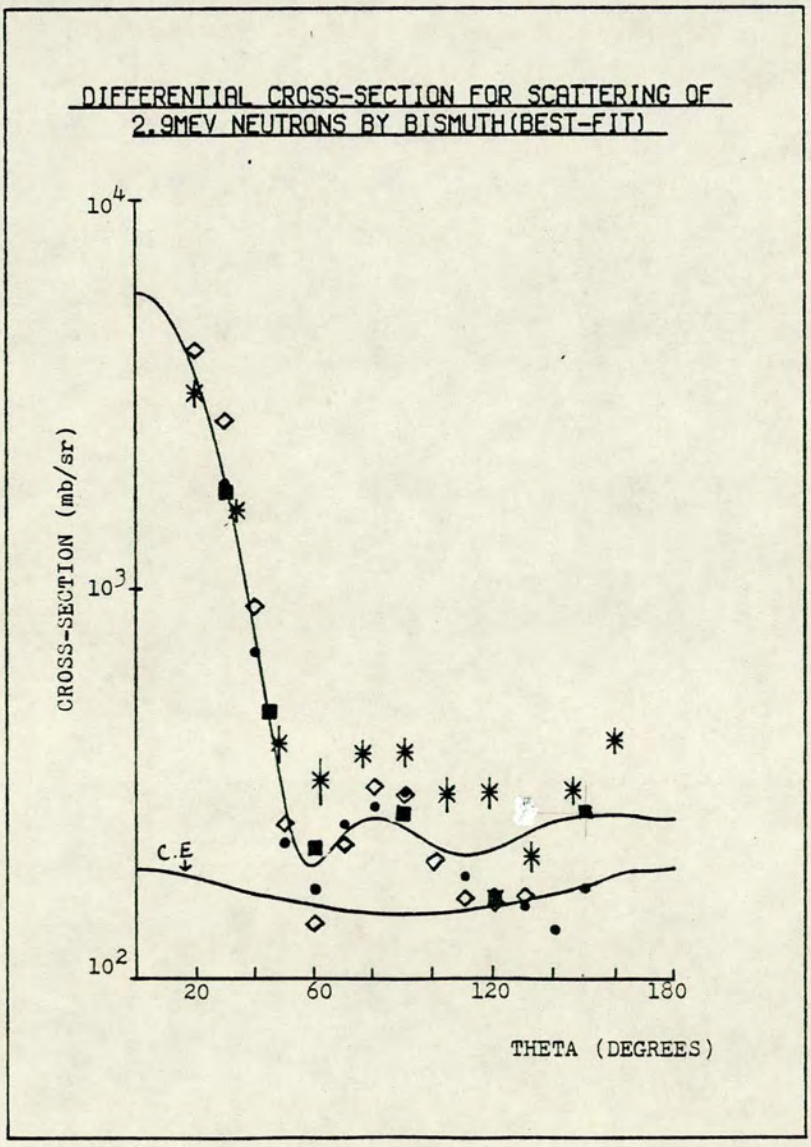
DIFFERENTIAL CROSS-SECTION FOR SCATTERING OF
2.9MEV NEUTRONS BY BISMUTH(BEST-FIT)
CROSS-SECTION (mb/sr)
10^4
10^3
10^2
C.E
20
60
120
180
THETA (DEGREES)

Fig. 6.14

correction are illustrated in Figs 6.12 and 6.13. Comparison of these two sets of figures leads to the same conclusion that, as far as the cross-section is concerned, inclusion of the MLF correction gives significantly closer agreement between calculation and experiment, while the polarization is not particularly well fitted by any calculation.

The optimum fitting to the Bi data that comprised of the present cross-section and polarization values and the cross-section data of Becker et al.[78], Popov[79] and Tanaka et al.[80] can be considered with reference to Fig. 6.14. The best fit parameters listed in Table 6.2 for Bi also resulted from the input data that included the Hauser-Feshbach compound nucleus contribution with the MLF correction factor. Because of the large scatter in the different experimental data on cross-section, very close agreement to any set of the data could not be expected. Unlike the case of Pb the polarization is quite well fitted up to about 120^{o}. The best fit parameter set has a notably large magnitude for the spin orbit potential.

URANIUM:- For the case of uranium, since the data could not be corrected for some inelastic contributions (two levels, Table 3.2), the comparison of the measured cross-sections and polarizations with calculation is carried out in the same way as for the case of tungsten, using calculated inelastic cross-sections. The calculations based on the global parameters of Rosen et al.[38] and Becchetti and Greenlees[39] are illustrated in Fig. 6.15 with the MLF correction included in the Hauser-Feshbach calculation, while those without the MLF components are shown in Fig. 6.16. Both the figures show a very similar fit to the differential cross-section and polarization data. However the overall agreement is not very close between the experiment and the calculation made with the two sets of parameters.

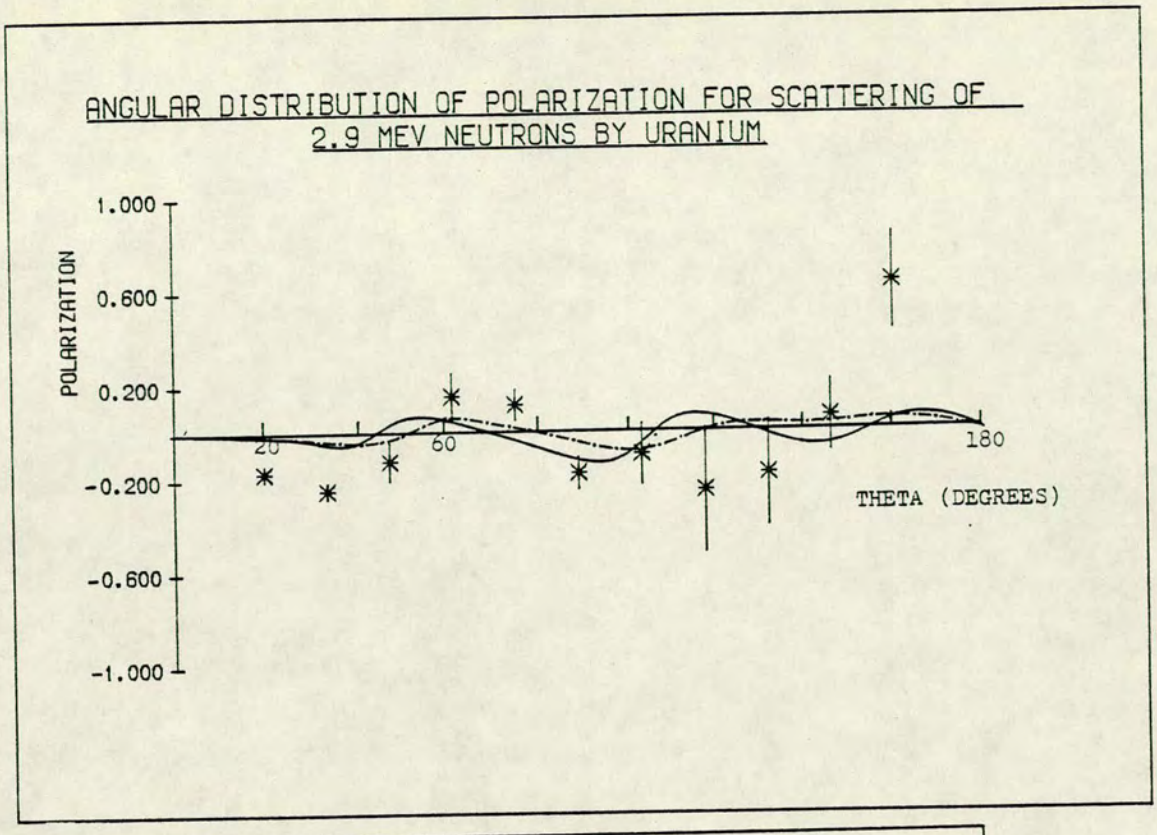
ANGULAR DISTRIBUTION OF POLARIZATION FOR SCATTERING OF 2.9 MEV NEUTRONS BY URANIUM
POLARIZATION
1.000
0.600
0.200
-0.200
-0.600
-1.000
20
60
180
THETA (DEGREES)

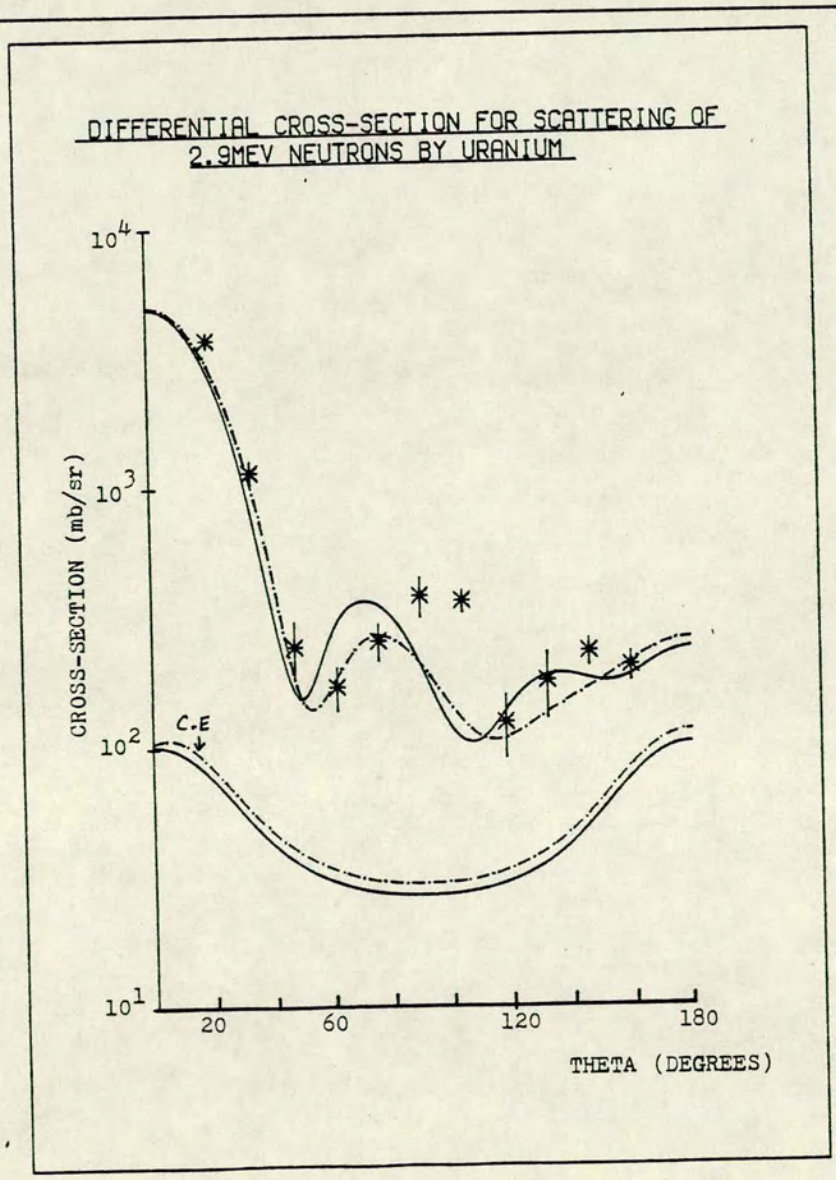
DIFFERENTIAL CROSS-SECTION FOR SCATTERING OF 2.9MEV NEUTRONS BY URANIUM
CROSS-SECTION (mb/sr)
10^4
10^3
10^2
10^1
C.E
20
60
120
180
THETA (DEGREES)

Fig. 6.15

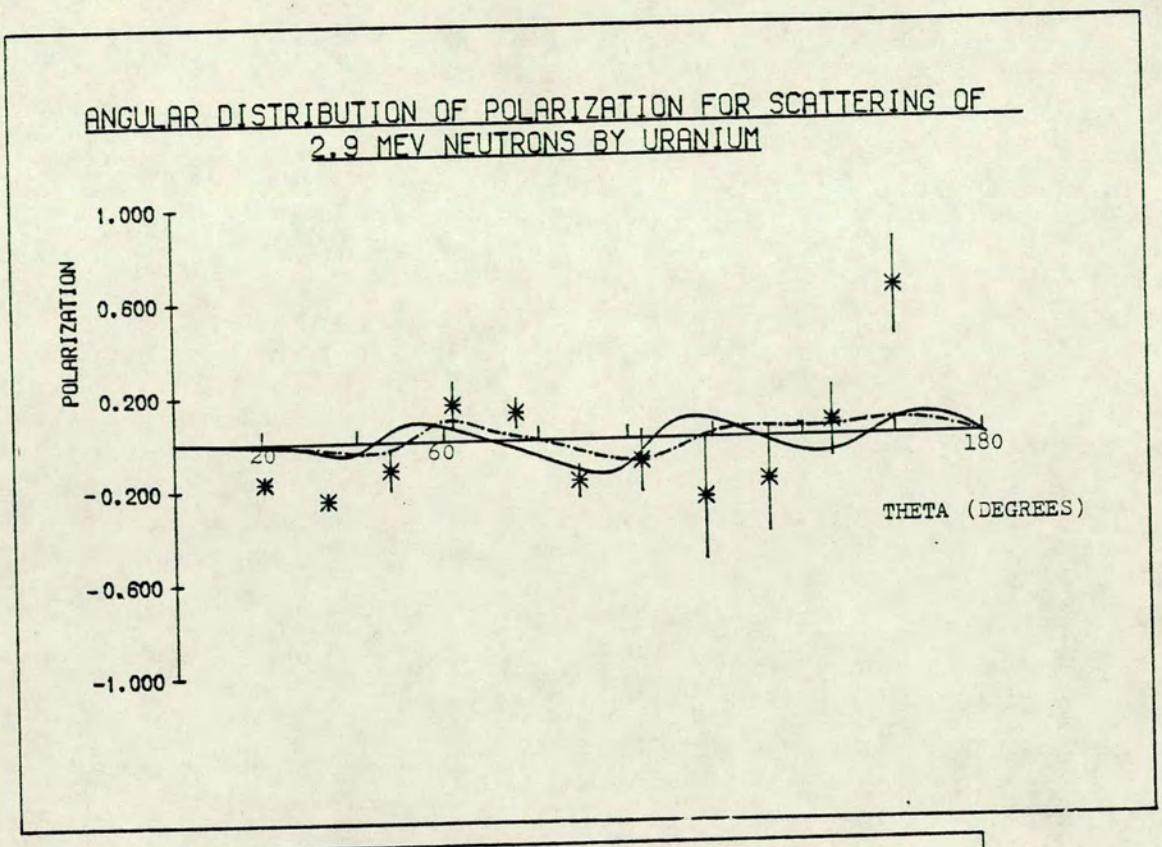
ANGULAR DISTRIBUTION OF POLARIZATION FOR SCATTERING OF 2.9 MEV NEUTRONS BY URANIUM
POLARIZATION
1.000
0.600
0.200
-0.200
-0.600
-1.000
20
60
180
THETA (DEGREES)

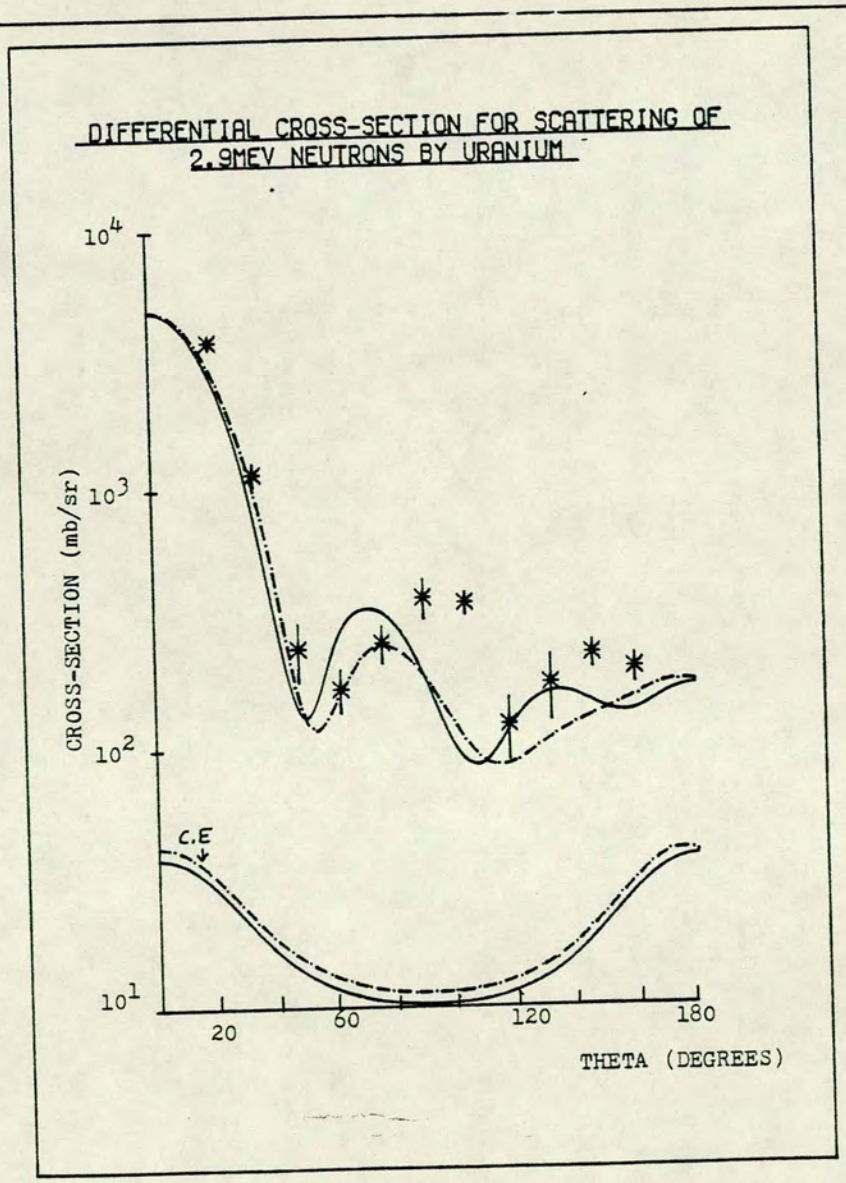
DIFFERENTIAL CROSS-SECTION FOR SCATTERING OF 2.9MEV NEUTRONS BY URANIUM
CROSS-SECTION (mb/sr)
10^4
10^3
10^2
10^1
C.E
20
60
120
180
THETA (DEGREES)

Fig. 6.16

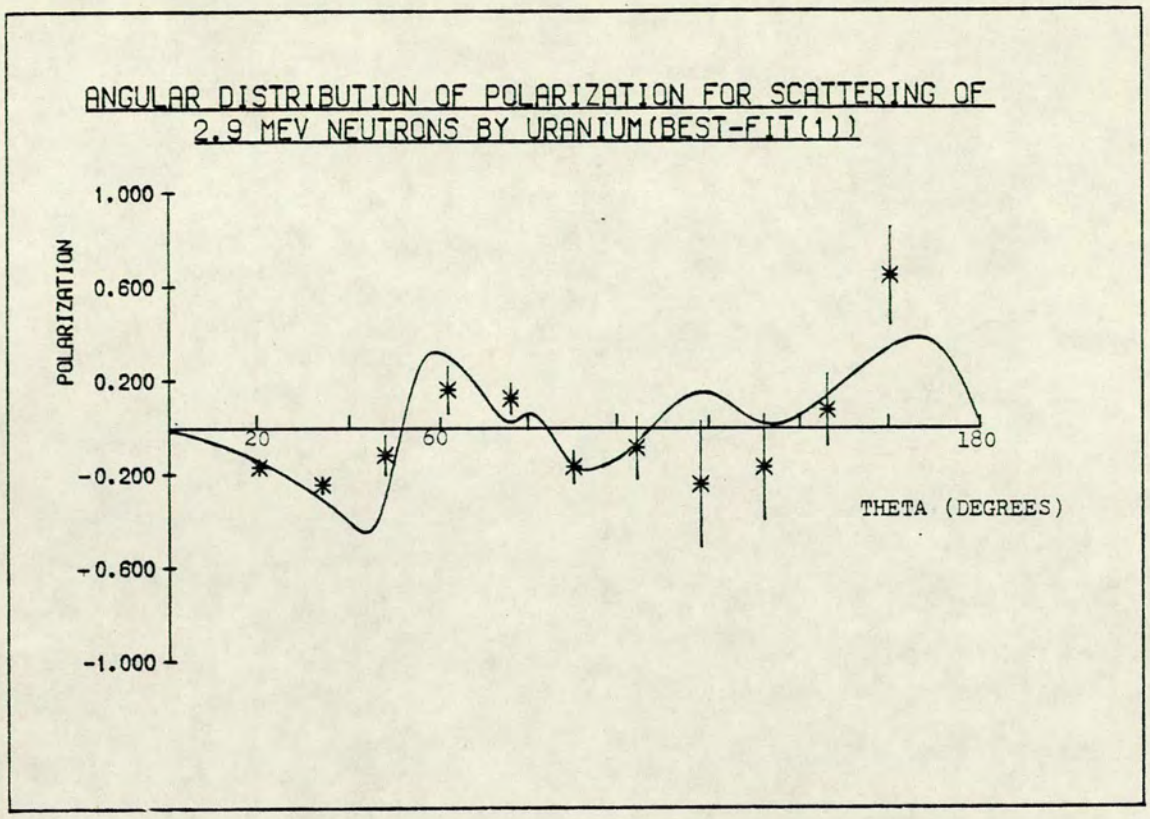
ANGULAR DISTRIBUTION OF POLARIZATION FOR SCATTERING OF
2.9 MEV NEUTRONS BY URANIUM(BEST-FIT(1))
POLARIZATION
1.000
0.600
0.200
-0.200
-0.600
-1.000
20
60
180
THETA (DEGREES)

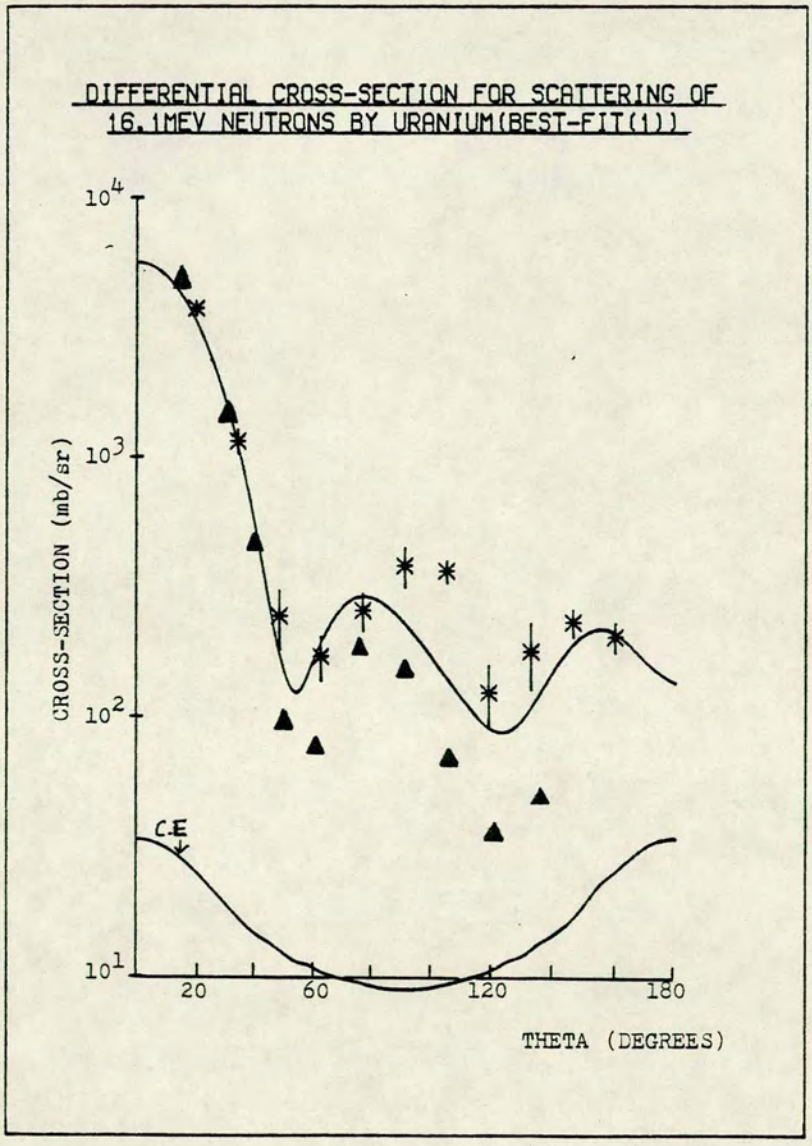
DIFFERENTIAL CROSS-SECTION FOR SCATTERING OF
16.1MEV NEUTRONS BY URANIUM(BEST-FIT(1))
CROSS-SECTION (mb/sr)
10^4
10^3
10^2
10^1
C.E
20
60
120
180
THETA (DEGREES)

Fig. 6.17

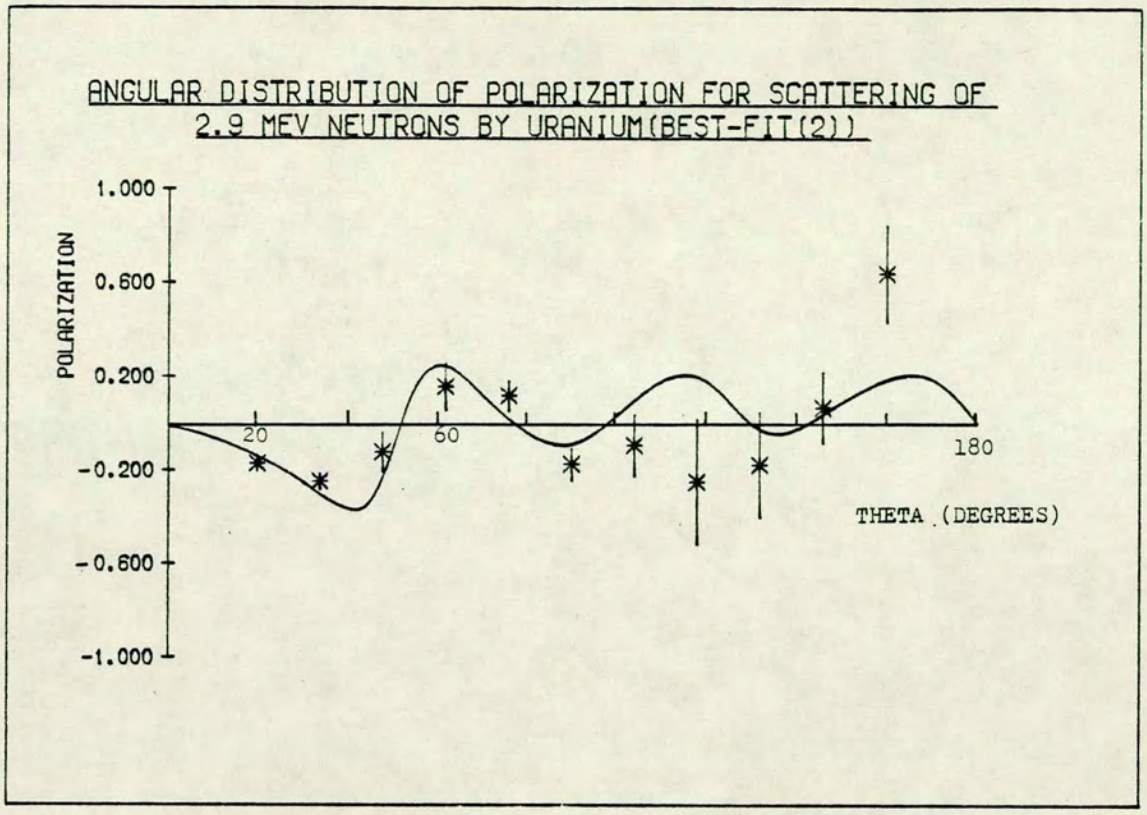
ANGULAR DISTRIBUTION OF POLARIZATION FOR SCATTERING OF 2.9 MEV NEUTRONS BY URANIUM(BEST-FIT(2))
POLARIZATION
1.000
0.600
0.200
-0.200
-0.600
-1.000
20
60
180
THETA (DEGREES)

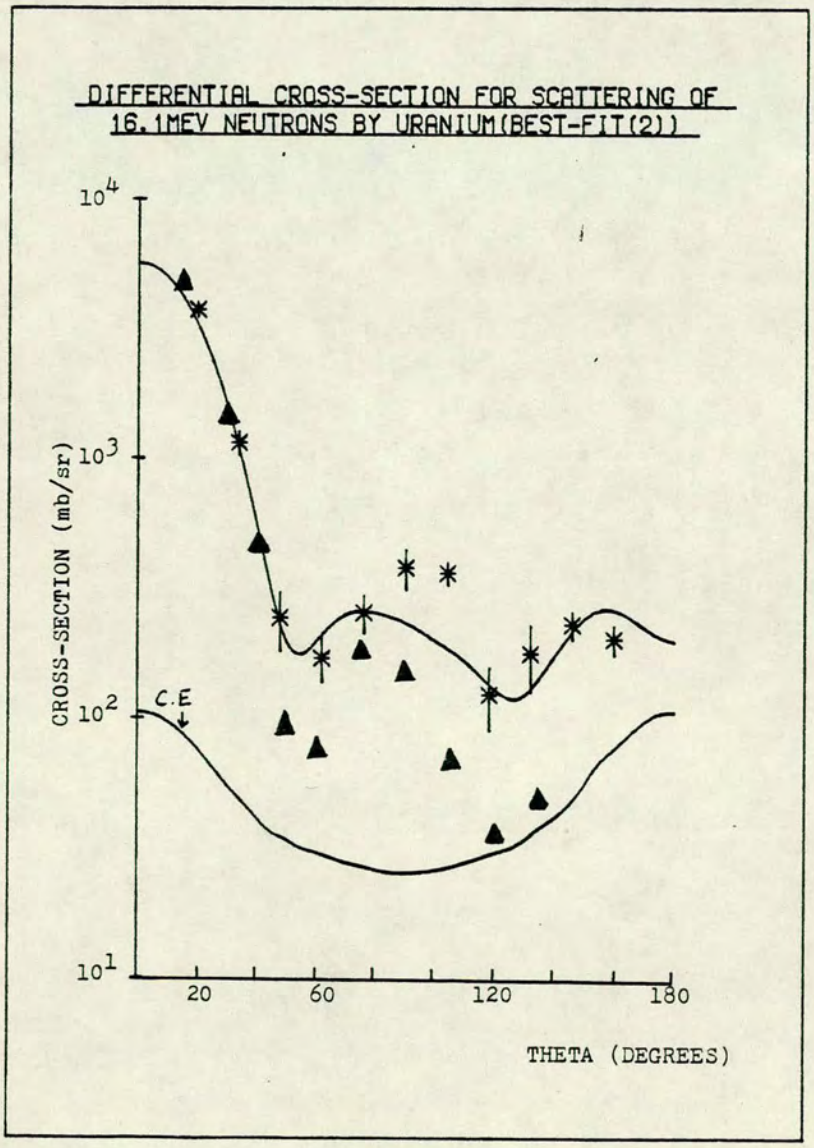
DIFFERENTIAL CROSS-SECTION FOR SCATTERING OF 16.1MEV NEUTRONS BY URANIUM(BEST-FIT(2))
CROSS-SECTION (mb/sr)
10^4
10^3
10^2
10^1
C.E
20
60
120
180
THETA (DEGREES)

Fig. 6.18

Nuclide	V_R MeV	R_R fm	A_R fm	W_S MeV	R_W fm	A_W fm	V_S MeV	R_S fm	A_S fm	JV/A	JW/A	JS/A	$\chi^2(\sigma)$	$\chi^2(P)$	$\chi^2(T)$
										MeV.fm^3					
Fe	57.36	1.15	0.57	7.03	1.15	0.60	3.84	1.01	0.75	426	77	6.7	—	—	—
W(1)	53.72	1.11	0.70	3.28	1.72	0.38	12.39	1.24	0.27	346	32	11.8	1.69	1.44	1.60
W(2)	46.93	1.23	0.57	2.84	1.51	0.67	12.22	1.21	0.14	385	39	11.4	2.71	2.28	2.57
Tℓ	43.94	1.25	0.75	5.99	1.23	0.50	16.16	1.30	0.30	393	39	15.1	7.01	2.52	5.68
Pb	41.61	1.34	0.58	8.91	1.36	0.14	7.78	1.31	0.26	435	20	7.35	5.23	15.23	8.66
Bi	51.07	1.13	0.52	10.85	1.52	0.27	22.99	1.01	0.75	328	57	16.4	5.34	5.37	5.35
U(1)	43.33	1.27	0.68	8.03	1.13	0.48	21.09	1.14	0.51	393	40	16.3	2.94	2.27	2.71
U(2)	42.52	1.26	0.85	10.93	1.27	0.34	22.59	1.16	0.55	392	49	17.0	3.22	1.95	2.78

Table 6.2. Optimum values of the optical potential parameters for 2.9 MeV neutrons.

Search for the optimum parameters comprised of the present cross-section and polarization data that included the calculated inelastic contribution and the cross-section data of Batchelor et al.[81]. Unlike the previous cases of Tℓ, Bi and Pb it was observed that a similar fit to the data resulted from similar combinations of parameters for the compound elastic contribution adjusted both with and without the MLF correction. The set of parameters listed in Table 6.2 as U(1) is from the search on data combined with compound nucleus contribution including the MLF correction, whereas the set U(2) resulted from the search on data that did not include the MLF correction. The corresponding best fit curves are illustrated in Figs. 6.17 and 6.18. Both sets of parameters have a large magnitude for the spin orbit potential, as in the case of Bismuth. Set U(1) may be preferred on the grounds that this set gives equally good fit to both polarization and cross-section while set U(2) gives a poorer fit to the polarization and also has a notably large value for A_R.

6.4.3 Optical model fitting at 16 MeV

The optical model fitting of the data at 16 MeV is much simpler since there is no need to allow for the compound elastic contribution. The calculations based on the Becchetti and Greenlees[39] parameters in this case include a volume imaginary term (Table 6.1). The results of the parameter search therefore fall into two categories, those done with the Becchetti and Greenlees parameters as starting values and therefore including the volume imaginary term and those which do not include the volume imaginary term. Thus the discussion of the optimum search for this case will be with emphasis on the importance of including the volume imaginary term for each nuclei. All the calculations in this case have been smeared over the $\pm 6^{\circ}$ spread in the scattering angle of the experimental system.

IRON:- The calculated distribution of polarization and cross-section for iron using the global potentials of Rosen et al.[38] and Becchetti and Greenlees[39] are compared with the experimental results in Fig. 6.19. It is clear from the figure that for both polarization and cross-section distributions, the calculations based on Rosen et al.[38] parameters give closer agreement to the data. However the polarization at 20^{o} has the least agreement between the calculation and the measured value.

The result of the search for optimum parameters for Fe are listed in Table 6.3, which does not include the volume imaginary term and the optimum fit is illustrated in Fig. 6.20. It was observed that the optimum parameter set that included the volume imaginary term led to W_V = 0.19 MeV with the other parameters closely similar to those listed in Table 6.3 and gives a fit to the data indistinguishable from that shown in Fig. 6.20.

COPPER:- Fig. 6.21 illustrates the optical model calculation done with the global parameters of Rosen et al.[38] and Becchetti and Greenlees[39] for the distributions of polarization and cross-section for Cu along with the present experimental results. Comparison of the calculation with experiment leads to the same conclusion as for the case of Fe, i.e. better agreement with calculations based on Rosen parameters for both cross-section and polarization as well as the poor agreement for polarization around 20^{o}.

The best parameter set obtained for Cu listed in Table 6.3 also does not include a volume imaginary term. The optimum search that included the volume imaginary term lead to W_V = 0.93 MeV and resulted in a slightly poorer fit than the fit illustrated in Fig. 6.22 without W_V.

IODINE:- Comparison of the optical model calculations based on the

Key to symbols used in Fig 6.19--Fig 6.33

* - Present measurements.

The curves used in the figures for comparison of experimental measurements with calculations based on optical model parameterisation of different authors are:

———— Rosen et al.[38)]

– – – – – Becchetti & Greenlees.[39)]

—··—··— Fu & Perey.[41)]

–·–·–·–·– Haouat et al.[88)]

The solid curve in the BEST-FIT figures represents the calculated distributions obtained with the optimum parameters presented in table 6.3.

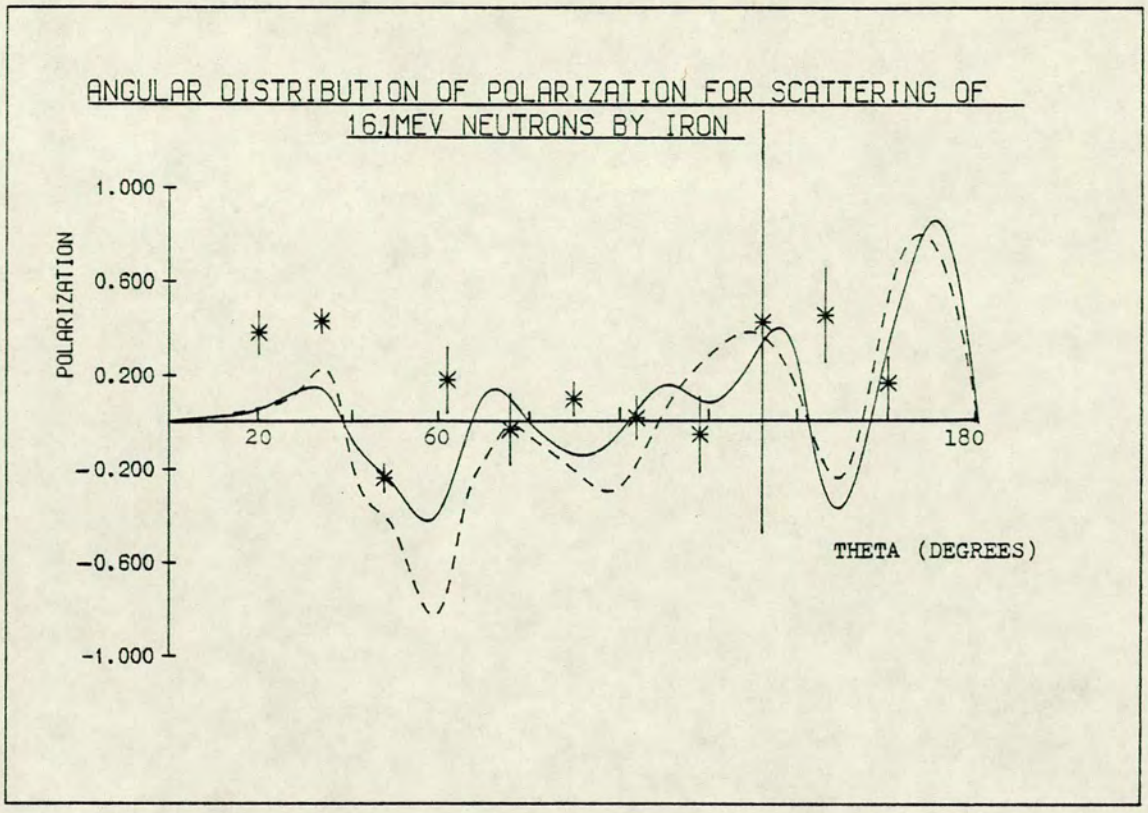
ANGULAR DISTRIBUTION OF POLARIZATION FOR SCATTERING OF
16.1MEV NEUTRONS BY IRON
POLARIZATION
1.000
0.600
0.200
-0.200
-0.600
-1.000
20
60
180
THETA (DEGREES)

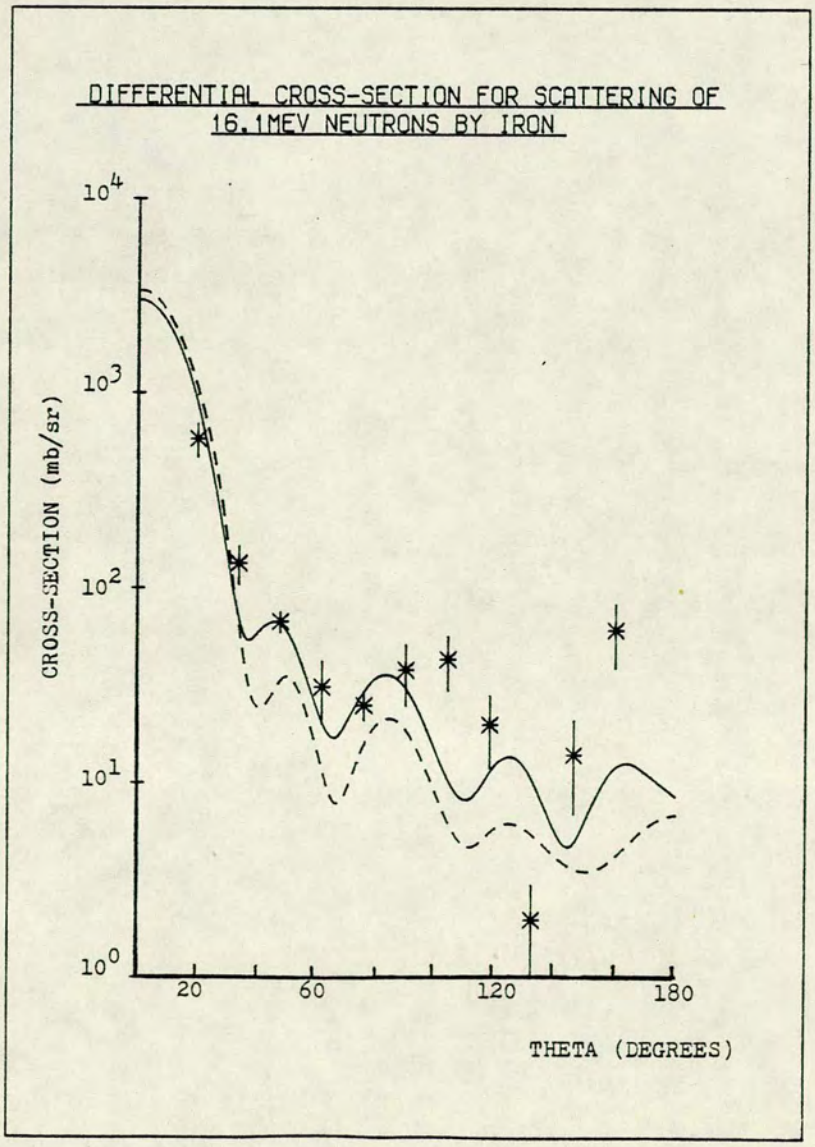
DIFFERENTIAL CROSS-SECTION FOR SCATTERING OF
16.1MEV NEUTRONS BY IRON
CROSS-SECTION (mb/sr)
10^4
10^3
10^2
10^1
10^0
20
60
120
180
THETA (DEGREES)

Fig. 6.19

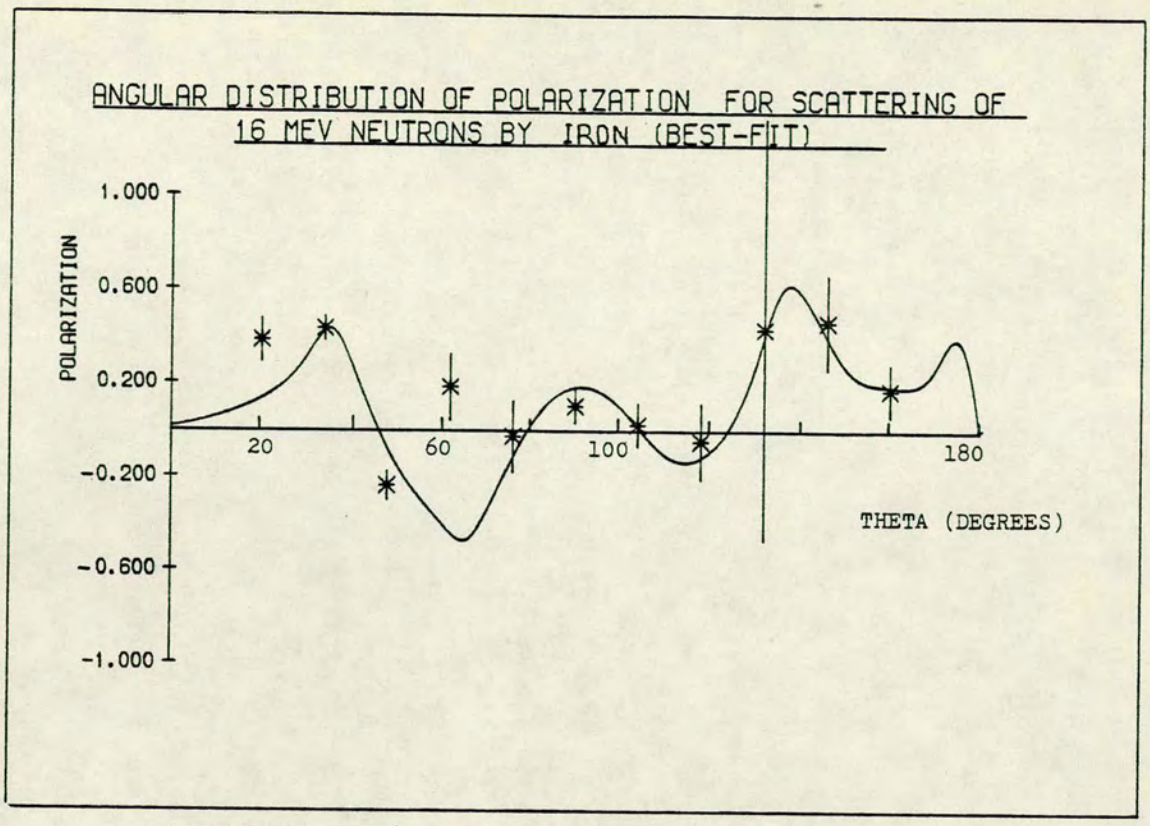
ANGULAR DISTRIBUTION OF POLARIZATION FOR SCATTERING OF
16 MEV NEUTRONS BY IRON (BEST-FIT)
POLARIZATION
1.000
0.600
0.200
-0.200
-0.600
-1.000
20
60
100
180
THETA (DEGREES)

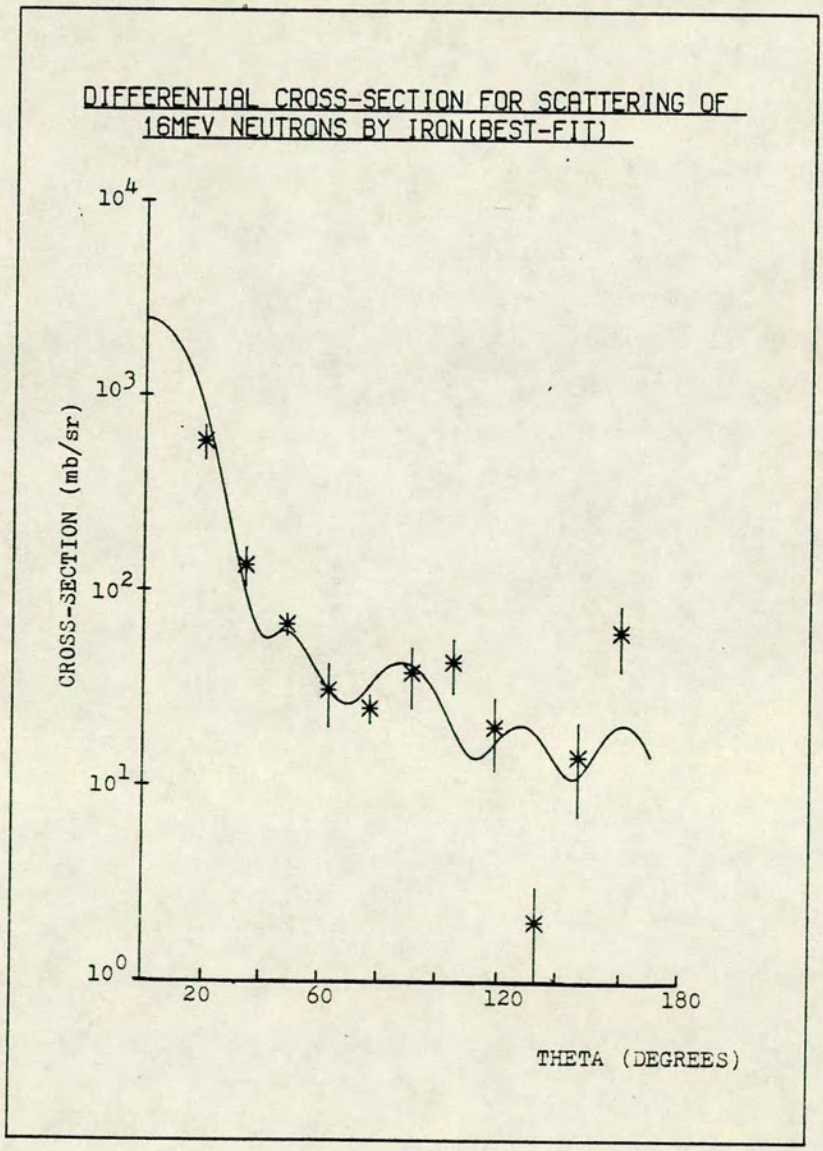
DIFFERENTIAL CROSS-SECTION FOR SCATTERING OF
16MEV NEUTRONS BY IRON(BEST-FIT)
CROSS-SECTION (mb/sr)
10^4
10^3
10^2
10^1
10^0
20
60
120
180
THETA (DEGREES)

Fig. 6.20

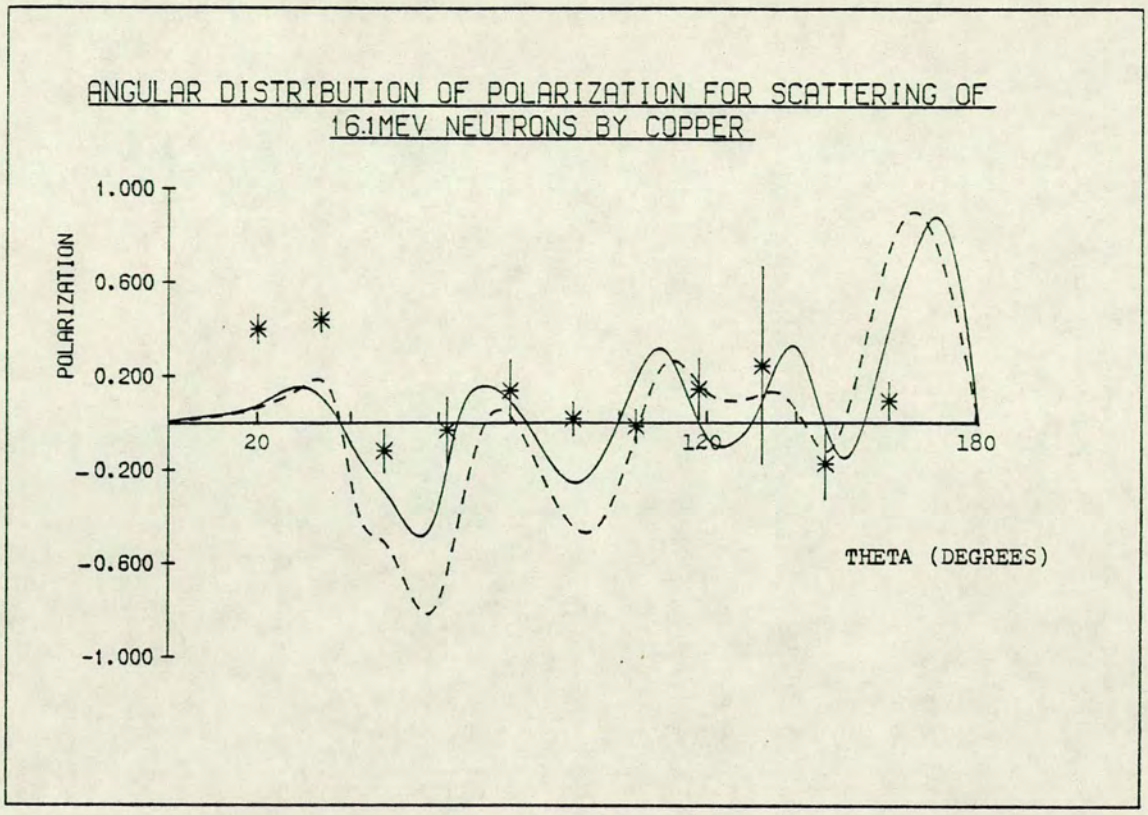
ANGULAR DISTRIBUTION OF POLARIZATION FOR SCATTERING OF 16.1MEV NEUTRONS BY COPPER
POLARIZATION
1.000
0.600
0.200
-0.200
-0.600
-1.000
20
120
180
THETA (DEGREES)

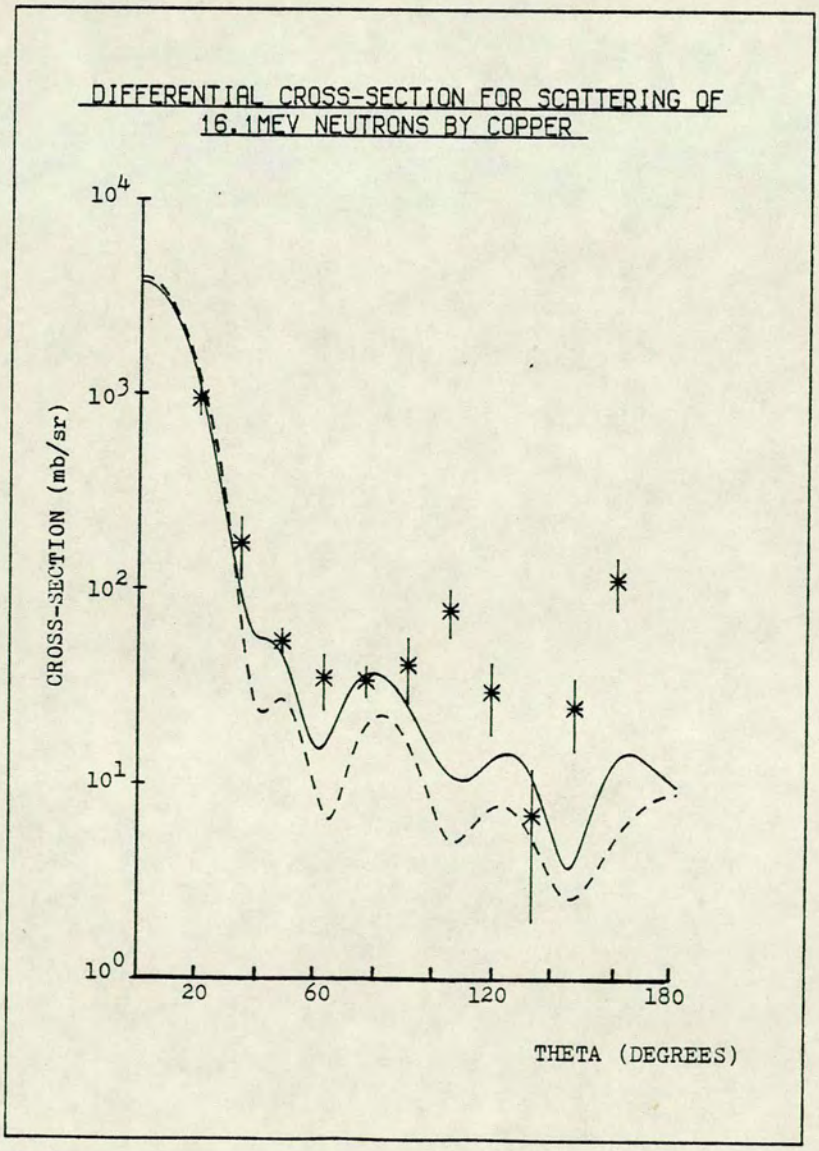
DIFFERENTIAL CROSS-SECTION FOR SCATTERING OF 16.1MEV NEUTRONS BY COPPER
CROSS-SECTION (mb/sr)
10^4
10^3
10^2
10^1
10^0
20
60
120
180
THETA (DEGREES)

Fig. 6.21

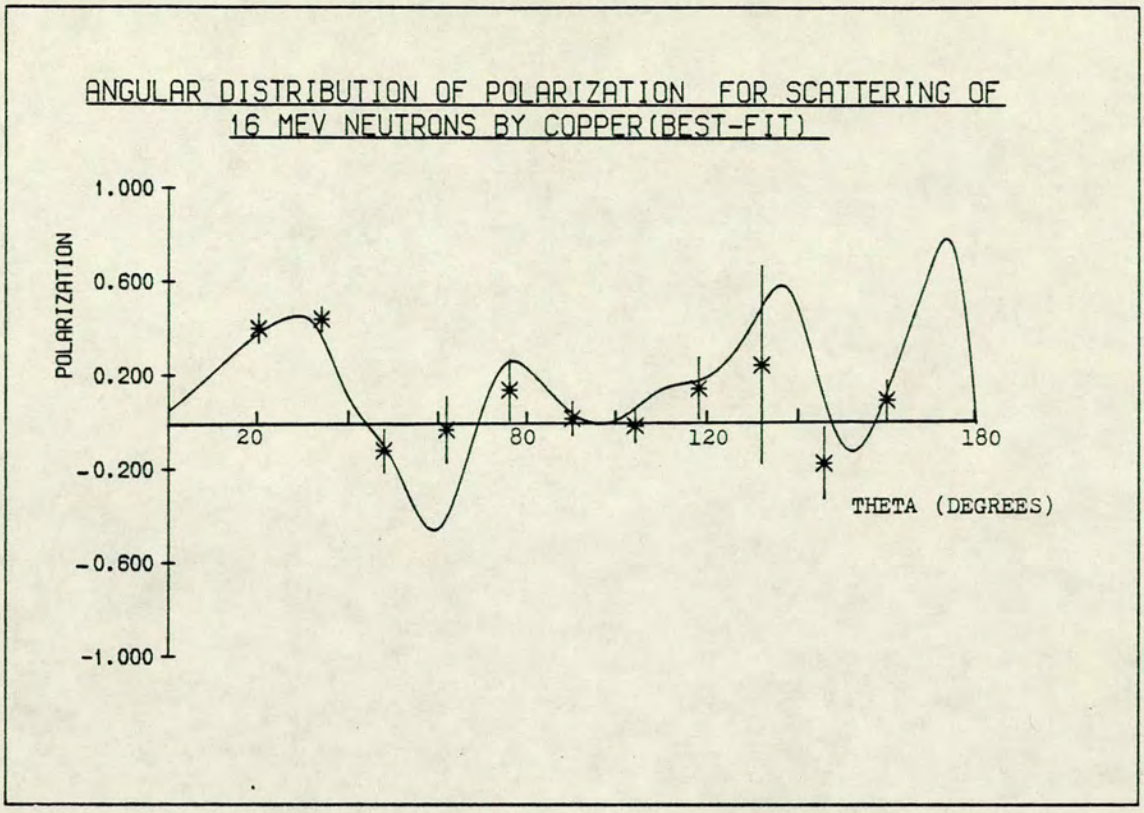
ANGULAR DISTRIBUTION OF POLARIZATION FOR SCATTERING OF 16 MEV NEUTRONS BY COPPER(BEST-FIT)
POLARIZATION
1.000
0.600
0.200
-0.200
-0.600
-1.000
20
80
120
180
THETA (DEGREES)

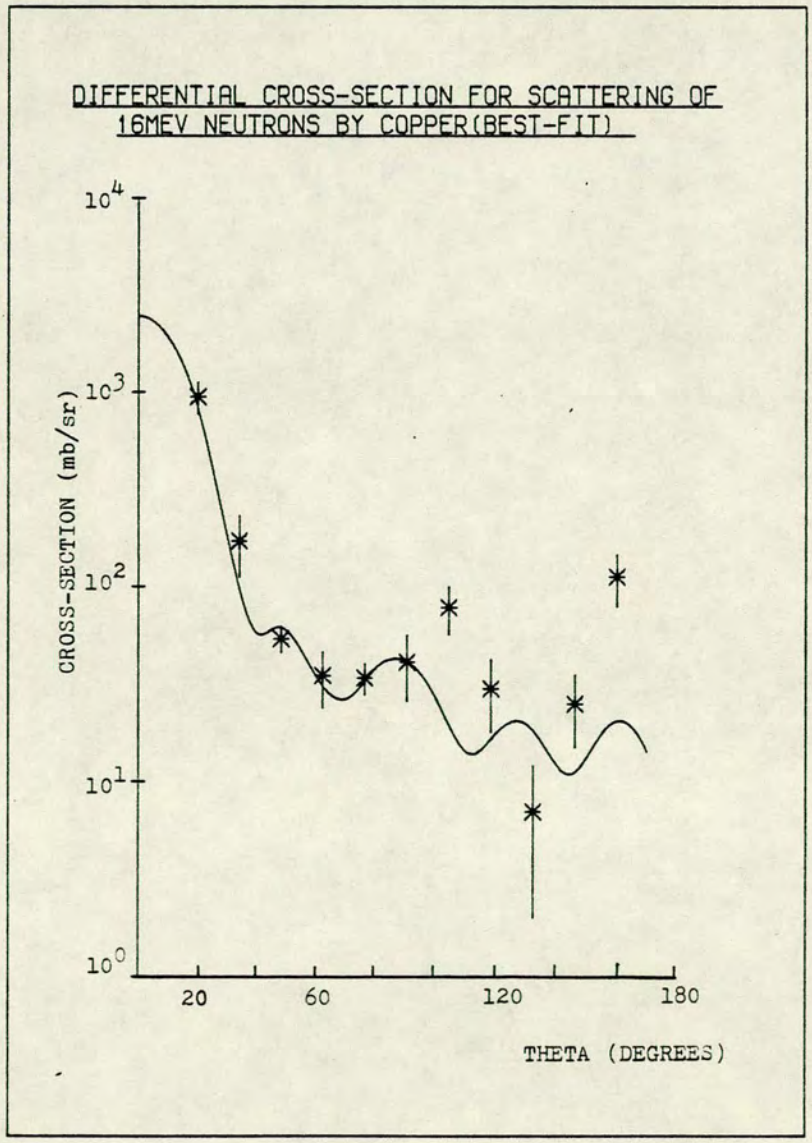
DIFFERENTIAL CROSS-SECTION FOR SCATTERING OF 16MEV NEUTRONS BY COPPER(BEST-FIT)
CROSS-SECTION (mb/sr)
10^4
10^3
10^2
10^1
10^0
20
60
120
180
THETA (DEGREES)

Fig. 6.22

global parameters of Rosen et al.[38] and Becchetti and Greenlees[39] in Fig. 6.23 shows that there is little to choose between the parameter sets as far as the polarization is concerned, while, for differential cross-section Rosen et al. parameters give better agreement.

The optimum parameters unlike Cu and Fe include a volume imaginary term listed in Table 6.3, as the best fit without the volume imaginary term underestimates the polarization at 20^{o} by about 50%. The best fit obtained is presented in Fig. 6.24.

TUNGSTEN:- Fig. 6.25 showing the comparison of the optical model calculations done with the 'global' potentials of Rosen et al.[38] and Becchetti and Greenlees[39] with the experimental results reveals that while the Rosen parameters are preferable in relation to the differential cross-sections, none of the parameters fit the polarization very well.

The best fit parameters found for tungsten that include the volume imaginary term, are listed in Table 6.3 and the best fit illustrated in Fig. 6.26. The best fit without the volume imaginary term gives a poorer representation of the polarization around 34^{o}.

MERCURY:- For the case of mercury it is apparent from the comparison of calculation with experiment in Fig. 6.27 that, while neither of the calculations done with the parameters of Rosen et al.[38] and Becchetti and Greenlees[39] are especially good in relation to the polarization data, the parameters of Rosen et al. are again to be preferred for the differential cross-section.

From the results of the search for optimum parameters for Mercury, the situation is not very clear as far as the inclusion of the volume imaginary term is concerned. Thus the best fit parameters found both without and with the volume imaginary term are quoted in Table 6.3

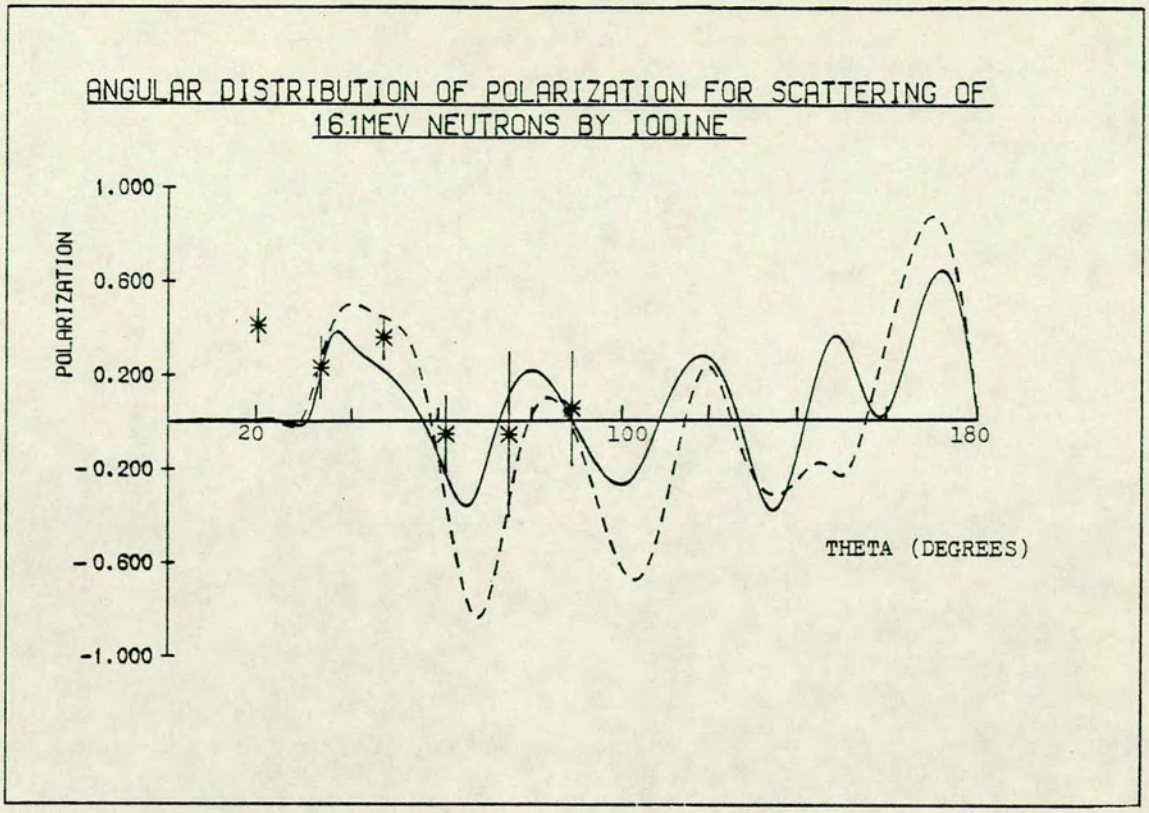
ANGULAR DISTRIBUTION OF POLARIZATION FOR SCATTERING OF 16.1MEV NEUTRONS BY IODINE
POLARIZATION
1.000
0.600
0.200
-0.200
-0.600
-1.000
20
100
180
THETA (DEGREES)

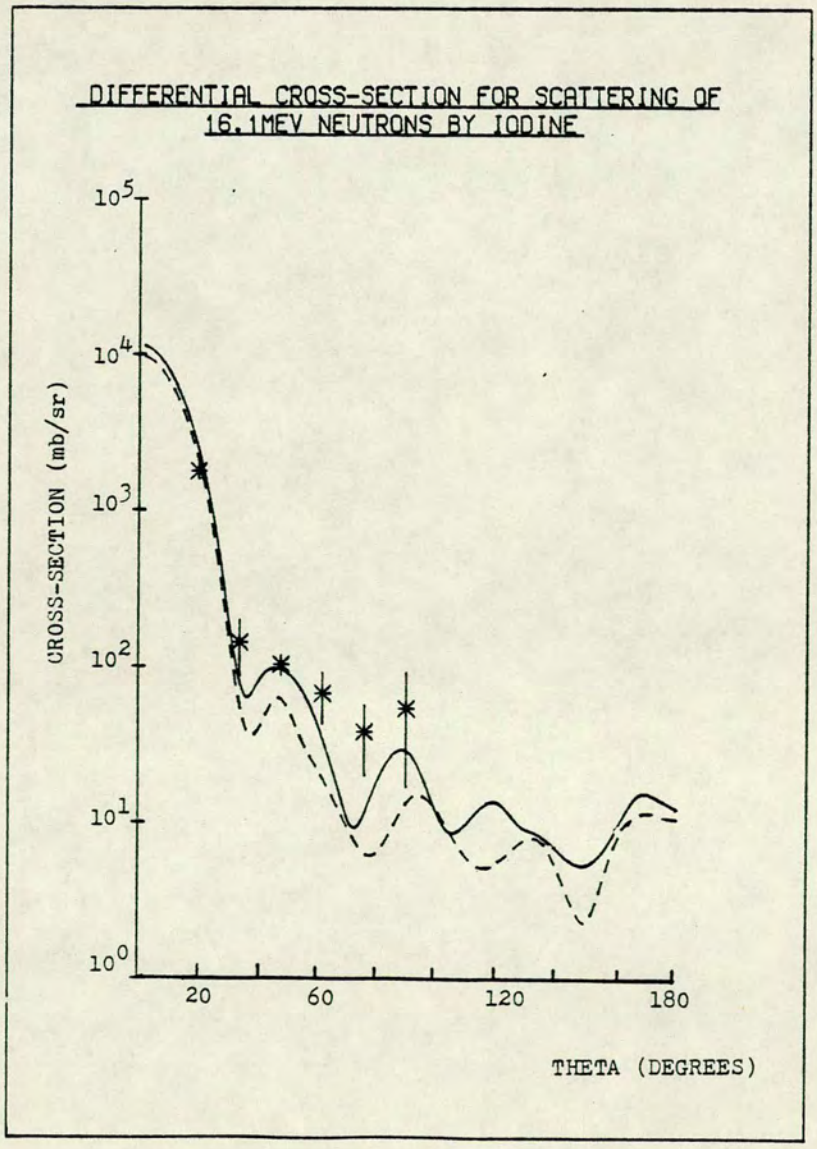
DIFFERENTIAL CROSS-SECTION FOR SCATTERING OF 16.1MEV NEUTRONS BY IODINE
CROSS-SECTION (mb/sr)
10^5
10^4
10^3
10^2
10^1
10^0
20
60
120
180
THETA (DEGREES)

Fig. 6.23

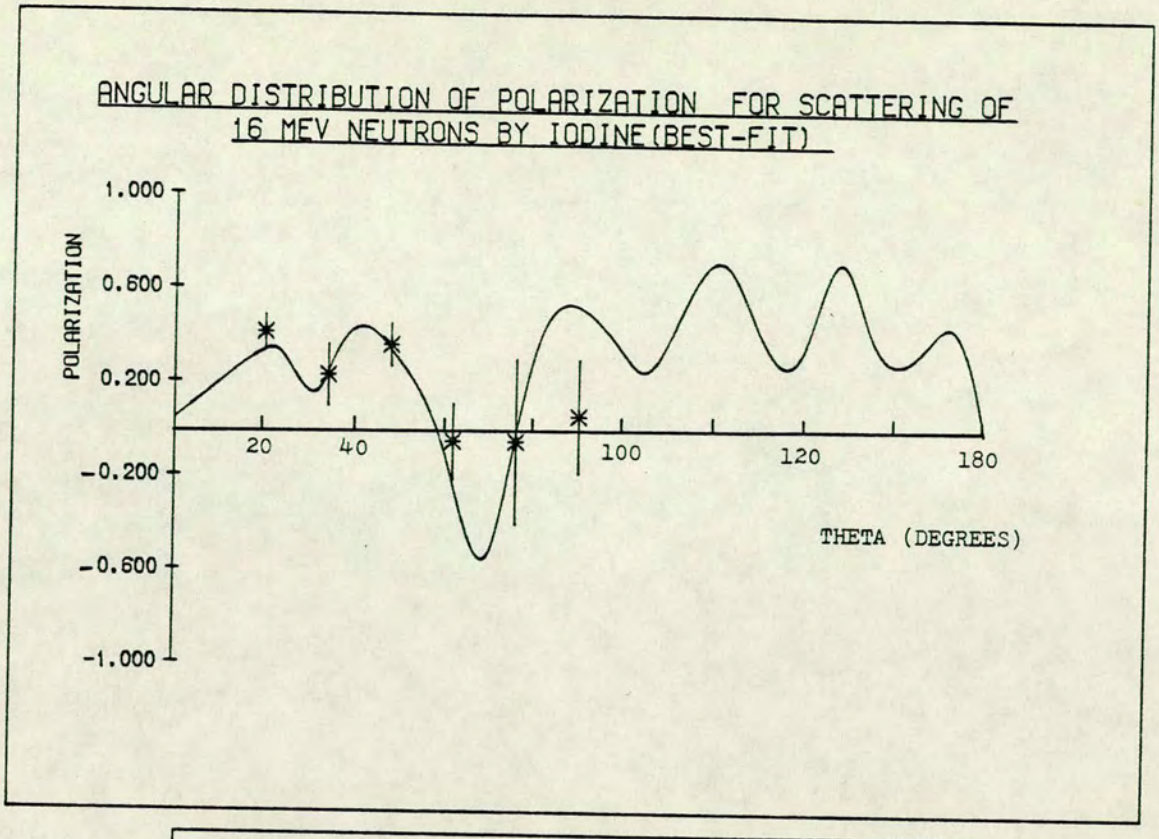
ANGULAR DISTRIBUTION OF POLARIZATION FOR SCATTERING OF 16 MEV NEUTRONS BY IODINE(BEST-FIT)
POLARIZATION
1.000
0.600
0.200
-0.200
-0.600
-1.000
20
40
100
120
180
THETA (DEGREES)

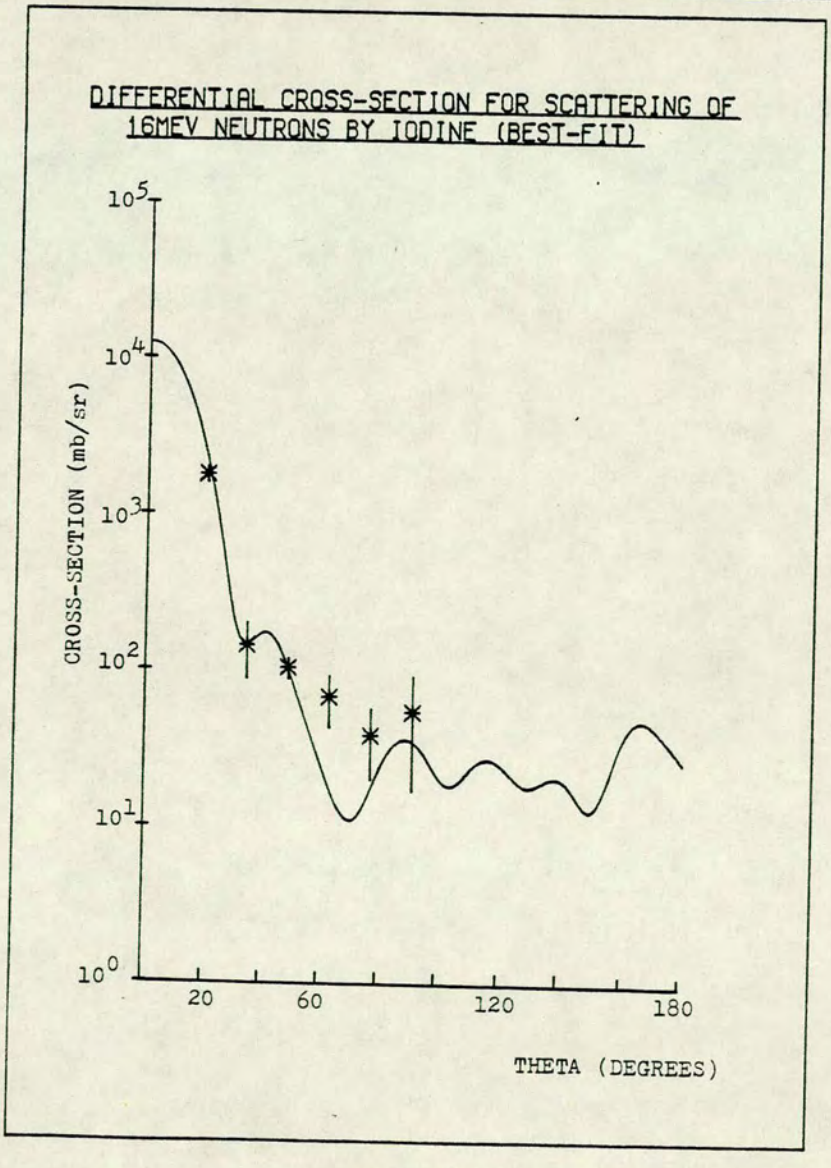
DIFFERENTIAL CROSS-SECTION FOR SCATTERING OF 16MEV NEUTRONS BY IODINE (BEST-FIT)
CROSS-SECTION (mb/sr)
10^5
10^4
10^3
10^2
10^1
10^0
20
60
120
180
THETA (DEGREES)

Fig. 6.24

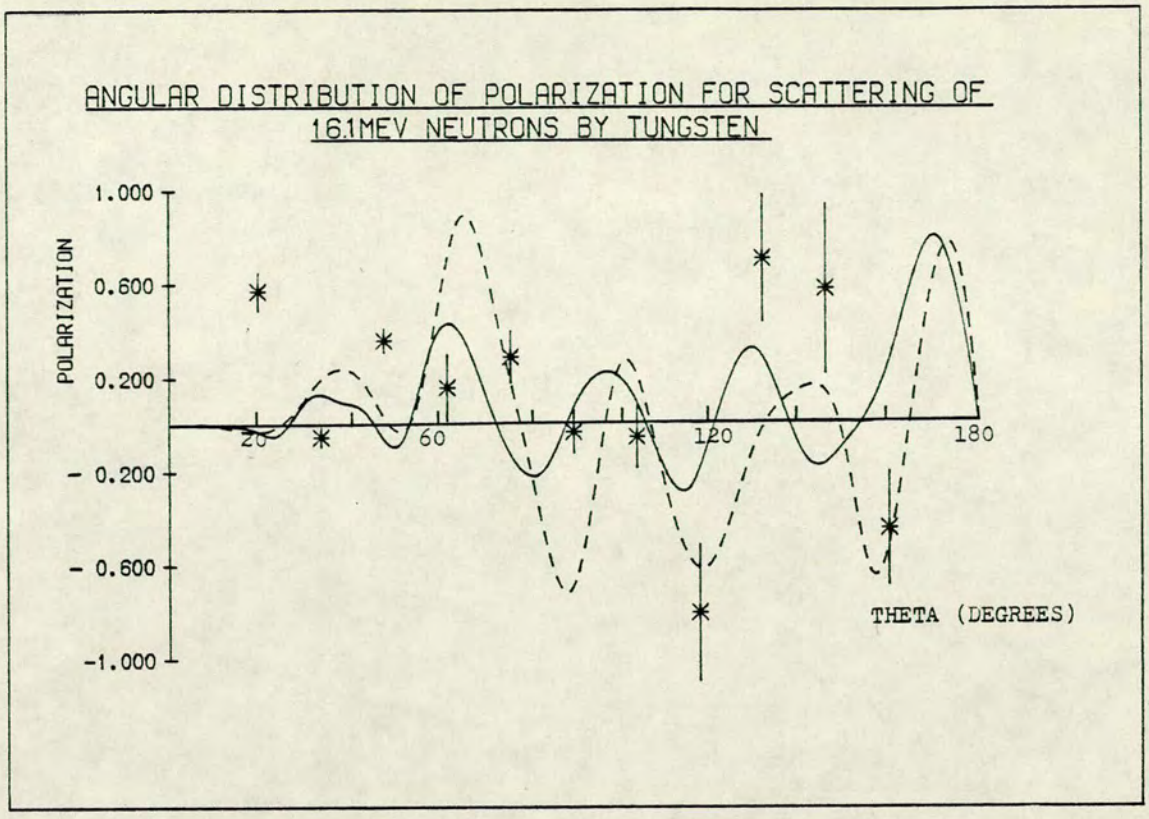
ANGULAR DISTRIBUTION OF POLARIZATION FOR SCATTERING OF 16.1MEV NEUTRONS BY TUNGSTEN
POLARIZATION
1.000
0.600
0.200
- 0.200
- 0.600
-1.000
20
60
120
180
THETA (DEGREES)

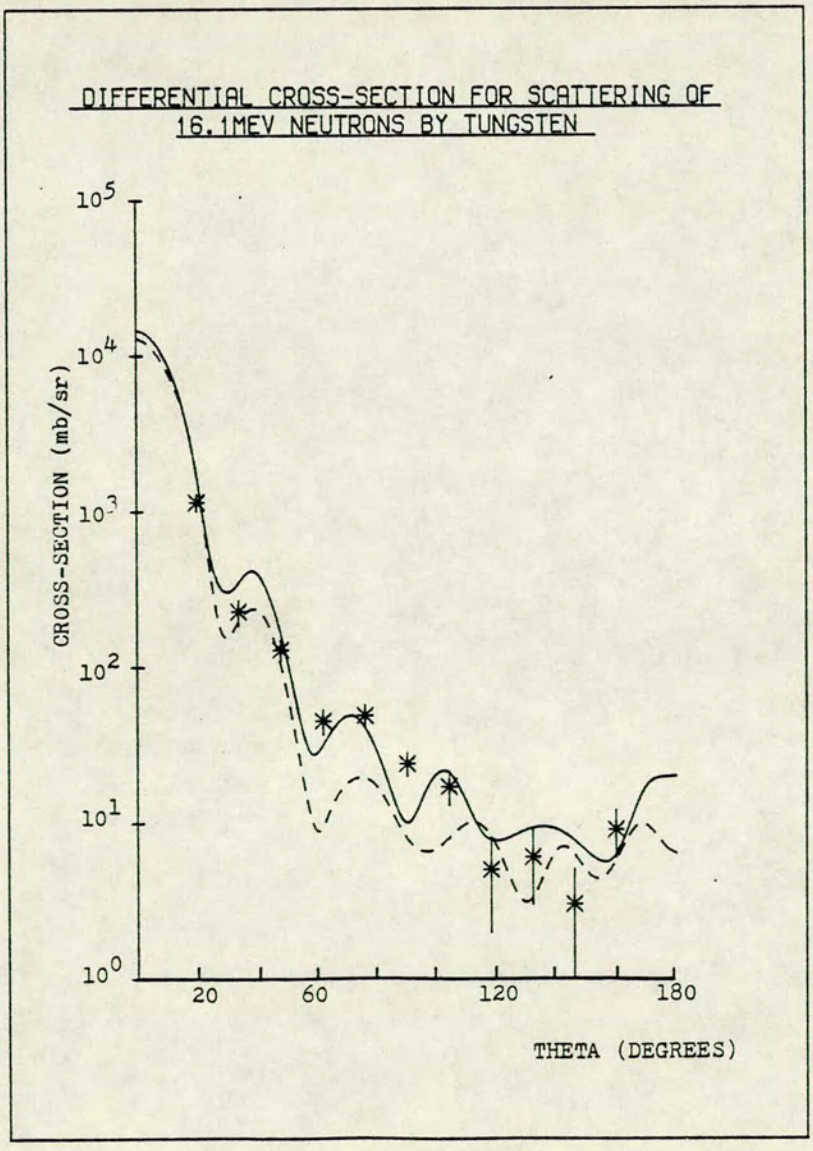
DIFFERENTIAL CROSS-SECTION FOR SCATTERING OF 16.1MEV NEUTRONS BY TUNGSTEN
CROSS-SECTION (mb/sr)
10^5
10^4
10^3
10^2
10^1
10^0
20
60
120
180
THETA (DEGREES)

Fig. 6.25

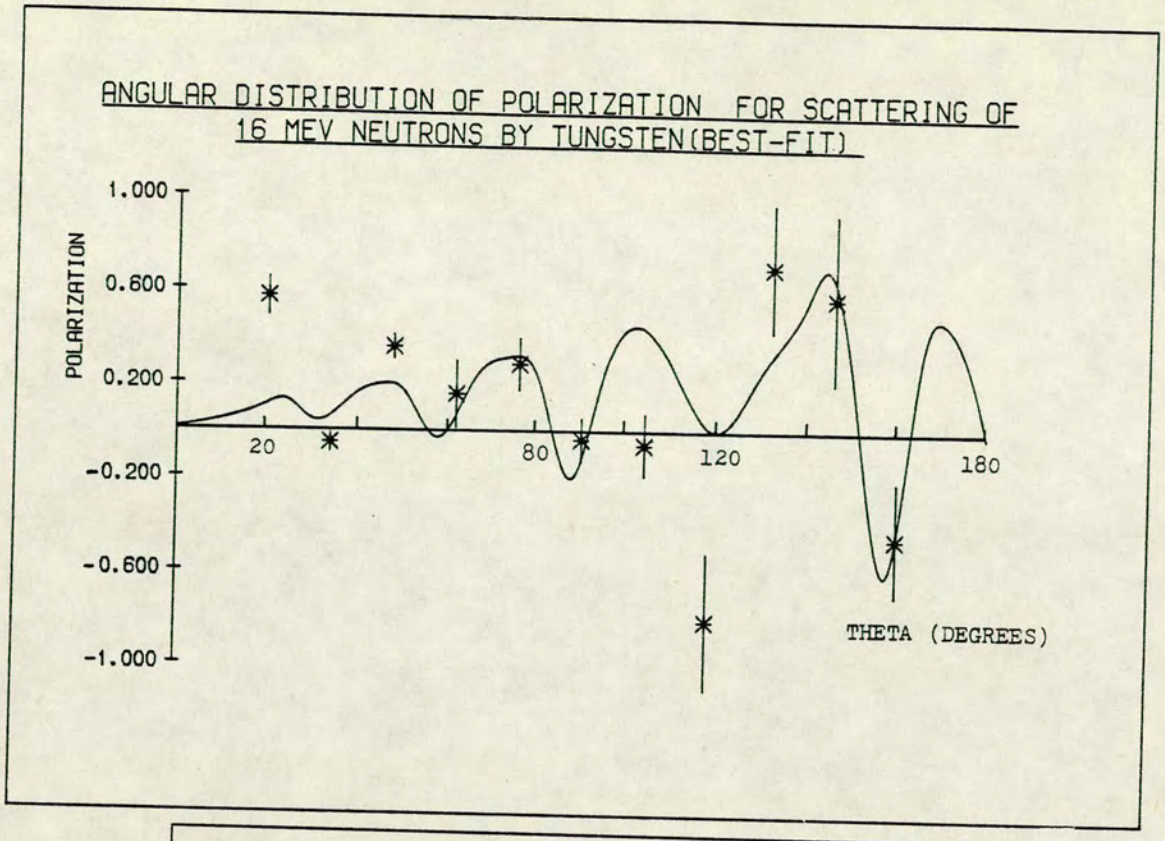
ANGULAR DISTRIBUTION OF POLARIZATION FOR SCATTERING OF
16 MEV NEUTRONS BY TUNGSTEN(BEST-FIT)
POLARIZATION
1.000
0.600
0.200
-0.200
-0.600
-1.000
20
80
120
180
THETA (DEGREES)

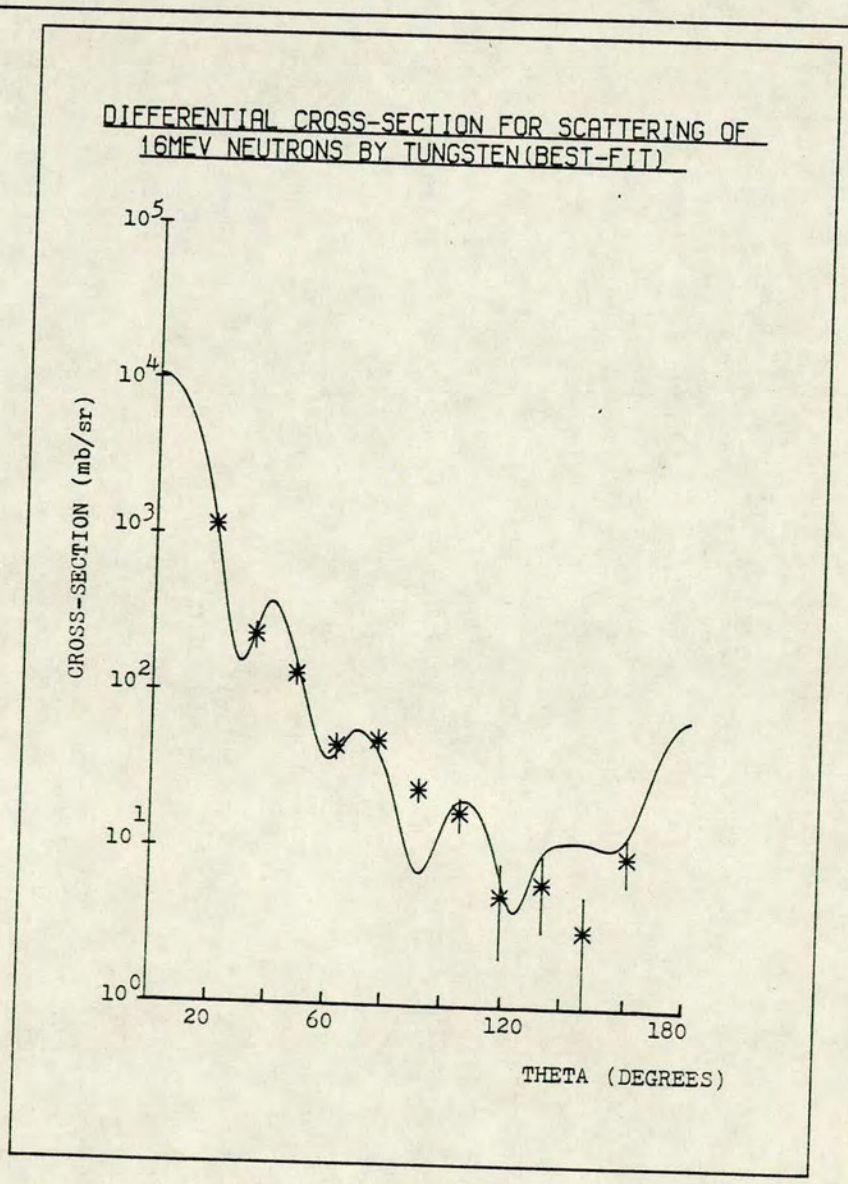
DIFFERENTIAL CROSS-SECTION FOR SCATTERING OF
16MEV NEUTRONS BY TUNGSTEN(BEST-FIT)
CROSS-SECTION (mb/sr)
10^5
10^4
10^3
10^2
10^1
10^0
20
60
120
180
THETA (DEGREES)

Fig. 6.26

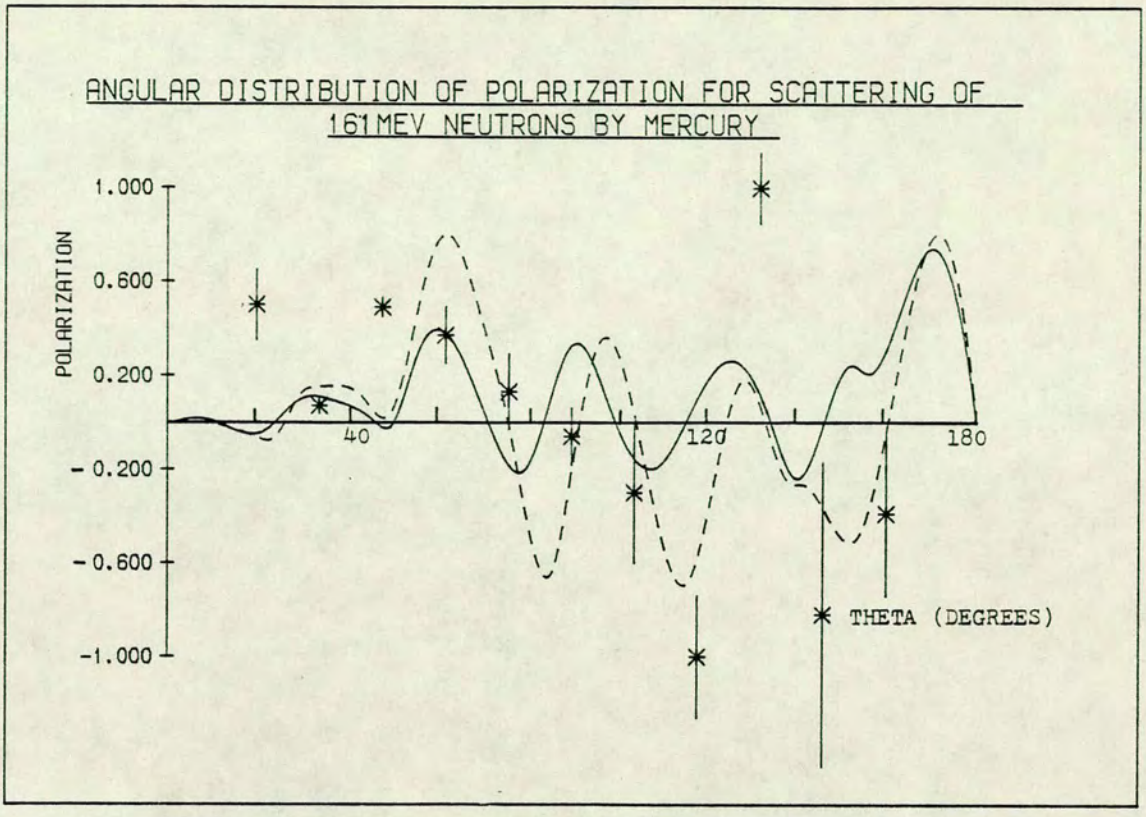
ANGULAR DISTRIBUTION OF POLARIZATION FOR SCATTERING OF
16.1MEV NEUTRONS BY MERCURY
POLARIZATION
1.000
0.600
0.200
- 0.200
- 0.600
-1.000
40
120
180
THETA (DEGREES)

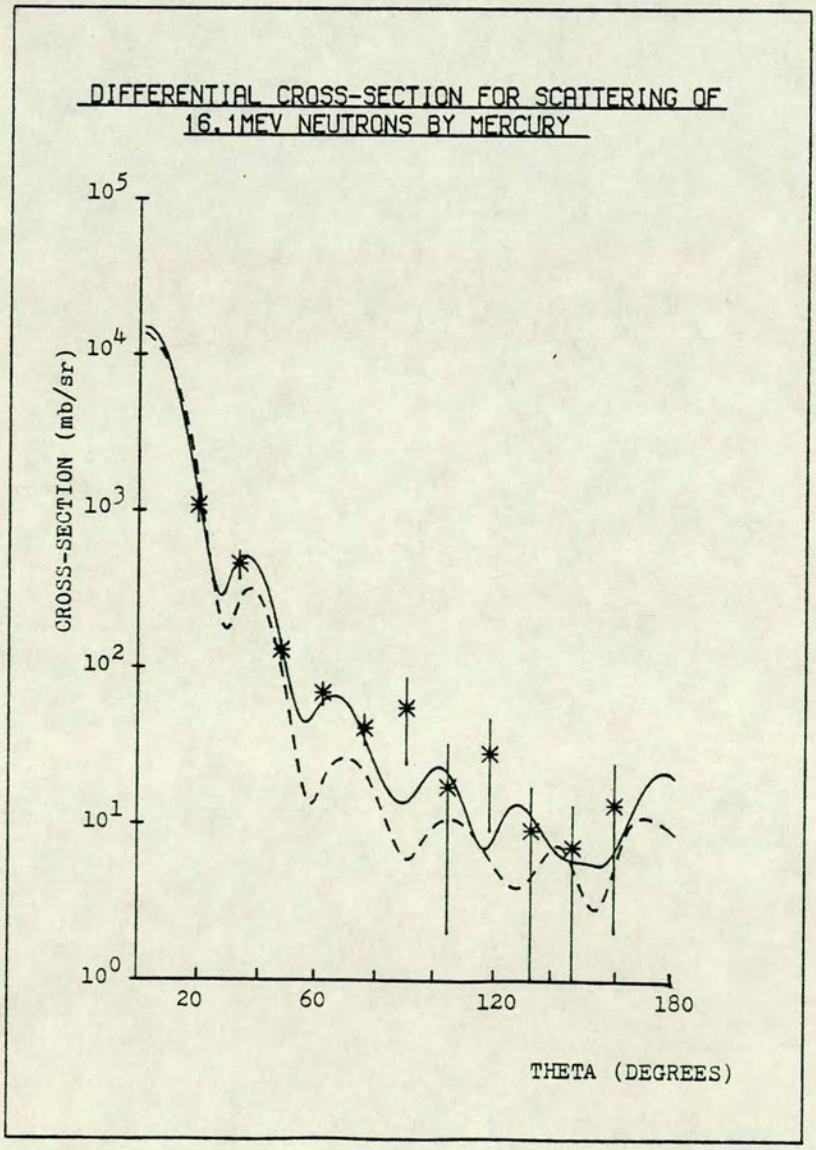
DIFFERENTIAL CROSS-SECTION FOR SCATTERING OF
16.1MEV NEUTRONS BY MERCURY
CROSS-SECTION (mb/sr)
10^5
10^4
10^3
10^2
10^1
10^0
20
60
120
180
THETA (DEGREES)

Fig. 6.27

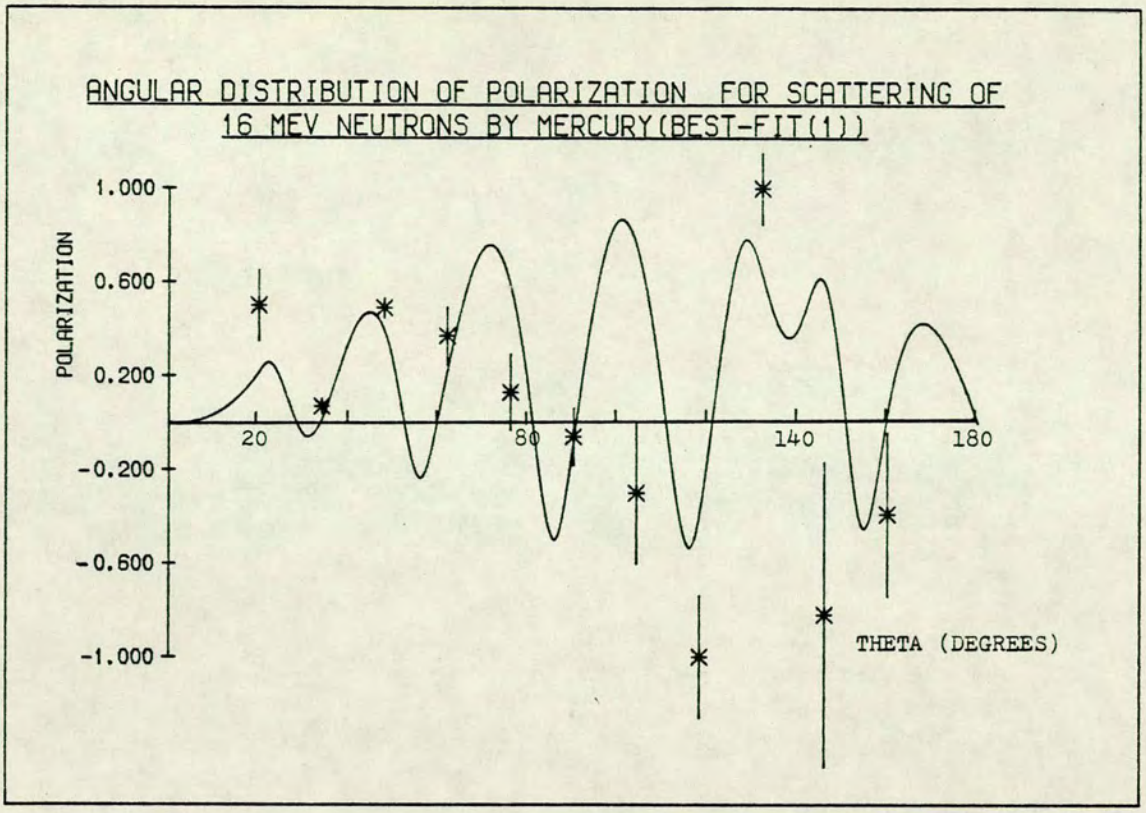
ANGULAR DISTRIBUTION OF POLARIZATION FOR SCATTERING OF
16 MEV NEUTRONS BY MERCURY(BEST-FIT(1))
POLARIZATION
1.000
0.600
0.200
-0.200
-0.600
-1.000
20
80
140
180
THETA (DEGREES)

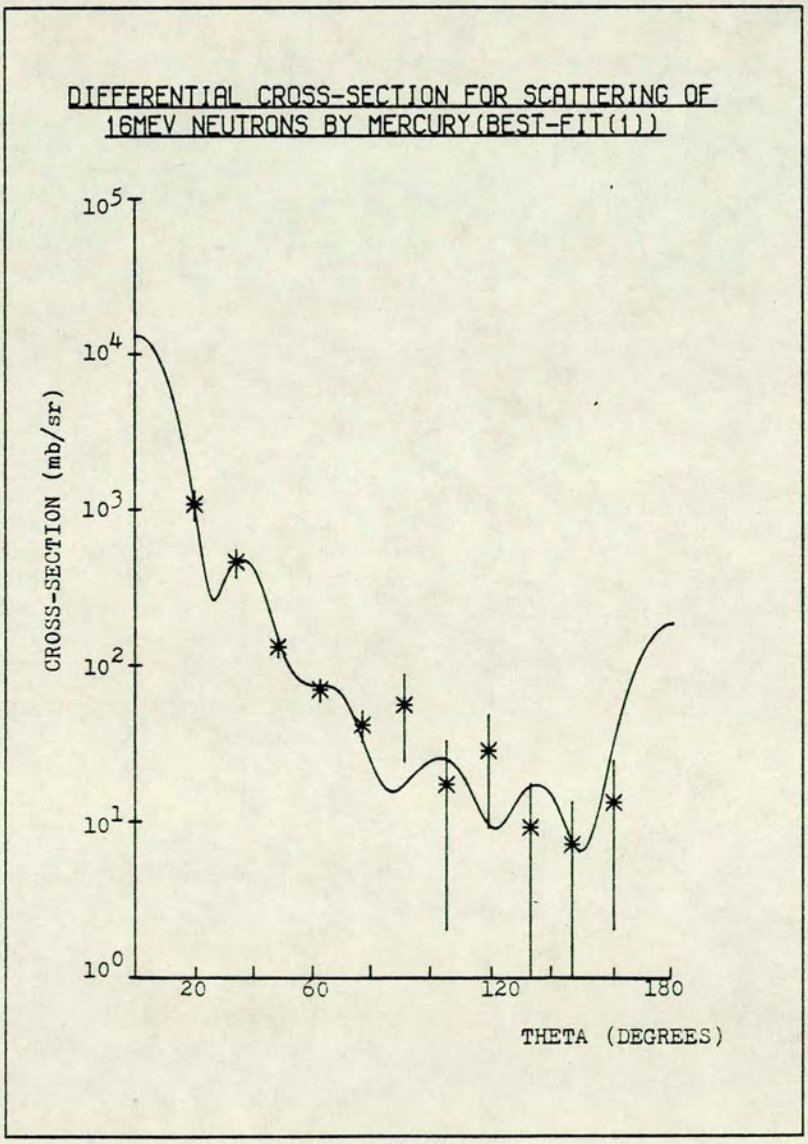
DIFFERENTIAL CROSS-SECTION FOR SCATTERING OF
16MEV NEUTRONS BY MERCURY(BEST-FIT(1))
CROSS-SECTION (mb/sr)
10^5
10^4
10^3
10^2
10^1
10^0
20
60
120
180
THETA (DEGREES)

Fig. 6.28

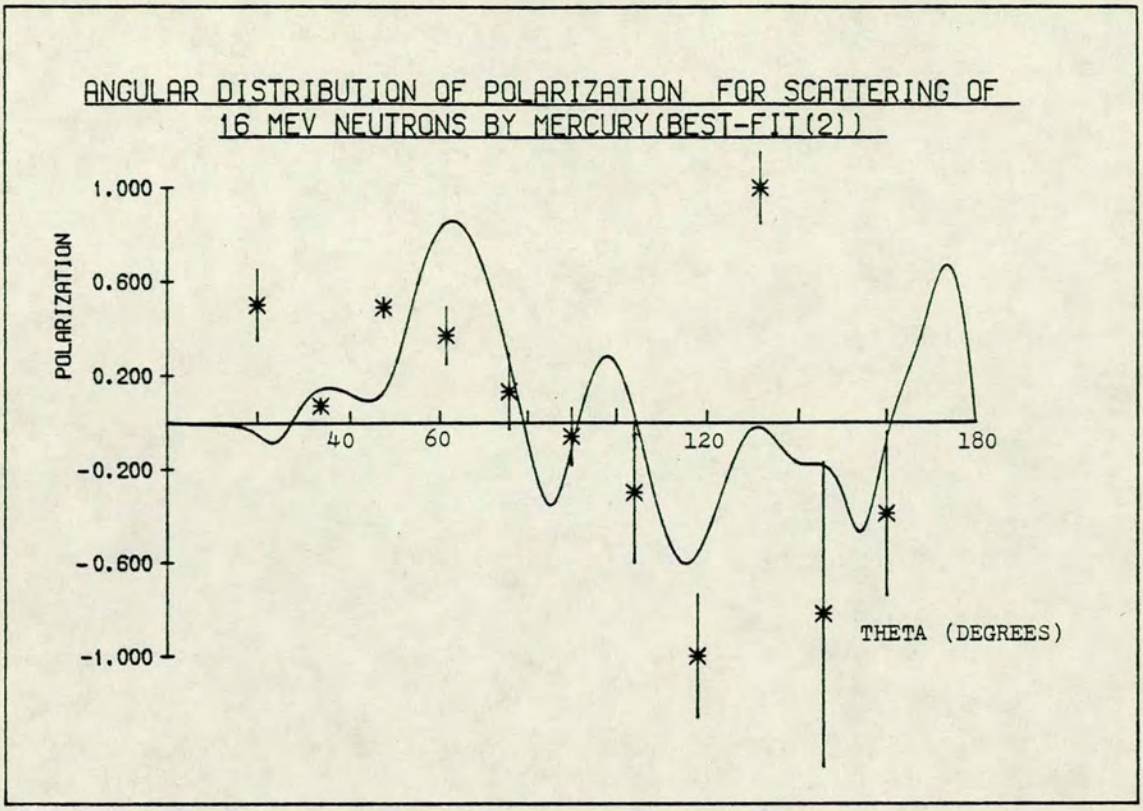
ANGULAR DISTRIBUTION OF POLARIZATION FOR SCATTERING OF
16 MEV NEUTRONS BY MERCURY(BEST-FIT(2))
POLARIZATION
1.000
0.600
0.200
-0.200
-0.600
-1.000
40
60
120
180
THETA (DEGREES)

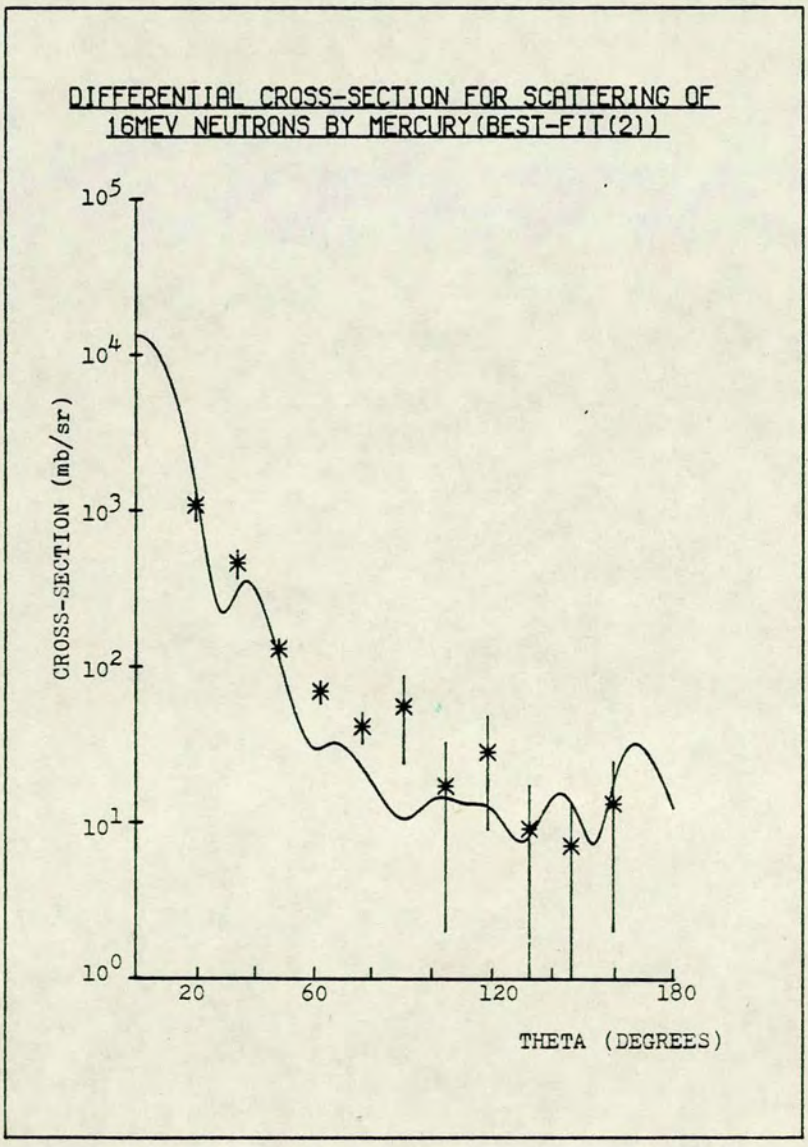
DIFFERENTIAL CROSS-SECTION FOR SCATTERING OF
16MEV NEUTRONS BY MERCURY(BEST-FIT(2))
CROSS-SECTION (mb/sr)
10^5
10^4
10^3
10^2
10^1
10^0
20
60
120
180
THETA (DEGREES)

Fig. 6.29

as Hg(1) and Hg(2) respectively. The corresponding best fit curves are presented in Fig. 6.28 and 6.29. It is clear from the two sets of figures that for both cross-section and polarization the curves without the volume imaginary term gives better agreement to the data. However the set Hg(1) has a high magnitude for the surface imaginary term W_S = 23.17 MeV. The set Hg(2), free from such abnormality, includes the volume imaginary term, but has a χ^2 value three times that of the first.

LEAD:- The experimental distributions of polarization and cross-section for lead are compared with the calculations based on the global parameters of Rosen et al.[38], Becchetti and Greenlees[39] and those proposed by Fu and Perey[41] in Fig. 6.30. As far as the cross-section is concerned, Rosen parameters give better overall fit than the others while there is little to choose between the different parameters for the case of polarization.

The result of the optimum parameter search on the Pb data can be considered with reference to Fig. 6.31, that resulted from a set which included the volume imaginary term, listed in Table 6.3. The best fit without the volume imaginary term gave a poorer fit to the data than the one illustrated in Fig. 6.31.

CARBON:- The measured cross-section and the polarization distributions on carbon are compared in Fig. 6.32 with the optical model calculation employing the parameters found by Haouat et al.[88] from fitting their elastic scattering data for 11.5 - 14.5 MeV neutrons. The calculated polarization distribution resembles the measured distribution without fitting closely. The measured cross-section values are about 25% lower than those calculated, which may be due to the resonance at 15.8 MeV between the energy for which the optical model parameters

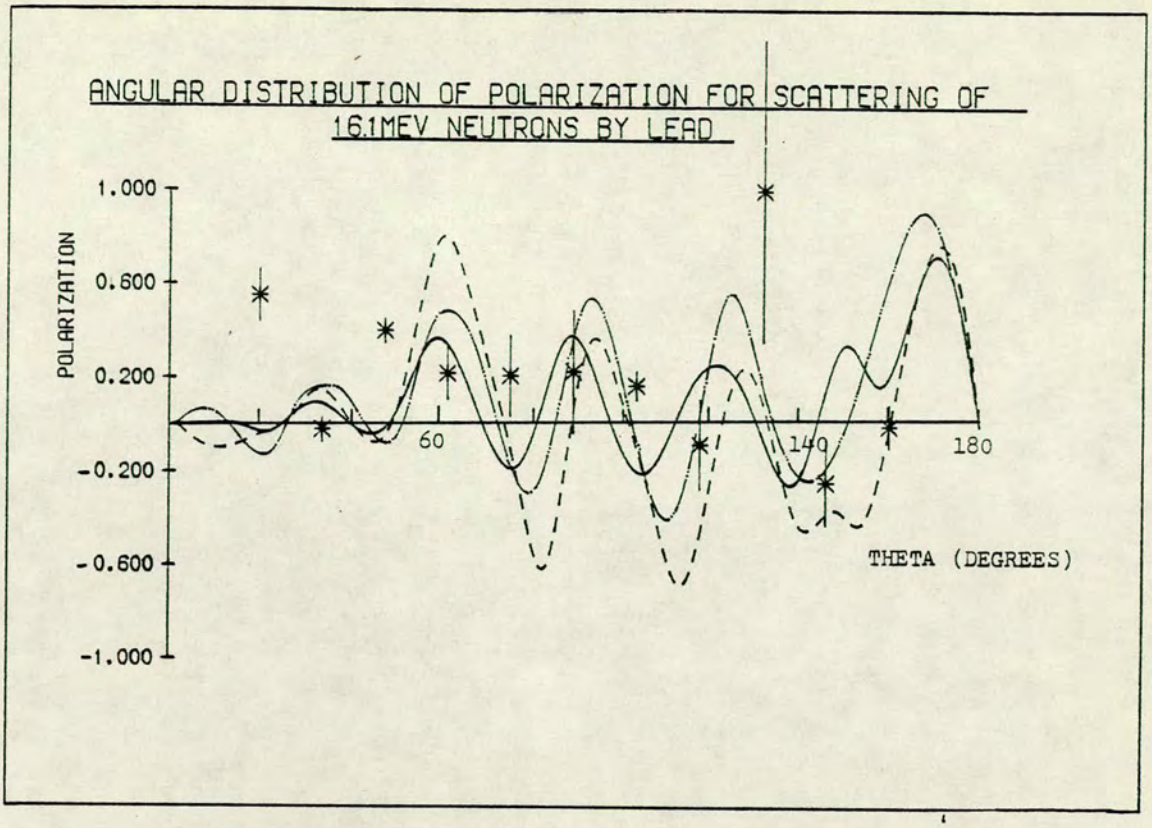
ANGULAR DISTRIBUTION OF POLARIZATION FOR SCATTERING OF
16.1MEV NEUTRONS BY LEAD
POLARIZATION
1.000
0.600
0.200
-0.200
-0.600
-1.000
60
140
180
THETA (DEGREES)

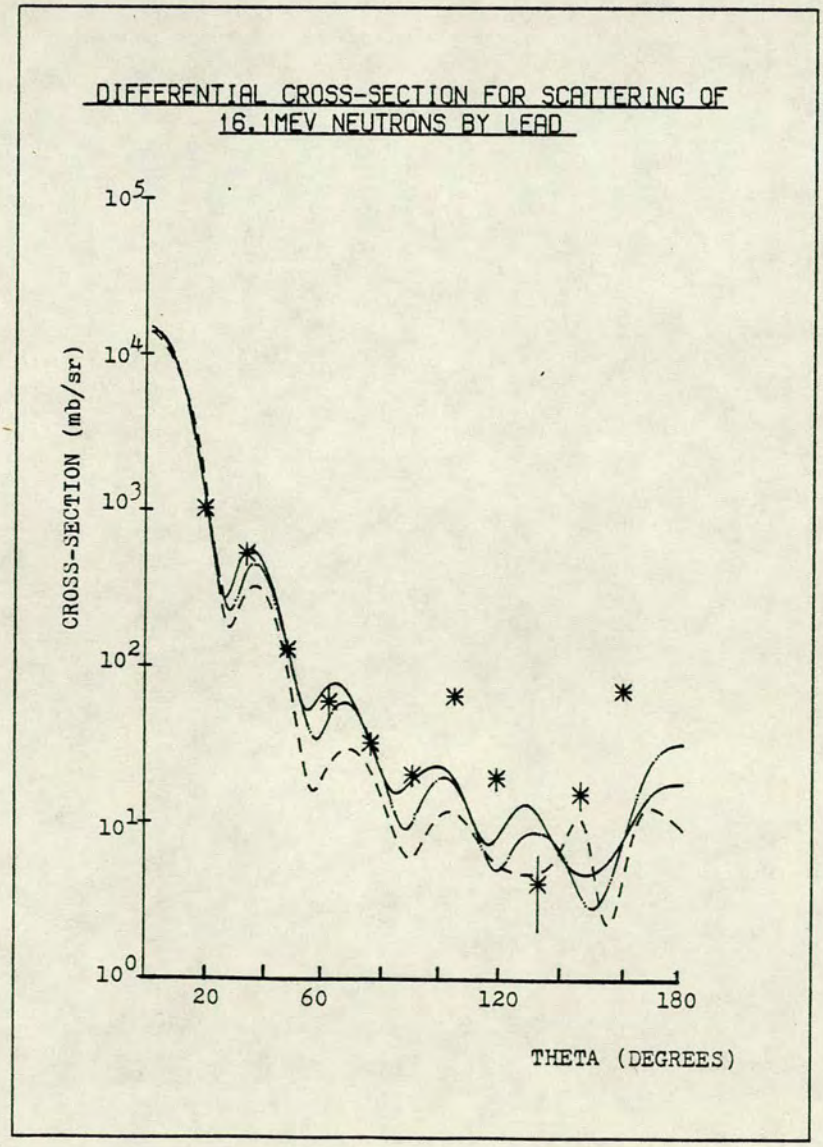
DIFFERENTIAL CROSS-SECTION FOR SCATTERING OF
16.1MEV NEUTRONS BY LEAD
CROSS-SECTION (mb/sr)
10^5
10^4
10^3
10^2
10^1
10^0
20
60
120
180
THETA (DEGREES)

Fig. 6.30

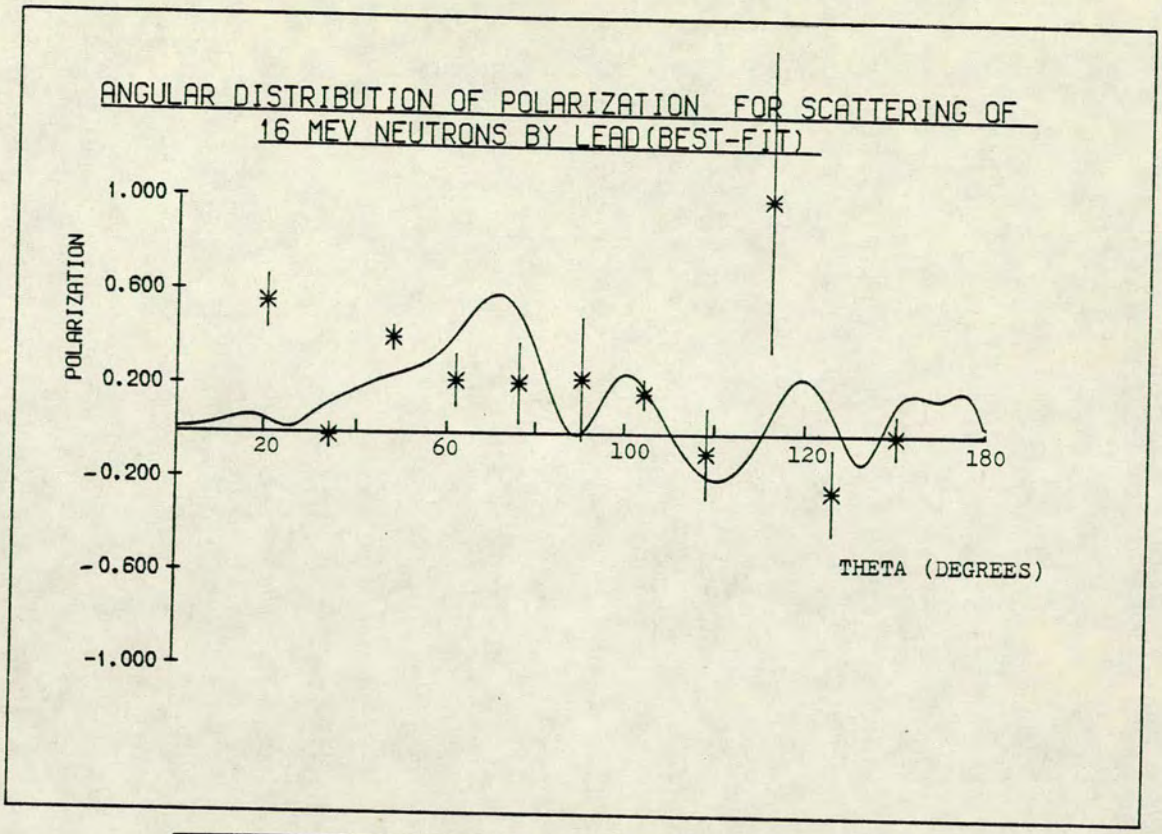
ANGULAR DISTRIBUTION OF POLARIZATION FOR SCATTERING OF 16 MEV NEUTRONS BY LEAD(BEST-FIT)
POLARIZATION
1.000
0.600
0.200
-0.200
-0.600
-1.000
20
60
100
120
180
THETA (DEGREES)

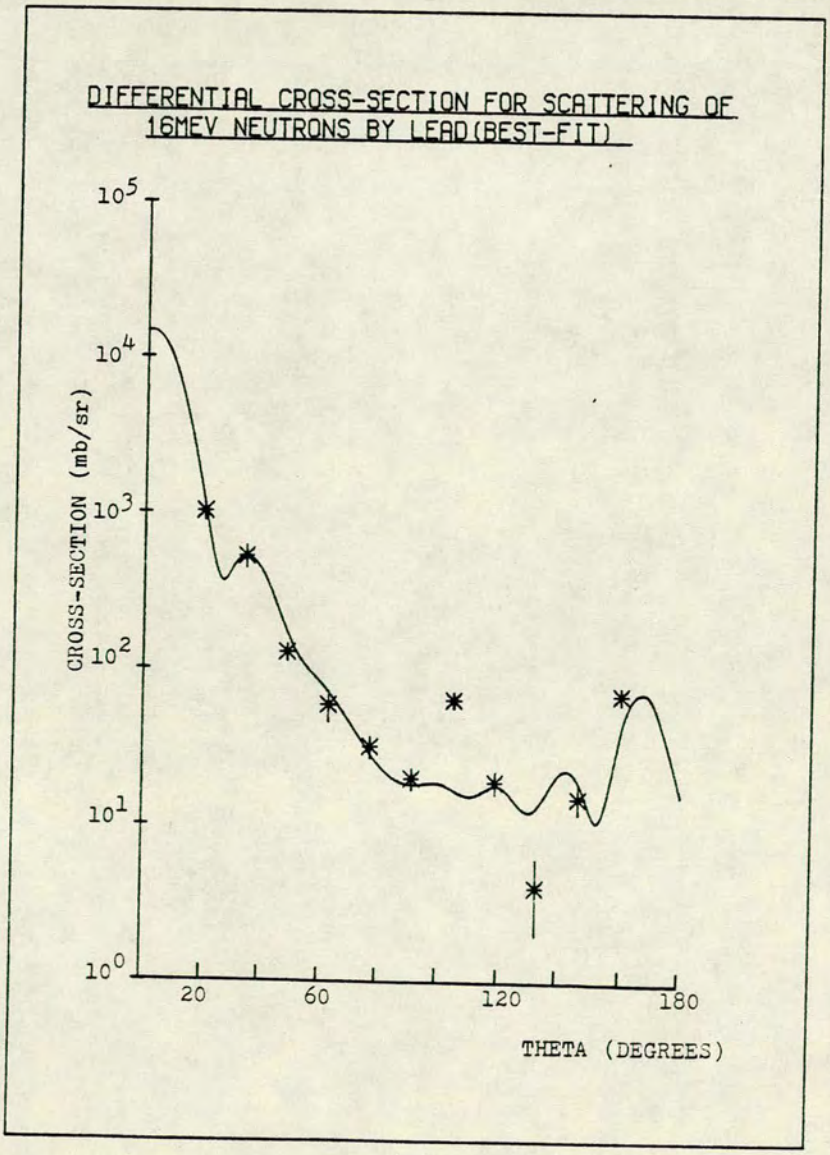
DIFFERENTIAL CROSS-SECTION FOR SCATTERING OF 16MEV NEUTRONS BY LEAD(BEST-FIT)
CROSS-SECTION (mb/sr)
10^5
10^4
10^3
10^2
10^1
10^0
20
60
120
180
THETA (DEGREES)

Fig 6.31

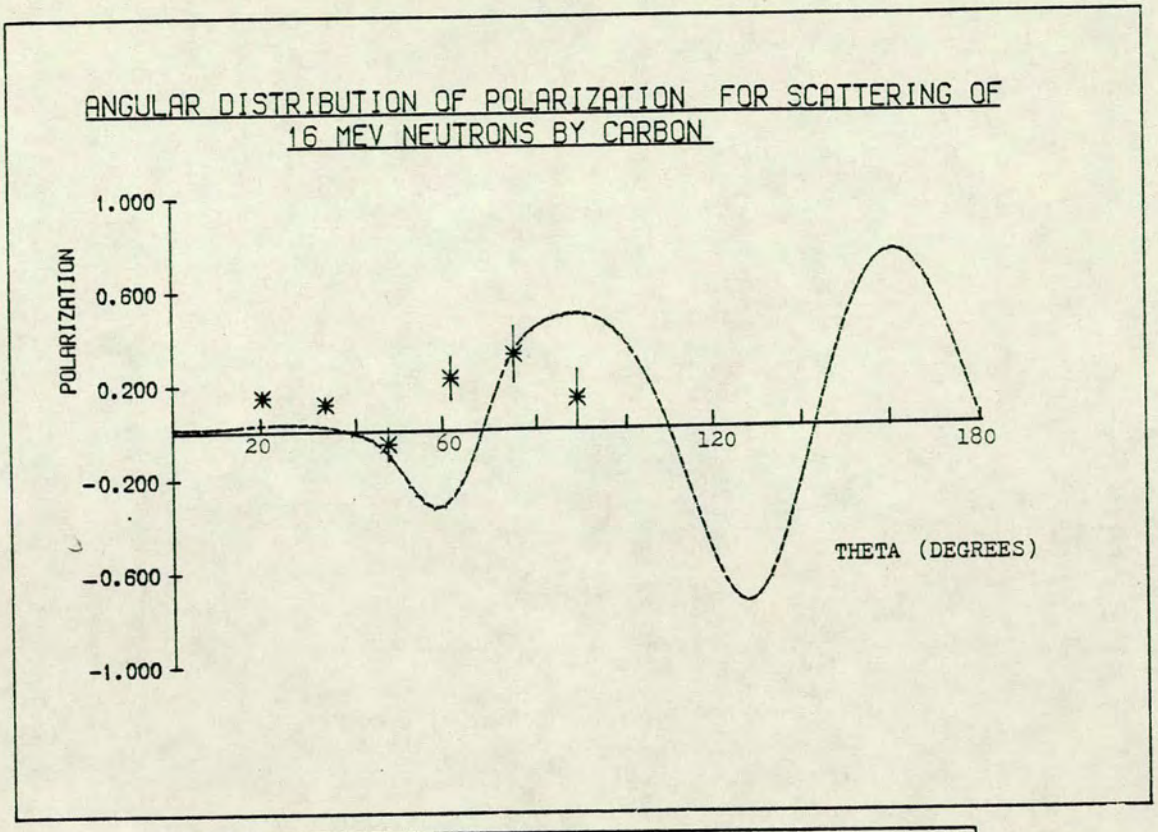
ANGULAR DISTRIBUTION OF POLARIZATION FOR SCATTERING OF 16 MEV NEUTRONS BY CARBON
POLARIZATION
1.000
0.600
0.200
-0.200
-0.600
-1.000
20
60
120
180
THETA (DEGREES)

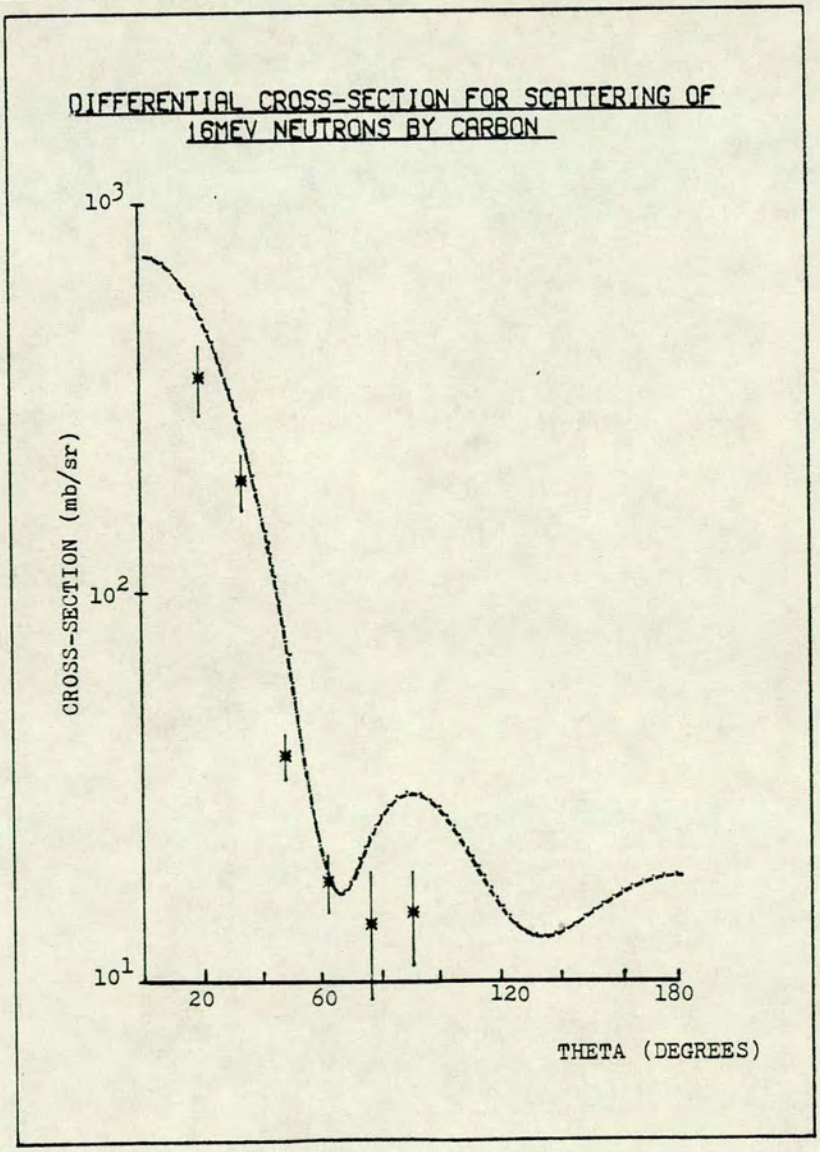
DIFFERENTIAL CROSS-SECTION FOR SCATTERING OF 16MEV NEUTRONS BY CARBON
CROSS-SECTION (mb/sr)
10^3
10^2
10^1
20
60
120
180
THETA (DEGREES)

Fig. 6.32

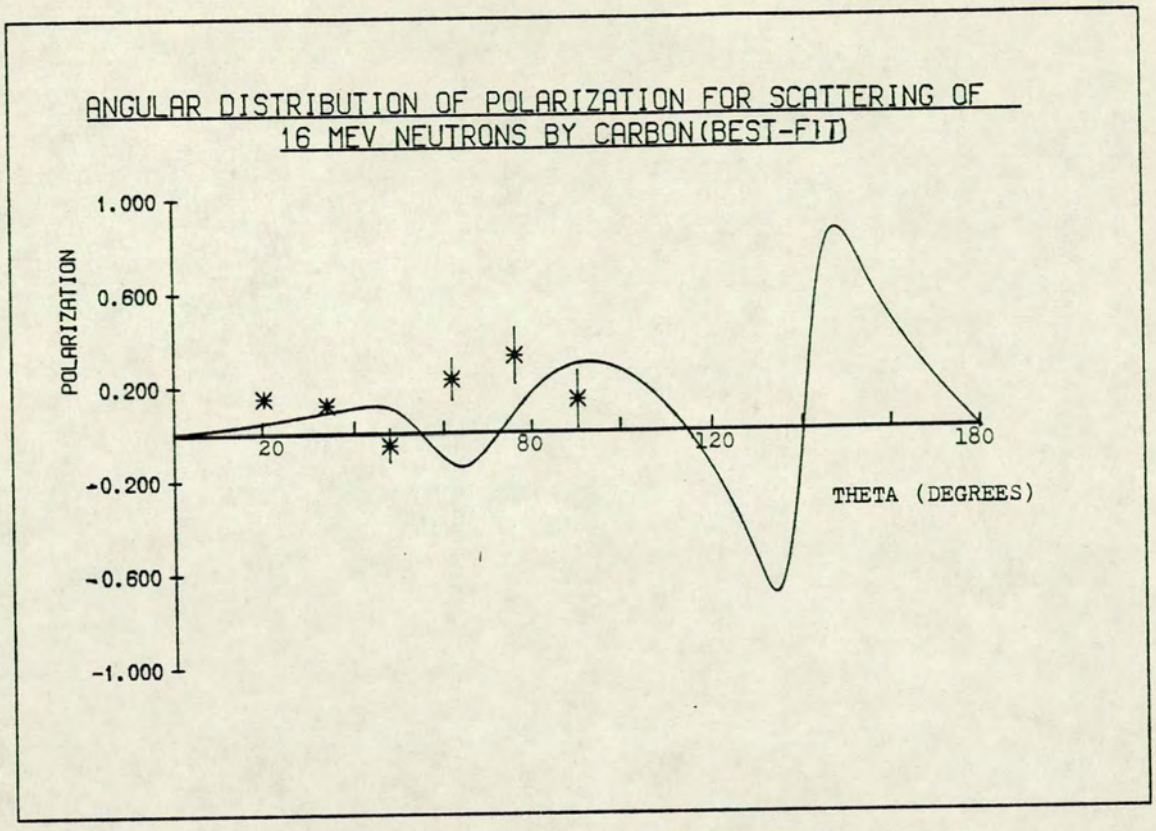
ANGULAR DISTRIBUTION OF POLARIZATION FOR SCATTERING OF
16 MEV NEUTRONS BY CARBON(BEST-FIT)
POLARIZATION
1.000
0.600
0.200
-0.200
-0.600
-1.000
20
80
120
180
THETA (DEGREES)

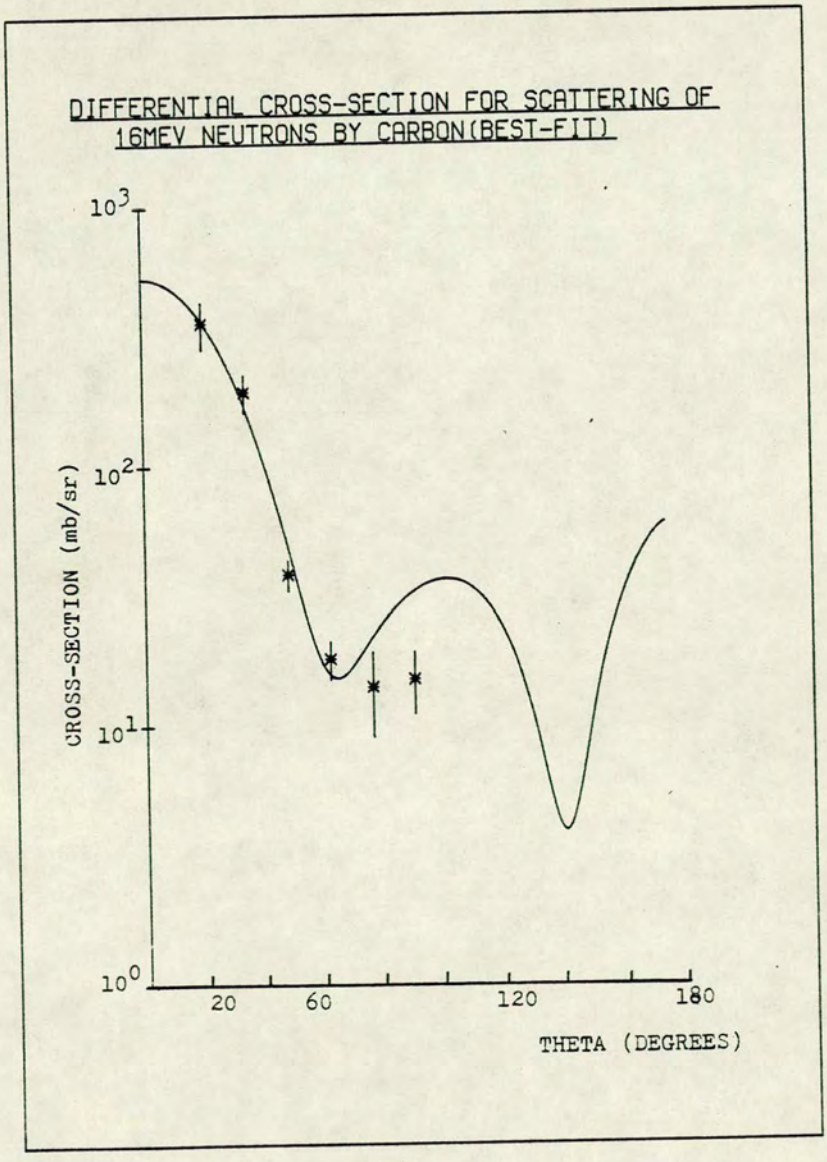
DIFFERENTIAL CROSS-SECTION FOR SCATTERING OF
16MEV NEUTRONS BY CARBON(BEST-FIT)
CROSS-SECTION (mb/sr)
10^3
10^2
10^1
10^0
20
60
120
180
THETA (DEGREES)

Fig. 6.33

Nuclide	V_R MeV	R_R fm	A_R fm	W_S MeV	R_W fm	A_W fm	W_V MeV	R_V fm	A_V fm	V_S MeV	R_S fm	A_S fm	JV/A	JW/A	JS/A	$\chi^2(\sigma)$	$\chi^2(P)$	$\chi^2(T)$
													MeV.fm^3					
Fe	51.72	1.09	0.67	7.11	1.19	0.39	-	-	-	8.74	1.06	0.74	348	52.8	15.7	2.54	3.49	3.00
Cu	44.28	1.20	0.64	7.81	1.18	0.40	-	-	-	7.00	1.22	1.06	377	56.6	13.4	2.48	1.50	1.99
I	49.94	1.17	0.88	4.63	1.29	0.58	1.54	1.26	0.58	6.61	1.54	0.76	405	59.3	10.0	1.84	0.89	1.36
W	49.91	1.21	0.75	11.38	1.26	0.30	1.98	1.26	0.58	3.70	1.40	0.30	410	64.8	4.0	3.11	7.51	5.31
Hg(1)	49.03	1.20	0.96	23.17	1.26	0.25	-	-	-	4.93	1.45	0.11	415	80.4	5.2	0.8	4.6	2.71
Hg(2)	46.86	1.19	0.82	5.15	1.28	0.35	3.29	1.30	0.25	7.42	1.03	0.75	373	55.7	5.5	2.2	14.6	8.4
Pb	46.77	1.21	0.88	7.90	1.20	0.30	1.98	1.26	0.58	8.86	1.17	0.99	395	46.3	7.3	7.97	4.81	6.4
C	57.82	1.25	0.36	7.41	1.25	0.27	-	-	-	2.16	1.25	0.36	547	70.6	12.9	4.58	8.62	6.60

Table 6.3. Optimum values of the optical potential parameters for 16 MeV neutrons.

were deduced and the energy of the present measurement.

Searches for optimum parameters were carried out with the Haouat et al.[88] parameters as the starting values. The best fit parameters are listed in Table 6.3 and the distributions illustrated in Fig. 6.33. The differential cross-section data are well fitted but the fit to the polarization is less satisfactory.

6.5 Conclusion

The motivation of the present work to add more neutron polarization data to that existing, to enable a better understanding of the success of the optical model has been carried out successfully. The measurement added data for heavy nuclei (W, Tℓ, Pb, Bi and U) in the energy range of < 5 MeV (2.9 MeV) and for medium and heavy nuclei (Fe, Cu, I, W, Hg and Pb) in the range 5-25 MeV (14.2 and 16 MeV). The differential cross-section data evaluated from the same measurements made it possible to attempt optical model analysis for each nucleus individually for each energy. From the result of the optical model analyses in Section 6.2.2 on 2.9 MeV neutron scattering the following observations are made:

(1) Optical model calculations combined with Hauser-Feshbach calculations based on global parameters and those suggested previously for particular nuclei provide a better overall agreement to measured differential cross-sections than polarizations.

(2) Hauser-Feshbach compound elastic calculations, that included the Moldauer level width fluctuation correction provide a better fit to the data on all the heavy nuclei except for Uranium which showed a similar fit both with and without the MLF correction.

(3) A much better fit to both cross-sections and polarizations is obtained from an individual analysis on each nucleus, with the optimum parameter sets listed in Table 6.2.

(4) The average value for the spin-orbit potential for the optimum parameter sets has a notably large value of 14.04 MeV. The mean value of the real, imaginary and spin-orbit radii are 1.21, 1.35 and 1.17 fm while the corresponding diffuseness parameters are 0.63, 0.40 and 0.47 fm respectively.

From the result of the optical model analyses for 16 MeV neutrons (Section 6.2.3) the following observations are made:

1) For all the nuclei the calculations based on the parameters of Rosen et al. give a better fit to the differential cross-section data. In the case of Fe and of Cu, the calculated polarization based on Rosen et al. parameters is closer to the measurement except for around 20^{o}, while for I, W, Hg and Pb none of the parameters does very well.

2) Results of the optimum parameter search (Table 6.3) shows the evidence of including a volume imaginary term for the heavier nuclei whose strength depends on mass number. The mean of the real, imaginary and spin-orbit radii for Table 6.3 are 1.19, 1.23 and 1.30 fm respectively while the mean diffusenesses are 0.73, 0.36 and 0.62 fm respectively.

3) Even with the optimum parameter set the fits to the polarization data for the heavier nuclei are much poorer than the lighter ones. The discrepancy of the polarization value around 20^{o}, still remained for most of the nuclei.

The result of the double scattering experiment with 14 MeV neutrons for Cu and Pb supports the evidence of large magnitude of polarization around 20^{o}. Optical model calculations done for 14.2 MeV neutrons on Cu and Pb also have a very small magnitude of polarization around 20^{o}. In fact there is little difference in the calculated values for 14 and 16 MeV neutron polarization at forward angles (Fig. 6.34). Attempts were made to modify the conventional optical model parameters to account for

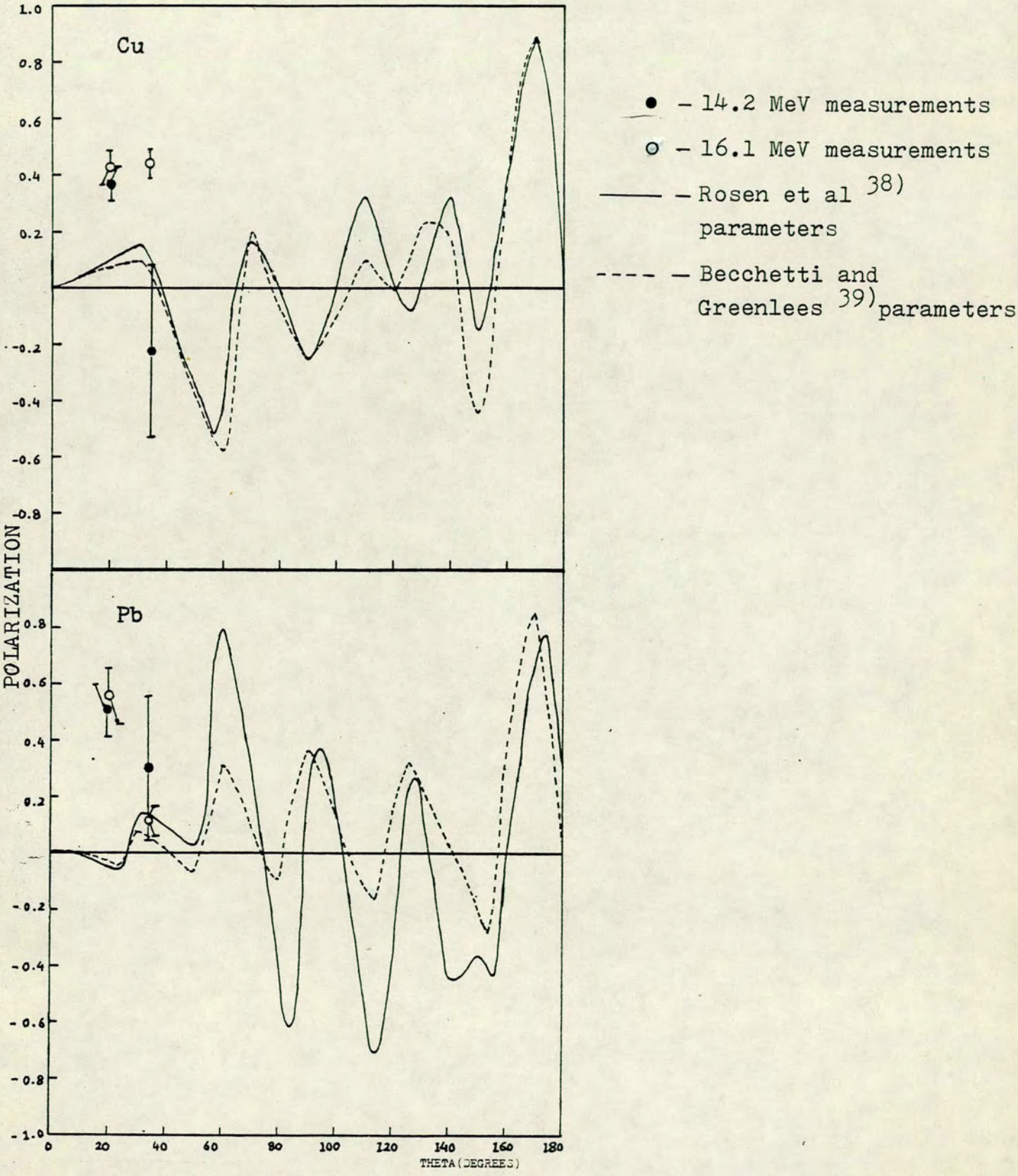

Fig. 6.34 Comparison of optical model calculation of polarization for 14.2 MeV and 16.MeV neutrons.

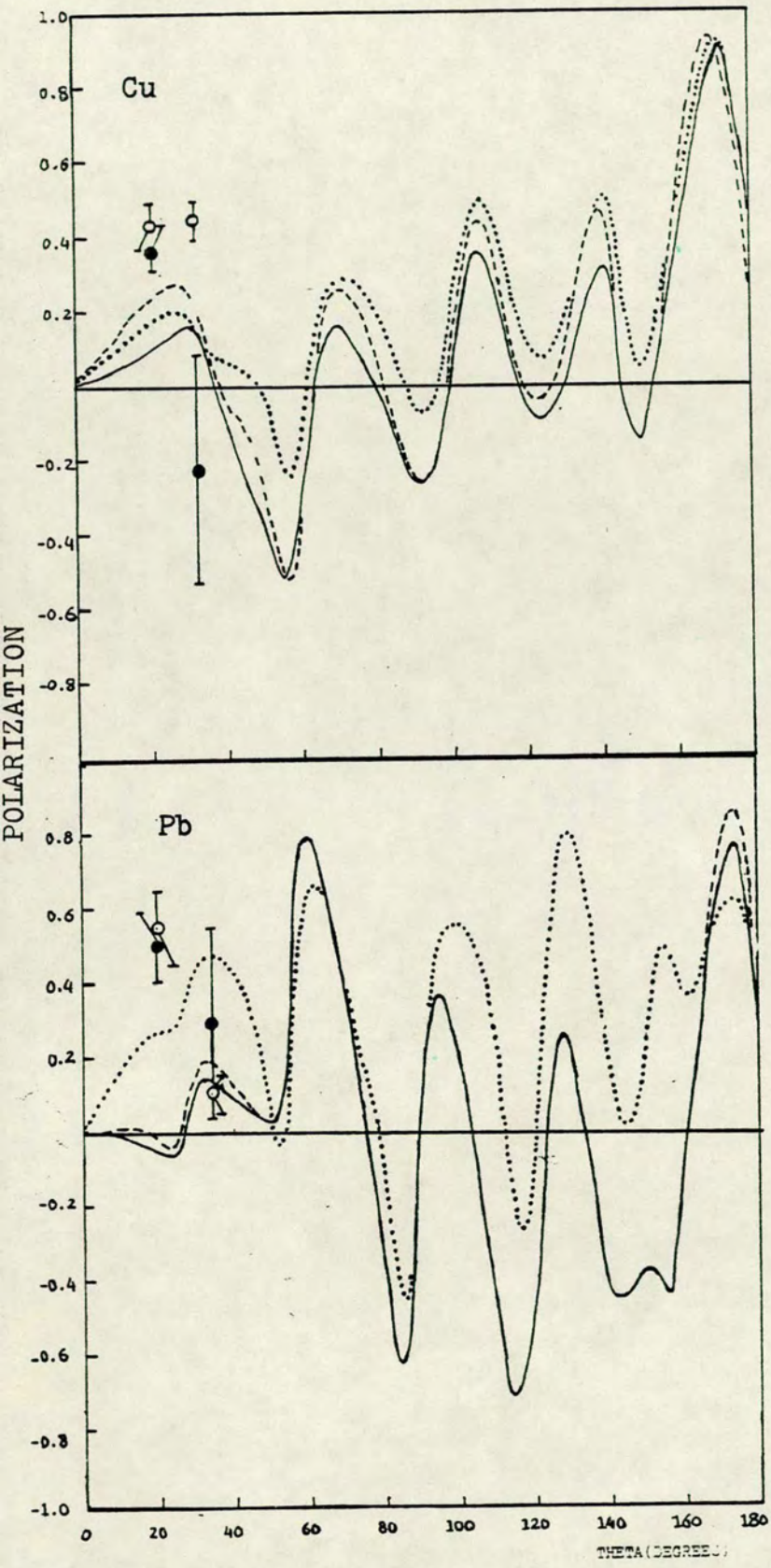

● —14.2 MeV measurements

o —16.1 MeV measurements

——— —Rosen et al [38] parameters

- - - - - —Diffuseness parameters of the spin-orbit term fixed at 1.0 fm.

····· —Radius of the spin-orbit term fixed at 1.4 fm.

Fig. 6.35 Optical model calculation of 16.1 MeV neutron polarization to modify the magnitude around 20°.

the 20^{o} effect for 16 MeV neutrons scattered from Cu and Pb. It was observed that increasing the radius or the diffuseness of the spin-orbit term increases the polarization (Fig. 6.35) at forward angles with little effect at the rest of the angles or on the cross-section.

REFERENCES

1. N. Bohr, Nature (London) 137 (1956), 344.
2. E. Amaldi, D. Bocciareli, B.N. Cacciapuoti and G. Trabacchi, Nuovo Cimento Ser. 9, 3 (1946), 203.
3. M. Walt and H.H. Barschall, Phys. Rev. 93 (1954), 1062.
4. L. Wolfenstein, Phys. Rev. 75 (1949), 342.
5. P. Huber and E. Baumgartner, Helv. Phys. Acta 26 (1953), 420
   Helv. Phys. Acta 26 (1953), 525.
6. R. Ricamo, Helv. Phys. Acta 26 (1953), 423.
7. W. Haeberli, "Fast Neutron Physics", Ed. J.B. Marion and J.L. Fowler (Interscience Publishers, New York, 1963) Part II, Chap. VG.
8. Proc. International Symposium on Polarisation Phenomena of Nucleons. (Basel 1960) Suppl. Helv. Phys. Acta 6 (1961).
9. H. Feshbach, C.F. Porter and V.F. Weisskopf, Phys. Rev. 96 (1954), 448.
10. H.H. Barschall, Phys. Rev. 86 (1952), 431.
11. W. Hauser and H. Feshbach, Phys. Rev. 87 (1952), 366.
12. F. Bjorklund and S. Fernbach, Phys. Rev. 109 (1958), 1295.
13. D. Wilmore and P.E. Hodgson, Nucl. Phys. 55 (1964), 673.
14. B. Holmqvist, Arkiv för Fysik 38 (1968), 403.
15. R.K. Adair, S.E. Darden and R.E. Fiddo, Phys. Rev. 96 (1954), 503.
16. R.B. Galloway, Proc. R.S.E. A70 (1971), 181.
17. A.E. Remund, Helv. Phys. Acta 26 (1956), 545.
18. B.M. McCormac, M.F. Steuer, C.D. Bond and F.L. Hereford, Phys. Rev. 108 (1957), 116.
19. J.D. Clement, F. Boreli, S.E. Darden, W. Haeberli and H.R. Striebel, Nucl. Phys. 6 (1958), 177.
20. D. Brown, A.T.G., Ferguson and R.E. White, Nucl. Phys. 25 (1961), 604.
21. C. Wong, J.D. Anderson, J.W. McClures and B.D. Walker, Phys. Rev. 128 (1962), 2339.
22. J. Durisch, R. Gleyvod, P. Huber and E. Baumgartner, Helv. Phys. Acta 36 (1963), 269.
23. A.J. Elwyn, R.O. Lane, A. Langsdorf and J.E. Monahan, Phys. Rev. 133B (1964), 80.

REFERENCES (Contd.)

24. F. Perey and B. Buck, Nucl. Phys. 32 (1962), 353.

25. D.J. Bredin, Phys. Rev. 135B (1964), 412.

26. R.J. Olness, K.K. Seth and H.N. Lewis, Nucl. Phys. 52 (1964), 529.

27. A.T.G. Ferguson, R.E. White and D. Wilmore, Nucl. Phys. 76 (1966), 369.

28. A.S. Mahajan, Nucl. Phys. A95 (1967), 193.

29. G.V. Gorlov, N.S. Lebedeva and V.M. Morozov, YAD. Fiz. 5 (1967), 910. (English Trans. Sov. J. Nucl. Phys. 6 (1968), 663.)

30. K. Wiedemann, E. Baumgartner, D. Ellgehausen, R. Gleyvod and P. Huber, Helv. Phys. Acta 42 (1969), 259.

31. D. Ellgehausen, E. Baumgartner, R. Gleyvod, P. Huber, A. Stricker and K. Wiedmann, Helv. Phys. Acta 42 (1969), 269.

32. L. Rosen, Proc. 2nd International Symposium. Polarization Phenomena of Nucleons. Karlsruhe, Ed. P. Huber and H. Schopper, Experimentia Suppl. 12 (1965), 253.

33. M.V. Pasechnik, I.A. Korzh, I.E. Kashuba, V.M. Mishchenko, N.M. Pravdivy and I.E. Sanzhur, YAD. Fiz. 11 (1970), 958. (English Trans. Sov. J. Nucl. Phys. 11 (1970), 533.)

34. E. Zijip and C.C. Jonker, Nucl. Phys. A222 (1974), 93.

35. A. Waheed, Ph.D. Thesis, University of Edinburgh, 1975.

36. A.H. Hussein, J.M. Cameron, S.T. Lam, G.C. Neilson and J. Soukup, Phys. Rev. C15 (1977), 233.

37. R.B. Galloway and A. Waheed, Phys. Rev. C19 (1979), 268.

38. L. Rosen, J.G. Beery, A.S. Goldhaber and E.H. Auerbach, Ann. Phys. 34 (1965), 96.

39. F.D. Becchetti and G.W. Greenlees, Phys. Rev. 182 (1969), 1190.

40. R.B. Galloway and A. Waheed, Nucl. Phys. A318 (1979), 173.

41. C.Y. Fu and F.G. Perey, Atomic Data and Nuclear Data Tables 16 (1975), 409.

42. F.H. Marshall and J.W. Coltman, Phys. Rev. 72 (1947), 528.

43. J.B. Birks, "The Theory of Scintillation Counting", Pergamon Press, New York, 1964.

J.B.A. England, "Techniques in Nuclear Structure Physics", MacMillan Press Ltd., London, 1974.

REFERENCES (Contd.)

44. H. Davie, Ph.D. Thesis, University of Edinburgh, 1972.

45. M.L. Roush, M.A. Wilson and W.F. Hornyak, Nucl. Instr. and Meth. 31 (1969), 112.

46. F.K. McN. Watson, Private Communication.

47. F.K. McN. Watson, Nucl. Instr. and Meth. 137 (1976), 193.

48. R.B. Galloway, Nucl. Instr. and Meth. 92 (1971), 537; 95 (1971), 393.

49. H. Davie and R.B. Galloway, Nucl. Instr. and Meth. 108 (1973), 581.

50. C.P.Sikkema and S.P. Steendam, Nucl. Phys. A245 (1975), 1.

51. A. Alsoraya, R.B. Galloway and A.S. Hall, Proc. 4th Int. Sym. Polarization Phenomena in Nuclear Reactions, Zürich 1975, Ed. W. Gruebler and V. Kronig (Birkhauser Verlag, Basel, 1976), p.520.

52. R.B. Galloway and R. Martinez Lugo, Proc. 4th Int. Sym. Polarization Phenomena in Nuclear Reactions, Zürich, 1975, Ed. W. Gruebler and V. Kronig (Birkhauser Verlag, Basel, 1976), p. 881. Nucl. Instr. and Meth. 158 (1979), 153.

53. C.D. Swartz and G.E. Owen, Fast Neutron Physics, Part 1, Chapter IIB (Ed. J.B. Marion and J.L. Fowler).

54. L.V. Groshev, A.M. Demidov, V.I. Pelekov, L.L. Sokolovskii, G.A. Bartholomew, A. Doveika, K.M. Eastword and S. Monaro, Nuclear Data Tables, A5 (1969), 243.

55. R.L. Auble, Nuclear Data Sheets 20 (1977), 253.

56. M.R. Schmorak, Nuclear Data Sheets 14 (1975), 559.

57. Agda Artna-Cohen, Nuclear Data Sheets 16 (1975), 267.

58. M.J. Martin and P.H. Stelson, Nuclear Data Sheets 21 (1977), 1.

59. M.R. Schmorak, Nuclear Data Sheets 13 (1974), 267.

60. R.L.Auble, Nuclear Data Sheets B5 (1971), 531.

61. M.R. Schmorak, Nuclear Data Sheets B6 (1971), 425.

62. Kamal K. Seth, Nuclear Data Sheets B7 (1972), 161.

63. M.R. Schmorak and R.L. Auble, Nuclear Data Sheets B5 (1971), 207.

64. M.B. Lewis, Nuclear Data Sheets B5 (1971), 243.

65. M.J. Martin, Nuclear Data Sheets B5 (1971), 287.

REFERENCES (Contd.)

66. Yurdanur A. Ellis, Nuclear Data Sheets B4 (1970), 635.

67. J. Block, C.C. Jonker, Physica 18 (1952), 809.

68. J.B. Parker, J.H. Towle, D. Sams, W.B. Gilbey, A.D. Purnel and H.J. Stevens, Nucl. Inst. and Meth. 30 (1964), 77.

69. B. Holmqvist, B. Gustavsson and T. Wielding, Arkiv für Physik 34 (1967), 481.

70. S.A. Cox, Nucl. Inst. and Meth. 56 (1967), 245.

71. W.E. Kinney, Nucl. Instr. and Meth. 83 (1970), 15.

72. D.E. Velkeley, J.D. Brandenberge and M.T. McEllistrom, Nucl. Instr. and Meth. 129 (1975), 231.

73. D.L. Drigo, (Private Communication), Instituto di Fisica dell Universita, Padova, Italy.

74. R.J. Howerton, UCRL 5351 (1958).

75. W.B. Gilboy and J.H. Towle, Nucl. Phys. 64 (1965), 130.

76. L. Cranberg, T.A. Oliphant, J. Levin and C.D. Zafiratos, Phys. Rev. 159 (1967), 969.

77. E,J. Feicht and H. Göbel, Z. Physik 245 (1971), 13.

78. R.L. Becker, W.G. Guindon and G.J. Smith, Nucl. Phys. 89 (1966), 154.

79. V.I. Popov, J. Nucl. Energy 9 (1959), 9. (Translated from Atomnaya Energya 3 (1957) 498).

80. S. Tanaka, Y. Tomita, K. Ideno and S. Kikuchi, Nucl. Phys. A179 (1972),513.

81. R. Batchelor, W.B. Gilboy and J.H. Towle, Nucl. Phys. 65 (1965), 236.

82. A.T.G. Ferguson, Contemporary Physics V (1963-64), 270.

83. R.B. Galloway and D.G. Vass, Nucl. Instr. and Meth. 83 (1970), 35.

84. J. Christiansen, F.W. Busser, F. Niebergall and G. Sohngen, Nucl. Phys. 67 (1965), 133.

85. W. Busse, J. Christiansen, D. Hilscher, U. Morfeld, J.A. Scheer and W.U. Schroder, Nucl. Phys. A100 (1967), 490.

86. G. Hentschel, Z. Physik 219 (1969), 32.

REFERENCES (Contd.)

87. J.R. Smith and S.T. Thronton, Nucl. Phys. A187 (1972), 433.

88. G. Haouat, J. Lachkar, J. Sigaud, Y. Patin and F. Cocu, Nuclear Science and Engineering 65 (1978), 331.

89. D.G. Foster and D.W. Glasgow, Phys. Rev. C3 (1971), 576.

90. J.H. Coon, R.W. Davis, H.F. Fethauser and D.B. Nicodemus, Phys. Rev., 111 (1958), 250.

91. O.A. Salnikov, N.I. Fetisov, G.N. Lovchikova, G.V. Kotelnikova, V.B. Anufirenko and B.V. Devkin, Sov. J. Nucl. Phys. 4 (1967), 831.

92. S. Pearlstein and E.J. Winhold, J. Nucl. Energ. 19 (1965), 497.

93. H. Lesiecki, G. Mack, G. Mertens, K. Schmidt and M. Thumm, Proc. 4th Int. Symp. on Polarization Phenomena in Nuclear Reaction, Zurich, 1975, p. E73.

94. F. Borelli, B.B. Kinsey and P.N. Shrivastava, Phys. Rev. 174 (1968), 1147.

95. V.I. Strizhak, V.V. Bobyr and L.Ya. Growa, Sov. Phys. J.E.T.P. 13 (1961), 506.

96. H. Nauta, Nucl. Phys. 2 (1956/57), 124.

97. R.L. Walter, Polarization Phenomena in Nuclear Reactions, Ed. H.H. Barschall and W. Haeberli (Univ. of Wisconsin Press, Madison, 1971) p. 317.

P.J. Pasma, Nucl. Phys. 6 (1958), 141.

98. P.S. Ot-Stavnov, G.N. Lovchikova, V.I. Popov, J.E.T.P. (U.S.S.R.) 45 (1963), 1754.

99. R.B. Perkins and E. Glashausser, Nucl. Phys. 60 (1964), 433.

100. R.J. Holt, F.W.K. Firk, R. Nath and H.L. Schultz, Nucl. Phys. A213 (1973), 147.

101. J.E. Bond and F.W.K. Firk, Nucl. Phys. A258 (1976), 189.

102. W. Tornow, Z. Physik 266 (1974), 357.

103. J.B. Marion and F.C. Young, Nucl. Reaction Analysis Graphs and Tables North Holland,(1968).

REFERENCES (Contd.)

104. Mahmud Ahmed, Munir Ahmed and M.S. Choudhury, Nucl. Instr. and Meth. 126 (1975), 309.

105. D.L. Smith, R.G. Polk and T.G. Miller, Nucl. Instr. and Meth. 64 (1968), 157.

106. P.E. Hodgson, "Nuclear Reaction and Nuclear Structure", O.U.P., 1971.

107. G.J. Pyle and G.W. Greenlees, Phys. Rev. 181 (1969), 1444.

108. E. Sheldon and V.C. Rogers, Comp. Physics Comm. 6 (1973), 99.

ACKNOWLEDGEMENTS

I wish to express my heartfelt gratitude to Dr. R.B. Galloway for suggesting the project and for continuous guidance, encouragement and interest. I am grateful to Messrs. H.J. Napier and G. Turnbull, the technical staff of the Neutron Physics laboratory, for their willing assistance even at inconvenient hours. I am indebted to Dr. K.J. Peach for his helpful attitude on computing problems.

I owe to my husband H. Alam a debt of profound gratitude, not only for taking over the domestic responsibilities in my absence but also for his patience, affection and constant encouragement. Needless to say, without his support this work would never have been completed.

I want to thank those elders, relatives and friends whose care and concern provided the mental peace so necessary for working smoothly. To the late Mrs. J.E.C. Fraser, my sister Khuku and my brother-in-law Dr. Islam, I shall always remain grateful for their care and love, without which the strain of separation from my family would have been unbearable. I am deeply thankful to Suraiya and Mahmood Bhai for their constant concern and attention. I wish to express my thanks to my friends, Edna, Winifred and Kamran whose friendship has been invaluable during the past three years.

I am indebted to the Edinburgh University Post-Graduate Studies Committee for the award of the Postgraduate Studentship which enabled me to come over to Scotland for the pursuit of higher studies. Finally I would like to thank Mrs. Chester not only for typing but also for her kindness and hospitality.